



Pilkington Library

Author/Filing Title PEARSON

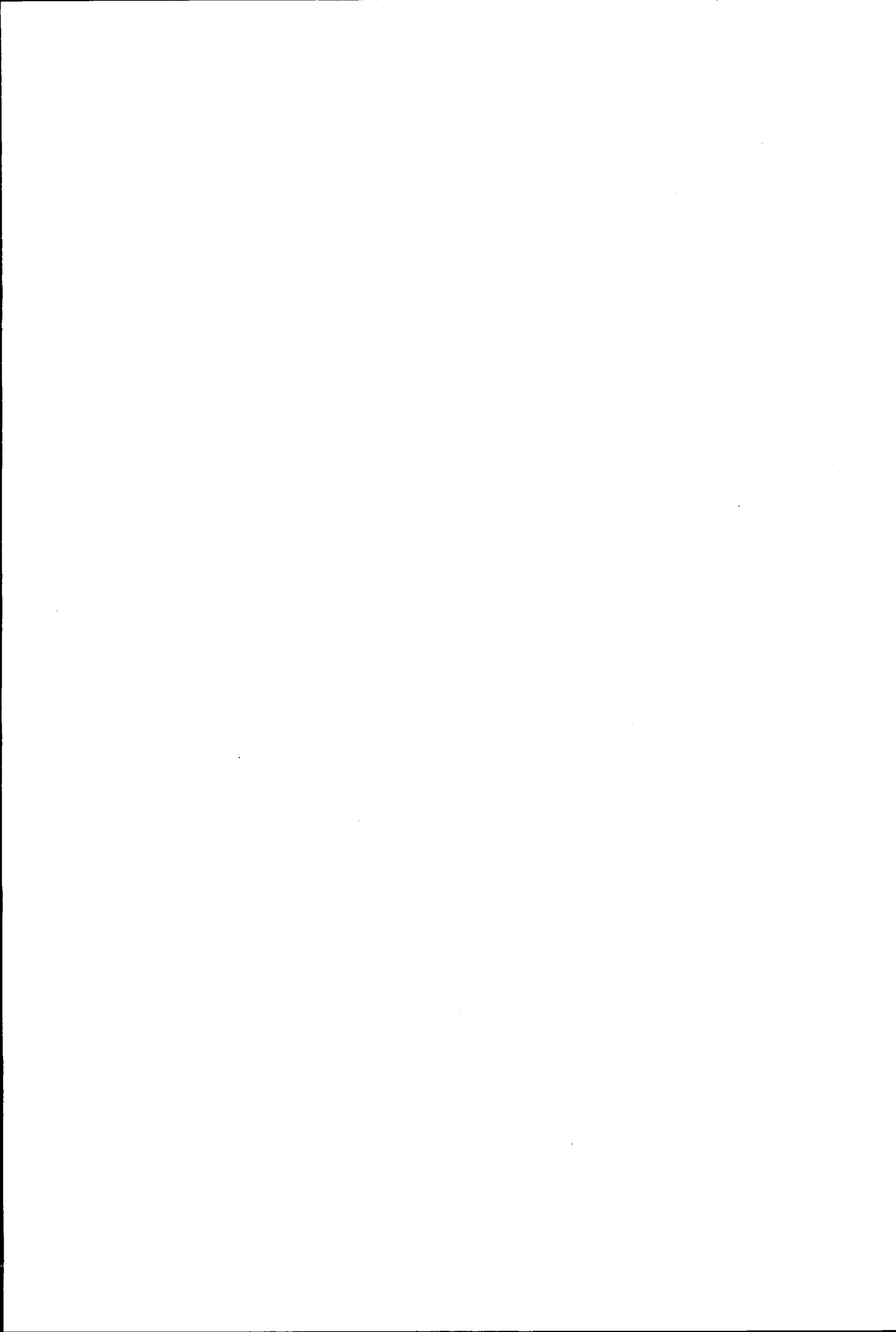
Vol. No. Class Mark T

**Please note that fines are charged on ALL
overdue items.**

RECEIVED
MAY 1988

0402587855





**THE AERODYNAMIC FLOW OVER A BLUFF BODY IN
GROUND PROXIMITY: CFD PREDICTION OF ROAD
VEHICLE AERODYNAMICS USING UNSTRUCTURED
GRIDS**

By


William Pearson

A Doctoral Thesis

Submitted in partial fulfilment of the requirements
for the award of
Doctor of Philosophy of Loughborough University

June 2000

©By William Pearson 2000

 Loughborough University Library
Date June 02
Class
Acc No. 040258785

**THE AERODYNAMIC FLOW OVER A BLUFF BODY IN GROUND
PROXIMITY: CFD PREDICTION OF ROAD VEHICLE AERODYNAMICS
USING UNSTRUCTURED GRIDS**

Abstract

The prediction of external automobile aerodynamics using Computational Fluid Dynamics (CFD) is still in its infancy. The restrictions on grid size for practical use limit the ability of most organisations to predict the full flow over an automobile. Some insight into the flow over a passenger car can be made by examining the flow over a bluff body in close proximity to the ground. One such body is the Ahmed body composed of a rounded front, straight mid-section and variable slant-rear section. This body exhibits many of the 3D flow structures exhibited by passenger cars. The main feature of the flow around this body is the change in flow structure as the angle of the slant surface at the rear of the body is increased. The flow starts fully attached and ends fully separated. In between these two regimes is a third high drag regime. The flow structure is characterised by strong counter-rotating longitudinal vortices originating from the interaction between the flow from the sides and top of the body, and a small separation from the top/slant edge on the centre-plane of the body. The flow reattaches to the slant surface and the low-pressure fluid within the separation bubble increases the drag considerably. The use of CFD incorporating time averaged statistical turbulence models to reproduce these flow patterns is assessed in this study.

Initial work concentrated on evaluating structured grid methods for this flow type. Some success was achieved with the flow fields for the attached and fully separated cases but the third high drag regime was not predicted. The flow field also exhibited a grid dependent flow structure and drag result. To examine these effects further without high grid overheads an unstructured mesh generator was developed and used to provide meshes with more grid cells clustered around the body and its wake. Analysis and refinement of the unstructured grids proved successful at removing the grid dependent flow field but still showed no evidence of the third high drag flow regime. Further, the bulk levels of drag in all cases was too high and the fully

separated flow regime occurred too late in the slant surface angle sweep, coming at 40° instead of the 30° seen in the wind tunnel results. Further analysis of the flow field using highly refined mixed meshes showed no improvement in the drag or flow field prediction with the high drag flow field still not present. The use of higher order differencing schemes and anisotropic turbulence models reduced the drag levels considerably but not to the levels seen in the wind tunnel results.

Comparison of the results from this work with the work of other authors is difficult for two reasons. Firstly, work on the specific body used in this thesis is sparse and, secondly, much of the work done by other authors was in conjunction with automotive manufacturers and details of the specific numerical methods employed are not available. The most important parallel conclusion from the work presented here and that of other authors is the inability of the CFD prediction to capture the change in flow mode as the angle of slant surface is increased. This failure can, in all probability, be attributed to the use of a steady-state CFD solution algorithm to capture the flow field around the body. A small possibility perhaps still exists that further grid refinement, very localised around the body, would help, but the detailed and careful predictions presented in this study make this highly unlikely. The most important piece of further work that could follow this work would therefore be the application of a time-accurate (unsteady) CFD solution algorithm to the bluff body in ground proximity problem. Whether these predictions should be of an unsteady RANS nature, or full LES predictions would be best answered by applying these methods to the present flow problem which is fundamental to the study of automobile aerodynamics.

Table of Contents

List of Figures	v
List of Tables	xix
Acknowledgements.....	xx
1 Introduction.....	1
1.1 Background.....	1
1.2 Outline of the Flow Over a Typical Automobile.....	8
1.3 Methods of Evaluating Aerodynamic Forces	17
1.3.1 Wind Tunnels.....	17
1.3.2 Coast-down Tests.....	20
1.3.3 Computational Fluid Dynamics	21
1.4 A Brief Introduction to CFD.....	22
1.4.1 The History of CFD	22
1.4.2 Grids.....	22
1.4.3 Discretisation and Differencing Schemes.....	26
1.4.4 Turbulence Models	30
1.4.5 Wall Functions	33
1.4.6 Pressure-correction Methods	34
1.4.7 Solvers and Multigrid	35

1.5	Why Use Bluff Bodies Instead of Full Cars?	37
1.6	Review of CFD on Automotive Type Bodies.....	41
1.7	Direction of the Present Work	47
1.8	Initial CFD Predictions	50
1.8.1	Table of Claculations	48
1.8.2	Coarse Grid Calculations	51
1.8.3	Medium Grid Calculations.....	61
1.8.4	Effect of Differencing Scheme	66
1.8.5	Effect of Reynolds Stress Turbulence Model	71
1.8.7	Conclusions.....	74
1.9	Objectives of thesis	76
2	Tetrahedral Grid Generation	79
2.1	Introduction.....	79
2.2.	Extant Tetrahedral Mesh Generation Techniques	81
2.2.1	The Delaunay Triangulation	81
2.2.1.1	The Bowyer-Watson Algorithm.....	83
2.2.1.2	The Green-Sibson Algorithm	84
2.2.1.3	The Tanemura-Merriam Algorithm	85
2.2.1.4	Difficulties with the Delaunay Triangulation Algorithms	87
2.2.2	The Advancing-Front Algorithm	88
2.2.3	Other Schemes	91
2.2.3.1	Delaunay Based Point Insertion Methods	91
2.2.3.2	Advancing-Front Delaunay Triangulations.....	92
2.2.3.3	Other Frontal Delaunay Methods.....	94
2.2.3.4	Advancing Layers Method	95
2.2.3.5	Other Methods.....	96

2.2.3.6	Conclusions	96
2.3	STORAGE SCHEMES	97
2.3.1	Heap List for the Faces	97
2.3.2	Quad/Octrees for the Points and Faces.....	100
2.4	The Advancing Front Algorithm	101
2.5	Intersection Tests	105
2.6	Initial Results	107
2.7	3D Initial Results	114
2.8	Completion Step for the Advancing Front Mesh Generator.....	117
2.9	Smoothing.....	123
2.10	Edge and face Swapping.....	126
2.11	Conclusions.....	131
3	Initial Calculations Using Unstructured Grids.....	133
3.1	Introduction.....	133
3.2	Description of Commercial Grid Generation Package	134
3.3	Lid driven cavity.....	135
3.4	Backward Facing Step	150
3.5	Ahmed Body	160
3.5.1	Comparison of the Delaunay and Advancing Front grids	160
3.5.2	Comparison of solutions for Delaunay and Advancing Front grids	164
3.6	Conclusions.....	171

4.	Ahmed Body Calculations Using Unstructured Tetrahedral Grids	174
4.1	Introduction.....	174
4.2	Coarse Grid Calculations	176
4.3	Fine Grid Results	192
4.4	Alternative Fine Grid Calculations	204
4.5	Grid Modification	206
4.6	Second Level Fine Grids.....	218
4.7	Results of Higher Order Differencing Scheme.....	232
4.8	Conclusions.....	245
5.	Calculations Using Mixed Meshes	249
5.1	Introduction.....	249
5.2	Grid Generation	250
5.2.1	Structured Mesh	250
5.2.2	Unstructured Mesh.....	251
5.2.3	Pyramidal Mesh:	252
5.3	Calculations.....	256
5.4	Conclusions.....	268
6.	Conclusions.....	270
	References	278

List of Figures

Figure 1.1 The flow over a generic sports car.	1
Figure 1.2 The flow through a channel over a bump and the resulting change in pressure and velocity.....	3
Figure 1.3 The flow through a channel over a large bump and the resulting change in pressure and velocity. Note the lower pressure at the rear	4
Figure 1.4 Diagram of flows over various rear body shapes. Taken from Ahmed et al [34].....	5
Figure 1.5 The variation of drag force with angle of rear body. Taken from Ahmed et al [34].....	7
Figure 1.6 The detailed airflow around a typical car. Taken from Ahmed et al [34]....	9
Figure 1.7 The flow over an estate car configuration. Taken from Ahmed et al [34].	11
Figure 1.8 The vortex system for a sloping rear end. (a) low drag flow, (b) high drag flow regime. Taken from Ahmed et al [34].....	12
Figure 1.9 The pressure distribution on the sloping rear end of a bluff body. In the graph on the left, (II) is the three dimensional vortex generating flow and (I) is the quasi two dimensional wake flow. Taken from Ahmed et al [34].....	13
Figure 1.10 The variation of total drag and drag shares with rear slope angle. Taken from Ahmed et al [34].....	14
Figure 1.11 The flow structure over the rear of a saloon car. Taken from Ahmed et al [34].....	15
Figure 1.12 A typical open jet, closed return wind tunnel.....	19
Figure 1.13 A table of the worlds larger automotive wind tunnels, taken from Hucho, et al [34].....	20
Figure 1.14 A structured grid over the Ahmed body	24
Figure 1.15 An unstructured grid over the Ahmed body	25
Figure 1.16 A mixed grid over the Ahmed body	25

Figure 1.17 The Ahmed body	38
Figure 1.18 The two modes of flow that occur over the rear of the Ahmed body. Taken from Ahmed et al [34].....	39
Figure 1.19 The total pressure contours and streaklines over the rear of the Ahmed body for the low drag case [2].	41
Figure 1.20 Coarse Grid 1C - far field view	51
Figure 1.21 Coarse Grid 1C (70 000 grid points)	51
Figure 1.22 Velocity Vectors in the Symmetry Plane. Hybrid Differencing and k- ϵ Turbulence Model.....	52
Figure 1.23 Zero Axial Velocity Contour on Slant (the backflow is white). Hybrid Differencing.....	53
Figure 1.24 Coefficient of Pressure on Symmetry Plane and Upper Surface. k- ϵ Turbulence Model.....	54
Figure 1.25 Drag Coefficient versus Slant Angle for the k- ϵ Turbulence Model.....	55
Figure 1.26 Normalised Total Pressure Contours (-0.2 - 0.95) From the coarse grid CFD results	56
Figure 1.27 Total Pressure Contours at $x/L = 1.0$ (taken from Ahmed et al. [2])	56
Figure 1.28 Velocity Vectors (tracking time = 0.003s.) From the coarse grid CFD results	57
Figure 1.29 Velocity Vectors at $x/L = 1.479$ (taken from Ahmed et al. [2]).....	57
Figure 1.30 Coarse Grid 2C (70 000 grid points)	58
Figure 1.31 Velocity Vectors in the Symmetry Plane. Hybrid Differencing and k- ϵ Turbulence Model.....	59
Figure 1.32 Zero Axial Velocity Contour on Slant (the backflow is white). Hybrid Differencing.....	60
Figure 1.33 Zero Axial Velocity Contour on Slant (the backflow is white). Hybrid Differencing.....	62

Figure 1.34 Drag Coefficient versus Slant Angle for the k-ε Turbulence Model.....	63
Figure 1.35 Axial Velocity Profiles in the Symmetry Plane above the Body. x/L=0.12	63
Figure 1.36 Overall Loss versus Grid Refinement for 35° Slant Angle. k-ε Turbulence Model.....	64
Figure 1.37 Contours of k/U_0^2 (0.0 - 0.064; 12 increments) on Symmetry Plane. Hybrid Diff	65
Figure 1.38 Velocity Vectors (tracking time = 0.003s.) and Normalised Total Pressure Contours (-0.2 - 0.95). QUICK and k-ε	67
Figure 1.39 Zero Axial Velocity Contour on Slant (the backflow is white). QUICK Differencing.....	68
Figure 1.40 Coefficient of Pressure on Symmetry Plane and Upper Surface. k- ε Turbulence Model.....	69
Figure 1.41 Axial Velocity Profiles in the Symmetry Plane Above the Body. x/L=0.12.....	70
Figure 1.42 Drag Coefficient versus Slant Angle for the k- ε Turbulence Model.....	71
Figure 1.43 Contours of k/U_0^2 (0.0 - 0.064; 12 increments) on Symmetry Plane. Hybrid Diff	72
Figure 1.44 Drag Coefficient versus Slant Angle. Grid 2C and Hybrid Differencing	73
Figure 2.1 The Structured grid over the Ahmed body.....	79
Figure 2.2 The solution to the hanging node problem created by grid embedding.....	80
Figure 2.3 The tessellation of triangles onto a line	80
Figure 2.4 The tessellation of tetrahedrals on a plane.....	81
Figure 2.5 The Delaunay grid (fine lines), Delaunay circumcircles (dotted lines) and Voronoi Tessellations (bold lines).....	82
Figure 2.6 Edge Swapping	84

Figure 2.7 The edge swapping used to convert a non Delaunay tessellation into a Delaunay one	85
Figure 2.8 The point selection process used in the Tanemura-Merriam Algorithm ...	86
Figure 2.9 An difficult geometry.....	87
Figure 2.10 An difficult geometry with a partial tessellation	87
Figure 2.11 The boundary grid (1D tessellation).....	89
Figure 2.12 The first face of the tessellation.....	89
Figure 2.13 The “snapping” of a new vertex to an existing one in the progressing tessellation	90
Figure 2.14 An example initial triangulation that ignores the boundary	91
Figure 2.15 Case one, there exists a suitable point already in the tessellation and the radius of the resulting triangle is less than $dstep$	92
Figure 2.16 Case two, no vertices were found so one is created along the line perpendicular to the edge at it’s median	93
Figure 2.17 Case three, no points within $.but$ some within 2 . The new point is put at the centre of the circle formed using the Tanemura-Merriam algorithm	93
Figure 2.18 The point placement strategy of the Rebay frontal method where the new point is placed along the line perpendicular to the front edge at it’s median such that the new edges have length equal to the local length scale.....	95
Figure 2.19 The insertion of new points into the heap list.....	98
Figure 2.20 The successive deletion of the smallest elements from the heap list	99
Figure 2.21 The insertion of new points into the quad tree	100
Figure 2.22 The initial 1D tessellation.....	102
Figure 2.23 The first triangle in the 2D tessellation	102
Figure 2.24 The possibility in the 2D triangulation of using an existing point for the top point of a triangle.....	103
Figure 2.25 The “new” points included in the list of possible top points for any new	

cell	104
Figure 2.26 The case where the “best” point is not allowed and the second best new point is used	104
Figure 2.27 The six surface tessellations that make up the boundary grid for a 3D mesh	105
Figure 2.28 The low quality faces on the boundary of a cube	108
Figure 2.29 The progression of the poor quality cells leading to failed cases.....	109
Figure 2.30 An example of why the interior and exterior angle tests must share the same limits	110
Figure 2.31 The testing procedure for new cells.....	111
Figure 2.32 An example of how a new cell maybe rejected from a grid due to the children cells it may produce.....	112
Figure 2.33 An example of a finished high quality surface mesh.....	112
Figure 2.34 The unsmoothed surface grid on the Ahmed body showing the various edge/face size differences	113
Figure 2.35 The grid on a curved surface that has been smoothed resulting in separation from the geometry	114
Figure 2.36 The problem of three faces that cannot see a point in front of themselves	115
Figure 2.37 The possibility of an acute or an obtuse angle between faces producing the same scalar product.....	116
Figure 2.38 The case of a face being completely contained within an existing tetrahedral	116
Figure 2.39 The proposed new element, note how it must intersect one of the other triangles.....	118
Figure 2.40 The deletion of a ‘bad’ element from the ‘hole’, and the subsequent re-triangulation.....	120

Figure 2.41 The initial grid (only the surface shown for clarity), unsmoothed and not utilising edge swapping	121
Figure 2.42 The distribution of internal face angles and volumes of tetrahedra for the above tessellation.....	122
Figure 2.43 The degrees of the internal vertices (top) and the boundary vertices (bottom)	123
Figure 2.44 The smoothed surface grid	125
Figure 2.45 The problem with Laplacian smoothing (The unsmoothed case is on the left)	125
Figure 2.46 The two neighbouring faces with the worst skewness from a node with a high vertex degree.....	127
Figure 2.47 Edge swapping between two faces	127
Figure 2.48 Two cell to three cell face swapping	128
Figure 2.49 Three cell to two cell face swapping	128
Figure 2.50 The four cell to four cell face swapping. If on the boundary it is analogous to 2D edge swapping.	129
Figure 2.51 The replacement of five cells (left) with six by face swapping. The view here is looking along the common edge of the five cell case	130
Figure 3.1 The fine boundary grid for the lid driven cavity (FLUENT package).	136
Figure 3.2 The cell skewness for the two coarse volume grids of the lid driven cavity. Advancing-Front on the top and commercial Delaunay method on the bottom.	137
Figure 3.3 The face skewness for the two coarse volume grids of the lid driven cavity. Advancing-Front on the top and commercial Delaunay method on the bottom.	138
Figure 3.4 Distribution of cell volumes for the two grids. On the top, Advancing-Front and on the bottom, Delaunay.	139
Figure 3.5 The 2D mesh slice on the centre plane through the domain, overlaid on the	

contours of cell volume on the centre plane of the lid driven cavity.....	140
Figure 3.6 The boundary conditions for the lid driven cavity test case.....	141
Figure 3.7 Contours of static pressure on the centre plane; Advancing-Front on the left and Delaunay on the right.....	141
Figure 3.8 Velocity vectors coloured by velocity magnitude on the centre plane; Advancing-Front on the left and Delaunay on the right.	142
Figure 3.9 Cell skewness for the two fine grids on the lid driven cavity test case. The Advancing-Front generated grid is on the top and the Delaunay is on the bottom.	144
Figure 3.10 Face skewness distributions for the two fine grids on the lid driven cavity test case. The Delaunay case is on the bottom and the Advancing-Front on the top.	145
Figure 3.11 Cell volume distribution on the fine grids. Advancing-Front on the top and Delaunay on the bottom.	146
Figure 3.12 The contours of cell volume on the centre plane of the lid driven cavity test case for the two fine grid, overlaid with the grid slice on that plane. The Advancing-Front method is on the left with the Delaunay generated grid on the right. (Note: The long thin sliver cells here do not necessarily indicate highly skewed cells).....	147
Figure 3.13 Contours of static pressure on the centre plane of the lid driven cavity test case for the two fine grids. The Advancing-Front method is on the left with the Delaunay generated grid on the right.....	148
Figure 3.14 Vectors of velocity on the centre plane of the lid driven cavity test case coloured by velocity magnitude on the fine grids. The Advancing-Front method is on the top with the Delaunay generated grid on the bottom.	149
Figure 3.15 The dimensions for the backward facing step test case.....	150
Figure 3.16 The surface grid on the backward facing step. The grid walls are coloured by boundary condition type: Black - wall; yellow - symmetry; red - outflow. .	151
Figure 3.17 the distribution of cell skewness on the two grids for the backward facing	

step, the Advancing-Front grid is on the top and the Delaunay on the bottom.	152
Figure 3.18 the distribution of cell volume on the two grids over the backward facing step. Advancing-Front on the top and Delaunay on the bottom.	153
Figure 3.19 The distribution of face skewness for the two grids over the backward facing step. Advancing-Front on the top and Delaunay on the bottom.	154
Figure 3.20 The contours of cell skewness on the centre plane overlayed with the grid itself (Advancing-Front on the left and Delaunay on the right).....	155
Figure 3.21 The contours of velocity magnitude on the centre plane of the three-dimensional backward facing step. The Advancing-Front grid is on the left. ...	156
Figure 3.22 The close up of the contours of velocity magnitude on the centre plane of the three-dimensional backward facing step. The Advancing-Front grid is on the left.	157
Figure 3.23 The streaklines coloured by velocity magnitude immediately after the step on the centre plane of the three-dimensional backward facing step. The Advancing-Front grid is on the left.....	157
Figure 3.24 The contours of static pressure on the centre plane of the three-dimensional backward facing step. The Advancing-Front grid is on the left. ...	158
Figure 3.25 The contours of x-velocity on the floor of the backward facing step. The number of contours is reduced to give a clearer picture of where the flow reattaches after the step.	159
Figure 3.26 The breakdown of cell skewness for the two grids. Delaunay on the bottom, Advancing-Front on the top.....	161
Figure 3.27 The breakdown of cell volume for the two grids. Delaunay on the bottom, Advancing-Front on the top. The range of volumes is from 0 to 0.022m ³	162
Figure 3.28 The breakdown of face (boundary and interior) skewness for the two grids. Delaunay on the bottom, Advancing-Front on the top.	163
Figure 3.29 The velocity magnitude contours for the two grids on the symmetry plane. Delaunay on the right, Advancing-Front on the left.	164
Figure 3.30 The contours of static pressure for the two grids on the symmetry plane.	

Delaunay on the right, Advancing-Front on the left.	165
Figure 3.31 The velocity vectors for the two grids coloured by velocity magnitude. Delaunay on the bottom, Advancing-Front on the top.	166
Figure 3.32 The velocity vectors for the two grids coloured by velocity magnitude on a vertical plane 0.5m behind the end of the body. Delaunay on the bottom, Advancing-Front on the top.	167
Figure 3.33 The contours of static pressure for the two grids on a vertical plane 1.5m behind the end of the body. Delaunay on the right, Advancing-Front on the left.	168
Figure 3.34 The contours of velocity magnitude for the two grids on the rear surfaces of the body. Delaunay on the right, Advancing-Front on the left.	168
Figure 3.35 The drag forces on the Ahmed body for the two grids. Also shown are the experimental results from Ahmed and MIRA.	169
Figure 3.36 The static pressure values on the upper body centreline for the two grids.	170
Figure 4.1: Geometry of the Ahmed body (copy of Figure 1.17, included here for ease of reference)	175
Figure 4.2: Coarse tetrahedral grid over Ahmed body.....	176
Figure 4.3: Quality of coarse tetrahedral grids	177
Figure 4.4: Comparison of drag force versus back slant angle for coarse tetrahedral grids. Also shown are the experimental values for MIRA and Ahmed results..	180
Figure 4.5 The contours of velocity (m/s) on the symmetry plane.....	181
Figure 4.6 The contours of static pressure (Pa) on the symmetry plane.....	182
Figure 4.7 The streaklines on the symmetry plane coloured by velocity magnitude (m/s).	184
Figure 4.8 The contours of velocity on the slant and rear surfaces of the body, reduced to 4 levels so as to give an impression of separation on the body. The symmetry	

plane is on the right side.	186
Figure 4.9 The velocity vectors (coloured by velocity) on the left and static pressure contours on the right for the plane $x = 0.5\text{m}$ (body is 0 to 1.044m). 20°	187
Figure 4.10 The velocity vectors (coloured by velocity) on the left and static pressure contours on the right for the plane $x = 0.5\text{m}$ (body is 0 to 1.044m). 25° to 35°	188
Figure 4.11 The velocity vectors (coloured by velocity) on the left and static pressure contours on the right for the plane $x = 0.5\text{m}$ (body is 0 to 1.044m). 40° to 50° .	189
Figure 4.12 The plot of static pressure on the upper surface centre line of the Ahmed body for the coarse grids.....	191
Figure 4.13 The plot of static pressure on the lower surface centre line of the Ahmed body for the coarse grids.....	191
Figure 4.14 The contours of velocity magnitude (m/s) on the symmetry plane of the fine grid over the Ahmed body for the 20° , 25° , 30° , 35° , 40° , 45° and 50° cases.	193
Figure 4.15 The contours of static pressure (Pa) on the symmetry plane of the Ahmed body.....	195
Figure 4.16 The velocity vectors (m/s) on the symmetry plane of the Ahmed body for the fine grid calculations.....	196
Figure 4.17 The contours of x velocity (m/s) on the slant and rear surfaces of the Ahmed body for the 25 to 50 back slant cases. The number of contours is reduced for clarity.....	198
Figure 4.18 The combined plots of in plane velocity vectors(coloured by velocity magnitude, m/s) with the contours of static pressure (Pa). Both are situated 0.5m down stream of the start of the body. 20°	199
Figure 4.19 The combined plots of in plane velocity vectors (coloured by velocity magnitude, m/s) with the contours of static pressure (Pa). Both are situated 0.5m down stream of the start of the body. 25° to 35°	200
Figure 4.20 The combined plots of in plane velocity vectors(coloured by velocity	

magnitude, m/s) with the contours of static pressure (Pa). Both are situated 0.5m down stream of the start of the body. 40° to 50°.	201
Figure 4.21 The static pressure (Pa) distribution on the centre line of the Ahmed body for the fine grid calculations.	203
Figure 4.22 Coefficient of drag for the coarse and fine grid results on the Ahmed body.....	203
Figure 4.23 The diversion of axial momentum by the coarse grid	204
Figure 4.24 The modified grid over the rear of the Ahmed body. Altered to allow the seperation of the flow to be aligned with the grid.	206
Figure 4.25 The two fine level grids. Original on the left and modified on the right. The plot of the modified grid also shows the interior plane on the back of the body that ensures the shape of the cells leaving the back/slant edge.....	206
Figure 4.26 The contours of velocity magnitude (m/s) on the symmetry plane for the modified fine grid cases.....	207
Figure 4.27 The contours of static pressure (Pa) on the symmetry plane of the modified fine grid calculations.	209
Figure 4.28 The velocity vectors on the symmetry plane of the modified grids on the Ahmed body. Coloured by the velocity magnitude (m/s).....	210
Figure 4.29 The contours of x-velocity (m/s) on the rear surface of the body.	212
Figure 4.30 The combined plots of in-plane velocity vectors(coloured by velocity magnitude m/s) with the contours of static pressure. Both are situated 0.5m down stream of the start of the body.25° and 30°.....	213
Figure 4.31 The combined plots of in-plane velocity vectors(coloured by velocity magnitude m/s) with the contours of static pressure. Both are situated 0.5m down stream of the start of the body. 35° to 45°.	214
Figure 4.32 The static pressure distribution on the centre-line upper surface of the Ahmed body for the modified fine grid.	215
Figure 4.33 The comparison of the drag coefficients for the Ahmed body over a range	

of back slant angles.....	216
Figure 4.34 The contours of velocity magnitude (m/s) on the symmetry plane for the fine-fine grids (left) and the modified fine-fine grids (right).....	219
Figure 4.35 The contours of static pressure (Pa) on the symmetry plane for the two types of grid. The modified grid is on the right.	221
Figure 4.36 The velocity vectors coloured by velocity magnitude (m/s) for the two grids (modified grids is on the right).	222
Figure 4.37 The contours of x-velocity (m/s) on the surfaces of the body (the modified grid is on the right).....	224
Figure 4.38 The combined plots of in-plane velocity vectors(coloured by velocity magnitude) with the contours of static pressure. Both are situated 0.5m down stream of the start of the body. For the fine-fine grids. 30° and 35° slant surface angles.	225
Figure 4.39 The combined plots of in-plane velocity vectors(coloured by velocity magnitude) with the contours of static pressure. Both are situated 0.5m down stream of the start of the body. For the fine-fine grids. 40° and 45° slant surface angles.	226
Figure 4.40 The combined plots of in-plane velocity vectors (coloured by velocity magnitude) with the contours of static pressure. Both are situated 0.5m down stream of the start of the body. For the mod-fine-fine grids. 30° and 35° slant surface angles.....	227
Figure 4.41 The combined plots of in-plane velocity vectors (coloured by velocity magnitude) with the contours of static pressure. Both are situated 0.5m down stream of the start of the body. For the mod-fine-fine grids, 40° and 45° slant surface angles.....	228
Figure 4.42 The static pressure values seen on the upper side symmetry plane centreline of the Ahmed body for the fine-fine grids.	229
Figure 4.43 The static pressure values seen on the upper side symmetry plane centreline of the Ahmed body for the modified fine-fine grids.....	230

Figure 4.44 The static pressures on the upper surface centreline of the Ahmed body for the 45° case with both mesh types.	230
Figure 4.45 The drag coefficients for the various grids compared to the experimental values.	231
Figure 4.46 The velocity contours on the symmetry plane for the second-order calculations. (The fine-fine grids are on the left and the mod-fine-fine grids on the right).....	233
Figure 4.47 The static pressure contours on the symmetry plane for the second-order calculations. (The fine-fine grids are on the left and the mod-fine-fine grids on the right).....	234
Figure 4.48 The velocity vectors coloured by velocity magnitude on the symmetry plane for the second-order calculations. (The fine-fine grids are on the left and the mod-fine-fine grids on the right).....	235
Figure 4.49 The static pressure contours and velocity vectors coloured by velocity magnitude on the plane 0.5m behind the body for the second-order calculations. (The fine-fine grids are shown here).....	237
Figure 4.50 The static pressure contours and velocity vectors coloured by velocity magnitude on the plane 0.5m behind the body for the second-order calculations. (The modified fine-fine grids are shown here)	238
Figure 4.51 The contours of velocity on the rear of the body reduced to 4 levels to emphasize the separated region. (The fine-fine grids are on the left and the modified fine-fine grids on the right).....	240
Figure 4.52 The static pressures distribution along the upper body centreline for the 45° angle case on both grids.	241
Figure 4.53 The static pressures distribution along the upper body centreline for the 40° angle case on both grids.	242
Figure 4.54 The static pressures distribution along the upper body centreline for the 35° angle case on both grids	242
Figure 4.55 The drag results for the second order calculations on both grids.	243

Figure 4.56 The drag values for the calculations from this work and the experimental and computational work from MIRA [6].....	244
Figure 5.1 The close up of the surface mesh over the Ahmed body for the mixed meshes.....	253
Figure 5.2 The boundaries of the hexahedral mesh over the Ahmed body. The region behind and below the green surface is hexahedral the rest tetrahedral.....	254
Figure 5.3 the contours of cell volume (m^3) on the symmetry plane close to the Ahmed body.....	255
Figure 5.4 The contours of velocity magnitude (m/s) on the symmetry plane for the mixed mesh calculations.	257
Figure 5.5 The contours of static pressure (Pa) on the symmetry plane for the mixed mesh calculations.	259
Figure 5.6 The velocity vectors over the rear of the body on the symmetry plane for the mixed mesh calculations (coloured by velocity magnitude, m/s).....	260
Figure 5.7 The contours of static pressure (Pa) on the left and the velocity vectors coloured by velocity magnitude (m/s) on the right. Shown here on the vertical plane 0.5 metres behind the body for the 25°, 30° and 35° cases. The symmetry plane is on the right of each picture.	262
Figure 5.8 The contours of static pressure (Pa) on the left and the velocity vectors coloured by velocity magnitude (m/s) on the right. Shown here on the vertical plane 0.5 metres behind the body for the 40° and 45° cases. The symmetry plane is on the right of each picture.....	263
Figure 5.9 The contours of velocity (m/s) on the rear of the Ahmed body for the mixed meshes. A lower number of levels are shown to give a clearer picture..	264
Figure 5.10 The comparison of the drag coefficient variation with angle of back slant for the various types of grids.	266
Figure 5.11 The static pressure on the upper body surface centreline for the mixed grid calculations.....	267

List of Tables

Table 1.1 The calculations done for the initial investigation	50
Table 1.2 Drag Coefficient Components for 30° Slant. k-e Turbulence Model and Hybrid. High and Low Drag Measurements.....	64
Table 1.3 Drag Coefficient Components for 30° Slant	71
Table 1.4 Drag Coefficient Components for 40° Slant. Hybrid Differencing and Grid 2C. Also shown are the experimental results	73
Table 3.1 The comparison of grid sizes from Advancing-Front and Delaunay methods.	140
Table 3.2 The fine grid sizes for the lid driven cavity test case.....	142
Table 3.3 The grid sizes for the backward facing step test case	155
Table 3.4 The breakdown of the grid sizes for the initial tetrahedral grid tests over the Ahmed body.....	160
Table 4.1 The grid size for the coarsest cases.....	176
Table 4.2 The boundary conditions used for the Ahmed test cases.....	178
Table 4.3 The drag and lift on the Ahmed body for the coarse grid results. Also shown is the breakdown of the forces into skin and pressure components.....	178
Table 4.4 The grid sizes for the coarse and fine grids.	192
Table 4.5 The grid sizes for the fine-fine grids.....	218
Table 5.1 The size of the mixed mesh	256
Table 5.2 The table of lift and drag values for the mixed mesh calculations.	265
Table 5.3 The break down of the drag over the Ahmed body for the 40° slant surface angle. Also shown (for 30°) are the wind tunnel high and low drag values [2] and the results of the structured grid tests from Chapter 1.	266

Acknowledgements

I owe my greatest thanks to Dr Martin Passmore and Professor Jim Mcguirk for their support and guidance throughout the period of this study. This thesis would not have been completed without the encouragement, support and English skills of my Wife Tracey. My parents have put up with many hours of discussion during the course of this thesis and have always tried to help. Dr. Robert Lewis and the staff of Advantage-CFD from Reynard Motorsport have provided invaluable advice and have been a superb sounding board for the ideas in this thesis. Finally to everyone I know for their patience.

1 Introduction

1.1 Background.

Engineering interest in the flow over an automobile is primarily concerned with the forces that the flow exerts on the body, that is, the lift, drag and side forces, in addition to the pitching and yaw moments. The purpose of studying this flow during the automotive design process is to reduce the drag force and minimise the pitching moment on the body whilst avoiding the creation of too much positive lift. Furthermore, it is important, for handling characteristics, that the forces on the body in all three directions are stable in nature. The presence of a crosswind can seriously alter the flow over a vehicle, therefore this is an important consideration at the outset of any design study. In addition, other factors affecting the external aerodynamics must be considered, such as the requirements for cooling of the engine/transmission [21]; the flow within the passenger compartment area; and the prevention of dirt build-up on the windows of the automobile [68]. These considerations, however, only concern the domestic automobile. An additional branch of external automotive aerodynamics covers racing vehicles. Here, the concern is more to provide a large amount of down-force whilst not generating excessive drag (see Figure 1.1).

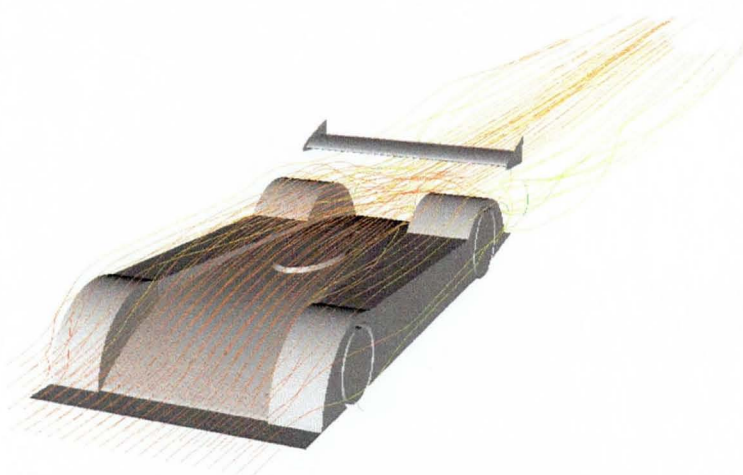


Figure 1.1 The flow over a generic sports car.

In both passenger and racing automobiles the flow consists of large regions of separated flow. In the former, this is simply due to the incompatibility of the current design/package constraints with the ideal shape for an aerodynamic automobile. The latter contains much more complex and larger scale separations. The generation of the down-force depends on large wings at high angles of attack to the flow. These wings can create large separated flow regions behind them. Open-wheeled racing cars also have wide tyres which have very complicated flow structures over and behind them.

Allowing considerations of such complex flow characteristics to be integrated into the design of a new vehicle requires the understanding of, and the ability to predict, the flow field early in the development programme. This can be done using a variety of methods: wind tunnel or water tank tests using clay mock up models, or Computational Fluid Dynamics (CFD). Clay models are expensive to build, both in time and cost. The initial costs involved in building a wind tunnel are considerable and once built, they still require upkeep and maintenance costs. By contrast CFD requires a smaller initial financial outlay and, with the increasingly widespread use of CAD models, involves less work, time and cost to produce a flow analysis for each vehicle. However, CFD is still in its infancy and there are several problems preventing engineers from using it as a reliable tool to develop new automobiles.

This thesis is concerned with understanding and making progress towards solving some of these problems. Specifically, it is concerned with those that surround the numerical techniques involved in CFD predictions. This will be done by examining the performance of existing methods on a known test-case that is related to the problem of the flow field over a car. Also, new methods will be proposed and tested on this test-case with the objective of improving the predictions.

The large separations that occur around passenger vehicles are created when the flow over the rear of a body is too steeply angled away from the direction of the local free stream. The static pressure recovery required to satisfy the conservation of momentum is large and the resulting adverse pressure gradient (which opposes the direction of the flow next to the body) grows to a point where the flow reverses. This is the start of a separation. This generation process can be seen more clearly in Figure 1.2

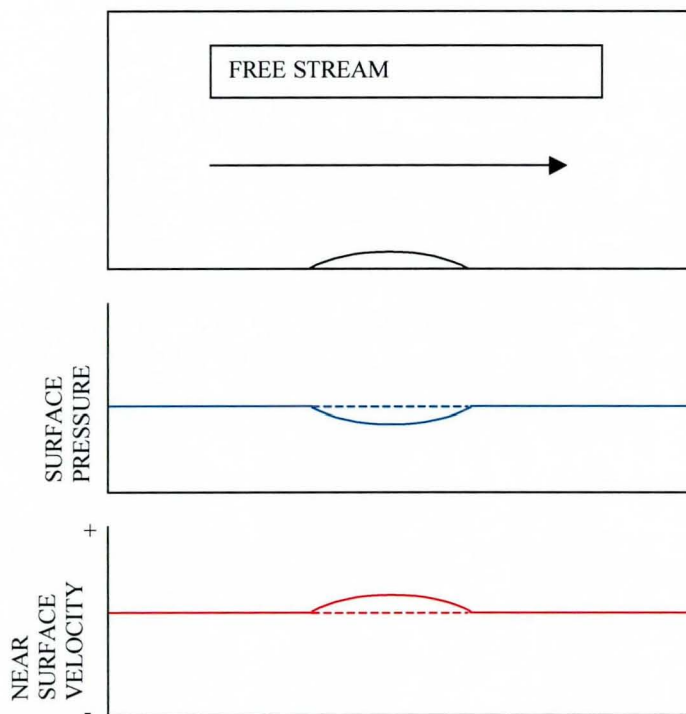


Figure 1.2 The flow through a channel over a bump and the resulting change in pressure and velocity

The pressure and velocity plots shown are only realised for small height-to-length ratios of the bump (a small pressure loss due to friction will occur, but this is negligible compared to that due to separation, see below). As the bump gets taller and shorter, the pressure rise required over the rear part of the bump will cause a higher adverse pressure gradient, which in turn will reverse the flow and cause separation. This is illustrated in Figure 1.3.

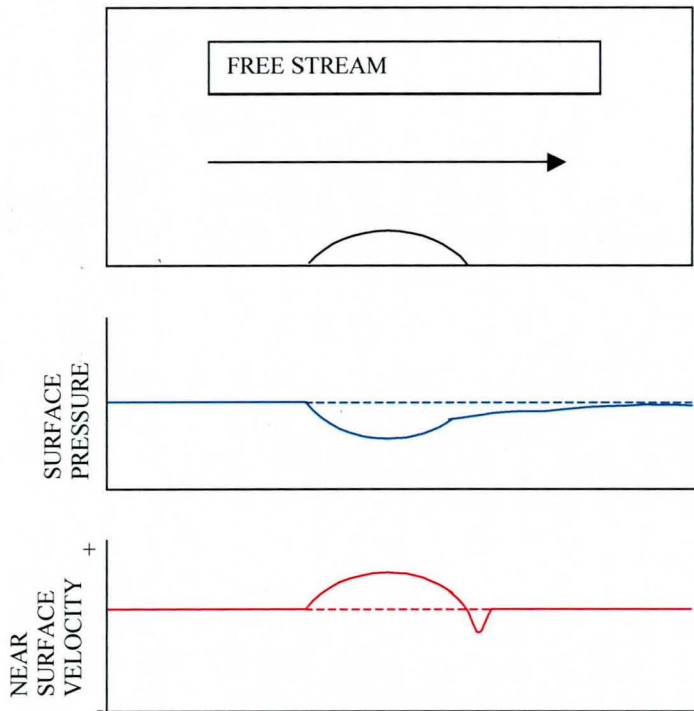


Figure 1.3 The flow through a channel over a large bump and the resulting change in pressure and velocity. Note the lower pressure at the rear

The pressure in the separated region remains at the value the flow possessed when it left the surface of the body, that is, lower than the upstream value (some pressure recovery will occur but the pressure loss is now longer). In the case of a bluff body like a car, high pressure will also be created at the front due to flow stagnation. It is this front/rear difference in pressure that makes up the majority of the drag formed in a separated wake region.

The majority of the drag from a racing car wing is different in that there is no separation from the back of the wing (if it has been correctly designed). The flow over the top of the wing is at a higher pressure than that on the underside. This pressure difference when resolved into horizontal and vertical components gives drag and lift for the wing.

In both cases, these pressure differentials contribute to the part of the drag force known as form drag. This is the main contributor to the overall drag, the remainder consisting of the effect of skin friction on the body. The drag force is usually expressed in a non-dimensional form, proportional to the square of the air speed of the vehicle and to the frontal area of the vehicle. The exact formula is:

$$D = C_D A \frac{\rho}{2} V^2 .$$

The parameter C_D (drag coefficient) depends on the amount of separation and other factors that are specific to each body shape.

There is a second contribution to pressure drag that is common to all automobiles. This is due to the three dimensional structure of the flow. The flow over the roof/rear of a car interacts with the flow coming off the sides to produce a pair of counter-rotating vortices in the longitudinal direction. These vortices originate from the c-pillars of the car, and are similar to the wing tip vortices generated by a finite span wing.

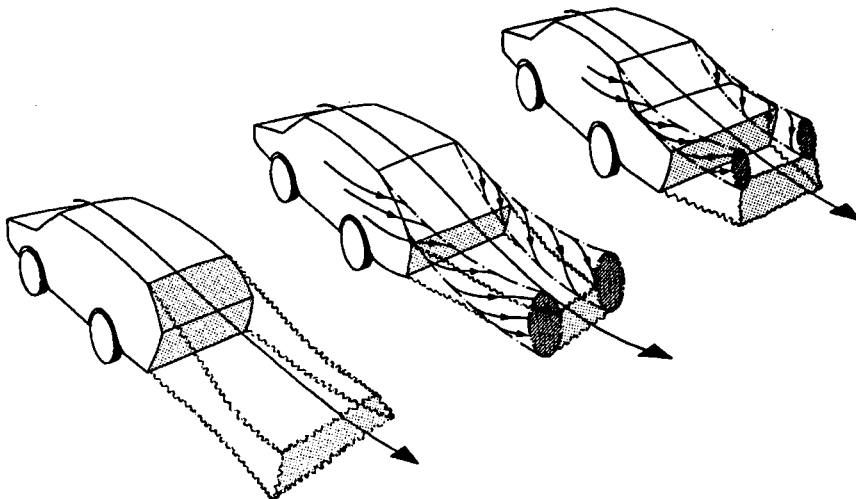


Figure 1.4 Diagram of flows over various rear body shapes. Taken from Ahmed et al [34].

These vortices have a low pressure core that is proportional to their strength. Since this pressure acts on the rear of the car, it is the cause of a new drag contribution. The vortices are strongest for a rear windshield angle of around 30° , and weakest for an estate car configuration. For the latter, there is no flow over the rear windshield, resulting in the much weaker vortex structure. This development of the vortex structure can be seen in Figure 1.4. These vortices are the decisive factor in how much drag a car will have for a given frontal area. The optimum (low drag) flow over this type of body lies somewhere between the two extreme cases. The flow over the body for an optimum case comprises attachment over the slant surface and weak longitudinal vortices. The behaviour of the circulation (and hence the drag component due to it) over a typical bluff body close to the ground, as the angle of the back slant varies, is presented in Figure 1.5 taken from Hucho et al [34]. This plot shows the three main vortex structures present in the wake of a hatchback type body (A, B and C) as well as the edge of the body from which they each originate. The twin "horseshoe" vortex structures behind the base surface of the body (A lower and B upper) behave differently as the slant surface angle is increased. A increases in strength up to a slant surface angle of $30^\circ - 35^\circ$ after which it is constant. The B vortex structure is present for low angles of slant surface and reappears for high angles. When B is not present, this is due to the strength of the longitudinal vortex structure C, that originates from the edges of the slant surface interacting with the flow coming off the sides of the body. This vortex increases in strength up to a high peak at a slant surface angle of $30^\circ - 35^\circ$, after which it disappears.

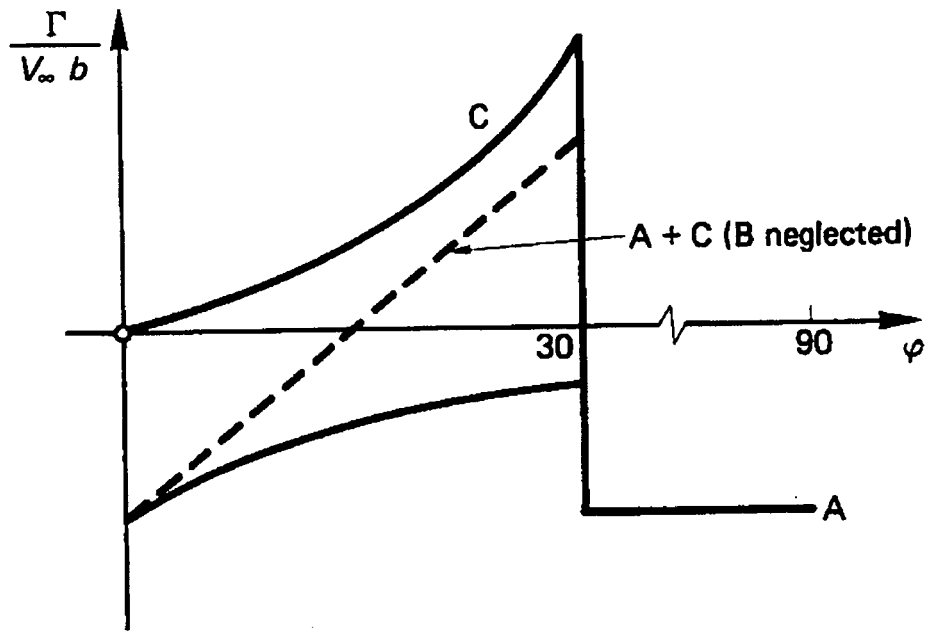
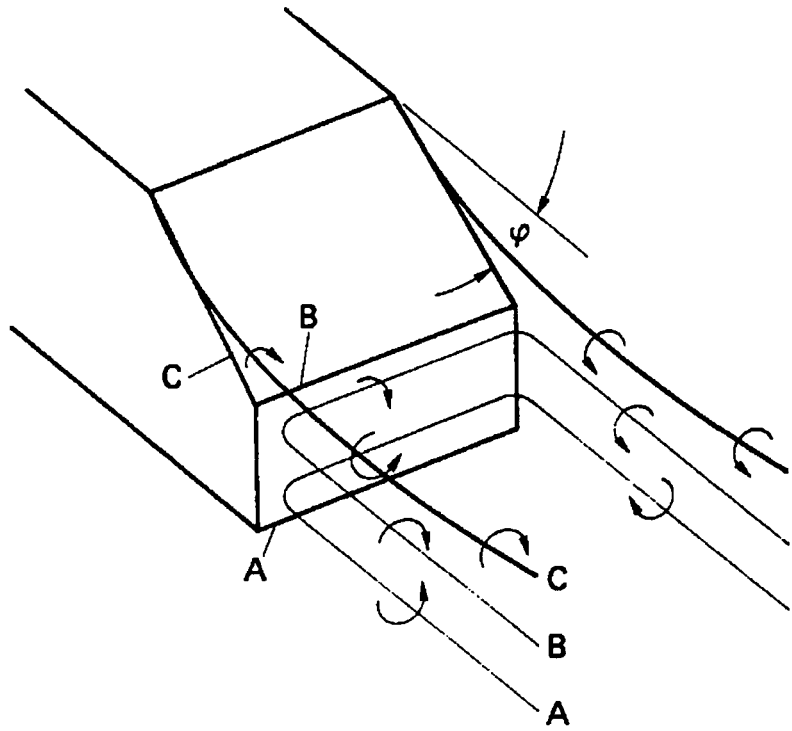


Figure 1.5 The variation of drag force with angle of rear body. Taken from Ahmed et al [34].

As stated above the purpose of all aerodynamic analysis on automobiles is to minimise this drag for given side and lift forces. Typically, at around 100km/h, approximately half of the total drag of an automobile is aerodynamic. The rest is made up of mechanical and tyre drag. Of the aerodynamic part, 80 - 85% of a modern production car's drag is due to pressure drag. There is, therefore, much scope for improvement of the aerodynamic drag. The obvious way to do this is by reducing the speed or frontal area of the vehicle. This, however, is often contrary to the original design specification. For example the size of the radiators is fixed and the size of the passenger compartment is required to be as large as possible. The remaining option is to reduce the coefficient of drag (C_D) and this requires a detailed understanding of the flow around the vehicle.

1.2 Outline of the flow over a typical automobile

The flow around a typical family car is rarely symmetric due to the presence of wind, which ensures that the car travels at a yaw relative to the free stream airspeed. However, for most conventional car shapes and small yaw angles, the structures and mechanisms within the flow are largely unchanged by the angled onset flow. For the purposes of this study, we will, therefore, focus on the particular case of symmetric flow.

Figure 1.6 is taken from Hucho [34] and shows the flow over several parts of a typical automobile. Taking these figures individually, it is evident that the first interaction of the car with the outside air occurs at the radiator inlet. Here, the flow must divide into several parts: the flow into the radiator and the flow over and under the car itself. The radiator flow is somewhat of a problem for the aerodynamicist. Sufficient airflow must be achieved through it to cool the engine. At first sight, this appears to be a simple task, however, problems occur when the vehicle is run at different speeds and with different engine loads. For example, the

airflow required to cool the engine at low speeds travelling downhill on a cold day, is much less than that at high speeds on hot days. Thus, the radiator is designed to cope with the worst case scenario and is substantially larger than required for normal (day-to-day) operation. Ultimately, the flow through the radiator and over the engine will exit the car, after causing significantly more skin friction drag than the rest of the flow over the car. In addition, the way this flow exits must be carefully decided. For example, if it were vented through the rear windshield (imagining, for a moment, that this were possible), the reduced velocity of this flow would increase the chances of separation in this area. This may, or may not, be advantageous depending on the flow structure there.

100

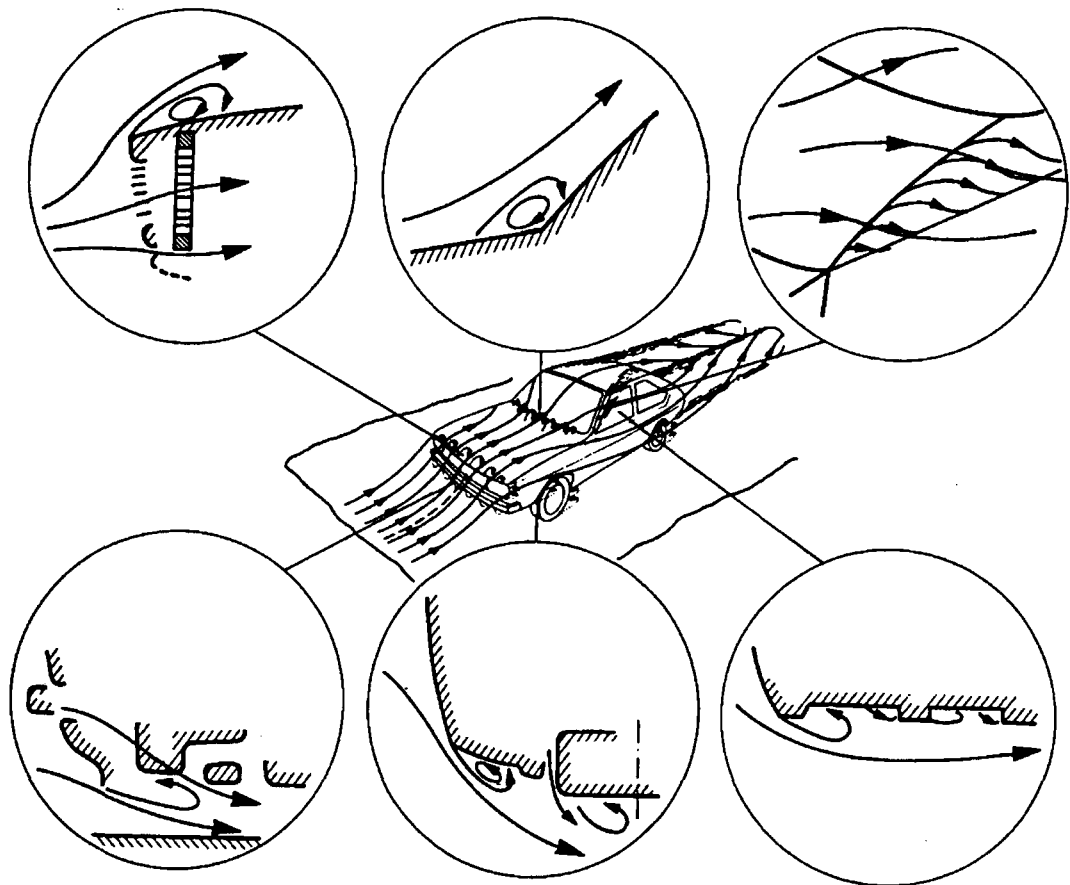


Figure 1.6 The detailed airflow around a typical car. Taken from Ahmed et al [34].

The remainder of the flow over the nose would be attached were it not for essential items, such as lights and bumpers, that must be incorporated into the front of the car. These cause localised separations to occur. The bottom left and middle frames in Figure 1.6 illustrate such features. Such essential design items can, usually, be integrated into an aerodynamic car by the use of flush glass, reduced rate of curvature bodywork and other innovative features.

The flow past the underside of the car should be as smooth as possible in order to reduce separations. It is only quite recently that designers have been attempting to achieve this. Over the upper surface, small re-circulating regions form in certain areas, for example, around the windscreen wipers and the wing mirrors. The flow around the sides of the front windscreen often separates from the a-pillars if the angle is too sharp. It can also separate from the glass/roof join for the same reason. Sharp surface curvature causes adverse pressure gradients within the flow as described in the previous section, which gradually reduce the velocity to zero and cause the separations.

The diagrams in Figure 1.6 highlight areas of local flow separation or potential separation which a designer would wish to eliminate. A complete CFD simulation might help to highlight these areas.

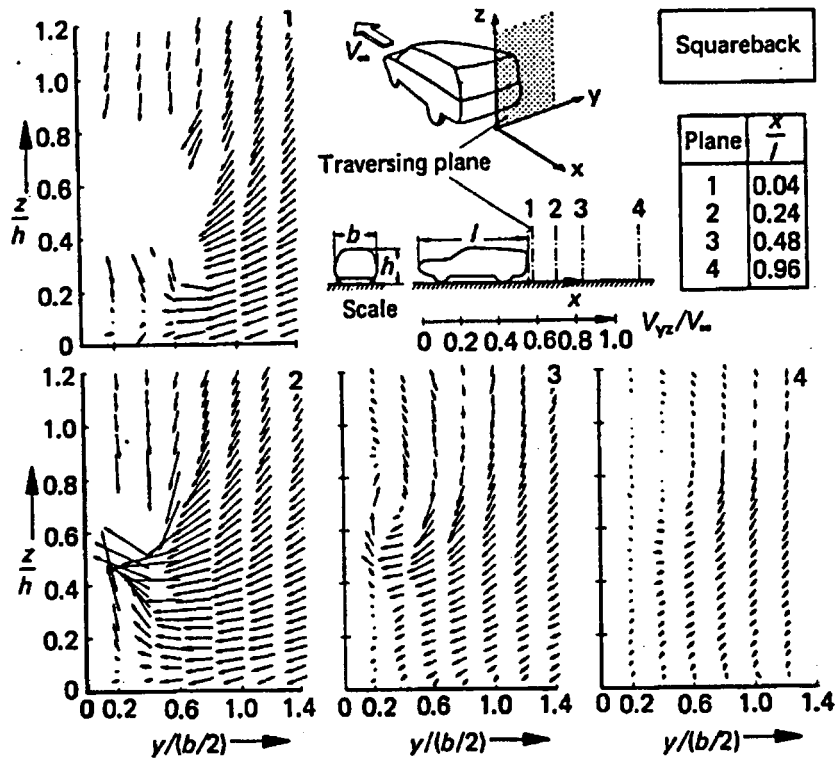


Figure 1.7 The flow over an estate car configuration. Taken from Ahmed et al [34].

The flow over the back of an estate-type vehicle can be seen in Figure 1.7. The flow from the roof, floor and sides rolls off the bodywork to drive a ring vortex rear of the body which, because the flow under the floor is at the highest velocity, is strongest nearer the floor. This vortex is immediately behind the body, and the flow inside it is at a low pressure. The flow from the bodywork then continues to develop, with the flow from the sides being drawn towards the flow from the floor (due to the pressure differential). In the axial direction, this flow expands upwards (due to the low-pressure region immediately behind the body). This action of flow being drawn inwards and upwards creates two counter-rotating longitudinal vortices (up wash), which are quite quickly dissipated after approximately one car length (see plane 3).

As the rear slant surface angle is increased, the vortex (pair) becomes stronger, attached to the rear upper corner, and leads to the occurrence of a down-wash, which keeps the flow attached down the centre, despite being slowed by the

adverse pressure gradient. The longitudinal vortex structures formed originate from the slant/side edge, and cause low-pressure regions on the edge of the body.

This can be clearly seen in diagram (a) in Figure 1.8; and the pressure distribution due to this flow is shown in Figure 1.9. The bodies in these diagrams are known as bluff bodies, which are typically used to demonstrate the behaviour of flow fields over automobiles.

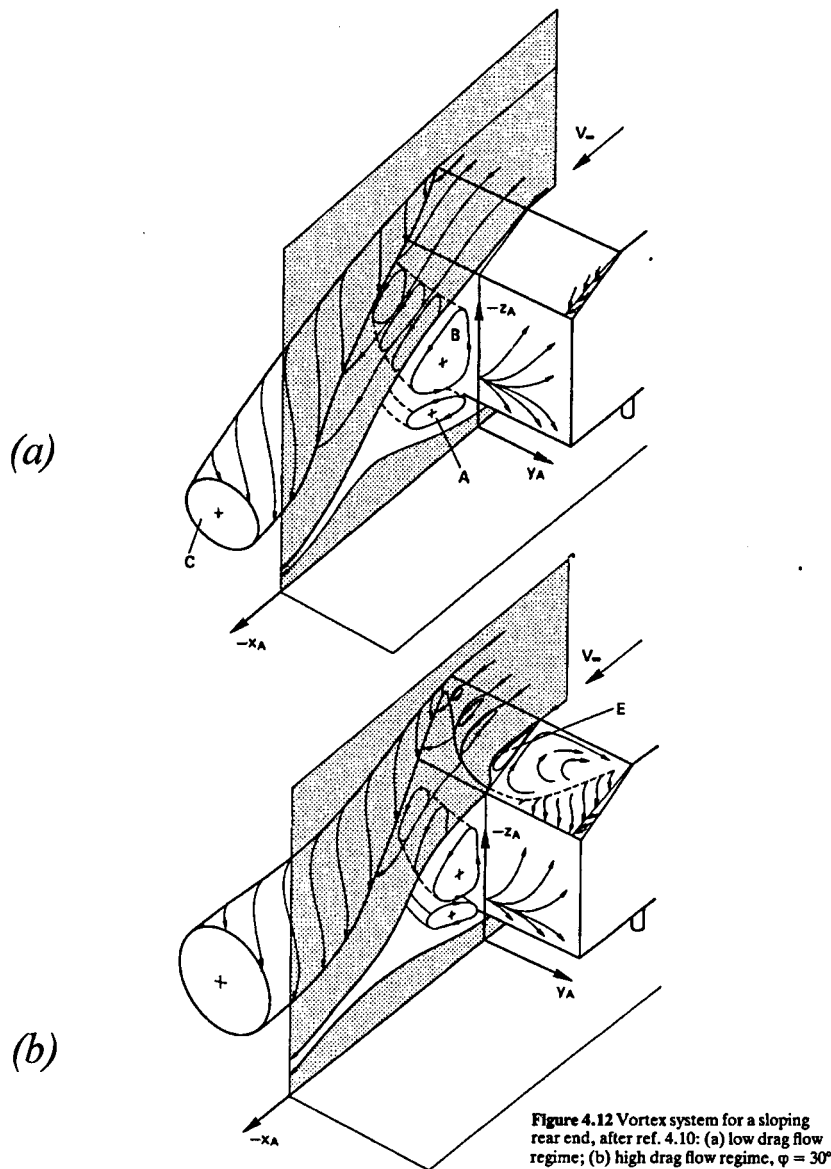


Figure 1.8 The vortex system for a sloping rear end. (a) low drag flow, (b) high drag flow regime. Taken.

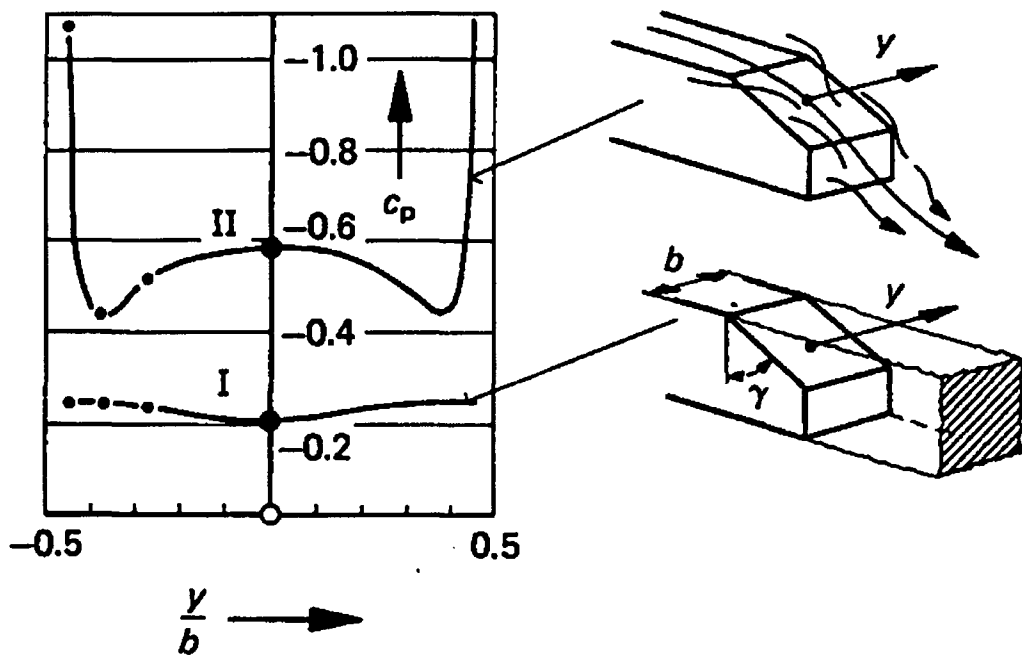


Figure 1.9 The pressure distribution on the sloping rear end of a bluff body. In the graph on the left, (II) is the three dimensional vortex generating flow and (I) is the quasi two dimensional wake flow. Taken from Ahmed et al [34].

The flow coming off the roof is drawn towards the low-pressure region behind the body. When combined with the downward motion, this creates a pair of counter-rotating longitudinal vortices. The vortex ring behind the vertical section (base area) of the rear body work is still in place, however, but obviously reduced in size due to the smaller area of this part of the body. The low-pressure region in this ring also serves to increase the intensity and downward motion of the longitudinal vortices and, as such, decreases the pressure in their respective cores. This, in turn, reduces the pressure at the point of origin of these vortices and increases the drag on the body.

As the angle of the rear slant surface is increased yet further, the flow begins to separate from the rear slant section as seen at location E in diagram (b) of Figure

1.8. This separation begins at the join of the angled section with the top and, for increasing angles increases until the whole of the rear surface is separated.

The effect of this extra separated region is to increase the drag coefficient due to the low pressure fluid contained within it. This provides a second major contribution to the drag coefficient, the other being supplied by the longitudinal vortices, which start at the side/slant join where the flow is still attached. It is clear, however, that soon after the onset of this extra vortex on the slant, it merges with the separated regions that form the start of the longitudinal vortices. The transfer of fluid from the comparatively high-pressure region behind the body (as seen in Figure 1.9) to the low-pressure region on the slant surface causes the separation to spread over the whole area. This causes the longitudinal vortex structure to break down which results in a massive drop in drag at a slant angle of around 30° (see Figure 1.10).

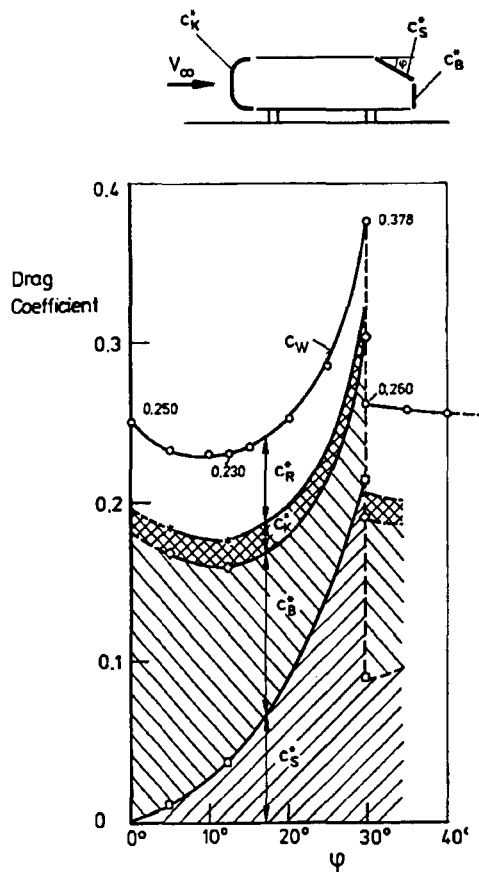


Figure 1.10 The variation of total drag and drag shares with rear slope angle.

Taken from Ahmed et al [34].

The flow regime throughout this critical angle range is probably very unstable, and the comments above relate only to the macro scale, time-averaged flow mechanisms. Several authors [34, 2] refer to the highly unstable nature of the flow, and how this instability always peaks at the angle at which the drag drops significantly. As the angle of the rear body increases further, the vortex structure returns to that of the estate car configuration, with weak longitudinal vortices in the wake. During this phase the drag is relatively constant.

For the case of a saloon or notch-back shape, the vortex structure behind the car is more complex, as shown in Figure 1.4 and Figure 1.11.

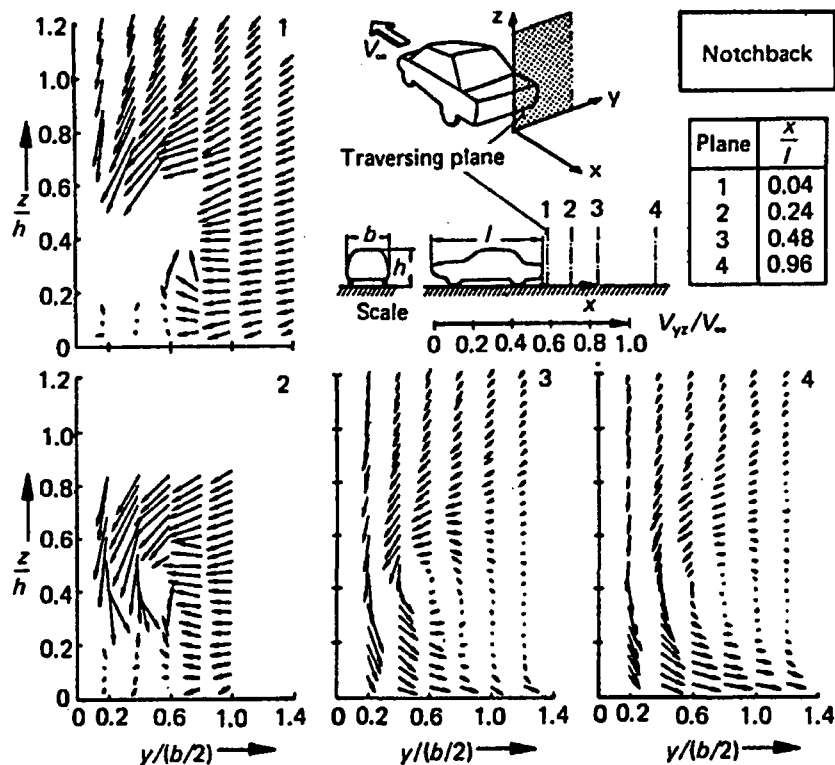


Figure 1.11 The flow structure over the rear of a saloon car. Taken from Ahmed et al [34].

The flow at the front is, of course, similar to the previous slant or square back configuration. It is at the rear that changes occur. The first thing to note is that the shape is, in fact, a sloped rear end for the initial rear section, followed by an estate section shape for the very back of the car. The flow field is, also, a mixture of the two. Flow over the sloped part resembles one of the two configurations for the hatchback case, that is, high drag or low drag, depending on whether the flow is separated from the surface. It is usual for the flow to be in the low drag regime. The C-pillars are the starting-point for the now familiar stream-wise counter-rotating vortices. The flow may separate towards the end of the sloped section and, if so, it re-attaches on the subsequent horizontal section. This re-attachment is sometimes aided by a small boot lip spoiler. The flow structure after this point is the same as for an estate car, with the added pair of stream-wise vortices.

Although the above discussion highlights the already complex flow pattern in ground vehicle aerodynamics, there are further variations on these basic designs. The lower horizontal surface of the car can be altered at the rear. Angling it upwards lowers the speed of the flow and, therefore raises the pressure. This, when combined with a downward sloping upper surface, can help to reduce drag by the same mechanism as before. The benefit is that the area of separation behind the car has been reduced, whilst the susceptibility of the flow to separation has not been increased. This effect can also be achieved along the sides of a body, resulting in a plan view of the car that resembles a boat tail. This improves the pressure recovery of the sides, which in turn increases the base pressure. The effect of these changes go some way to producing the optimum streamlined shape for a body. The designer cannot, of course, afford to allow the length of the car to be so great that the end of the body goes to a point, however, important gains can be made in drag reduction using these methods.

1.3 Methods of evaluating aerodynamic forces

Alternatives to Computational Fluid Dynamics studies to evaluate forces on road vehicles are the wind tunnel and/or coast-down tests. These are discussed in turn here.

1.3.1 Wind tunnels

The wind tunnel is the most common tool of the aerodynamicist. It allows the most accurate control of the conditions over a body. The main disadvantage is that it is difficult to build a wind tunnel large enough or fast enough to model accurately the flow over the car at realistic Reynolds numbers. The models used for development are usually 30-50% scale models. The speeds of the cars are also scaled down to between 25% and 50% of those experienced on the road. The aim of scaled wind tunnel tests is to reduce overhead costs. The reduction of scale has the effect on the flow of lowering the test Reynolds number. For example, a 50% scale wind tunnel model, with a 40m/s air speed (at atmospheric conditions) gives a Reynolds number of 1/4 that of the full scale body at 80m/s. This raises the problem of removing the local Reynolds number effects from the model that would not be seen on the full scale vehicle. For example, small separations over the front of the car may not be present on the tunnel model but these can become important flow features at full scale.

The majority of the aerodynamic work is completed at the "clay" stage with scale models, and completed in large tunnels. There do exist tunnels that will run full size cars and at reasonable speeds. As mentioned above, the lower Reynolds numbers produced by small-scale tests may have effects (in particular local ones) on the flow. For example, a re-circulation on a model may not be present at full scale, due to a change from laminar to turbulent boundary layer at higher Reynolds

numbers. These Reynolds effects must be checked for, and resolved before the model is signed off.

The costs involved with tunnels, whilst low for 'steady state' operation, must include the set up costs of both the model and the tunnel itself, which are often considerable. In commercial wind tunnels, these costs are often integrated into the costs of tunnel usage over its expected working life. Cost is, therefore, a major contributory factor when manufacturers consider the continued prolonged use of wind tunnels for model development.

There are many variations of wind tunnel, but these can be categorised to some extent. The first distinction is between closed and open-jet tunnels, when referring to the format of the working section (where the car is placed). Both formats have mutually exclusive advantages. The open-jet has a reasonably constant value of dynamic pressure throughout the working section and allows easier access to the models. In addition, the blockage effect of the models within it, that is, the percentage reduction in the uniform flow cross sectional area over the car, is minimised. The smaller the area of a closed tunnel, the larger the increase in free stream velocity to conserve mass; the open jet allows for the expansion of the flow as it is drawn over the car. The advantages of the closed test section type of tunnel are the ability to be pressurised to a level other than atmospheric and the comparative increased length of working section.

A second distinction can be made between closed return and open return tunnels. This differentiates tunnels according to the path of the air once it has left the working section until it re-enters. The closed return refers to tunnels that have a 'pipe' that connects the end and the beginning of the section with a motor/fan unit somewhere in between. The open return refers to a tunnel that is, essentially, a long straight cylinder, with the motors and fan at one end and the working section in the middle. In this case, the whole tunnel is usually encased in a large building

to ensure the same air is used repeatedly. This allows the dynamic pressure of the tunnel to be kept relatively constant.

Other factors which can be used to categorise tunnels include the provision of a rolling road, how the floor boundary layer is removed (if at all) and whether the tunnel is climate controlled. The tunnel shown in Figure 1.12 is a closed return, open jet tunnel with a rolling road and climatic capabilities.

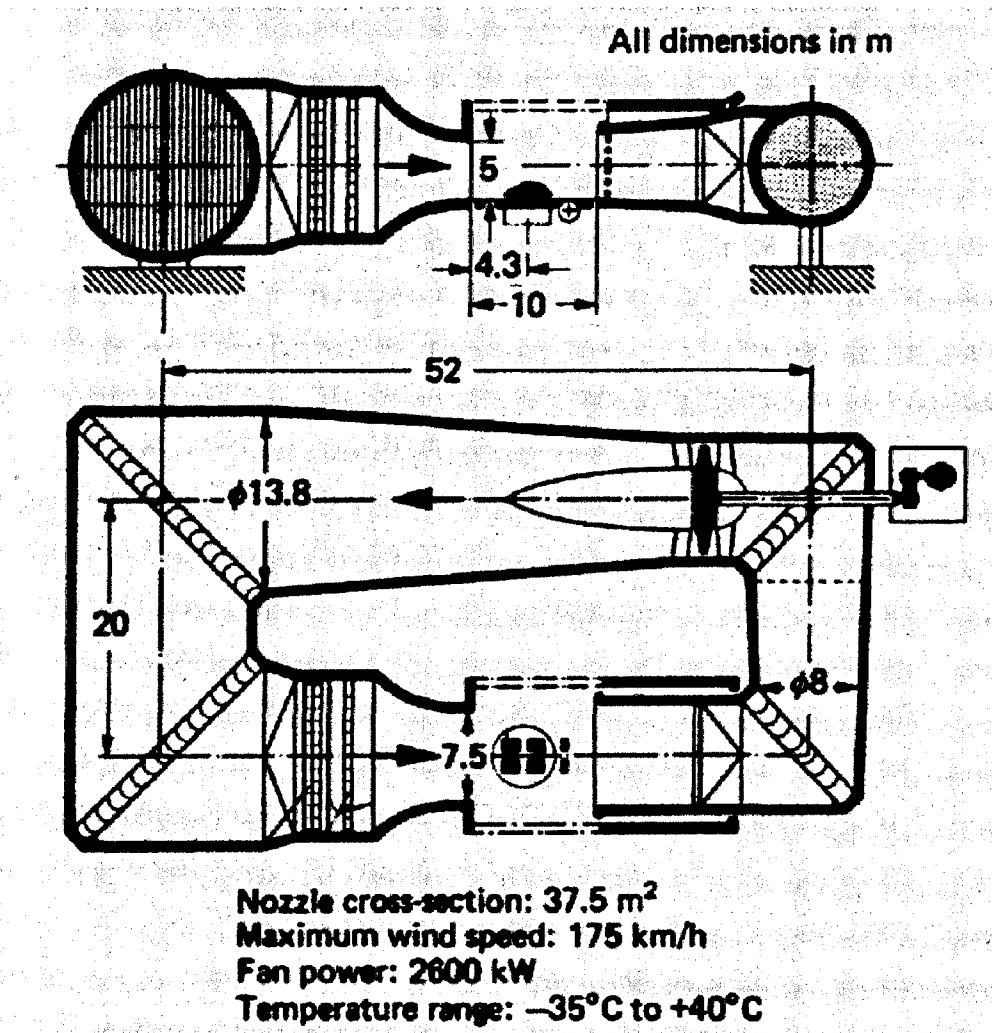


Figure 1.12 A typical open jet, closed return wind tunnel

The table in Figure 1.13 from [34] provides a list of some of the large wind tunnels available in the world to give some idea of the range of wind tunnels currently in use.

	A_T (m ²)	L_M (m)	V_{max} (km/h)	TS	K	L (m)	P (kW)	Reference
DNW	90.25	15.0	220	c	4.8	320	12700	11.66
	48.0	16.0	400	c	9.0			
General Motors	65.9	23	240	c	5	303	2950	11.21
Volkswagen	37.5	10.00	180	o	4.0	114.0	2600	11.41
Lockheed-Georgia	35.1	13.10	406	c	7.02	238.0	6700	11.51
MIRA	35.0	15.24	133	c	1.45	50.5	970	11.52
Daimler-Benz	32.6	10.00	270	o	3.53	125.0	4000	11.40
Fiat	30.0	10.50	200	o	4.0	144.0	1865	11.27
Volvo	27.06	15.8	200	sw	6.0	165.3	2300	11.71
Ford (Cologne)	24.0/8.6	10.0	182/298	o	4.0	124.0	1650/1960	11.62
Mazda	24	12.0	230	c/o	6	?	1600	11.63
Mitsubishi	24	12.0	216	c/o	?	?	2350	11.63
Ford (Dearborn)	23.2	9.15	201	c	3.80	?	1865	11.53
FKFS	22.5	9.5	220	o	4.41	150	2550	11.67
Porsche	22.3	12.0	230	sw	6.06	149.9	2200	11.68
Nissan	21.0	10.00	119	c	2.86	?	?	11.25
BMW	20.0	12.5	160	sw	3.66	45	1676	11.61
Toyota	17.5	8.00	200	c	3.66	95.0	1500	11.54
Nippon Soken	17.5/12	12.5/8.5	120/200	c	3.66	104	1450	11.63
Inst. Aérotechnique St. Cyr	15.0	10.00	144	sw	5.0	39.2	516	11.12
Fiat (2 x Climate)	12.0	11.60	160	o	4.0	99.0	560	11.27
JARI	12.0	10.00	205	c	4.06	83.3	1200	11.55
Pininfarina	11.75	9.5	150	o	6.2	27.3	625	11.42
Ford (Cologne Climate)	11.0	9.00	180	c	6.0	113.4	1120	11.56
Sofica	11.0/4.3	16.5/14.0	80/170	c	?	?	380	11.45
FKFS	6.0	15.8	200	o	4.16	84	1000	11.69
Volkswagen II	6.0	7.2/6.0	170/180	o	6.0	73.4	460	11.70
Chrysler	4.74	8.6	190	o	5.56	58.8	560	11.57
Volvo	4.32	8.6	190	o	6.60	93.2	500	11.58
Behr	5.24	14.00	120	o	6.0	48.0	147	11.60
Opel	4.30	-	120	c	?	?	460	11.59
Audi	1.5	11.0	95	o	4.3	21.0	60	
Porsche	1.5	7.5	168	o	5.0	30	160	11.68

A_T Nozzle cross-section TS Type of test section: K Contraction ratio
 L_M Length of test section o = open L Length of tunnel axis
 V_{max} Maximum wind speed c = closed
sw = slotted walls

Figure 1.13 A table of the worlds larger automotive wind tunnels, taken from Hucho, et al [34].

1.3.2 Coast-down tests

The coast-down method is a well-established technique widely used throughout the automotive industry to measure total vehicle drag. In brief, the vehicle is driven up to a known speed and, with the drive disconnected, allowed to decelerate freely. The time rate of change of vehicle velocity is proportional to the total resistive force. Extending this method to isolate the various contributions to the resistive forces - tyres, transmission, aerodynamics - is more difficult, however, using the correct experimental approach and analytical techniques, it can be achieved. A detailed description of this type of analysis is beyond the scope of this study, but can be found in Passmore [59]. The advantages of this technique are that it ensures the correct 'real world' simulation, and it may, with appropriate analysis, generate the most accurate results of all the methods outlined here.

However, as the technique cannot be applied until there is a running prototype, it is not readily applied to early aerodynamic shape development. The better solution for this type of work should be CFD analysis.

1.3.3 Computational Fluid Dynamics

CFD is the use of a computer simulation to model the flow in almost any scenario, specifically here, automobile aerodynamics. The computer uses the Navier–Stokes equations (usually in time averaged form) on the flow problem in question by separating the domain space into many smaller portions in which the flow is assumed constant. The interaction between these small portions (termed volume elements), governed by the Reynolds-averaged Navier–Stokes equations and a set of boundary and initial conditions, produces the solution of the flow over the whole domain.

With the pressure and velocity known at every point in the domain, including the surface, the forces on the body can be obtained. This is, however, a fraction of the information provided by CFD. The knowledge of the above variables, along with turbulence quantities, can be used to interrogate the flow to a higher level than ever before. CFD is beginning to be used as a powerful tool for the aerodynamicist by reducing the time taken and the cost for developing an aerodynamically efficient car.

1.4 A Brief Introduction to CFD

1.4.1 The History of CFD

The history of CFD can be traced back to the 1960's, when high speed computers became available along with developments in numerical methods. The initial calculations, it can reasonably be said, were very basic and, over time, the level of complexity that can be modeled by CFD has increased dramatically. It is only very recently that computers have developed far enough for complete systems to be modeled rather than small sub-systems of it. The numerical algorithms used in CFD have also developed substantially. The initial solutions were modeled using Euler's, equations with no account taken of the fluid viscosity. This is suitable for inviscid fluid flows, however, the majority of problems are viscous in nature, therefore, the Navier-Stokes equations must be applied. A detailed history of CFD development is too broad a topic to be discussed here in full and the reader is referred to Anderson [3] and Versteeg et al [79]. However, to familiarize the reader with what will be referred to here as 'contemporary' methods, particularly those which form the basis of the work described in this thesis, a brief summation of the numerical methods used will now be outlined.

1.4.2 Grids

The initial phase of any computational analysis of a large physical system is to divide it into smaller sub-problems, this is known as spatial discretisation. In CFD, this is the process of dividing the fluid domain to be simulated into portions of known shape (cells or mesh elements), in which the solution for the fluid variables are to be determined. By adding up the interactions of these cells with each other, a picture of a much more complex problem can be gained.

There are currently two main fields of mesh generation: structured and unstructured. Both involve body fitted meshes. A structured grid has a fixed number of grid lines, defined using families of coordinate surfaces, distributed in each coordinate direction, with the cell-to-cell connectivity defined at a global level. An unstructured grid, however, has no restrictions on grid lines as the connectivity is locally defined involving only reference to each cell's immediate neighbours. Structured grids may only be made up of hexahedrals whereas unstructured grids can be made up of any shaped elements in any combination (e.g. hexahedrals, tetrahedrals, prisms, pyramids).

A computational grid is generated in stages. Firstly, a solid model of the geometry of interest (e.g. a car model sitting in a wind tunnel) is constructed using a CAD-based description, e.g. surface patches (usually Bezier splines or non-uniform rational B-splines). For a single block structured grid, where the computational domain defined by the solid model may be considered as a topological cube, a surface grid is then constructed using a two dimensional algebraic grid generation algorithm. This surface grid is then smoothed by solving a set of elliptic partial differential equations. This smoothing is important as the accuracy of the solution is directly linked to the rate of change of cell size of the grid. Finally, the internal grid is algebraically specified from the surface grid by interpolation and smoothed using a similar set of elliptic equations. An example of a structured grid can be seen in Figure 1.14.

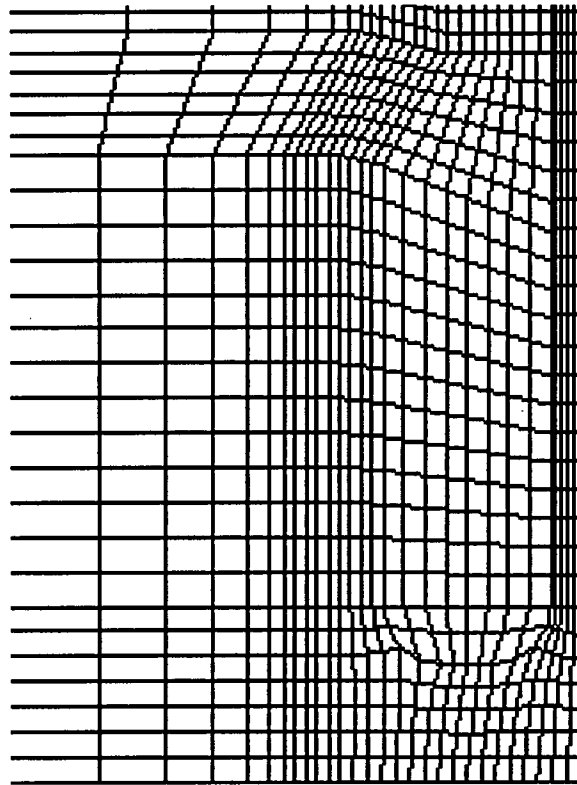


Figure 1.14 A structured grid over the Ahmed body

An unstructured tetrahedral grid (see Figure 1.15) is generated in a similar fashion. This first requires a surface tessellation composed of triangles which are fitted to the surfaces of the CAD geometry data. This is smoothed and used as the boundary condition for an internal grid generator of which there are several types, the most common being Advancing-Front and Delaunay. The quality of an unstructured mesh, again, comes from two factors. Firstly, the rate of change of cell size and, secondly, the skewness of the cell/faces. Highly skewed elements in the mesh will result in low accuracy in that region of the solution. The meshes produced can be improved using edge/face swapping and Laplacian smoothing, thereby reducing the skewness of any 'bad' cells (more details on this are provided below).

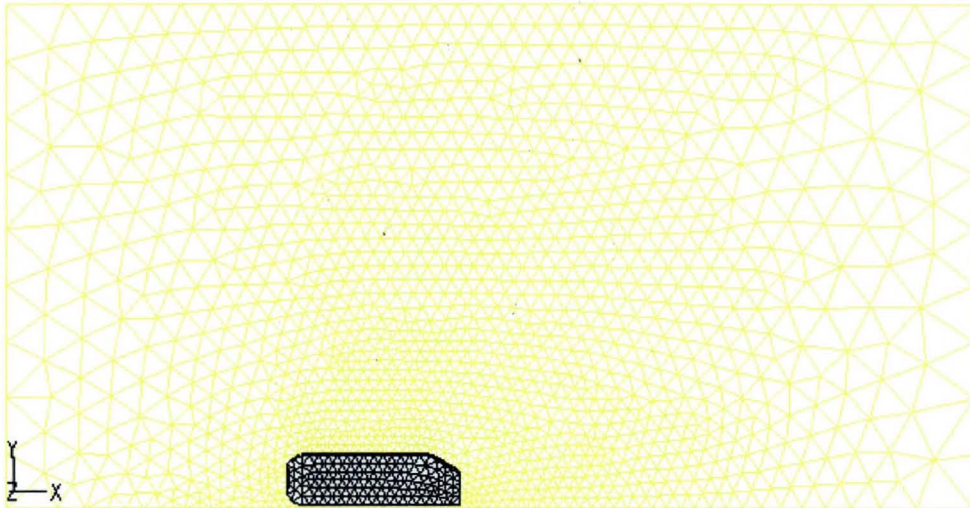


Figure 1.15 An unstructured grid over the Ahmed body

A hybrid or mixed grid is also unstructured in nature, but is not entirely made up of tetrahedrals. It will also make use of elements containing a higher number of faces, that is, five faces (pyramid), six faces (prisms) and eight faces (hexahedrals). An example of a mixed grid is seen in Figure 1.16. Hybrid grids may be used to reduce cell skewness/poor quality in sensitive regions, but continue to use tetrahedral shapes in less important regions of the flow.

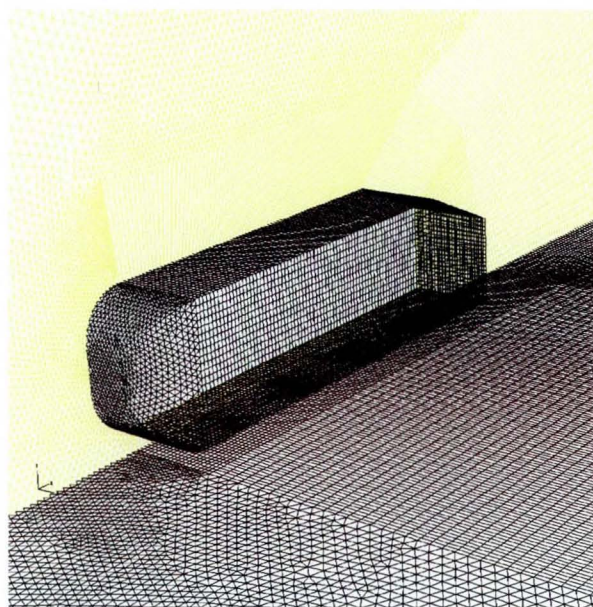


Figure 1.16 A mixed grid over the Ahmed body

1.4.3 Discretisation and differencing schemes.

Having divided the domain into small elements, the partial differential equations governing the flow must then be converted to algebraic equations relating the flow properties within each small element. This is known as discretisation. There are three main types of discretisation: finite-difference, finite-element and finite-volume. All three share the same basic mathematical approach. The most widely used in the field of CFD is the finite-volume method whilst the simplest is finite-difference. The finite-element method is rarely used and will not be covered here.

At this stage, the governing partial differential equations the discretisation method is applied to are stated here for reference. In all CFD of relevance to this thesis, it is the Reynolds-Averaged Navier-Stokes (RANS) equations for constant fluid property (i.e. low-speed, constant temperature) flow which must be solved. The description of these equations is contained in many basic texts (e.g. [3]) and the equations are also quoted here; the equation set, for given fluid density ρ and dynamic viscosity μ may be written in tensor notation as:

$$\frac{\partial(\rho U_i)}{\partial x_i} = 0$$

$$\frac{\partial(\rho U_i U_j)}{\partial x_{ji}} = -\frac{\partial P}{\partial x_i} + \frac{\partial}{\partial x_{ji}} \left(\mu \frac{\partial U_i}{\partial x_{ji}} \right) - \frac{\partial}{\partial x_i} (\overline{\rho u_i u_j})$$

Here upper case letters represent time-mean properties and lower case letters a fluctuation about the mean. To solve the above equations, a turbulence model must be provided to relate the Reynolds stresses $(\overline{\rho u_i u_j})$ to the mean velocity field, this is the subject of the following section. Once this is done, it is the role of the discretisation method to solve the above set of partial differential equations using algebraic equations relating the four variables (U_i, P) in any cell to the values in neighboring cells.

The finite-difference method replaces each of the partial derivatives in the partial differential equations with algebraic difference quotients. The most common algebraic difference quotient is taken from the Taylor series expansion, e.g.

$$U_{i+1,j} = U_{i,j} + \Delta x \cdot \frac{\partial U_{i,j}}{\partial x} + \frac{1}{2} \cdot \Delta x^2 \cdot \frac{\partial^2 U_{i,j}}{\partial x^2} + \frac{1}{6} \cdot \Delta x^3 \cdot \frac{\partial^3 U_{i,j}}{\partial x^3} + \dots$$

(Where, for convenience, and without loss of generality, a 2D (i,j) or (x,y) structured grid discretisation has been used)

By rearranging these terms:

$$\frac{\partial U_{i,j}}{\partial x} = \frac{U_{i+1,j} - U_{i,j}}{\Delta x} + \frac{1}{2} \cdot \Delta x \cdot \frac{\partial^2 U_{i,j}}{\partial x^2} + \frac{1}{6} \cdot \Delta x^2 \cdot \frac{\partial^3 U_{i,j}}{\partial x^3} + \dots$$

In addition, neglecting the higher order terms:

$$\frac{\partial U_{i,j}}{\partial x} = \frac{U_{i+1,j} - U_{i,j}}{\Delta x}$$

This approximates the partial differential term with a truncation error of:

$$T = \frac{1}{2} \cdot \Delta x \cdot \frac{\partial^2 U_{i,j}}{\partial x^2} + \frac{1}{6} \cdot \Delta x^2 \cdot \frac{\partial^3 U_{i,j}}{\partial x^3} + \dots$$

That is, this is a first order approximation

It can be easily shown (see Anderson [3]) that similar terms can be derived using this method to give a complete finite-difference approximation to the equations used.

The finite-volume method uses a slightly different approach, which is set up so as naturally to conserve fluxes across cell boundaries and, thus, throughout the domain. The approach here is to take the basic partial differential equations and first integrate over a cell volume. For example, consider just the convection (non-linear) term of the RANS equations quoted above in Cartesian coordinates:

$$\frac{\partial}{\partial x}(\rho UU)$$

Integrating over a cell of volume δVol (e.g. for a cartesian grid $\delta Vol = \Delta x \Delta y \Delta z$) gives:

$$\int_{Vol} \frac{\partial}{\partial x}(\rho UU) dVol$$

By the application of Gauss' Divergence Theorem we get:

$$\oint_{Area} (\rho UU) \cdot \underline{n} \cdot d\underline{A}$$

(where \underline{n} is the unit normal out of the cell perpendicular to the cell face area $d\underline{A}$)

If the fluid variables are considered as piecewise constant over a cell, and after suitable methods are introduced to calculate average values between neighboring cells to be applied on the faces (see below), this integral may be rewritten as the following summation:

$$\sum_{faces} (\rho UU) \cdot A_x$$

where A_x is the projected area of the cell faces perpendicular to the x direction. One of the U velocities in the expression is considered the mass flux carrying a transporting velocity and is evaluated by simple linear interpolation at the cell-face. The other U velocity is considered the convected or transported quantity and various discretisation schemes have been developed to approximate it's cell-face

value. These vary from simple first-order accurate upwind differencing (which, however, then leads, on coarse grids, to numerical diffusion), to various second order accurate methods that are preferred (e.g. QUICK or T.V.D based differencing), see Anderson [3] for a full discussion of the various types.

Therefore for each cell the term becomes:

$$(\rho UU)_{\text{East}} - (\rho UU)_{\text{West}}$$

This is easily evaluated. The same process can be performed on the other terms in the equations.

As the Navier -Stokes (conservation of momentum and mass) equations are applied in this way over each cell, the conservation of momentum is ensured due to the fluxes out of one cell being identically equal to the influx of it's neighbour.

In the FLUENT solver used for the majority of this work, the higher order spatial discretisation scheme is a QUICK type scheme. This is a weighted average of a second order upwind scheme and a second order central interpolation scheme. The standard QUICK scheme uses a 7/8's weight in favour of the upwind scheme. The value in the FLUENT solver is solution dependant and unavailable for inclusion in this thesis. It is however known that the second order upwind part of the scheme is unavailable for tetrahedral elements. With this in mind all the calculations included in this thesis use the second order central interpolation scheme.

1.4.4 Tubulence models

Although the instantaneous Navier-Stokes equations may be applied to the prediction of vehicle aerodynamic flow, as stated above, all practical CFD requires the solution of the Reynolds-Averaged derivative of these equations. This is because, at the high Reynolds numbers of interest, to resolve the turbulent motion fully, a grid of size able to resolve the smallest turbulent length scale, the Kolmogorov scales, is required. Even approximate estimates for a simple problem would require 10^{20} grid points to resolve all turbulence scales at a Reynolds number of 10^6 . This problem is far too large for the power of current computers. Therefore, a time averaged (RANS) equation must be adopted and a numerical model must be used for turbulence. There are many in existence. In this study, the k- ϵ turbulence model and two Reynolds stress transport turbulence models have been used. For a fuller discussion of turbulence models the reader can refer to [79].

The k- ϵ turbulence model [35] uses the Boussinesq (or eddy viscosity) assumption to model the Reynolds stress components as:

$$\overline{\rho u_i u_j} = -\mu_t \left(\frac{\partial U_i}{\partial x_j} + \frac{\partial U_j}{\partial x_i} \right) + \frac{2}{3} \rho k \delta_{ij}$$

where the eddy viscosity (μ_t) is given by:

$$\mu_t = C_\mu \rho \frac{k^2}{\epsilon}$$

k is the turbulent kinetic energy; ϵ the dissipation rate of the turbulent kinetic energy. Both are determined by solving two further modelled transport equations:

$$\frac{\partial}{\partial x_i} (\rho U_i k) = \frac{\partial}{\partial x_i} \left(\mu + \frac{\mu_t}{\sigma_k} \right) \frac{\partial k}{\partial x_i} + P - \rho \epsilon$$

$$\frac{\partial}{\partial x_i}(\rho U_i \epsilon) = \frac{\partial}{\partial x_i} \left(\left[\mu + \frac{\mu_t}{\sigma_\epsilon} \right] \frac{\partial \epsilon}{\partial x_i} \right) + \frac{\epsilon}{k} (C_{\epsilon 1} P - C_{\epsilon 2} \rho \epsilon)$$

where:

$$P = \mu_t \left(\frac{\partial U_i}{\partial x_j} + \frac{\partial U_j}{\partial x_i} \right) \frac{\partial U_i}{\partial x_j}$$

The empirical constants above take the values:

$$C_\mu = 0.09, \quad C_{\epsilon 1} = 1.44, \quad C_{\epsilon 2} = 1.92, \quad \sigma_k = 1.0, \quad \sigma_\epsilon = 1.3$$

Two alternative Reynolds stress transport turbulence models have been used in this study, those were based on the proposal of Gibson and Launder [20], and differed only in the model provided for the wall reflection part of the redistribution terms in the Reynolds stress transport equations (see [20] for details). The transport equations for the Reynolds stress tensor and the isotropic dissipation rate are given by:

$$\begin{aligned} \frac{\partial}{\partial x_k} (U_k \rho \overline{u_i u_j}) &= C_s \frac{\partial}{\partial x_k} \left(\frac{k}{\epsilon} \overline{u_k u_m} \frac{\partial}{\partial x_m} (\rho \overline{u_i u_j}) \right) + \rho P_{ij} + \rho \phi_{ij} - \frac{2}{3} \delta_{ij} \rho \epsilon \\ \frac{\partial}{\partial x_i} (U_i \rho \epsilon) &= C_\epsilon \frac{\partial}{\partial x_i} \left(\frac{k}{\epsilon} \overline{u_i u_j} \frac{\partial}{\partial x_j} (\rho \epsilon) \right) + \frac{\rho \epsilon}{k} (C_{\epsilon 1} P - C_{\epsilon 2} \epsilon) \end{aligned}$$

where the production term is given by:

$$P_{ij} = - \left(\overline{u_i u_k} \frac{\partial U_j}{\partial x_k} + \overline{u_j u_k} \frac{\partial U_i}{\partial x_k} \right)$$

and the redistribution term is modelled by:

$$\phi_{ij} = \phi_{ij1} + \phi_{ij2} + \phi_{ij(w)}$$

where:

$$\phi_{ij1} = -C_1 \left(\overline{u_i u_j} - \frac{2}{3} k \delta_{ij} \right)$$

$$\phi_{ij2} = -C_2 \left(P_{ij} - \frac{1}{3} P_{kk} \delta_{ij} \right)$$

The model of Shir [76] for the wall reflection term is given by:

$$\phi_{ij(w)} = \frac{l}{x_n} \left(C_3 \frac{\varepsilon}{k} \left(\overline{u_k u_m n_k n_m} \delta_{ij} - \frac{3}{2} \overline{u_k u_i n_k n_j} - \frac{3}{2} \overline{u_k u_j n_k n_i} \right) + C_4 \left(\phi_{km2} n_k n_m \delta_{ij} - \frac{3}{2} \phi_{ik2} n_k n_j - \frac{3}{2} \phi_{jk2} n_k n_i \right) \right)$$

where n_i are the components of the normal to the wall; x_n is the distance normal to the wall; and the length scale, l , is given by:

$$l = \left(\frac{k^{1.5}}{\varepsilon} \right) \left(\frac{\kappa}{a^{1.5}} \right)$$

This model is referred to as RST 1 in the text below. The alternative model of Craft and Launder [12] for the wall reflection term is given by:

$$\phi_{ij(w)} = \frac{l}{x_n} \left(C_3 \frac{\varepsilon}{k} \left(\overline{u_k u_m n_k n_m} \delta_{ij} - \frac{3}{2} \overline{u_k u_i n_k n_j} - \frac{3}{2} \overline{u_k u_j n_k n_i} \right) - C_5 \frac{\partial U_l}{\partial x_m} \overline{u_k u_m} (\delta_{ij} - 3n_i n_j) + C_6 k \frac{\partial U_l}{\partial x_m} n_l n_m \left(n_i n_j - \frac{1}{3} \delta_{ij} \right) - C_7 k a_{lm} \left(\frac{\partial U_k}{\partial x_m} n_l n_k \delta_{ij} - \frac{3}{2} \frac{\partial U_i}{\partial x_m} n_l n_j - \frac{3}{2} \frac{\partial U_j}{\partial x_m} n_l n_i \right) \right)$$

This model is referred to as RST 2 in the text and performs better for flow impinging on solid surfaces.

The empirical constants used in the Reynolds stress transport turbulence models are:

$$C_s=0.22, C_\varepsilon=0.16, C_{\varepsilon 1}=1.44, C_{\varepsilon 2}=1.92, C_1=1.8, C_2=0.6, C_3=0.5, C_4=0.3, C_5=0.044, C_6=0.08, C_7=0.6, \kappa=0.41 \text{ and } a=0.3$$

1.4.5 Wall functions

Wall functions are a collection of semi-empirical formulae and functions that in effect "bridge" or "link" the solution variables at the near-wall cells and the corresponding quantities on the wall. The reason for using wall functions is to avoid the need for an exceedingly fine grid in the immediate near-wall regions that would be needed to resolve the steep gradients, and to avoid also the need to use low Reynolds number models (the models used in the previous section were all high Reynolds number turbulence models). The wall functions comprise:

- laws-of-the-wall for mean velocity and temperature (or other scalars);
- formulae for near-wall turbulent quantities.

The standard wall functions used in this work are based on the proposals of Launder and Spalding [44], and have been widely used for industrial flows.

The law-of-the-wall for mean velocity yields, for any point P next to a solid surface:

$$U^* = \frac{1}{\kappa} \ln(Ey^*)$$

where:

$$U^* \equiv \frac{U_P C_\mu^{1/4} k_P^{1/2}}{\tau_w / \rho}$$

$$y^* \equiv \frac{\rho C_\mu^{1/4} k_P^{1/2} y_P}{\mu}$$

and	κ	=	Von Karman's constant (= 0.42)
	E	=	empirical constant (= 9.81)
	U_P	=	mean velocity of the fluid at point P parallel to the wall
	k_P	=	turbulent kinetic energy at point P
	y_P	=	normal distance from point P to the wall
	μ	=	dynamic viscosity of the fluid

The logarithmic law for mean velocity is known to be valid for $30-60 < y^* < 300 - 600$ (at least for small pressure gradients). In the codes used here, the log-law is employed when $y^* > 11.225$. When the mesh is such that $y^* < 11.225$ at the wall-adjacent cells, the law is replaced with the laminar stress-strain relationship that can be written as:

$$U^* = y^*$$

Wall functions are used to allow accurate estimation of the effects of a boundary layer without the need to dedicate a large number of cells to specifically resolving the flow within it. This can be done, as wall shear stress due to the boundary layer can be estimated from the velocity and turbulence properties at the outside of the boundary layer. Getting the wall shear stress correct is important, as it is this that controls the separation of the flow from a body. For this reason the typical y^* values for the Ahmed body calculations will be included in the relevant chapters.

1.4.6 Pressure-correction methods

The discussion in section 1.4.3 above has explained how the governing equations can be discretised to provide conservation of mass. It remains to decide how to tackle the pressure/velocity coupling before a suitable equation set is obtained. Two alternative

approaches are available, density-based and pressure-based. The former is suitable for compressible and high Reynolds number flows, the latter approach is more suitable for low speed, essentially incompressible flows of interest here.

Pressure-based, or more commonly called pressure-correction methods, are described in more detail in references [60] and [79]. Essentially they involve a segregated approach (momentum transport equations solved one-by-one in a scalar fashion) and a guess-evaluate-correct procedure. A guessed pressure field is first used in the momentum equations; the resulting velocity field does not automatically satisfy the continuity equation and the mass imbalance in each cell is used to evaluate a pressure-correction equation used to improve the pressure and velocity fields. Repeated iterations (usually requiring under-relaxation) leads to a velocity/pressure set which simultaneously satisfies both the continuity and momentum equations. Various forms of pressure-correction procedure are available, but the SIMPLE method [60] has been used in the results presented in this thesis.

1.4.7 Solvers and Multigrid

Having discretised the equations in every cell, the algebraic equations must then be solved to provide the flow at each point. Various forms of algebraic solver exist that link the equations in different ways. There are "point solvers", which step through every point on the grid using the latest values of the flow variables in the solution matrix, before moving on to the next iteration. "Line solvers" assemble the solution matrices on all points along a line through the domain and solve along that line. Another type of solver is the "matrix solver". These assemble the coefficients for every point into one large n - dimensional matrix (where n is the number of dimensions plus one). This relies on matrix solution algorithms, which, in turn, rely on the matrices in question being sparse and banded.

A multi-grid solver consists of a fine mesh constructed by the user, upon which some initial iterations are performed. Subsequently, the grid is coarsened (usually automatically) and the solution from the fine grid interpolated onto this grid. This grid is then solved for a few iterations. The process is repeated for a few more steps of coarsening and solving before the process is reversed and the coarse grid solution interpolated back onto the finer grids, until the finest grid is reached. The intention here is to quickly damp out any long wavelength oscillations, or large scale features, that would take a long time to decay on the fine grid.

To summarise the models used in the work presented here: structured, unstructured and mixed grids are generated and calculations performed using appropriate solvers with first, second or QUICK upwind differencing in conjunction with a $k-\epsilon$ two equation of full Reynolds Stress Transport turbulence model.

1.5 Why Use Bluff Bodies Instead of Full Cars?

The aerodynamic features of a car are numerous and wide-ranging. There are bulk flow characteristics, for example, the formation of the longitudinal vortex structure behind the car. At the same time, there are detailed flow structures, such as the flow over wiper blades and mirrors; as well as internal flows to cool the engine and passengers. To accurately model these features using a CFD model, for comparison with the data available from wind tunnels and on road measurements, would be nearly impossible due to the size of grid this would require. Hence, the validation of CFD for use on automobiles requires the removal of some of the smaller features mentioned.

When examining the flow over automobiles the flow structures that relate to the body's proximity to the ground and its 3D nature are logically those that should be studied first, as the other features are present in other types of flow not considered here. The question of what simplifications should be made to the body is, therefore, restricted to what shaped body produces the same ground influenced vortex structure as automobiles. The shapes used are simple bluff bodies (that is, not sharp), with rear end configurations that can be interchanged to represent the different types of car seen on the road.

The ideal body would have attached flow over the front portion and a rear end that can be altered to produce both 3D (longitudinal vortex dominated) separations and quasi 2D separations (base flow). In addition it would be helpful if the body was easy to model geometrically. There have been many variations on this theme in the past, some of which have been simpler than others. Some, such as Ahmed's body and Morel's Body [2,53], are simple brick-like shapes whilst others are simplified production car models, such as that used by Volvo [69,26]. Other studies have concentrated on truck-like bodies [62].

Several suitable bodies have been experimentally tested in wind tunnels. MIRA have tested a simplified automobile shape with three different rear ends, corresponding to a

saloon, a hatchback and a van [9]. Morel tested a blunt nosed cylinder with a series of base slant angles [53], Ahmed et al. tested a rectangular body with a rounded front end and a series of base slant angles [2]. Yamada and Ito [87] studied a similar body to Ahmed's, however, with a much shorter mid-section. Graysmith et al. [22] repeated Ahmed's experiment, but in a different wind tunnel and with a moving ground plane.

The Ahmed body [2] has thus been selected as the natural choice for the present calculations, as it is one of the simplest, yet best documented examples of such simplified bluff bodies. Ahmed's body is shown in Figure 1.17.

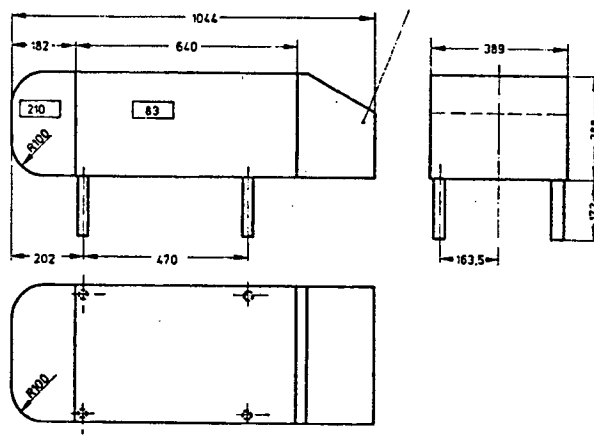


Figure 1.17 The Ahmed body

It has a rectangular cross-section, rounded front-end, straight mid section followed by a rear end with a set of base slant angles from 0° to 40° in 5° steps. As an experimental shape to be used for comparison between CFD methods it is particularly suitable, due to the repeated nature of the experiments performed by Ahmed et al [2] and Graysmith et al [22]. Both studies used the same body, however, the latter differs due to the inclusion of a moving ground plane, a smaller wind tunnel and a lower Reynolds number (1.2×10^6 based on the length of the body).

The flow field is very similar in structure to that of a hatchback automotive body as described previously in this chapter. The important features of the flow will, however, be repeated here. The flow impinges on the front of the body and accelerates around

the curved front end without separation. For small slant angles, the flow remains fully attached to the slant, and separates at the slant/base edge (see Figure 1.18).

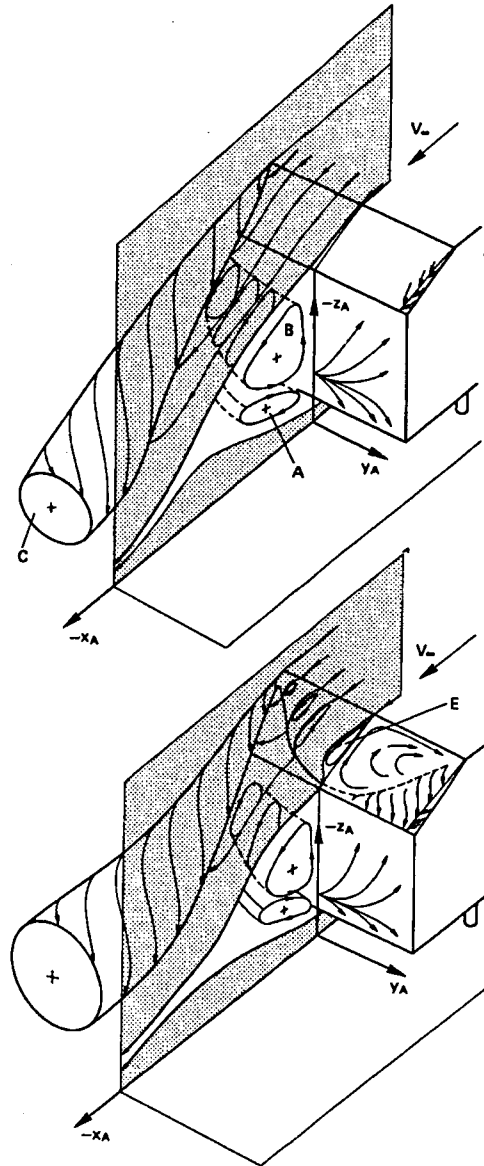


Figure 1.18 The two modes of flow that occur over the rear of the Ahmed body. Taken from Ahmed et al [34].

This separation starts at the top/slant edge and grows down the slant surface, out from the symmetry plane edge, to produce a semi circular shaped region. This is atypical of most modern automotive shapes. The rounded nature of the rear for most of these shapes gives a gradual increase in the acceleration needed to keep the flow attached. Thus, the separation occurs later, where the deceleration has affected the flow

sufficiently for flow reversal to occur. In the Ahmed body, the very angular nature of the top/slant edge means that the acceleration is much greater there than for further down the slant, thus the flow separates at this edge.

Stream-wise vortices are formed on the outer edges of the slant as the flow down the side of the body moves inward to relieve the low pressure downstream of the top/slant edge. This helps to hold the flow onto the slant at its edges, preventing total separation on the slant. The vortices become stronger as the pressure difference increases with slant angle. The effect of this low pressure on the upper part of the slant is to increase the drag of the body, as the slant angle is increased. However, for a critical slant angle around 30° - 35° , the increasingly low pressure behind the top/slant edge cannot be maintained, and the flow fully detaches from the slant. This raises the pressure on the slant and base, close to that of the free stream, and significantly reduces the drag. Further increases of the slant angle have minimal effect on the drag. The two flow modes are illustrated in Figure 1.18 for a slant angle of 30° . Figure 1.19 shows the velocity vectors and pressure contours behind the body, which show mirrored contours of total pressure and velocity streaklines for two sets of experimental data.

The similarity of the flow over the Ahmed body with that over a hatchback type automotive vehicle illustrates it to be an excellent test case for the assessment of the ability of CFD to predict external aerodynamic phenomena over an automotive-type body over a range of hatchback angles

It should be noted that in order to maintain the high drag flow behind the Ahmed body with the 30° slant surface in the wind tunnel, a vertical splitter was placed downstream of the body. This had the effect of preventing the instabilities in the flow structure from promoting the more stable low drag flow structure. This implies that something important is happening in the flow and it may be the case that steady state CFD predictions using symmetry models are incapable of capturing this behaviour.

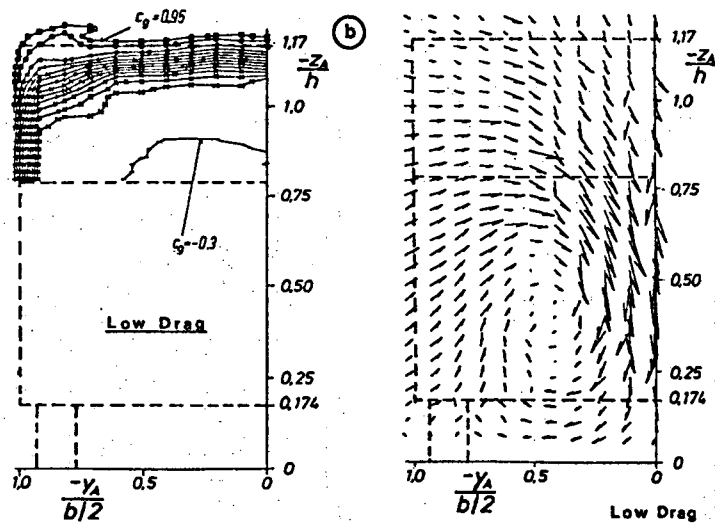


Figure 1.19 The total pressure contours and streaklines over the rear of the Ahmed body for the low drag case [2].

1.6 Review of CFD on Automotive Type Bodies

The MIRA simplified automobile shapes (a bluff bodies with a set of interchangeable rear ends) have been predicted by Shaw et al. [74,32], using a first-order finite volume scheme, a $k-\epsilon$ turbulence model and 150,000 cells. They saw reasonable correlation (a similar shape) to the surface pressure measurements, that improved with grid resolution. Furthermore, a suction peak, at the top of the rear window, was seen in the calculation, a factor not present in the experimental results. The overall under-floor pressure level was however not accurately predicted, and the drag coefficient was too large, coming almost entirely from the front of the body. This shape was the subject of a “competition” of CFD codes [10]. The codes, generally, shared the same basic, good agreement with the wind tunnel results. There were, however, a few common problems. For example, in the areas of high flow curvature, such as the bonnet or the roof/rear screen edge, where there was a lack of resolution for pressure peaks and troughs. These were neither high nor low enough. This could have been due to the lack of grid resolution or the turbulence models used. It was interesting that the codes

all exhibited similar predictions and problems with the results. The most recent piece of work done on this body [17], used an RNG $k-\epsilon$ turbulence model with 1.3×10^6 cells. Several upwind differencing schemes were evaluated. The best drag results were obtained with the QUICK differencing scheme, and there was a 7% error in C_d for this case.

Another study on this shape was conducted by Rawnsley and Tatchell [71] using the PHOENICS CFD code. This was an early computation, and used only 17,000 cells with a $k-\epsilon$ turbulence model. The pressure agreement was generally good, however, significant disagreement was seen near regions of high flow-curvature, e.g. the nose. This can probably be attributed to the poor grid resolution. The number of cells used in this study was insufficient to completely describe the geometry properly, let alone the flow around it.

The Morel body (similar in shape to the Ahmed body) has been predicted by Tsuboi et al. [78] using a steady state solution algorithm, third-order upwind finite difference scheme and no turbulence model, despite the high Reynolds number of the flow. The drag coefficient was fairly well predicted, and the switch of flow mode at a critical slant angle was accurately predicted. This, interestingly, points to the differencing scheme being very important when attempting to predict separation.

Yamada and Ito [87] performed a wind tunnel test as well as a parallel CFD study. Again, the predictions were made without a turbulence model, but with a third-order upwind differencing scheme. Some predictions were made with a $k-\epsilon$ turbulence model with a lower order differencing scheme. They used a body similar to Ahmed's body with a grid of 712,000 nodes. Comparing against the wind tunnel measurements showed the $k-\epsilon$ predictions to have more accurately predicted the features of the flow field. For the 25° -slant angle, the $k-\epsilon$ case has predicted the surface pressure distribution more accurately. As the angle increased, the solution using the higher order upwinding improved, and the prediction using the $k-\epsilon$ turbulence model struggled to predict the peak of negative pressure that occurs on the roof/rear-slant

edge. This suggests that the extra diffusion created by the turbulence model is detrimental to the accurate capture of the change in flow structure. The drag coefficient change at 35° to 40° was (roughly) picked up by both methods, however, much more accurately in the higher order upwind case. The same was true for the lift values. Yamada and Ito concluded that the use of either an anisotropic k - ϵ turbulence model, or an even higher order upwind differencing scheme, would improve the results. It is difficult to assess the results from a solution that does not use a turbulence model, as this does not represent a physically realisable solution.

Han [27], Larsson et al. [43] and Hashiguchi, et al. [30] have all performed CFD predictions using the Ahmed body. Han used a k - ϵ turbulence model and a grid of up to 404,000 cells. The results were good except that the base pressure was consistently predicted to be too low, and hence the drag was too high. He concluded that the turbulence model was to blame for this, even allowing for the large errors in numerical accuracy due to the lack of grid resolution.

Larsson et al. used a zonal method to divide the solution domain into wake, boundary layer and outer region. Inside the wake region, a k - ϵ turbulence model was used, a boundary layer method (3D momentum integral), and a potential flow method for the remaining regions respectively. The results demonstrated a similar flow field to the wind tunnel experiments also included in the study. However, again, they could not reproduce the change in drag at the 30° slant angle. Larsson et al suggested this may be due to the lack of resolution of the flow gradients near the wall incurred by using the law of the wall.

Hashiguchi, et al. also predicted Ahmed body flow with a grid of 967,000 cells. An unsteady solution was obtained using a third order upwind differencing scheme for the convection terms without the use of a turbulence model. The results demonstrate a good agreement in the drag “jump” values, and the pressure was, also, in broad agreement. They concluded that, however, these types of flow are far more unsteady

and asymmetric than previously believed. Hashiguchi et al suggested that more work was required in finding accurate data for test cases.

MIRA [6] repeated the original wind tunnel experiments of Ahmed and compared the results with two sets of CFD predictions. The first set employed structured grids with 166,200 cells or 224,030 cells in a second mesh. The second set used an unstructured grid with 100,800 cells or 132,000 cells in a second mesh. No quantitative data was presented for the unstructured grids and the results below are only for the structured grid work. Both predictions used a $k-\epsilon$ turbulence model, a second set of solutions were obtained using the RNG $k-\epsilon$ turbulence model (a description of the RNG $k-\epsilon$ turbulence model is contained in [79]). The details of the differencing scheme are not included in the reference. The results showed good correlation for C_p in regions of unseparated flow. In the 25° to 30° slant angle case there should have been a partial separation on the rear surface, which was not seen. Instead, the calculated flow was fully attached. At 35° , the flow fully separated, being seen first as a partial, and then full separation, as the mesh density increased. Whilst still only demonstrating the trends, the drag coefficient moved closer to the wind tunnel values as the grid was refined. The results of this work, both experimental and CFD, will be used for comparison with the work presented in this thesis in chapter four.

Other bluff body work includes that of Halijoo et al [26] who found reasonable results on a simplified car shape within 10% of C_d but gave no grid size. Work on developing unstructured grid methods for use in the automotive field has been repeated by Przekwas et al [67], however, no specific correlation data is presented.

The above summary represents work carried out by CFD researchers. In addition, many studies have been completed by automotive manufacturers in assessing the viability of CFD for use in the design process. Most of these [42, 1, 75, 7, 86, 63, 25, 69, 78] have used a $k-\epsilon$ turbulence model [35]. The earlier papers [1, 63,75], using only a small number of grid points (of the order 10^5), found reasonable agreement in the measured and calculated results for the drag and lift values, whilst not fully

capturing any changes due to bodywork alterations. The correlation with measured surface pressures was reasonable with a lack of resolution in the pressure peaks and troughs, attributable to the inadequate grid resolution.

Later computations [42, 7, 86, 25, 69] used more grid points (of order 10^6), which gave much better results for surface pressure and, therefore, in the drag and lift values. Volkswagen [86] noted that the k - ϵ turbulence model over-predicted the Reynolds stresses in regions of high flow curvature. Volvo [25, 69] also performed some 2D calculations of this type of flow. Their conclusions stated that the grid cell shape and refinement was an important factor in the accuracy of the results. They have also done work on a truck-based [62] bluff body that gave good correlation with wind tunnel results using a mesh of 5×10^6 nodes. The accuracy of the drag prediction depended on the differencing scheme and turbulence model; however, the best results were within 0.005 of the correct C_d value.

A different approach taken by some (predominantly Japanese) authors is to neglect to use a turbulence model and use a third-order upwind differencing scheme for the convection terms. Examples of this method [31, 37, 88, 38, 55, 56] use quite fine grids (of order 10^6 to 10^7) and give good agreements in the surface pressure values. These improve with grid density, and the drag values are consistent with the wind tunnel experiments, although the lift values can sometimes be inaccurate [55]. Mazda [31, 37] used this type of solution method with a car at a non-zero angle of yaw, giving a 13% error in the correlation with experiments. These good results were obtained despite the lack of a turbulence model. The removal of the turbulence model from most CFD solution algorithms results in lower levels of diffusion, often resulting in unstable flow. This removal of the turbulence model also may allow greater resolution of the time accurate flow properties, improving the prediction of unsteady results. It is difficult to assess these results further without access to more specific details about the methods used than provided in the literature.

Some other manufacturers have studied bluff bodies to evaluate CFD codes. These include Toyota [29] and General Motors [28]. These papers give no specific accuracy results, however, they do give some indication that their success was minimal and that the forces seen were not in line with wind tunnel results.

In general, although the manufactures say they are pleased, the results were disappointing, with unacceptable errors in the prediction of the drag and lift coefficients for the vehicles. None of the predictions used a more sophisticated turbulence model than the standard $k-\epsilon$ model [35]. Wustenburg [86] suggested that a Reynolds Stress Transport turbulence model combined with high grid resolution near to the body would help to improve the accuracy of the solution.

In summary, the previous work done provides no clear indication of the ability of CFD to predict the flow over automotive bluff bodies. There appears to be confusion over the effects of grid density and the numerical model (i.e. discretisation method and turbulence model) on the solution. There is, therefore, a need to perform a careful study of these aspects on a single well-documented test case.

1.7 Direction of the Present Work

The brief overview provided in the previous section of the extant literature on the use and applicability of CFD to vehicle aerodynamics has raised several questions regarding the accuracy and credibility of the existing studies and revealed a number of potential research areas. In order to permit a thorough analysis, the focus of the present study will be the application of CFD to the problem of the flow over a bluff body in close proximity to the ground. The principle objective will be to assess and improve the application of CFD to this area. Having identified a suitable bluff body in the Ahmed body, and surveyed previous studies, the following questions were identified as forming the central issues to be considered:

- Are the flow fields produced in the CFD predictions similar to the ones suggested by experiments?
- Are the bulk levels of drag in the CFD results similar to those seen in the experiments?
- Can the CFD calculations reproduce the rise and sudden drop of the drag factor seen in the experiments?
- Can the CFD results be improved upon - in terms of accuracy or efficiency?
- Can this type of flow pattern be represented by the time-averaged CFD predictions or can some aspects only be captured by unsteady CFD?

The last question cannot completely be answered in a study restricted to steady flow predictions, but it is an important consideration when interpreting and examining the success or failure of the CFD results. However, the remaining questions will form the focus of the analysis throughout this study. The questions can be further divided into two: an assessment of current CFD methods on the Ahmed body; and secondly, a more detailed investigation into the effect of certain specific aspects of the CFD model, with the objective of improving the accuracy of results and widening our knowledge of the behaviour of CFD, when used to predict the flow over the Ahmed body.

The remainder of this chapter will build on the brief overview of CFD studies presented above by presenting a detailed and specific analysis of current structured CFD methods carried out at the start of the present project. It sets the scene for investigation into improvements in current CFD models and methods, which will be subsequently discussed in Chapters Two to Five.

1.8 Initial CFD Predictions

1.8.1 Introduction

The studies completed by previous authors on the subject of ground vehicle aerodynamics are comprehensive, with much of it done by commercial organisations, some of whom were CFD code development or consultancy companies. The main aim of such studies, therefore, has been the demonstration to prospective users or purchasers of the suitability of methods for bluff body flow application. Other companies that have been principally involved with such applications of CFD models have been the automotive manufacturers. The aim for these companies has again been the validation of methods for the problem of ground vehicle aerodynamics. Most of the results from such studies have probably been withheld from external publication. Indeed a request for data, information or, indeed, anything about CFD use within the automotive industry sent to every major automotive manufacturer in the world at the outset of this project, did not receive any replies.

The results from existing studies as discussed in section 1.6 above, cannot therefore be regarded as exhaustive. In order to highlight the questions previously outlined, the first task was therefore, to assess the "current" state of CFD when applied to the problem of a bluff body in ground proximity. In this study, "current" is here defined as work completed in 1994-5 at the start of this research. The assessment should involve a parametric study of the effect of grid density, differencing scheme, grid topology and turbulence model selection on the Ahmed body flow.

The methods current at the outset of this project were more limited than at present (mid 2000). Unstructured grid generator, for example, were in their infancy and unavailable for widespread use. Many aspects, however, have not changed. The differencing schemes investigated in this section (first order upwind or second order QUICK) methods and the turbulence models ($k-\epsilon$ or full Reynolds Stress) are still the most widely used. The main development, however, has been the change in the size of CFD meshes possible. In the initial study presented in this chapter, a maximum of 350,000 structured grid cells were used, whereas upwards of 2 million are presently possible. This expansion can be attributed to the increases in computing power and the associated lowering in price. It is not believed, however, that this would dramatically change the majority of the conclusions drawn from the initial study.

The bluff body identified as most suitable for the objective of this study was the Ahmed body. As discussed above, the Ahmed body shape exhibits many of the complex flow details seen in real cars. A further consideration was the relative inability of contemporary grids to pick up the detail in the boundary representation of complex bodies. This is attributable to the quite small number of cells available for the grid which, in turn, allows for only a small number of boundary faces with which to cover the geometry.

This study uses two different topologies of grid, at two levels of refinement (70,000 and 350,000 cells). The two topologies will be described later in the chapter. To complete the analysis of current CFD methods, the differences between the first order hybrid and QUICK differencing schemes for the momentum equations and the effects of using a full Reynolds Stress turbulence model as opposed to the standard $k-\epsilon$ model were evaluated. All calculations were performed using a three dimensional, single block, structured mesh, pressure-correction code based on the methodologies presented in the earlier section and available in-house at the Department of Aeronautical and Automotive Engineering.

1.8.2 Table of Calculations

Calculation Number		1	2	3	4	5	6	7	8
Grid Level	Coarse	X	X			X	X	X	X
	Medium			X	X				
Grid topology	Follow Body Shape	X		X		X			
	Leave Body at Edge		X		X		X	X	X
Differencing Scheme	Hybrid (1st order)	X	X	X	X				
	QUICK (2nd order)					X	X		
Turbulence Model	K-e	X	X	X	X				
	Reynolds Stress Model 1							X	
	Reynolds Stress Model 2								X

Table 1.1 The calculations done for the initial investigation.

Table 1.1 shows the matrix of CFD predictions completed in this section of the study, It shows the various different types of grid, differencing scheme and turbulence model investigated. This table will help to understand the progress of the work and how each calculation may be compared to the others. The results of the calculations will be presented and discussed below. They are grouped by certain factors: grid density, grid topology, differencing scheme and turbulence model.

The solution domain used for these initial calculations consisted of the symmetry model (that is, one half of it) of the Ahmed body close to the ground in a large box that extends for several model lengths above, the sides, in front and behind the body. The grid cells on the inside of the Ahmed body are treated as blockage cells. The boundary conditions used were a symmetry condition on the plane of symmetry, a velocity inlet of 60m/s at the inlet and a zero gradient outflow condition at the exit. The rest of the boundaries were defined as walls. The inlet value for the turbulent kinetic energy (k) is set as 1% of the kinetic energy of the free stream ($0.01 * 1/2 \rho 60^2$). The inlet value for ϵ is evaluated from the equation in section 1.4.4.

1.8.3 Coarse grid calculations

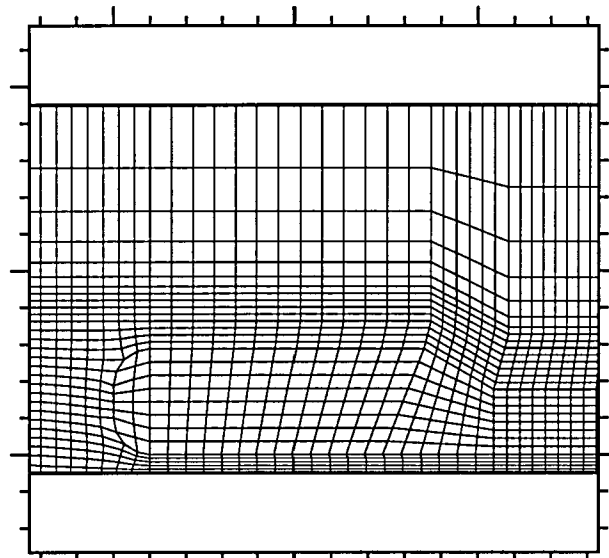


Figure 1.20 Coarse Grid 1C (70 000 grid points)

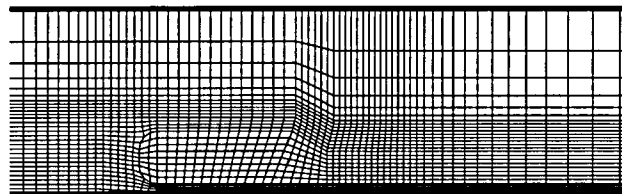


Figure 1.21 Coarse Grid 1C - far field view.

The initial coarse grid (“Grid 1C”) had dimensions of $81 \times 30 \times 29$ (70,470 cells). A close-up plot of the grid on the symmetry plane is shown in Figure 1.20 for the 30° back slant angle. Figure 1.20 does not show the entire solution domain, were it to do so the grid around the Ahmed body would be indecipherable. For all the slant angles, the grid topology was bent around the top/slant edge which appears to be the best option when considering the quality of the cells. This approach to dealing with the slant surface was also used in the work on the Ahmed body done by Graysmith et.al. [22].

The initial sets of predictions used first order hybrid differencing for the convection terms and the $k-\epsilon$ turbulence model.

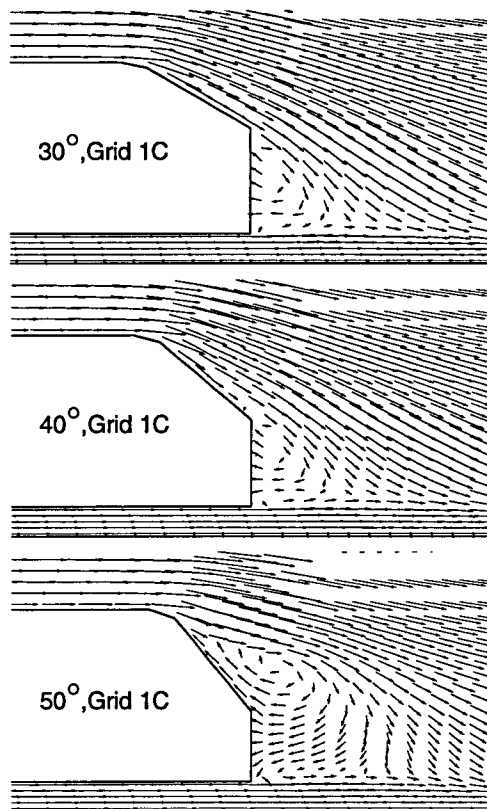


Figure 1.22 Velocity Vectors in the Symmetry Plane. Hybrid Differencing and k - ϵ Turbulence Model.

The predicted flow impinged on the front and flowed around the body without separation. At the rear of the body, the flow remained fully attached to the slant for all angles below 40° . Above this, the area of recirculation on the slant grew, although, even at an angle of 50° , it still remained partially attached immediately after the top/slant edge. This can be clearly seen in Figure 1.22, which compares the velocity vectors on the symmetry plane for the fully attached 30° and 40° case and the partially attached 50° case.

Figure 1.23 indicates how the region of separation on the slant grows with increasing slant angle. The slant surface of the body is viewed from behind.

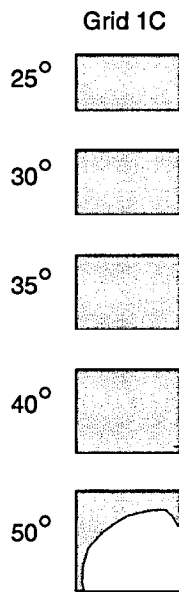


Figure 1.23 Zero Axial Velocity Contour on Slant (the backflow is white). Hybrid Differencing. The symmetry plane is on the right

The strong pressure drop behind the top/slant edge can be seen in the plots of pressure coefficient versus axial distance along the top of the body in Figure 1.24. The dip in the pressure coefficient, which coincides with the top of the slant surface for all the angles, show the flow to be attached over the top/slant edge for all cases. In the 50° this is despite the separation from the slant that occurs part-way along it.

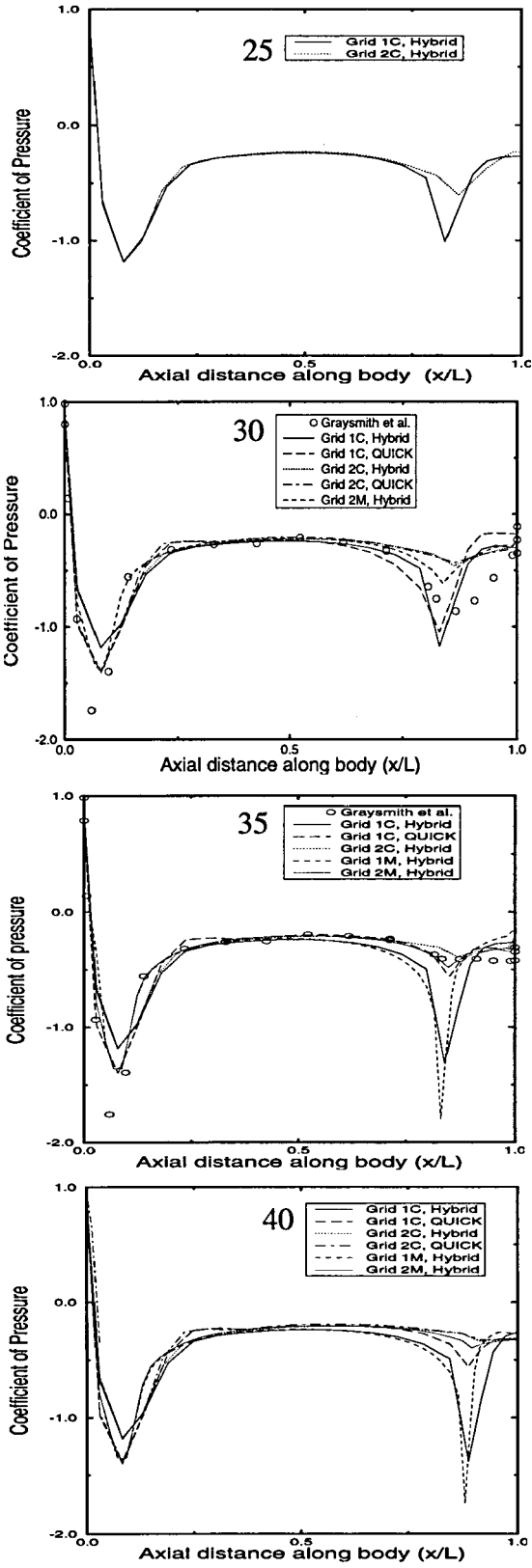


Figure 1.24 Coefficient of Pressure on Symmetry Plane and Upper Surface. $k-\epsilon$ Turbulence Model.

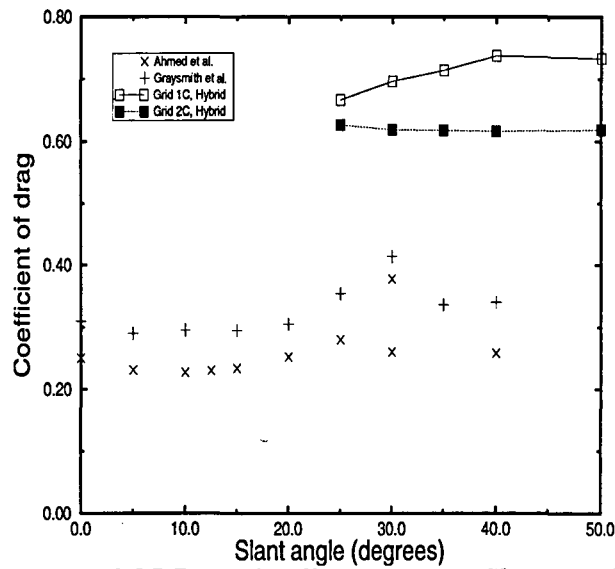


Figure 1.25 Drag Coefficient versus Slant Angle for the $k-\epsilon$ Turbulence Model

Figure 1.25 illustrates the variation of drag coefficient with slant angle for the 1C set of predictions. Clearly, the predicted drag is much too large. However, an increase in drag with increasing slant angle is predicted, since the flow remains largely attached, creating a progressively deeper pressure drop downstream of the top/slant edge. A sudden switch in flow mode does not occur, although the drag coefficient stops rising and the pressure depression begins to lessen for slant angles greater than 40° , when the flow is largely detached from the slant (Figure 1.24).

The formation of the streamwise vortices on the outside of the slant was clearly present in the predictions although, because of the coarse grid and the use of a first order method, more diffused than those measured by Ahmed et al. (Figure 1.26, Figure 1.27, Figure 1.28 and Figure 1.29). The plots from the wind tunnel (Figure 1.27 and Figure 1.29) are for the low and high downforce flow fields whereas the CFD results are for the 30° and 40° slant angles, in an attempt to show the range of flow behavior behind the body. The streamwise vortex depicted in these plots is not as strong and clearly defined in the CFD predictions, which is consistent with inadequate grid resolution.

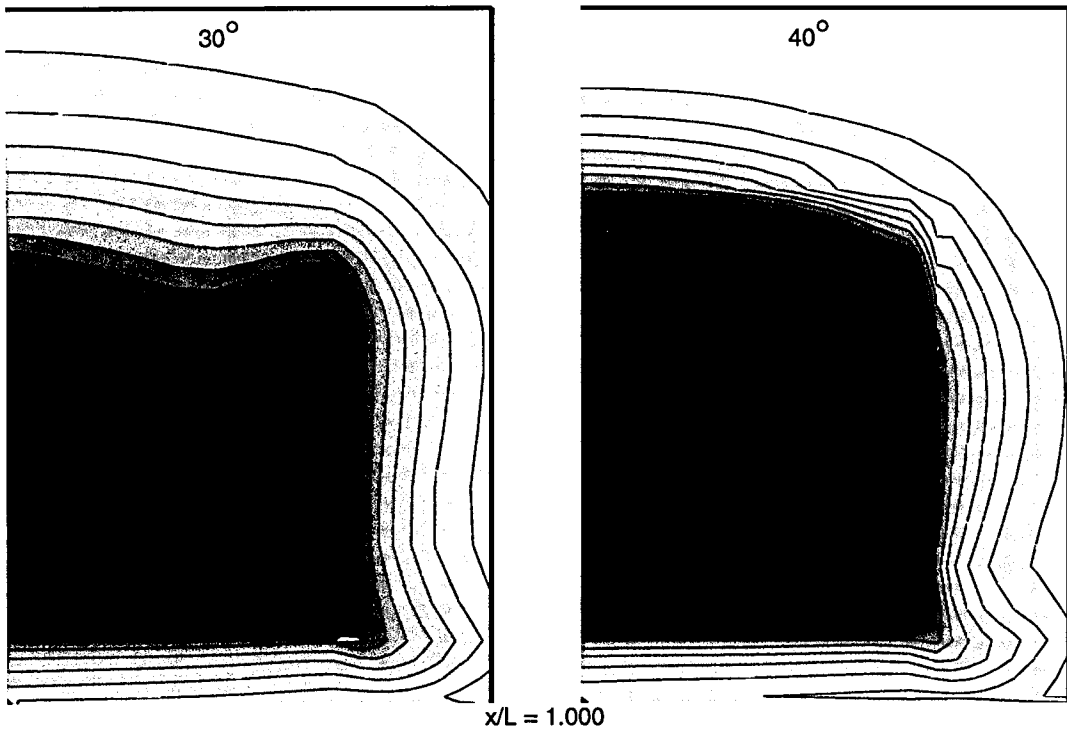
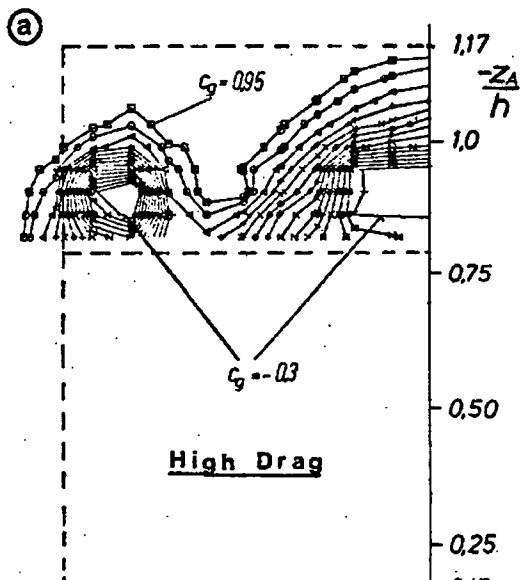


Figure 1.26 Normalised Total Pressure Contours (-0.2 - 0.95) from the coarse grid CFD results.



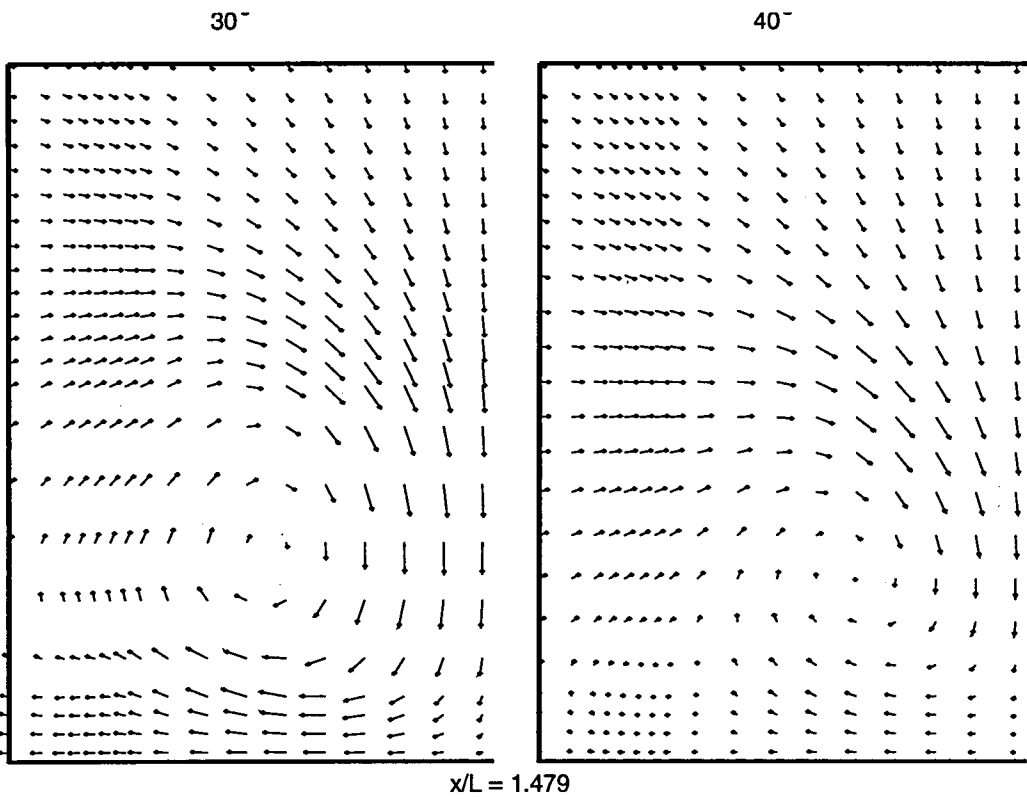


Figure 1.28 Velocity Vectors (tracking time = 0.003s.) from the coarse grid CFD results.

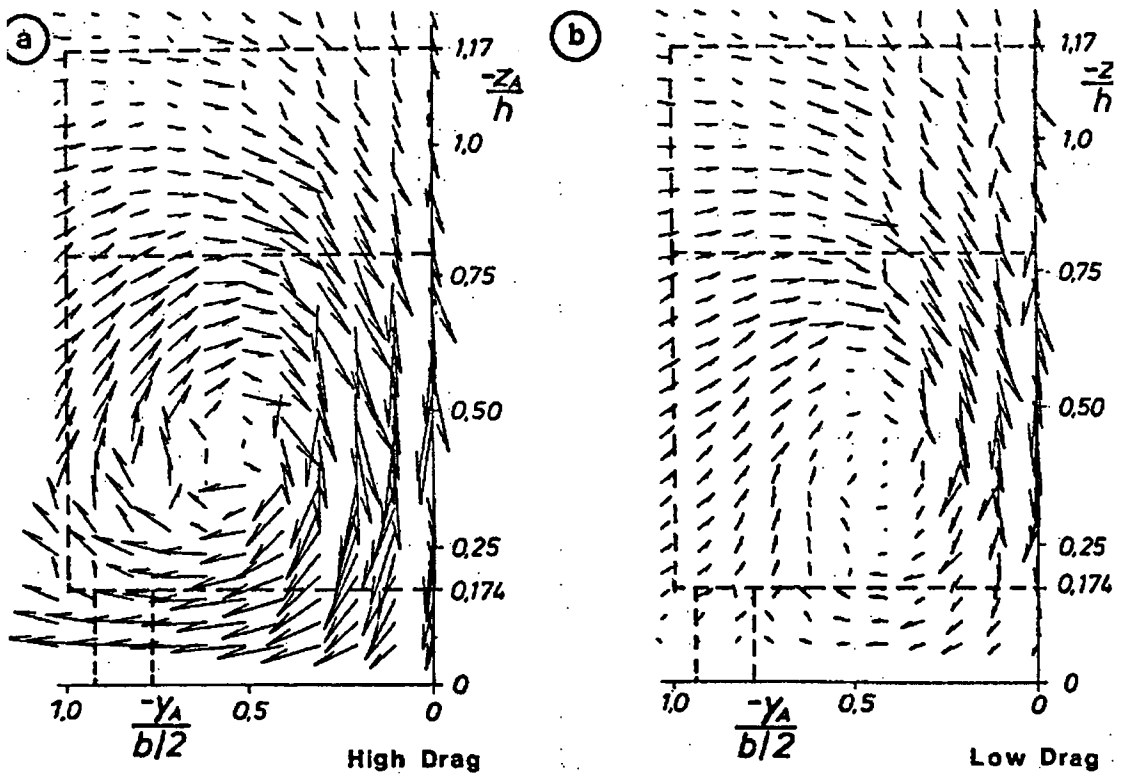


Figure 1.29 Velocity Vectors at $x/L = 1.479$ (taken from Ahmed et al. [2]).

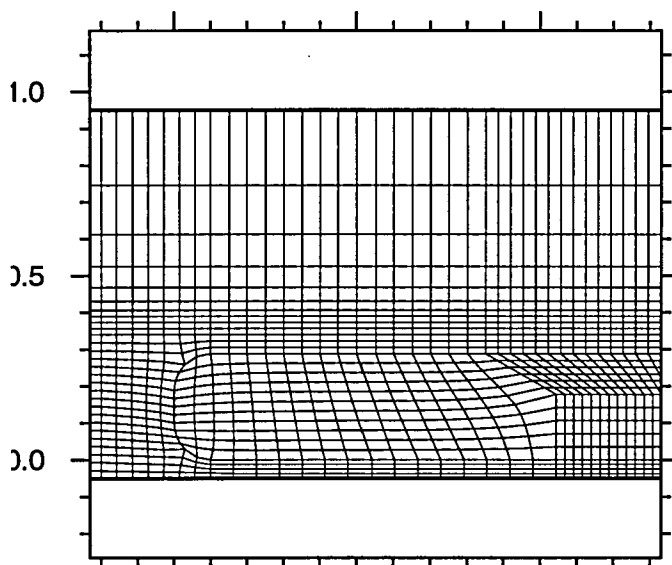


Figure 1.30 Coarse Grid 2C (70 000 grid points)

By bending the grid around the top/slant edge, the grid of Figure 1.20 was, to a large extent, suspected to be “helping” the flow to remain attached to the body. This was suggested by the high slant angle seen in the CFD results before separation occurred and also the still high pressure drop across the top/slant edge despite this separation. The steep flow gradient, that would be present if the flow separated, would be at a large angle to the grid, and could not be adequately resolved. In addition, the cells on the slant immediately downstream of the top/slant edge have a large convective flux of axial momentum on the upstream face. It is theorised that this flux will continue to follow the angle of the slant and “help” the flow to remain attached. This theory will be investigated in more detail in Chapter 4.

A second coarse grid (“Grid 2C”) was generated that would permit further investigation into the dependency of the solution on the grid without increasing the grid density. A plot of the grid on the centre plane is shown in Figure 1.20. The grid dimensions were the same as the initial grid at 81x30x29 although there was a small change in grid resolution on the front of the body. Therefore, following the theory set out above, if the flow were to separate, the cells on the slant immediately downstream of the top/slant edge will not see a large convective flux of axial momentum. Instead, they will see a large diffusive flux of axial momentum on the top face, causing a local

decrease in pressure in order to entrain mass (satisfy continuity). If this decrease in pressure becomes large, the main flow will be sucked onto the slant.

The non-orthogonal grid lines had little effect on the convergence rate, except for the 25° slant angle. This can be attributed to the very skewed grid just after the top/slant edge for this angle, affecting the influence coefficients of the cells.

Figure 1.22 provides the flow vectors on the symmetry plane for grid 2C and, by comparison with Figure 1.22, the effect of the grid topology is examined. Clearly, the

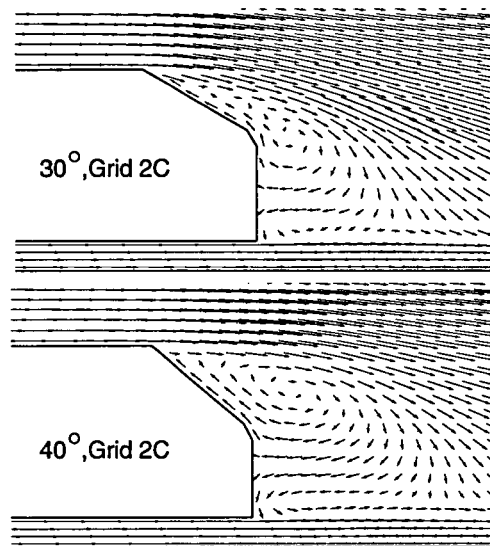


*Figure 1.31 Velocity Vectors in the Symmetry Plane.
Hybrid Differencing and $k-\epsilon$ Turbulence Model.*

second grid has allowed the flow to separate from the top/slant edge, unlike the first grid. Figure 1.32 shows the extent of the recirculation over the slant looking in the axial direction. The first grid is fully attached for all slant angles except 50° while the second grid is essentially fully detached for all slant angles above 30°, partially attached for 30° and almost fully attached for 25°. These results are closer to the observations in the experiments conducted by Ahmed [2] and MIRA [22].

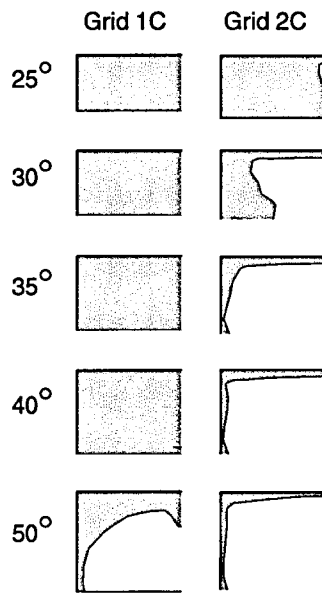


Figure 1.32 Zero Axial Velocity Contour on Slant (the backflow is white). Hybrid Differencing. The symmetry plane is on the right.

Figure 1.24 also contains plots of the pressure coefficient on the upper surface against axial distance for the grid 2C cases. The pressure at the rear is fairly accurately predicted for the separated flow, however, it is poorly predicted for the attached flow when the pressure decrease is greatly under-predicted, indicating less curvature of the main flow. The pressure decrease is noticeably deeper for the 25° slant compared with the 30° slant, suggesting that the flow is starting to attach “properly” at the lower slant angles. Figure 1.25 shows that the drag coefficient has been reduced but is essentially independent of slant angle, which corresponds with the separated flow mode. There is a small increase of 2% at the 25° slant angle compared with that of 30°, which corresponds with the slightly deeper pressure decrease observed in pressure coefficient profiles.

Clearly, the two different coarse grids are largely maintaining the flow over the rear in the two alternative flow modes. Since the grid density is essentially the same, there is some justification in following the coarse grid 1 drag curve up to 30°, and the coarse grid 2 curve beyond. If this is done, the predicted trends correspond well with the measured trends, and the predicted flow field structures correspond well with the

measured flow fields. That is to say, the size of the drag jump seen in the experiments by Ahmed [2] is reproduced by the change in drag seen between the predictions made on the two grids for the same angle of slant surface. However, the drag is still much too large. The grid resolution in the region of the top/slant has been proven to be inadequate, and having to repeat predictions with remeshed corners is not a desirable property of a CFD method.

1.8.4 Medium grid calculations

The medium grids are referred to as “Grid 1M” and “Grid 2M” in the figures. Both had dimensions of 146x56x43 (350,000 cells), and concentrated a greater proportion of the grid lines around the body than the coarse grids. The grid topology is identical to the coarse grids 1C and 2C respectively. The separation from the slant surface for each back slant angle and calculation can be seen in Figure 1.33.

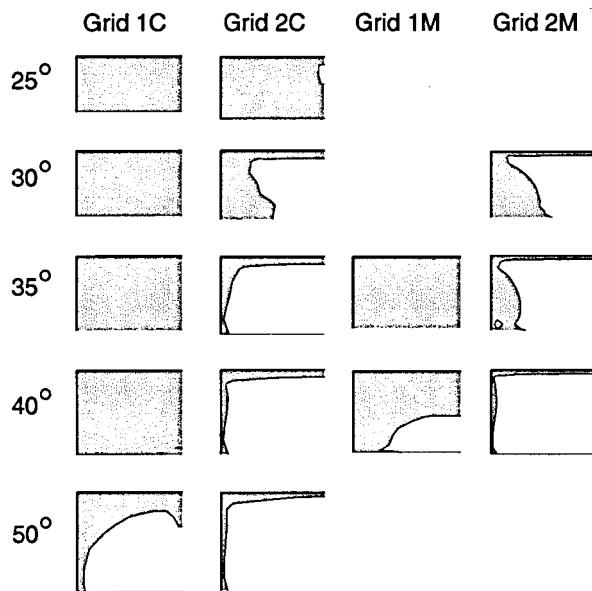


Figure 1.33 Zero Axial Velocity Contour on Slant (the backflow is white). Hybrid Differencing.

The flow field was largely similar to that of the coarse grid, although, in contrast, the medium grid 1 did predict some separation at a slant angle of 40° . For a 45° slant angle, the flow was almost fully separated and a corresponding (slight) drop in drag coefficient can be seen in Figure 1.34. For medium grid 2, the first fully separated slant angle is 40° , which also coincides with a slight drop in drag coefficient. Although the change in drag coefficient with flow mode is slightly more accurately predicted with the medium grids in comparison to the coarse grids, the results remain unsatisfactory for the reasons outlined above.

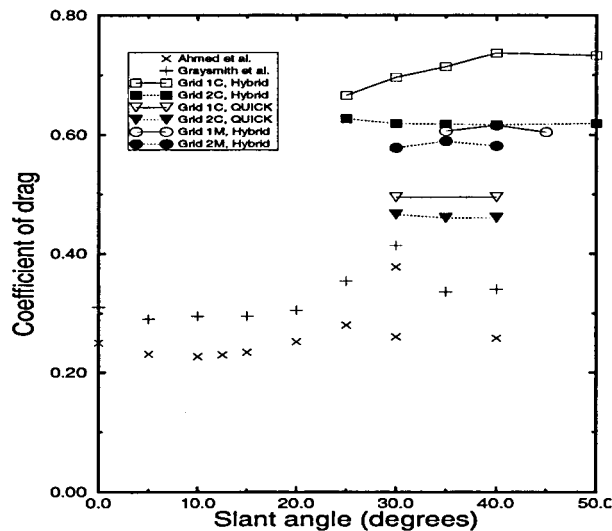


Figure 1.34 Drag Coefficient versus Slant Angle for the $k-\epsilon$ Turbulence Model

The medium grids do, however, predict a reduction in the size of the drag coefficient (see Figure 1.34). This is mainly attributable to a reduction in the numerical error over the front of the body caused by velocity “smearing”. If the velocity close to the body is reduced (as in the coarse grid work with the hybrid scheme), the total pressure lost in this area is also reduced. Figure 1.35 illustrates the velocity profile at the start of the mid section in the symmetry plane on top of the body. As is evident, the medium grid has a smaller degree of “smearing” of the velocity profile next to the body than the coarse grid. This smaller change in velocity profile results in a smaller loss of total pressure. Resulting in lower drag.

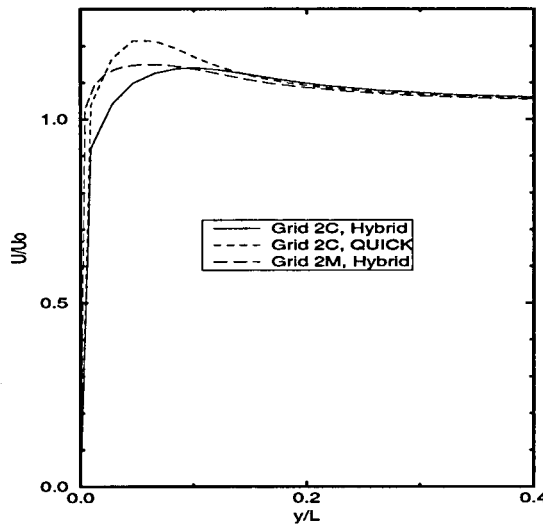


Figure 1.35 Axial Velocity Profiles in the Symmetry Plane Above the Body. $x/L=0.12$

Table 1.2 compares the drag coefficient components for the 30° slant angle on the second grid topology for the coarse and medium grids with the measurements. The two sets of Ahmed's measurements are for the high and low drag flow modes.

	Shear	Front	Slant	Base	C_D
Grid 2C	0.046	0.278	0.132	0.163	0.619
Grid 2M	0.071	0.205	0.126	0.176	0.578
Ahmed high drag	0.057	0.016	0.213	0.092	0.378
Ahmed low drag	0.051	0.019	0.089	0.101	0.260

Table 1.2 Drag Coefficient Components for 30° Slant. $k-\epsilon$ Turbulence Model and Hybrid. High and Low Drag Measurements

The increase in grid density gives a significant improvement in the CFD prediction of the flow over the Ahmed body. This grid dependency is undesirable, and in an effort to determine whether the solution was still affected by numerical error on the medium grid, the following total pressure loss assessment was carried out (following the idea

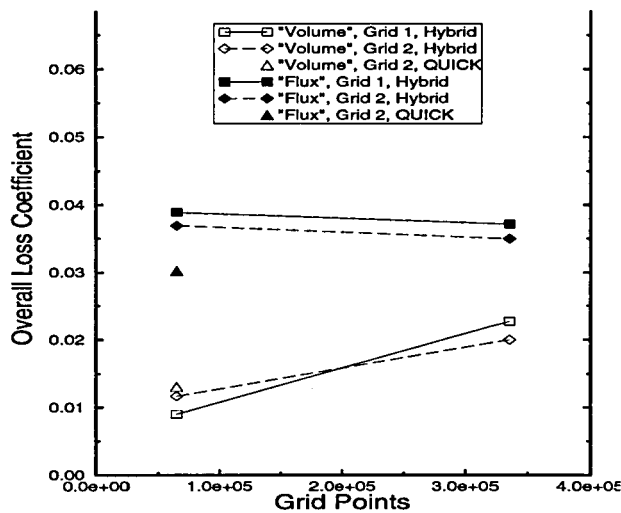


Figure 1.36 Overall Loss versus Grid Refinement for 35° Slant Angle. $k-\epsilon$ Turbulence Model.

discussed in Little and Manners [46]). The loss of mechanical energy within the flow is a quantity which changes significantly with the degree of numerical error in the predictions unlike, say, the general velocity field. In a prediction, total pressure loss can be evaluated in two ways: firstly, by integrating throughout the volume the work done by the mean flow against the Reynolds stresses (the "Volume" method); and, secondly, by integrating the flow across the inlet and exit planes (the "Flux" method). The second method is much more susceptible to the input of numerical diffusion errors in dissipating total pressure (mechanical energy) than the first, which measures the transfer of mean kinetic energy into turbulent kinetic energy. Since both methods are evaluating the same quantity, any difference in value is a measure of the numerical error in the solution.

The plot of loss coefficient versus grid point number for the two methods provides a pair of lines which represent the level of numerical error present. Where they are far apart there is significant numerical error and, therefore, scope for improvement in the numerical scheme/grid. Where they are close to each other numerical errors, particularly diffusive ones, are small (see Little and Manners [46] for a further discussion of this method). The losses for the two levels of grid refinement are shown in Figure 1.36 for the 35° slant angle. It is evident that the predicted flow still includes a substantial level of numerical error even in the medium grid. By following the trend

given by these lines, we can conclude that, for the CFD methods used here, a reasonably accurate calculation could only be obtained by using upwards of half a million grid points. Hence, the 350 000 grid point predictions cannot not be labelled “fine”, and were labelled “medium” instead.

The increase in predicted skin friction drag above the measured value in Table 1.2 indicates a problem with the k-ε turbulence model in impingement regions. This is better illustrated in Figure 1.37, which shows contours of turbulent kinetic energy.

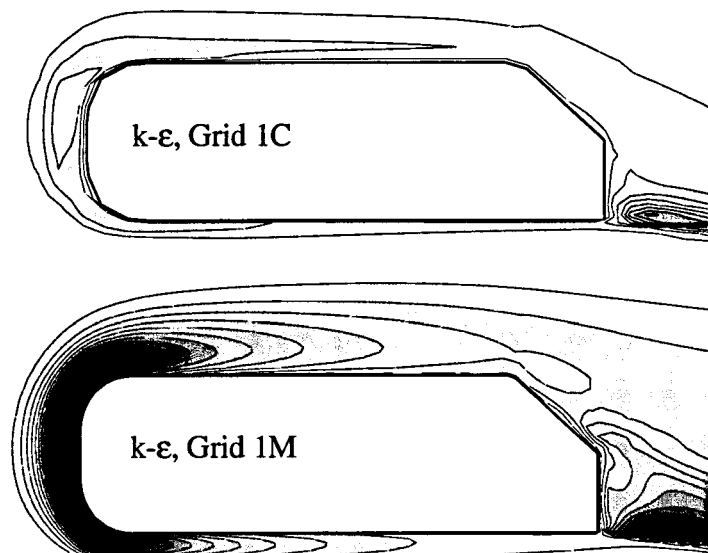


Figure 1.37 Contours of k/U_0^2 (0.0 - 0.064; 12 increments) on Symmetry Plane. Hybrid Differencing.

The better resolved gradients on the medium grid increase the levels of turbulent kinetic energy on the front-end of the body. Unfortunately, the levels are excessive, due to the use of an eddy-viscosity model for the normal Reynolds stresses. This gives rise to squared velocity gradients in the turbulence generation terms [49]. Hence, for fine grids, the modelled diffusion will create excessively thick boundary layers over the front curved section, leading to larger drag coefficients than occur in reality. This helps to explain the poor reproduction of the drag change seen at the rear of the body as the turbulence is carried along and over the body.

1.8.5 Effect of Differencing Scheme

A set of predictions with the two coarse grids was performed using the second-order accurate QUICK differencing scheme for the convection terms instead of the first-order accurate hybrid differencing scheme. Three slant angles were used: 30° , 35° and 40° .

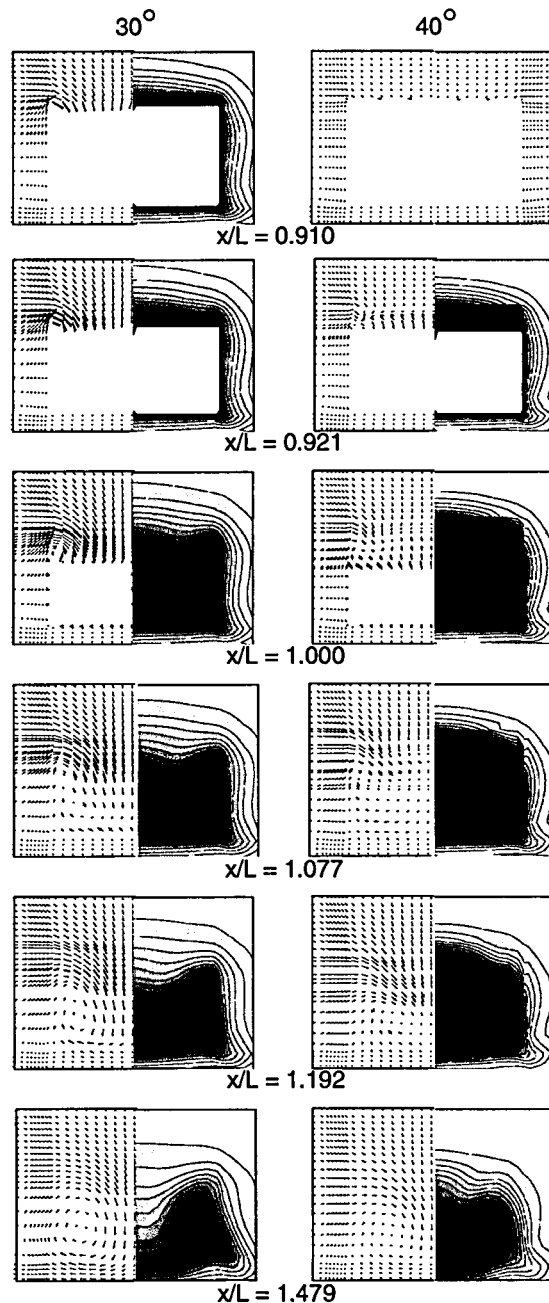


Figure 1.38 Velocity Vectors (tracking time = 0.003s.) and Normalised Total Pressure Contours (-0.2 - 0.95). QUICK and $k-\epsilon$, Grid 2C.

The general flow field was similar to the predictions using hybrid differencing. Figure 1.38 shows the development of streamwise vortices for the 30° and 40° slant angles. For comparison, the data of Ahmed et al. is shown in Figure 1.27 (total pressure contours) and Figure 1.29 (velocity vectors). The 30° QUICK flowfield corresponds to the high drag flow mode, and the 40° flowfield to the low drag flow mode.

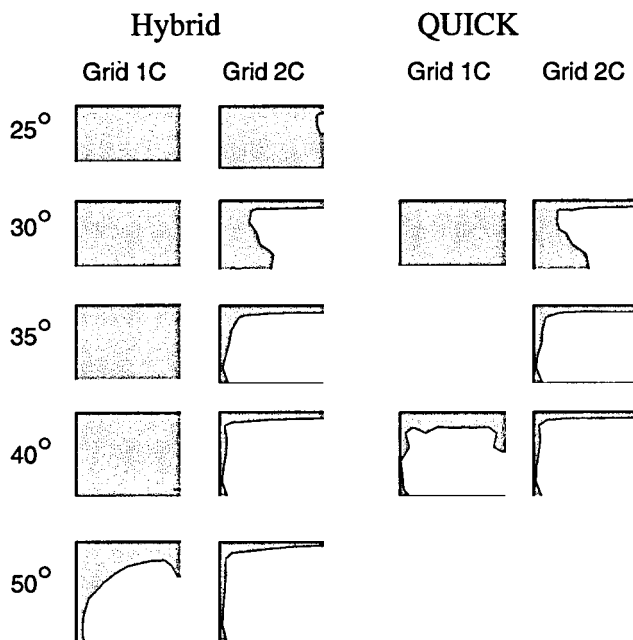


Figure 1.39 Zero Axial Velocity Contour on Slant (the backflow is white). QUICK Differencing.

Figure 1.39 illustrates the recirculations on the slant for the two grids, and the two differencing schemes. On the first grid, the flow is fully attached for the 30° slant angle and largely separated for the 40° slant angle, in contrast to the equivalent hybrid prediction. The prediction with the 35° slant angle would not settle down to a converged solution, with the flow continually attaching and separating from the slant. This could have been indicating unsteady flow behavior being captured by the CFD, but this conclusion is uncertain until predictions are made using a time accurate CFD solver. It may, equally, be attributable to some other critical factor in the CFD solution preventing further convergence. The second grid has partially attached flow over the slant for a 30° angle and largely detached for the two larger angles. This is comparable to the hybrid differencing results. Figure 1.40 plots the pressure coefficient on the symmetry plane along the top of the body against axial distance.

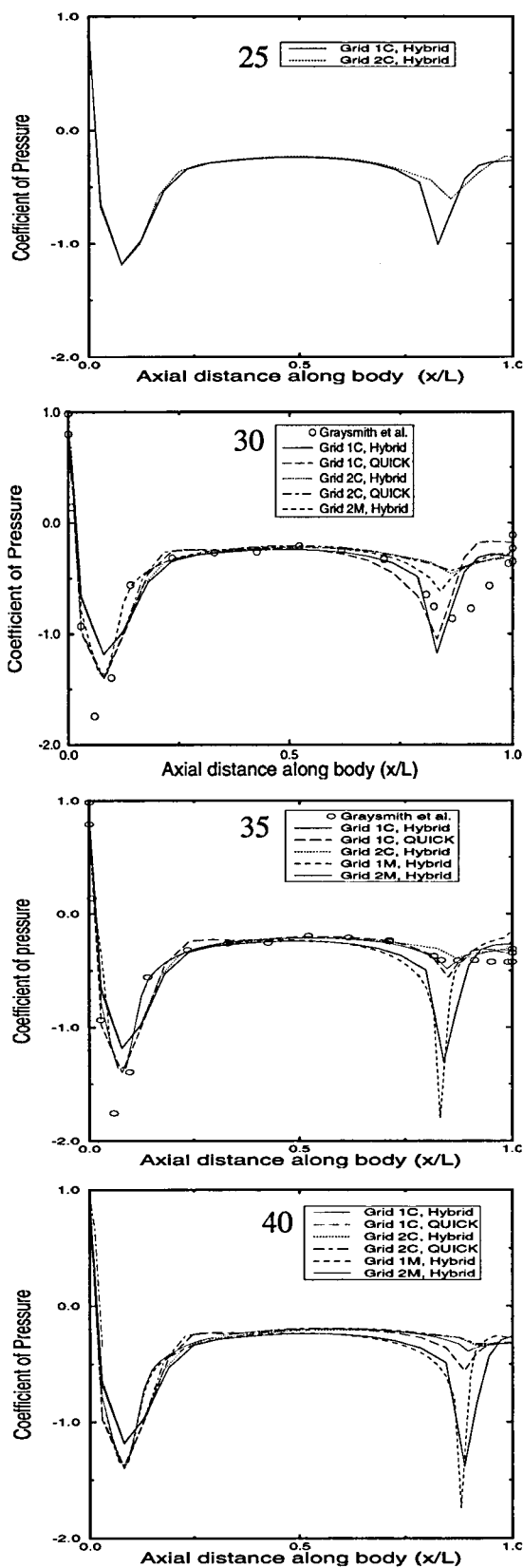


Figure 1.40 Coefficient of Pressure on Symmetry Plane and Upper Surface. $k-\epsilon$ Turbulence Model.

At the rear end, the hybrid and QUICK predictions are similar to each other for the second grid. However, for the first grid, the QUICK predictions are closer to the results for the second grid, than to the hybrid predictions. The notable exception to this is the 30° case for the grid 1C, QUICK calculation. It is in the attached, high drag mode, demonstrating that a change of drag mode has occurred between 30° and 40°.

At the front end, there are significant differences between the QUICK and hybrid predictions. The decrease in pressure over the rounded front section is deeper with the QUICK differencing due to the flow in this region being less diffused. This causes, as is the case in the medium grids, the peak velocity to be closer to the body, as illustrated in Figure 1.41, which shows the axial velocity profile in the symmetry plane above the body at $x/L=0.12$. The effect of this decrease in pressure at the front of the body, is a significant decrease in the drag as shown in Figure 1.25 arising from the reduced loss of total pressure.

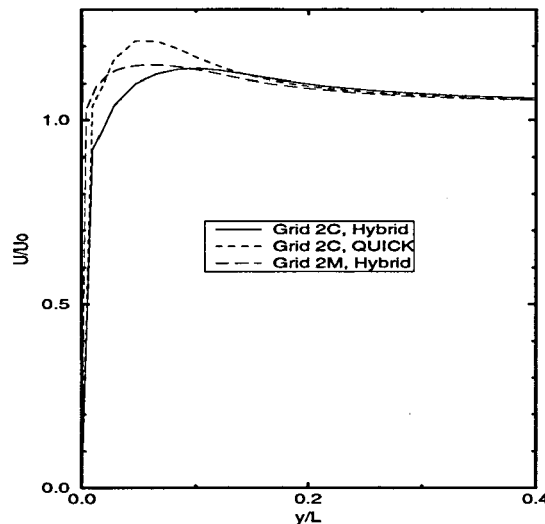


Figure 1.41 Axial Velocity Profiles in the Symmetry Plane Above the Body. $x/L=0.12$

Table 1.3 shows the four drag coefficient components for the 30° slant and the second grid: skin friction, pressure on the front of the body, pressure on the slant and pressure on the base. Evidently, the reduction in drag has arisen mainly from changes in the flow at the front of the body and not the rear. Also included are the experimental results

of Ahmed for the high and low drag results. They demonstrate that there is still a significant amount of extra drag generation coming from the front of the body. These results also show that, when the drag from the slant and base surfaces are added, the CFD predictions are very similar to the high drag Ahmed results. This suggests that the majority of the error in the drag prediction is coming from the front of the body, and reinforces the assertion that the CFD predictions for this angle of back slant are substantially in the high drag mode. The drag coefficients for the QUICK predictions are shown in Figure 1.25, the drag values for the hybrid differencing predictions and wind tunnel results are also shown.

	Shear	Front	Slant	Base	B+S	C_D
Hybrid	0.046	0.278	0.132	0.163	0.295	0.619
QUICK	0.051	0.128	0.131	0.156	0.287	0.466
Ahmed high drag	0.057	0.016	0.213	0.092	0.305	0.378
Ahmed low drag	0.051	0.019	0.089	0.101	0.190	0.260

Table 1.3 Drag Coefficient Components for 30° Slant. $k-\epsilon$ Turbulence Model and Grid 2C. Also shown are the experimental results.

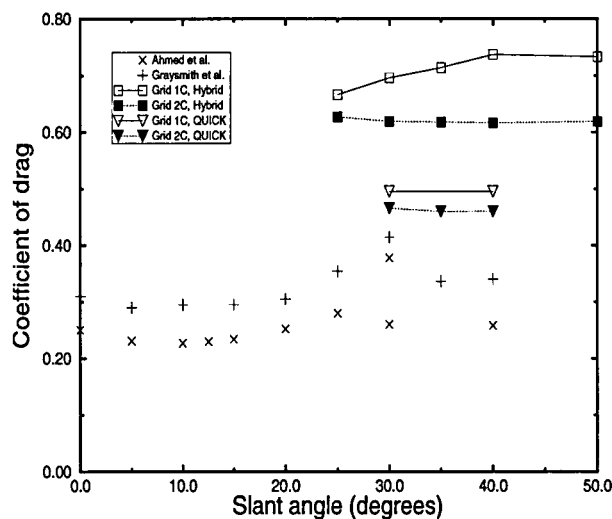


Figure 1.42 Drag Coefficient versus Slant Angle for the $k-\epsilon$ Turbulence Model

1.8.6 Effect of Reynolds Stress Turbulence Model

The excessive generation of turbulent kinetic energy by the $k-\epsilon$ turbulence model in regions with strong normal strain rates, such as the impingement region on the front of the body, is a problem for many practical flows. A Reynolds stress transport turbulence model, as used in impinging jet test-cases [12], does not require a model for the generation of turbulence terms and, so, is largely free of the excessive build up of turbulence in the impingement regions. It also models the generation and destruction of turbulence due to streamline curvature, which may influence flow over the front and rear parts of the body. Furthermore, it does not always predict solid body rotation within vortices, unlike the $k-\epsilon$ model.

The first Reynolds Stress Transport (RST 1) model was developed largely for free and wall shear flows, and can still exhibit un-physical behavior in impingement regions, caused by the wall reflection correction to the redistribution term [12, 76]. The second Reynolds Stress Transport (RST 2) model uses an alternative model for this term, which has been developed recently, by considering the behavior in impinging flows [12, 20].

Figure 1.43 illustrates a large reduction in turbulent kinetic energy on the front of the body for the RST 2 model. The RST 1 model generates a higher level of turbulence than the $k-\epsilon$ model on the front of the body. However, this is reduced below the $k-\epsilon$ level, due to the streamline curvature effect in the stable region between the curved front section and the velocity peak in the boundary layer. The large reduction in the levels of turbulence on the front of the body only produces a small reduction in drag coefficient (Figure 1.44). This may well be attributed to the numerical diffusion caused by first-order upwind differencing which dominates the turbulent diffusion. Table 1.4 shows the drag coefficient components for the 40° slant angle and the second coarse grid. The reduction in shear drag for RST2 is more clearly seen here.

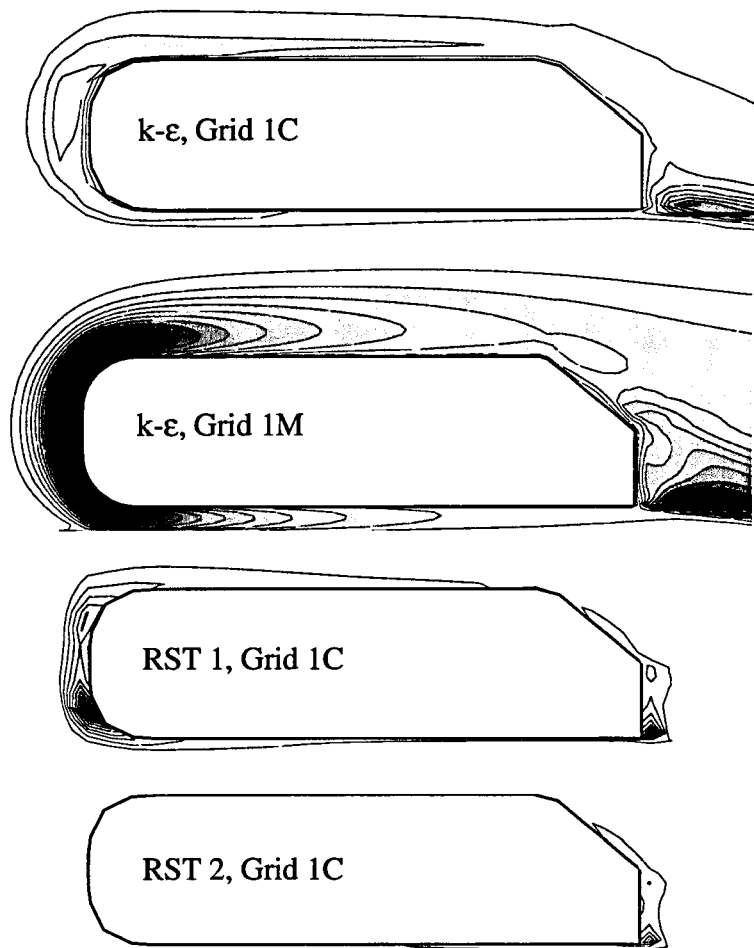


Figure 1.43 Contours of k/U_0^2 (0.0 - 0.064; 12 increments) on Symmetry Plane. Hybrid Differencing.

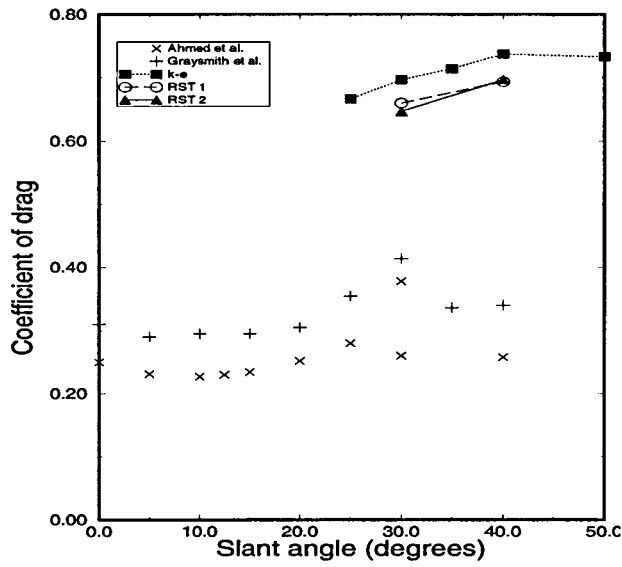


Figure 1.44 Drag Coefficient versus Slant Angle. Grid 2C and Hybrid Differencing.

	Shear	Front	Slant	Base	C_D
k-ε	0.049	0.299	0.360	0.029	0.737
RST 1	0.044	0.238	0.381	0.033	0.696
RST 2	0.026	0.281	0.351	0.036	0.693
Ahmed high drag	0.057	0.016	0.213	0.092	0.305
Ahmed low drag	0.051	0.019	0.089	0.101	0.190

Table 1.4 Drag Coefficient Components for 40° Slant. Hybrid Differencing and Grid 2C. Also shown are the experimental results.

1.8.7 Conclusions

The results of this study of the Ahmed body flow and which used numerical and physical modelling practices representative of very similar studies repeated in the literature can be summarised as follows:

- Flow field and drag level are influenced by grid density
- Flow field and drag level influenced by differencing method
- Flow field and drag level influenced by turbulence model
- Flow field influenced by grid topology over top/slant edge

The objective of these calculations was to establish the sensitivity of the Ahmed bluff body flow to CFD modelling practices and, in particular, to examine the prediction of the drag force on the body and the change in that force as the angle of the slanted rear surface is varied. Repeated wind tunnel experiments show a sharp exponential-type rise in the drag up to 30° , at 30° there are two flow modes: a high drag and a low drag related to the affected separated flow seen on the slant surface.

The results of all calculations showed high levels of drag compared to the wind tunnel results. The drag seemed to be almost constant for all angles of back-slant. When examined further, the flow shows no evidence of the gradual separation from the slant surface starting at the top edge, that is evident in the wind tunnel experiments. Rather, the flow separated gradually starting from the bottom edge due to an adverse pressure gradient. The results of the calculations also revealed, as discussed, no change in the drag levels with altering angle of back slant.

The use of a higher-order accuracy convection discretisation (the QUICK differencing method) on the momentum equations gave lower levels of drag for all the angles of back slant. However, these were still too high and, again, fairly constant over the

range. The flow was still separating gradually from the bottom of the slant upwards, where it should have started from the top and gradually increased downwards.

The final investigation used the hybrid differencing scheme with the full Reynolds Stress turbulence model. These results still gave no drag change over the range of back slant angle tested, however, the levels were now closer to those seen in the wind tunnel experiments. This improvement in drag prediction was mainly attributed to the Reynolds stress turbulence model's better prediction of the turbulence levels where the flow impinges on the front face of the body. Hence, it can be concluded that the most accurate results would probably be provided by the use of finer grids using the QUICK differencing scheme for convection and the full Reynolds Stress turbulence model. It is evident from the grid refinement work in this chapter that further increases in grid size would be a good starting point for further work, but it is not clear that the most effective way of refining the grid is by refining a structured grid approach, since grid refinement in the important region very close to the body would also introduce an added overhead as the grid would also be refined away from the body.

Of more importance is the failure of the prediction on structured grids to pick up the change in the flow structure and the related change in drag. The re-attachment to the end of the back slant is not seen in any of the calculations in this chapter. Indeed, the first type of grid topology predicts the separation completely inaccurately. The separation seen there is typical of the type seen in smooth bodies, not sharp edged ones such as the Ahmed body. The second type of grid is more accurate - predicting the correct type of separation, however, the problem, now, is the failure of the flow to attach for all but the lowest angles of back slant. When it does, at a very early angle, it is over most of the surface and there is no sign of the re-attachment. The results of this chapter suggest that the topology and density of the grids is critical to achieving the correct flow pattern at a specific angle of the slant surface. In addition, the drag prediction would also appear to be grid dependent. This area should, therefore, form a main focus for the work undertaken in this thesis.

1.9 Objectives of thesis

The main objective of the present study is to assess and improve the application of CFD to ground vehicle external aerodynamics. A number of questions were outlined in Section 1.7 and repeated here for convenience:

- Are the flow fields produced in the CFD predictions similar to the ones suggested by experiments?
- Are the bulk levels of drag in the CFD results similar to those seen in the experiments?
- Can the CFD calculations reproduce the rise and sudden drop of the drag factor seen in the experiments?
- Can the CFD results be improved upon - in terms of accuracy or efficiency?
- Can this type of flow pattern be represented by the time-averaged CFD predictions or can some aspects only be captured by unsteady CFD?

The structured mesh CFD predictions carried out as an initial exercise, answer, in part, these questions:

- The flow field produced by the CFD is correct for the fully attached and fully separated cases but the partially separated case is not seen.
- The bulk levels of drag are too high (approximately twice the experimental values).
- The drag “jump” is not seen.
- The CFD results can clearly be improved.

The CFD results discussed in Section 1.8 also revealed a number of aspects, which influence the ability of CFD models to predict the flow. The main areas which it is

believed worthy of primary study is grid development. Therefore, the principle focus of this study will be the CFD grid, both in terms of type and topology of grid over the body and in terms of the level of refinement.

Various options for further grid development are available:

- Maintain structured grid approach but increase in size (increasing ijk number of cells in grid)
- The grid could be locally refined (embedding)
- The type of grid could be changed (unstructured/mixed meshes)

As mentioned above, the increase in grid size option can be rejected due to its inefficiency; this is a fundamental inadequacy with structured grids.

The option of embedding is a possibility but it was believed that the study of the fully unstructured/mixed grids should be undertaken first as this provides a more convenient approach for efficient grid refinement, and mixed grids can be used to introduce the local refinement of embedded grids in any case.

The use of unstructured/mixed grids will enable work to be performed on the Ahmed body with grids that will place higher numbers of cells in the regions of high change near the ground and body and less fine grids away from those regions. It will also permit greater freedom of cell faces, which should reduce the amount by which the flow pattern over the top/slant edge is being dictated by the mesh in the structured grid work above.

The application of unstructured/mixed grids to the Ahmed body flow required initially some work to be carried out on unstructured (tetrahedral) grid generation; this is reported in Chapter 2. Subsequently, unstructured grid calculations were carried out

using both the mesh generators developed as part of the present work, and a commercially available grid generator. All unstructured grid solutions were carried out with the Fluent CFD package. The grid generator available in this commercial software also enabled mixed grids to be generated and flow solutions obtained on these grids. Finally, the thesis ends with a discussion of the success of these unstructured grid calculations for vehicle aerodynamic predictions.

2. Tetrahedral Grid Generation

2.1. Introduction

An important problem outlined in Chapter One, and central to a test case such as the Ahmed body (a relatively small body in a large tunnel) is that, if the same resolution is used for the entire solution domain, then the grid will either be too coarse near the solid body boundaries or there will be too many cells in the region far-removed from the body (Figure 2.1 demonstrated the extra cells required in the far-field region for a coarse surface mesh on the surface of the body). Therefore, a technique to alter the number of grid lines in those regions where there are high gradients of pressure or velocity is required.

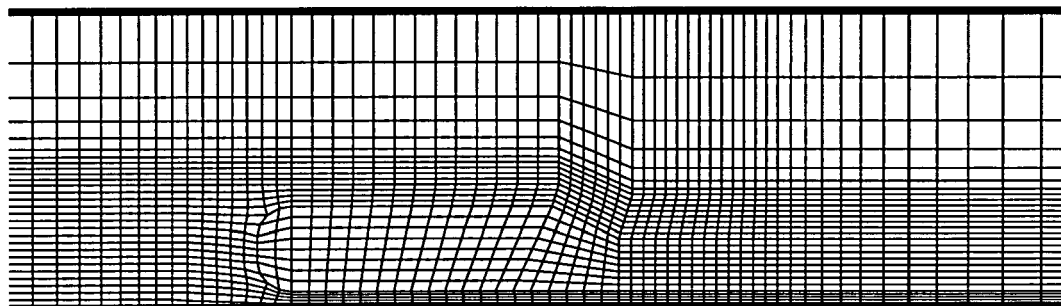
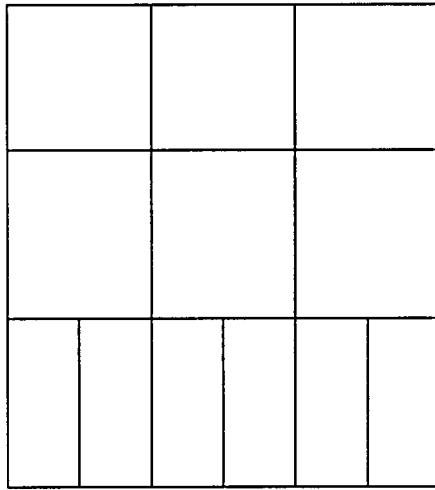


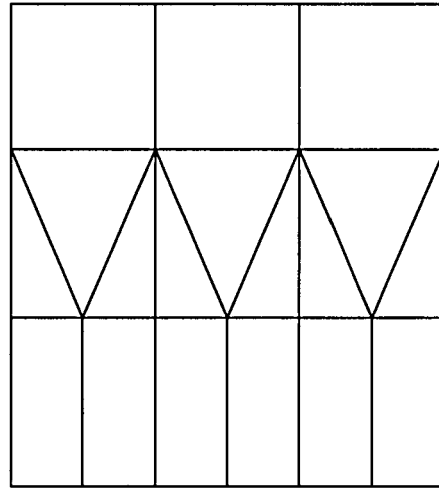
Figure 2.1 The Structured grid over the Ahmed body.

One solution to the problem is to use, instead of hexahedral elements as in a structured grid, different shaped elements, such as triangles/tetrahedrals to tessellate the solution domain. These shapes allow cells to be of different sizes throughout the domain without, the need for intersections of two faces onto one, as in embedding. (see Figure 2.2).

Unstructured tetrahedral grid generation for CFD has been the subject of intense work and research during the last ten years. Several quite varied approaches have been proposed [11,16,33,47,51,54,64,65,83,84]. Some of these have been based on ideas from computational geometry constructions, for example, the Delaunay triangulation, whilst others adopt a more heuristic approach, as seen in the Advancing-Front scheme.



The embedded solution: hanging nodes.



The unstructured solution: no hanging nodes.

Figure 2.2 The solution to the hanging node problem created by grid embedding.

Both a 2D and 3D mesh generator are required, since both surface and volume meshes must be generated, with the 2D grids serving as boundary conditions for the 3D case. Whilst a 2D grid generator is complex, there is an extra problem that occurs in 3D. This can be attributed to the fact that there is no perfect number of tetrahedrals that can be fitted next to each other on a plane. In 2D, by contrast, three equilateral triangles will fit perfectly on to a line (see Figure 2.3).

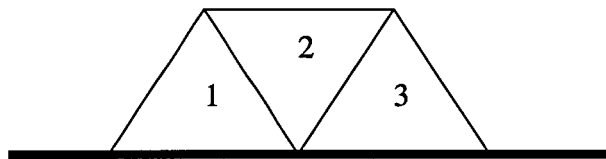


Figure 2.3 The tessellation of triangles onto a line.

In 3D, with tetrahedrals, the angle between two faces of an equilateral tetrahedral is approximately 70° . This means that, along a plane on which two equilateral tetrahedrals are butted together (Figure 2.4) a problem arises because the angle between the two is only 40° .

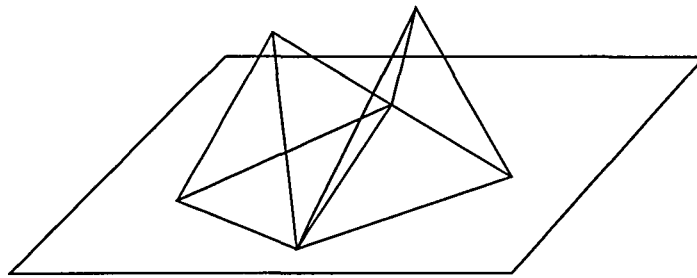


Figure 2.4 The tessellation of tetrahedrons on a plane.

Consequently, the element formed from this third 'base' tetrahedron will be both badly skewed and smaller than the ideal size for a cell on the boundary. One solution is to reduce the interface angle to 60° , i.e. a flattened tetrahedron. However, this would result in the faces on those tetrahedrons being skew and too small. The problem is, therefore, ill-posed, and one to which there is no easy solution.

A brief review of the existing methods in tetrahedral grid generation will be presented, along with each method's suitability to the problem of meshing around a bluff body in close proximity to the ground. This will be followed by a description of the implementation of the chosen method and the inherent problems. Finally, examples of the current capabilities of the chosen grid generator will be discussed.

2.2. Extant Tetrahedral Mesh Generation Techniques

2.2.1. Delaunay Triangulation

There are many ways of connecting a set of points in a plane or on a surface, which result in a triangulation of that plane or surface. One of these is the Delaunay triangulation or tessellation, which has specific properties. The Delaunay tessellation is the dual of the Voronoi tessellation. The Voronoi tessellation was

discovered in 1850 by Dirichelet and is defined by the following (taken from Watson [80]):

“For a set of points $P_k\{k=1\dots K\}$ the regions $\{V_k\}$ are the territories which have every point within that region closer to the point P_k than any other point, i.e.

$$V_k = \{P_i: |p - P_i| < |p - P_j|\} \text{ for all } j \neq i$$

This is true for N-dimensional space.

An important property of the Delaunay tessellation is that the points forming the Delaunay triangles form an N-sphere, of which the centre is the vertex of the Voronoi diagram, that is, a circle in 2D and a sphere in 3D (see Figure 2.5.). This

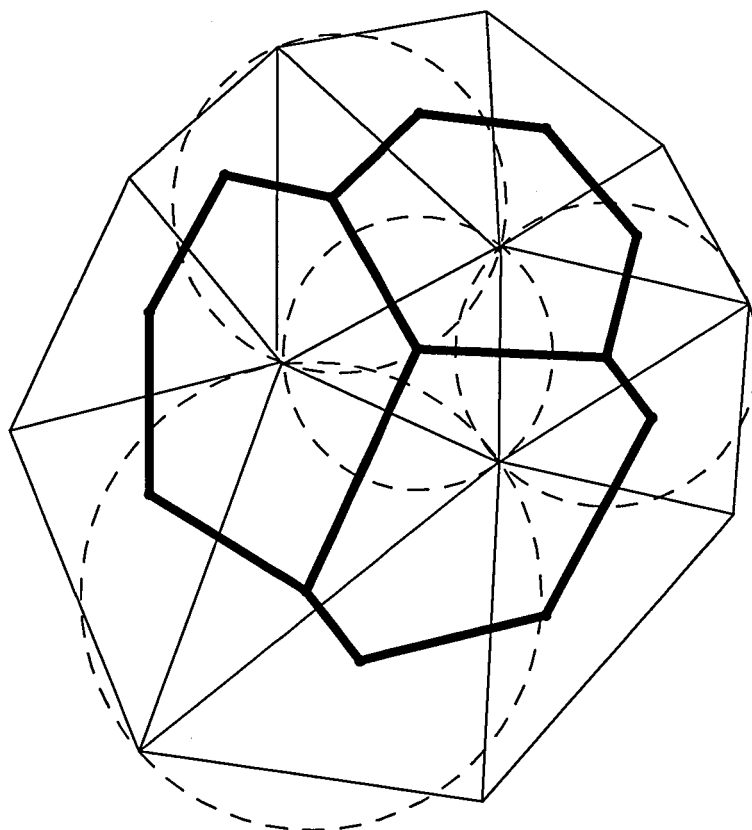


Figure 2.5 The Delaunay grid (fine lines), Delaunay circumcircles (dotted lines) and Voronoi Tessellations (bold lines).

results in the empty circumcircle property, whereby no point (that is, a vertex of the Delaunay tessellation) in the set can be inside the circumcircle of any triangle. This

property ensures that all the triangles or tetrahedra are of a regular shape and of high quality in terms of skewness. To visualise this property, imagine several tetrahedrals inside their circumspheres. The spheres act like bubbles, preventing points from other cells from entering and thus preserving cell quality. Furthermore, the Delaunay triangulation maximises the minimum angle of all possible triangles for the points, and therefore, produces well-shaped elements, that is, it is a minimum/maximum triangulation. Further discussion of these properties can be found in Aurenhammer [4] and Preparata et al. [66].

Having a triangulation with these properties is desirable. The question must be posed, however, as to how it is generated. There are several possible ways.

2.2.1.1. The Bowyer-Watson Algorithm

The Bowyer-Watson algorithm uses an initial mesh and a list of points, which must be inserted into it. The triangulation proceeds as follows:

1. Find the triangle which surrounds the point.
2. Test to see whether this cell's neighbours have circumcircles that also contain the new point. If so, test that cell's neighbours and repeat, until a complete list of all triangles that 'contain' the new point is achieved.
3. Delete all these elements and any edges that have had both elements that it surrounds deleted.
4. Reconnect all points that are part of the remaining convex hull to the new point. All these triangles are automatically Delaunay.

The proofs of the convexity of the hull after the deletion of the elements and the Delaunay-ness of the final tessellation can be found in Watson [80] and Baker [5]. This triangulation requires an initial triangulation to be created before the point insertion can begin. This can be any triangulation and need not contain all of the points that will be in the final tessellation. It need contain only those boundary

points required for the tessellation. In addition, this method works in 3D using tetrahedrals and spheres in place of triangles and circles.

Whilst the Bowyer-Watson algorithm is the most widely used Delaunay method there are several others.

2.2.1.2. The Green-Sibson Algorithm.

The Green-Sibson algorithm is similar to the Bowyer-Watson algorithm in that it, too, requires an initial triangulation into which a list of prior known points must be added [23]. Each new point is added to the triangulation and the triangle that surrounds it is removed. The resulting trio of visible points are then connected to this new point, to form three new triangles, that may or may not be Delaunay in structure.

To convert this triangulation into a Delaunay one requires edge swapping, whereby a pair of triangles that share an edge can have this edge deleted and replaced by an edge formed by joining the other pair of points (see Figure 2.6).

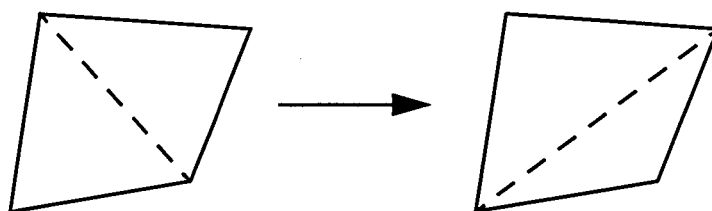


Figure 2.6 Edge Swapping

If the circumcircle of one of the new triangles contains another point of the existing triangulation, then the outside edge of this triangle (that is, the one that does not touch the new point) must be deleted and swapped for the edge which joins the new point and the one found by the circumcircle test. The two new triangles formed must subsequently be re-checked for Delaunay-ness as in the above test. This

process continues until all triangles are Delaunay (see Figure 2.7). The method is very similar to the schemes used to improve the Delaunay-ness of already completed triangulations. This algorithm is, like the others, applicable in three dimensions also.

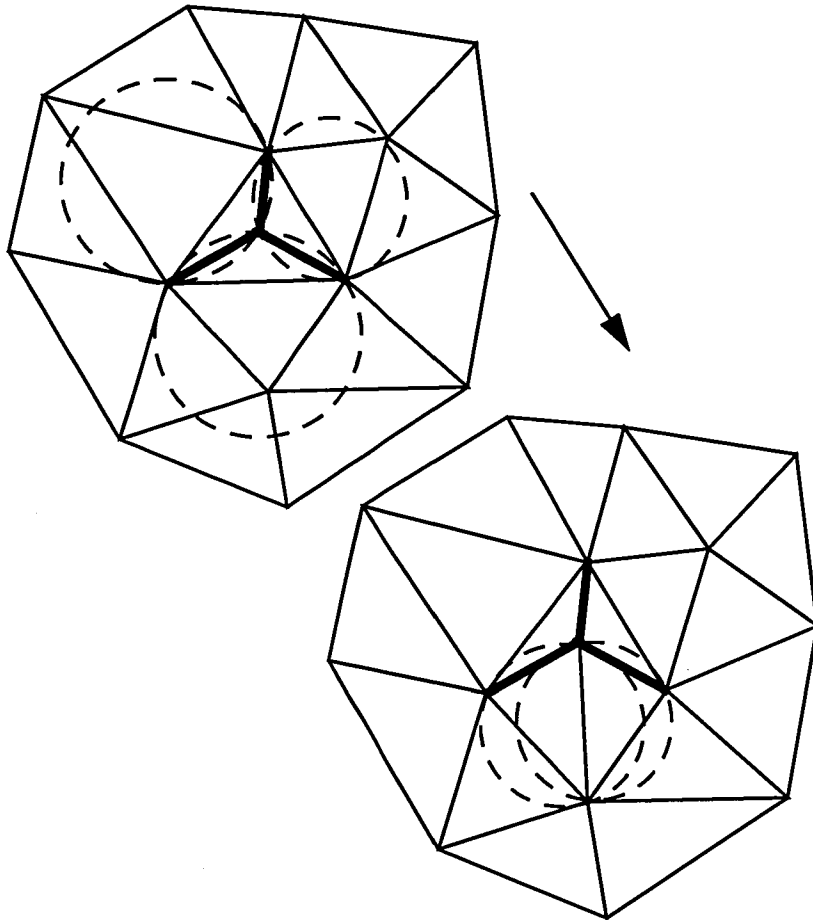


Figure 2.7 The edge swapping used to convert a non Delaunay tessellation into a Delaunay one.

2.2.1.3. The Tanemura-Merriam Algorithm

The Tanemura-Merriam Algorithm [52] differs from the previous two methods in that it does not require any initial mesh, except for the initial boundary edge tessellation. These boundary edges comprise the initial front from which the mesh grows from.

The algorithm proceeds as follows:

1. An edge from the list of front edges is chosen according to some parameter associated with those edges, e.g. edge length.
2. An arbitrary interior point is selected from the list of points, and the circumcircle that results from the two edge points and the point, is constructed.
3. If this circumcircle contains any other interior point, then this point should replace the one chosen previously, and the steps from point 2 repeated until no alternative point is found.
4. The triangle of the 3 vertices of the circle is formed and the front updated, that is one or two edges are added according to whether they already exist.
5. The process is continued until the front is empty.

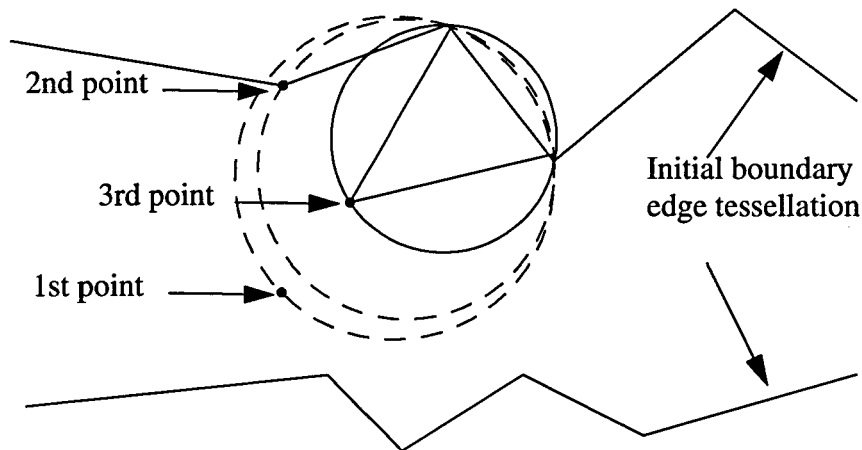


Figure 2.8 The point selection process used in the Tanemura-Merriam Algorithm

For the Tanemura-Merriam algorithm to be formed, the Delaunay criterion must be restated, albeit in a slightly different way. Imagine if the Tanemura-Merriam algorithm were to be applied to a geometry as portrayed in Figure 2.9. The geometry depicts a rectangle that has had a slot cut in it creating two forks. If the edge tessellation was comparable to the height of the two forks, then any circumcircle could easily contain a vertex of the other fork (see Figure 2.10). This situation will, according to the original Delaunay criterion, imply an invalid tessellation. However, here there is no other option, and the tessellation is Delaunay when each part of the geometry is considered in turn. Therefore, we can conclude that the geometry is responsible for this un-Delaunay-ness and not the triangulation.

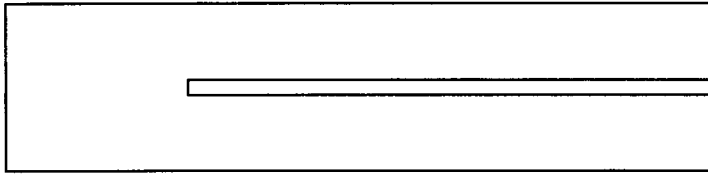


Figure 2.9 A difficult geometry

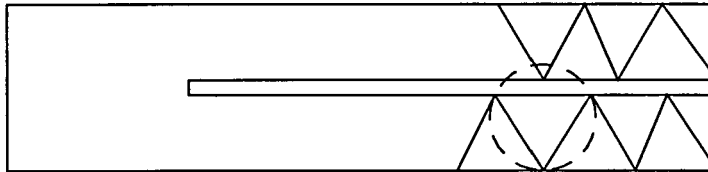


Figure 2.10 A difficult geometry with a partial tessellation.

It is essential, therefore, to define a constrained Delaunay tessellation [52] whereby a given tessellation, which must contain a given set of edges, is as close as possible to a Delaunay tessellation. The empty circumcircle property is re-stated, as every triangle's circumcircle contains no other vertex which is visible to it. Visible is defined, here, as those vertices that, when a line is drawn between it and any point on the interior of the triangle (not restricted to those in the tessellation), do not intersect any of the edges in the prescribed set of edges to be kept (This constraint is also necessary for defining the boundaries of any Delaunay tessellation algorithm).

This re-definition is not possible in 3D, therefore, problems associated with tessellations, which must lie within a set of defined surface triangulations, will arise.

2.2.1.4. Difficulties with the Delaunay Triangulation Algorithms

For more automatic mesh generation, a method of point insertion is required to speed-up the above methods. Methods do exist, for example, simple placement of new points at the circumcentre of triangles where further refinement is required. The more insoluble problem connected with point placement is that of defining a

grid spacing, stretching and clustering functions over the domain. To implement these kinds of functions, however, could invalidate the Delaunay-ness of the triangulation. A more satisfactory solution would be to place points as the grid develops, rather than at steps between completed grids; and to base the position of the new points on known quantities in this localised area of the domain. This property is inherent in the following algorithm.

2.2.2. The Advancing-Front Algorithm

The Advancing-Front (AF) method of grid generation [54] differs from the Delaunay method, in the fact that the tessellation of the 2D or 3D space requires neither any initial triangulation covering the entire domain, nor a list of points to be added into this triangulation. It does, however, require that the boundary of the space to be gridded must be triangulated, in the 1D or 2D sense, respectively. The algorithm itself can, however, be used in 2D to provide this boundary triangulation for a 3D tessellation. In 2D, all that is required is to split the boundary geometry edges into lengths comparable with the desired local grid spacing, defined by the user for the triangulation.

The AF algorithm is important and of interest here since it has not been applied to the problem of the automotive bluff body in close proximity to the ground. This method may prove to be more suitable to capturing the flow pattern of the test case than the more widely used Delaunay methods. Therefore, the Advancing-Front algorithm will be described and its development detailed in the rest of this chapter.

A 2D triangulation will be used to demonstrate the workings of the AF algorithm (the process is similar in 3D). The method follows the same basic structure defined by Lohner and Parikh [47]:

1. Set up a background grid defining the spatial variation of the size, the stretching and the stretching direction of the elements to be generated.

2. Define the boundaries (surfaces) of the domain to be gridded.
3. Using information stored on the background grid, set up faces on all these boundaries. This yields the initial front of triangular faces (Figure 2.11). At the same time, find the generation parameters (element size, element stretching and stretching direction) for these faces from the background grid. It is helpful at this point to set up a list of the grids points, faces and cells.

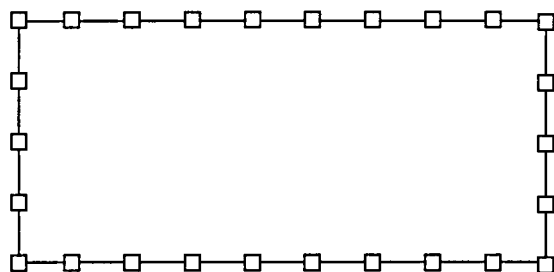


Figure 2.11 The boundary grid (1D tessellation)

4. Select the next face within the front to have a cell generated from it. In order to avoid large elements crossing over regions of small elements, the face forming the smallest new element is selected as the next face to be deleted from the front and list of faces.
5. For the face to be deleted:
 5. 1 Select a best point position for the introduction of a new point (VERTEX A), Figure 2.12.

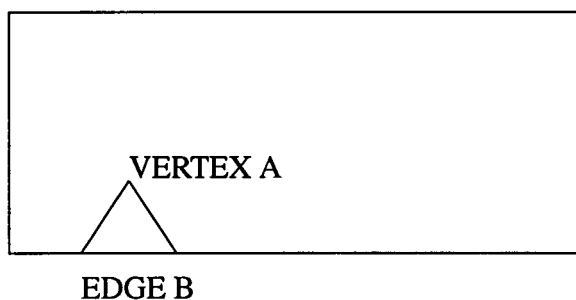


Figure 2.12 The first face of the tessellation

5. 2. Determine whether a point already exists in the generated grid that should be used in lieu of the new point. If there is such a point, set this point to VERTEX A and continue to search for other possible vertices (go to 5.2.), see Figure 2.13. Form these vertices into a list ordered by closeness to the best point (from 5.1).

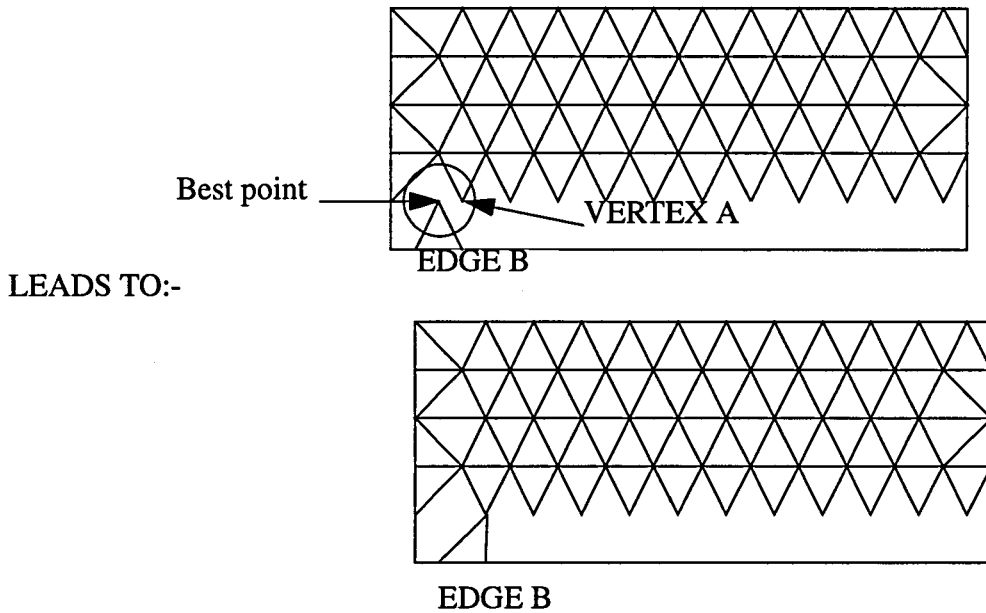


Figure 2.13 The "snapping" of a new vertex to an existing one in the progressing tessellation.

5. 3. Verify that the element formed with the selected point VERTEX A does not cross any given faces. If it does, select a new point from the list (from 5.2) and continue.
6. Add the new element, point and faces to their respective lists.
7. Find the generation parameters for the new faces from the background grid.
8. Delete the known faces from the list of faces.
9. If there are any faces left in the front, go to 4.

The main benefit of this strategy is the automatic point placement. The elements formed are of a high quality, due to the optimal position of these points. These advantages are further enhanced by the local nature of all intersection and angle checks, which are performed in the process. The algorithm, by its frontal nature, cannot violate the boundary in any way, since the initial front is the boundary itself.

The disadvantages are mainly in areas of efficiency encountered when checking for intersection, which involves potentially expensive search algorithms to find the list

of close points and edges. Another problem is the generation of only one triangle per new point. A more satisfactory solution would be to generate all triangles that could use the new point. A potentially more serious problem, however, is the question of robustness. If, for example, a very small edge is incident on a large edge (in 2D), the algorithm will fail, as it cannot “see” any point within range that is not behind this edge. This problem is considered in more detail later in this chapter.

2.2.3. Other Schemes

2.2.3.1. Delaunay Based Point Insertion Methods

Delaunay based point insertion methods offer an attractively simple method, by adding vertices at the centre of circumcircles of triangles that are too large (defined by a preset grid parameter) in the existing triangulation. This method still relies on an initial triangulation on the region, although this can be simply defined as all the boundary points linked to a central point (Figure 2.14). The necessary boundary recovery stage can be completed later, using edge swapping and face swapping along with deletion of fully external elements. These methods are covered fully in Muller [54].

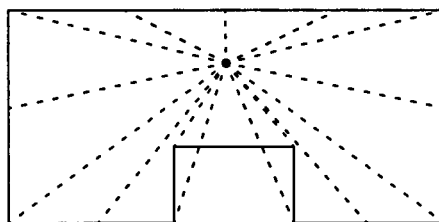


Figure 2.14 An example initial triangulation that ignores the boundary.

The method works well for 2D tessellations, however, the extra complexity of retrieving the boundary, and the lack of a robust constrained Delaunay tessellation in 3D, precludes further consideration here.

2.2.3.2. Advancing-Front Delaunay Triangulations

This improvement to the Advancing-Front method was proposed by Mavripilis [51]. The basic structure of the Advancing-Front method is retained as used in 2D or 3D, however, the Tanemura-Merriam algorithm is implemented, as each potential new triangle is considered, to give a maximum Delaunay structure to the resulting mesh.

The algorithm is as follows:

1. Construct an initial front from all boundary edges.
2. Choose a front edge based on some criterion, e.g. length.
3. Find all points in the front which are within 2ρ of either end point of the edge (where ρ is the local grid spacing taken from the background grid).
4. If there are any such points, use the Tanemura-Merriam algorithm to find the Delaunay triangle that results from this point.
5. If the triangle formed has a circumcircle of less than ρ , then keep it, update the front accordingly and proceed to 14 below (Figure 2.15).

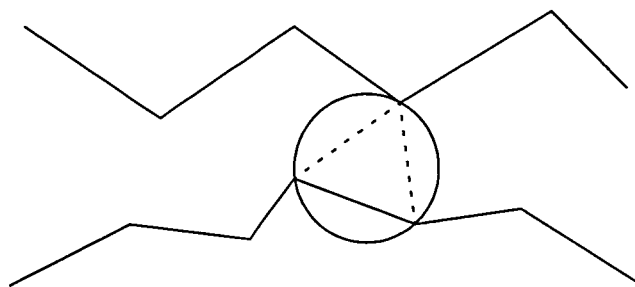


Figure 2.15 Case one, there exists a suitable point already in the tessellation and the radius of the resulting triangle is less than ρ .

6. Otherwise create a new point, there are two cases here:
 - 6.1. No points were found in search 3. above. In this case, form a new point along the line normal to the front edge at its median. The point should be ρ from the end points of this edge (Figure 2.16)

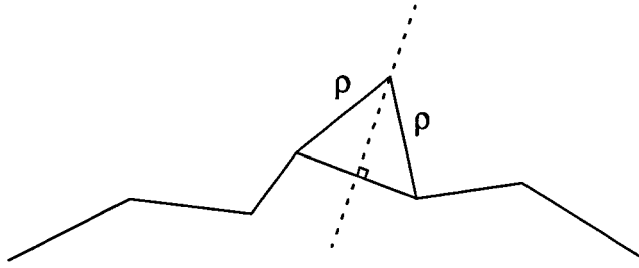


Figure 2.16 Case two, no vertices were found so one is created along the line perpendicular to the edge at it's median.

6.2. Some points were found in search 3. above. Form the new point at the circumcentre of the Delaunay triangle formed by the Tanemura-Merriam algorithm in step 4 (Figure 2.17).

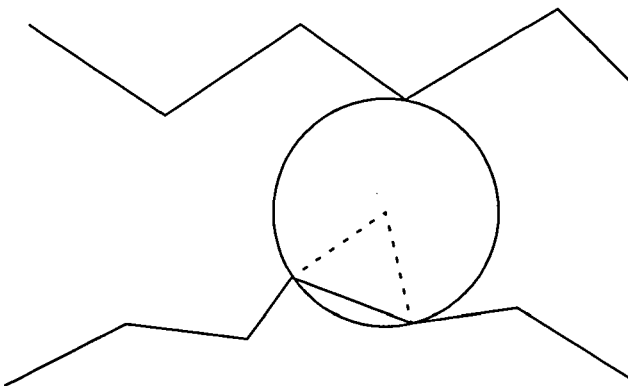


Figure 2.17 Case three, no points within ρ .but some within 2ρ . The new point is put at the centre of the circle formed using the Tanemura-Merriam algorithm.

7. Connect this new vertex to the two end points of the front edge.
8. Test to see if any of the front triangles have a circumcircle that contains this point, (this could be a costly and lengthy test).
9. Using a “neighbour search” on only those triangle that are found in the test 8., test the interior triangles for the new point being inside their circumcircles. If it is, then also test this triangle’s neighbours in this way and repeat, until a complete list of all the triangles intersected in this way is formed.
10. Remove all the triangles that are intersected in the test, and update the front edges and points.
11. If the circumradius of any of the deleted triangles is greater than the value of ρ

at this point, then change ρ to this value and locate any front points within 2ρ of the new point.

12. Form all the Delaunay triangles using the new point and two of the points found within 2ρ of the new point. Do not form any triangles with a circumradius greater than ρ .

13 Add the triangles to the tessellation and update the front as in the Advancing-Front method.

14. If the front is empty, then stop, otherwise go to step 2.

This algorithm gives very smoothly varying and regular meshes, even before mesh improvement techniques are employed. This can be attributed to the mesh paying close attention to both sides of a converging front, instead of just one, in as in the Advancing-Front method. This method has many desirable properties. However, due to time pressure it was not implemented into the grid generator developed as part of the present project.

2.2.3.3. Other Frontal Delaunay Methods

There are several other frontal methods that offer automatic point creation. These include those which require an initial mesh on which to operate, and as such will not be considered in detail here. For a complete discussion see Muller [54]. Having generated an initial tessellation using one of the methods described above, the triangles/tetrahedrals are separated into two groups, acceptable and unacceptable. The acceptable ones are those which satisfy the Delaunay in-circle criterion; unacceptable those that don't. The unacceptable group is, then, further split into two subgroups: active and non-active, the former being those that share an edge with acceptable triangles. The front is made up of all of these edges between acceptable and active triangles.

When an active triangle is selected from the set for improvement (that is, the edge

of the front is chosen), a new vertex is placed somewhere along the line formed perpendicular to the front edge, at its median point. The exact position of this new vertex is dependant on which of the two algorithms is being employed (Figure 2.18).

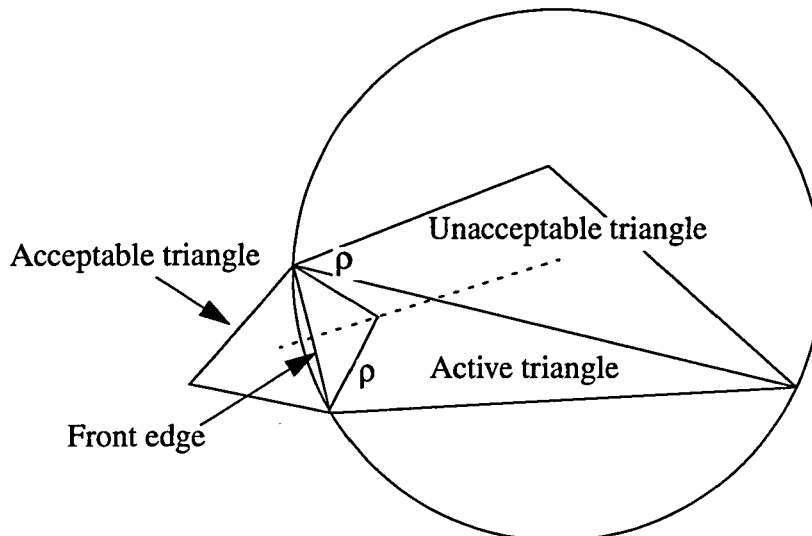


Figure 2.18 The point placement strategy of the Rebay frontal method where the new point is placed along the line perpendicular to the front edge at its median such that the new edges have length equal to the local length scale ρ .

Elements are then added and deleted as necessary and, so, the algorithm proceeds. At least one new Delaunay triangle is formed at each stage, ensuring the progression of the front.

2.2.3.4. Advancing Layer Method

Another frontal modification to the Advancing-Front method is that of Pizradeh [65], the advancing layer method. The method adds the restriction that an element must be grown from all faces in the front, before the front is updated. In this manner, the mesh advances in layers, rather than in the rather haphazard method used previously. When this method is used in conjunction with an appropriate background grid, it helps ease the problem of converging fronts of different length scales, as well as reducing the complexity of the search algorithms complexity.

2.2.3.5. Other Methods

It is also possible to use a combination of these methods as proposed by Corral [11]. The Delaunay methods give smoother grids in a shorter time, but require an initial grid, whereas the Advancing-Front method is better at producing grids that are stretched or growing in size in some direction. The above authors have used an Advancing-Front method to produce the initial grid and refined it using a Delaunay point insertion method. High quality results were reported, combining the best elements of both schemes.

2.2.3.6. Conclusions

Following initial analysis of the different methods available, it was decided to begin by implementing a basic Advancing-Front grid generator in 2D and then 3D. It was felt that this would provide the smoothly varying volume change between elements that is required for accurate CFD solutions. Following this, improvements such as the Delaunay point placement strategies mentioned above could be implemented, should that be indicated as capable of improving the quality of the meshes produced.

It is to be noted that the above survey of mesh generation algorithms does not include a discussion of the mesh improvement techniques available including edge/face swapping and smoothing of the vertices, for example by the Laplace method. These are discussed later.

2.3. Storage Schemes

The Advancing-Front mesh generation algorithm is very search intensive, with the need for local edges/faces and vertices to be found for every step, in addition to locating the background grid element that contains the new point to determine grid spacing and stretching functions. These searches could slow down the algorithm and, therefore, efficient storage schemes must be developed to reduce this overhead.

The searches mentioned above are:

1. Finding the base triangle face from the front of the existing triangulation.
2. Finding the list of close points to this face.
3. Finding the list of faces close to this face.
4. Finding the parameters associated with this face from the background grid.

We can make use of three widely used schemes to help with these searches (see Lohner [48] for a more complete discussion). These three schemes will be discussed in the following sections. The three methods are all implemented in the Advancing-Front grid generator used in this study.

2.3.1. Heap list for the faces

Heap lists are binary tree data structures. The tree is formed by each element (the root) being the father to, at most, two sons (the branches), such that the value associated with the root is lower than that associated with either branch. In this way, the element at the top of the tree has the lowest value and those at the bottom are the highest, all the way to the top of the tree (but not sideways). A good example is the word 'example' which considers the letters of the alphabet in

ascending numerical order (see Figure 2.19).

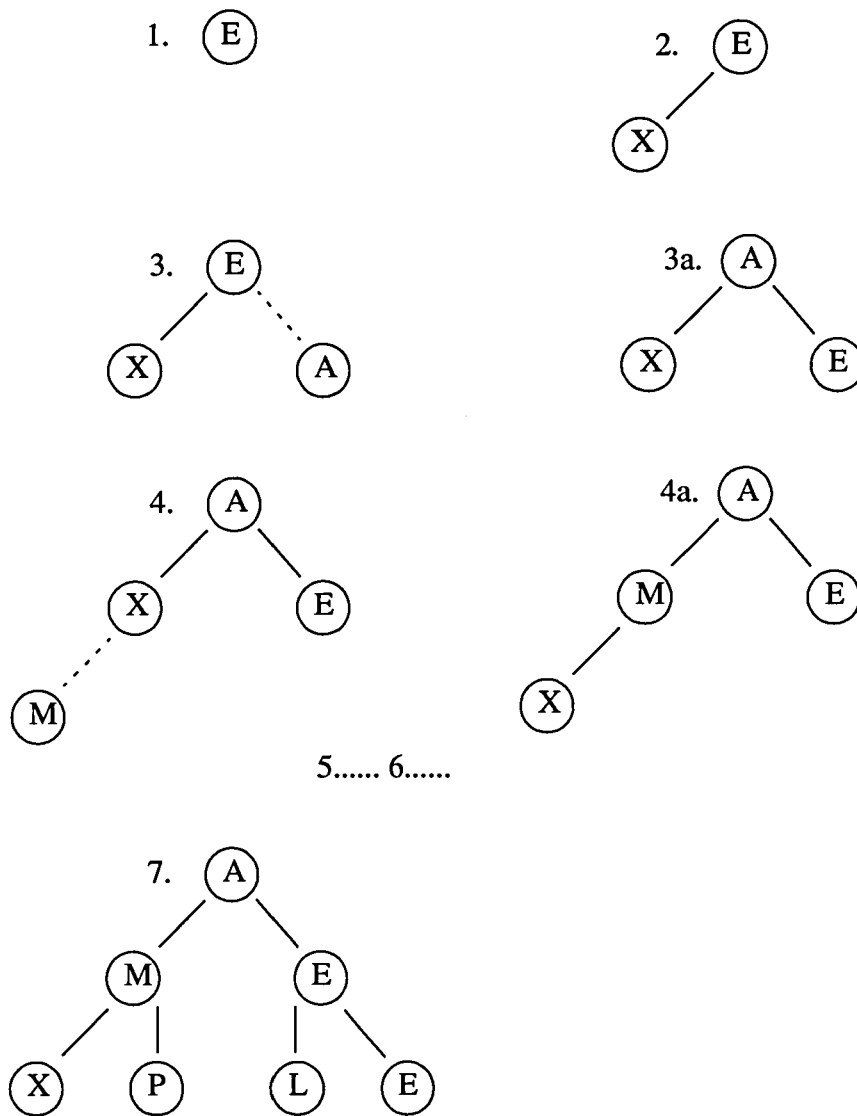


Figure 2.19 The insertion of new points into the heap list.

Elements are added to the list, initially at the bottom of the tree, and then compared to its parent to see if it is of a lower value. If it is, then the root and the new element are swapped. The new father is, then, compared with its inherited son from the original root. If it is of higher value, then it must be swapped with this branch and possibly sent further down it. It is, also, compared to the father of its new position and swapped if of a lower value. In this manner, the tree is shuffled to find the final order of the elements.

When deleting an element from the heap (the whole point of the heap in the first place), the element at the top is chosen for deletion and the element at the bottom of the heap is moved to the top. The shuffling algorithm is used to reassess the ordering of the heap, see Figure 2.19.

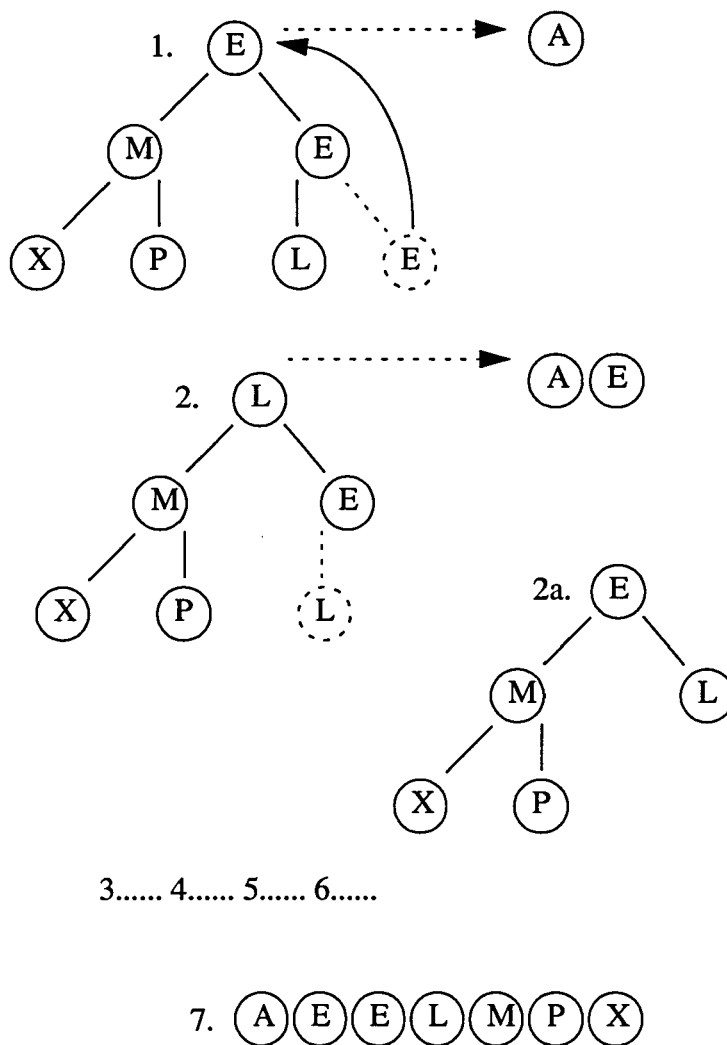


Figure 2.20 The successive deletion of the smallest elements from the heap list.

This scheme reduces the time to find the frontal edge to be used as the base edge for the new triangle and then deleted. This is because the edge we require is the smallest one.

2.3.2. Quad/oct-trees for the Points and Faces.

The principle used for the quad-tree and oct-tree data structures are the same, however, they operate in 2D and 3D respectively. As the idea is better demonstrated in 2D, the quad-tree is described below. The 3D version is completely analogous.

The quad-tree covers the entire domain or geometry and, as points are defined on that boundary, they are added into the tree. The initial quad is the root quad and is the starting point for all searches. The points are added to that quad until there are more than four vertices in it. At this point, it is split into four smaller quads (children of the root), with the vertices being placed in the new quads as required. As the vertices are added to the quad-tree, this child cell, in turn, may contain more than four vertices. This cell is then split into four as previously, and the vertices distributed. See Figure 2.21.

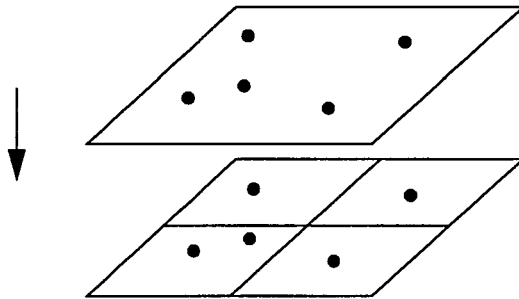


Figure 2.21 The insertion of new points into the quad-tree

The deletion of vertices from the tree simply involves checking the tree levels above the deleted vertex to see whether their four sub quads still contain more than four vertices in total.

This algorithm is a very efficient way of finding vertices that are close to a chosen point in space, by simply descending down the quad-tree. It can also be used for faces and edges.

2.4. The Advancing-Front Algorithm

The method developed here is basically as described in section 2.2.2. The algorithm and specific methods implemented are defined further here.

Advancing-Front grid generators can utilise background grids to reduce the mesh density away from the boundary. This is undesirable here for several reasons. Firstly, whether a grid can be termed coarse or fine is related to the flow structure as much as the geometrical structure. The complexity of the flow field cannot be known in advance and, therefore, the associated cell clustering cannot be achieved. Secondly, the comparison with the Delaunay grid generator in the following chapters is only valid if the two grids have no prior knowledge of the cell spacing in a particular area (in the Delaunay case this knowledge is impossible to achieve). Thirdly, the cell spacings are already interpolated from the boundary tessellation by the nature of the algorithm. This will provide sufficient grid resolution around the geometry. For all the calculations in this study a background grid is not implemented as we are using the same grid parameters throughout the solution domain. This is advantageous for two reasons: firstly, implementation will be less problematic; and secondly, testing of the grid generator should be more straightforward.

The 3D Advancing-Front grid generator works from a starting point of a 2D triangular tessellation, which may be formed in various ways, including a 2D version of the Advancing-Front grid generator. This, in turn, relies upon a 1D tessellation. Therefore, the first task with any grid is to divide the edge set into 1D triangles, which are merely lines of the same length as a given grid parameter. This forms the boundary grid for the 2D tessellation.

Following the method outlined earlier in this chapter, an example would proceed as follows:

Set up the initial front to be all the edges on the boundary of the box (Figure 2.22).

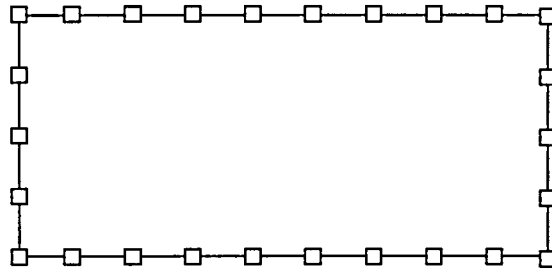


Figure 2.22 The initial 1D tessellation.

The smallest face (EDGE B) is chosen from the front and the best point constructed (VERTEX A). This point is constructed such that it and the two points of the chosen face (EDGE B) form an equilateral triangle. This can be seen in Figure 2.23.

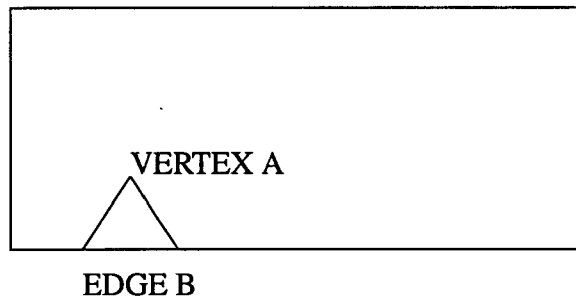


Figure 2.23 The first triangle in the 2D tessellation.

There are no other points existing in the vicinity of the best point. This is tested by placing a circle with a radius equal to the element size parameter. If applicable, the circle is squashed in relation to the defined stretching parameter and direction. This circle surrounds the best point and if any points are found inside it they are used as VERTEX A instead of the best point (in order of distance from the best point as there could be more than one).

No faces are crossed so we can add the new element, point and face to the lists. Simultaneously, any parameters for the faces are set up.

Delete the first face chosen from the front. The front is not yet empty so we return to choosing another frontal edge for tessellation and begin the above process again.

The process can continue like this until the grid is complete (the front is empty), however, it is likely that other situations may occur and left purely in the above form the grid generator would fail to provide a mesh over the desired domain.

If any points are found inside the testing sphere around the best point, these points should go into the list of possible vertices above the new points, in order of closeness to the best point. Figure 2.24 shows how such a point may occur.

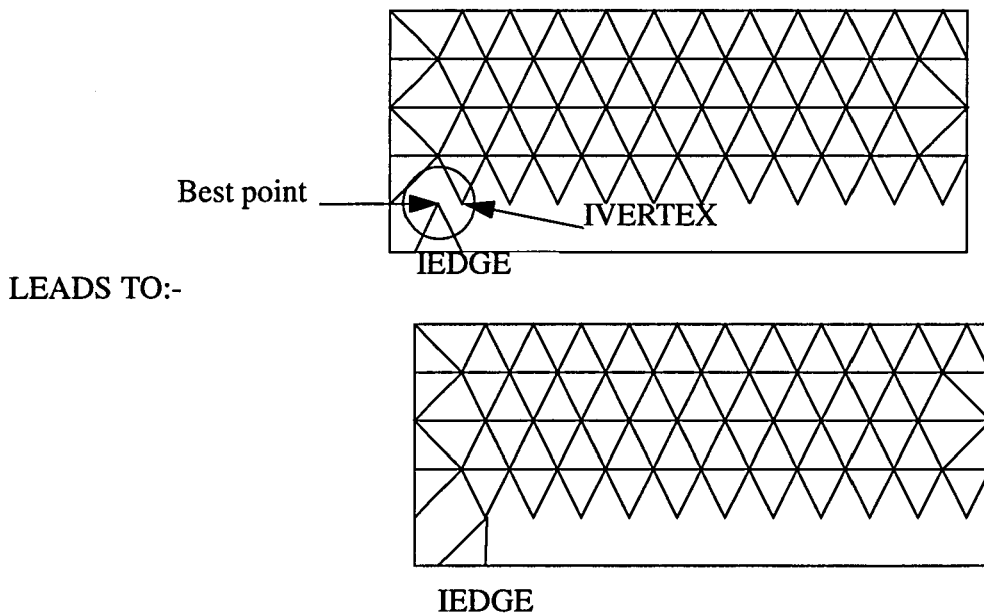


Figure 2.24 The possibility in the 2D triangulation of using an existing point for the top point of a triangle.

If a face is crossed in order to get to one of the possible new point locations, it cannot be used, as it violates the algorithm. If this is the case, then the next possible point location in the list must be used. At this stage it is useful to highlight that, as well as the best point, the list of possible points also includes four other 'new' ones, these are shown in Figure 2.25.

These are placed at various distances along the line from the best position for the new point and the middle of the base edge. Thus, if there are no existing vertices round the best point, and it forms an element that crossed another existing edge, then the next point is chosen from the list. This point is the next 'new' one along the line from the best point's position to the middle of base edge.

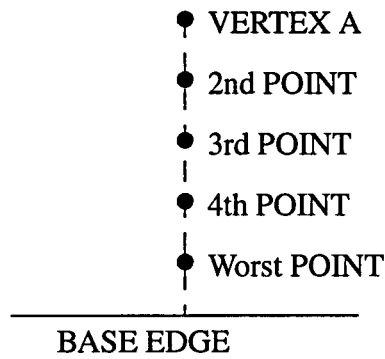
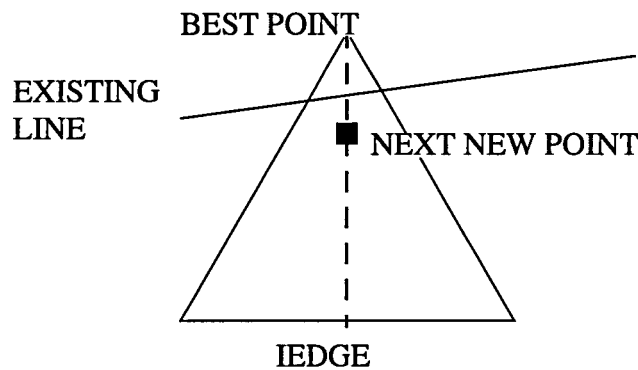


Figure 2.25 The “new” points included in the list of possible top points for any new cell.



LEADS TO:-

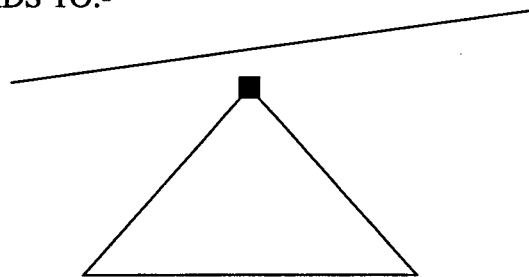


Figure 2.26 The case where the “best” point is not allowed and the second best new point is used.

The procedure is identical in 3D. The boundary edges are replaced by triangles and the circle around the ideal point (which is itself now a distance away from the face of 0.81 times the average of the lengths of the edges that form the face) is a sphere. This sphere has radius d_{step} , where d_{step} is the user specified search length that controls the growth rate of the mesh.

The boundary surface triangulation must be mapped from the 2D tessellation onto the actual geometry surface for each region, for example a cube will require 6 different surface tessellations to be mapped on to its boundary (Figure 2.19).

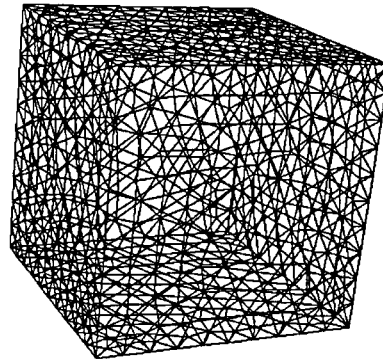


Figure 2.27 The six surface tessellations that make up the boundary grid for a 3D mesh.

2.5. Intersection Tests

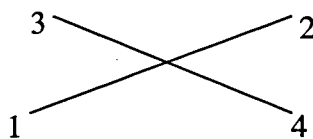
The process of testing a new triangle or tetrahedral requires, as mentioned in Section 2.4, examination of the edges of the new element for intersections with existing elements.

In 2D the intersection test is the solution of two simultaneous equations that represent the two lines being tested:

$$\underline{x}_a = (\underline{x}_1 - \underline{x}_2)t_a + \underline{x}_2$$

$$\underline{x}_b = (\underline{x}_3 - \underline{x}_4)t_b + \underline{x}_4$$

That is, the equations of any points along two straight edges:



If the vectors x_a and x_b are equal, then the two points are the same point in space; and if t_a and t_b are in the interval $\{0,1\}$, then the edges intersect within their bounds. If either t_a or t_b is outside $\{0,1\}$, then the lines would intersect if they were of infinite length but not otherwise.

The intersection routines in 3D are more complex involving planes as well as edges. The situation is eased somewhat by the realization that all intersections in 3D can be detected using an intersection test between all faces and edges. The procedure for the intersection test is the same as for 2D, however, one of the edges is replaced by the equation for a face:

$$x_b = \alpha_1 g_1 + \alpha_2 g_2 + x_f$$

where x_f is the corner of the face, g_1 and g_2 are the edge vectors leading away from that point, along the edges of the face. If we solve the set of 3 equations provided by the above, with the coefficients relevant to each edge, we will find the intersection point of the face and the edge. This, again, will only lie on the edge and the face if α_1 and α_2 are in the interval $\{0,1\}$ and the edge parameter t also lies between 0 and 1.

This test can be long and cumbersome, therefore, it is speeded up by checking to see if the edge and the face remotely overlap before the test. This is done using a simple box test set at the extremities of the edge and the face. If this test is positive, then we test for matching vertices, which will need to be handled differently, by implementing angle and shape tests to ensure the quality of the mesh. Otherwise the above intersection test is performed.

Following this methodology several authors [5, 4] have produced excellent results in terms of robustness and speed of the grid generator. During initial tests of the grid generator developed here, it was found that this intersection algorithm gave satisfactory results.

2.6. Initial Results

Implementing the methods of Sections 2.3, 2.4 and 2.5, initially in a 2D grid generator, and subsequently in a 3D grid generator, a number of problems were identified that were not documented in the literature.

An initial test case of a 2D box of side one was used. The grid suffered from serious variations in cell size and skewness due to lack of suitable grid quality restrictions, as well as the lack of smoothing. It was decided to improve the grid's basic structure before proceeding to smoothing/swapping of the grid.

This poor quality of faces affects the 3D tessellation, which must use the 2D grid as a boundary grid. It means that the natural layering of the Advancing-Front grid generator cannot be used when the frontal face selection is limited to the smallest face, as set out in the algorithm.

Initially, this problem of a lack of grid quality was highlighted by 2D domains filled with poor triangles (see Figure 2.28).

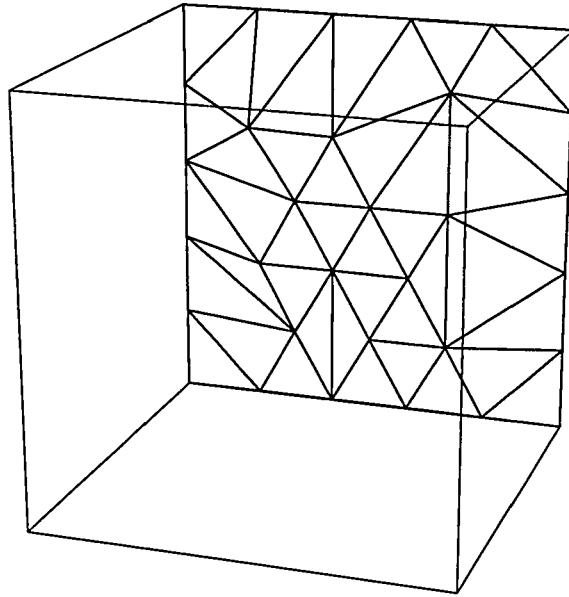


Figure 2.28 The low quality faces on the boundary of a cube

With decreasing grid size the problem can actually get worse and sometimes lead to failed cases (see Figure 2.29).

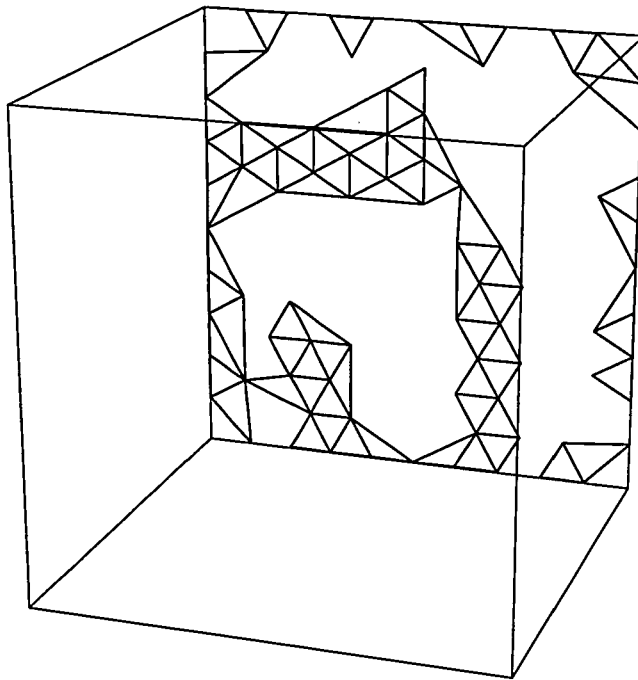


Figure 2.29 The progression of the poor quality cells leading to failed cases.

In an attempt to solve this problem, any vertices connected by any existing edge to either of the vertices that make up the base edge, were made part of the list of vertices to check. That is, if any point and the base edge are connected by another extant edge, then it should be tested as a possible point for the triangulation to use. This removed the possibility of the failed case outlined above, however, it still left cells that were very badly skewed and which varied considerably in size. When these surface grids were used as boundary tessellations to generate 3D grids, this generally met with little success.

To improve the completion rate of the 3D grid generator, it is clear that the quality of the 2D boundary grids must be improved. Such an improvement was implemented in the form of exterior angle and interior angle (skewness) lower bound tests to any possible new triangles in the tessellation. If the new triangle failed this test, it was rejected.

The two angle tests must have the same limits, otherwise, if the exterior angle limit is smaller than the interior angle limit, a cell further on in the tessellation may violate the interior test having passed an exterior angle test (see Figure 2.30). The angle test is formed in both cases by taking the scalar product of the two edges.

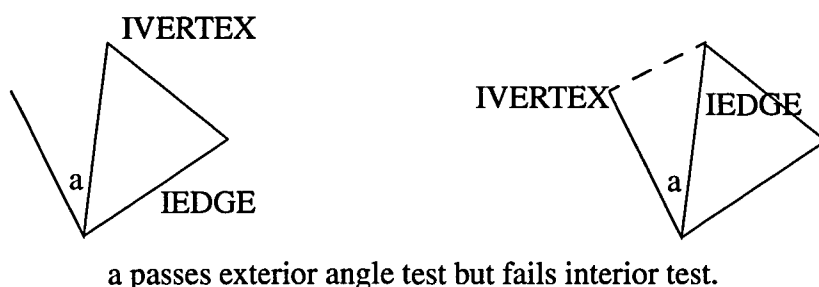


Figure 2.30 An example of why the interior and exterior angle tests must share the same limits

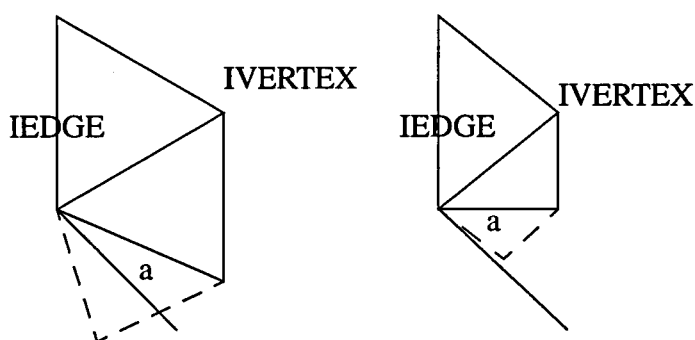
With these tests in place, the algorithm produced much more regular cells. However, it generally failed to complete, due to a new point often being generated too close to an existing edge or point, precluding the generation of a cell between them. (Note: at this point in the algorithm, that an existing mesh vertex found during the circumcircle test around the best point may fail to be used as the proposed new triangle's top vertex. This is due to an angle test within the algorithm designed to reduce the number of poor quality cells).

The next attempted solution to the failed case was to specify a minimum distance between two points. Though variable, this was initially set to $0.5 \cdot dstep$, where $dstep$ is the preset parameter used to define the rate of growth of the cells away from the boundaries. In addition, a distance check was included for edges and points, as the existing meshes suggested that this, too, could help prevent points being placed too close to existing edges. This allowed the grid generator to produce a complete volume grid with almost all test cases

The final addition to the grid generator, that allowed it to be sufficiently robust, for use on the 2D test cases, was the relaxation of the parameters (angles and minimum distances) used in the tests above. This relaxation was done after all the faces in the

front had either been used or flagged as being unable to form the base edge for a new triangle. This “end of front” list forms a set of closed loops or cohesive holes in the mesh. The aim of the relaxation was to allow less “perfect” faces to be generated in these holes in order to allow the grid generator to completely mesh the required space.

Although this completed the 2D algorithm (that is, produced complete meshes over the required shapes), it did leave some very skew cells. To prevent these bad shaped cells, the algorithm was modified to test every new edge to see if a legal cell could be generated from it. This, in effect, ensures at each stage of the front, that the next cell from the new “proposed” front will not fail. This is done using the code already in place, by looping back with the new edge in place of the base edge and, if this passes, then generating the cell projected from the base edge. If it fails, then the next vertex in the list is chosen for the new cell, and the whole process of testing is restarted. This helps to divide errors in cell size and skewness between two cells. This process can be seen in Figure 2.31 and Figure 2.32.



The angle a is too small so the original triangle is reduced in size to help the next cell in the tessellation

Figure 2.31 The testing procedure for new cells

These alterations provided 2D grids of high quality for all values of length ratio and variations of size along each edge.

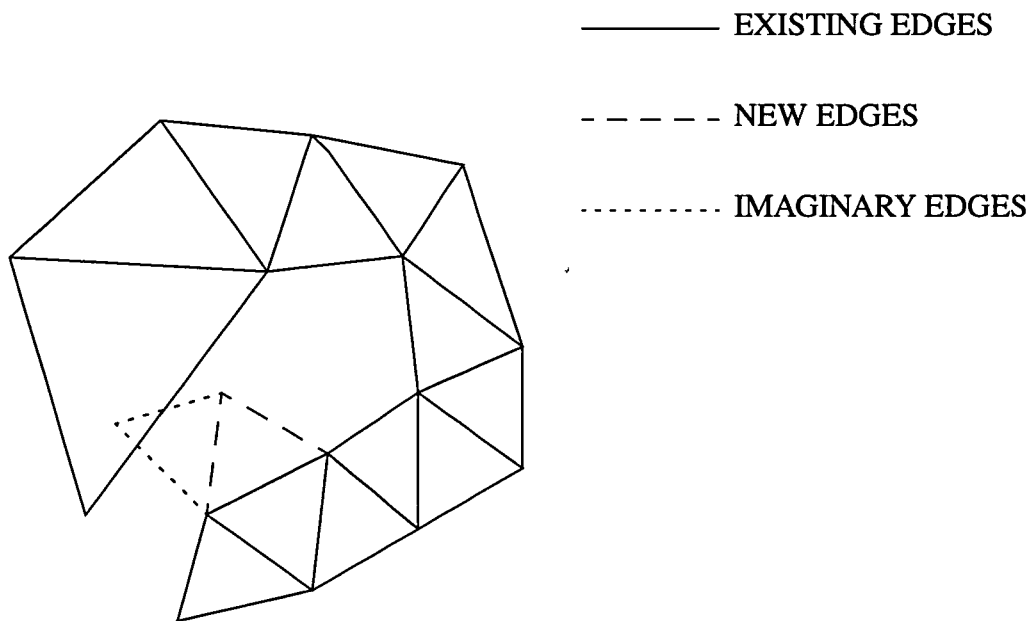


Figure 2.32 An example of how a new cell may be rejected from a grid due to the children cells it may produce.

For example, on a box of side 1.0 and meshed using an edge size of 0.1, the final tessellation is seen in Figure 2.33.

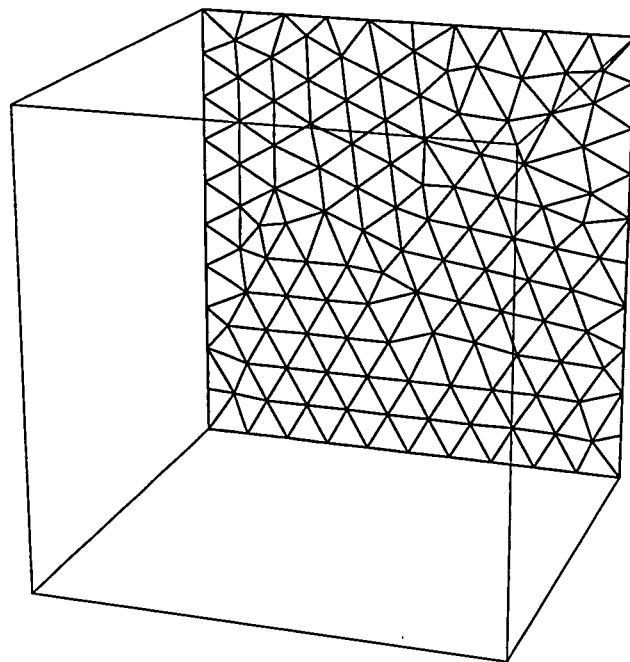


Figure 2.33 An example of a finished high quality surface mesh.

In addition, when edge spacings of differing sizes and/or faces of differing spacing parameters are used, the 2D triangulator has been proven to provide satisfactory grids (see Figure 2.34).

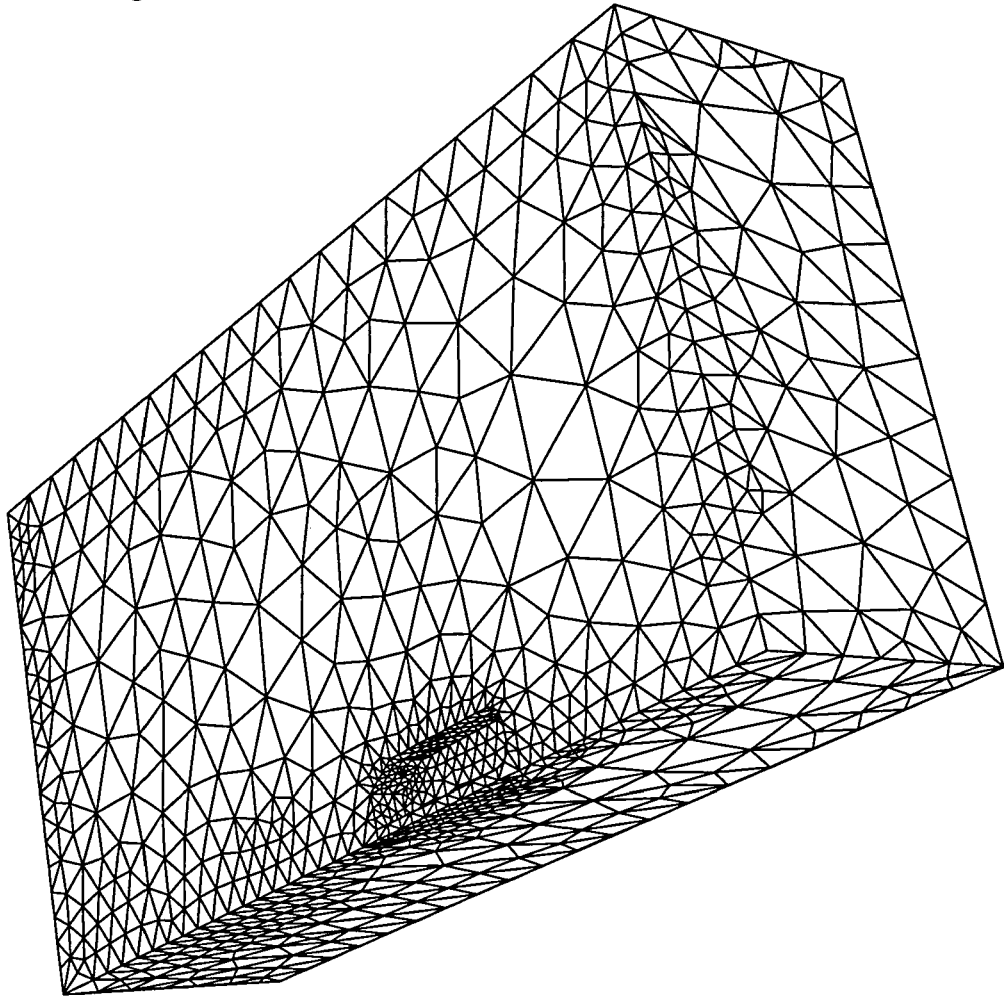


Figure 2.34 The unsmoothed surface grid on the Ahmed body showing the various edge/face size differences.

These grids are, however, as yet unsmoothed. This is to ensure that the grid on curved surfaces does not leave the geometry. Smoothing on surface grids will, without intelligent application, pull the nodes of the mesh away from the surface. To avoid this, the 2D grids can be smoothed in two ways, both of which use a Laplace method. The first of these is implemented in uv space after the grid is transformed from xyz space using a transformation function. This method prevents the grid from separating from the geometry, however, it does not necessarily provide well-smoothed elements in the xyz space. It can also be impossible to provide a transformation for complex surfaces. The second, more common

smoothing algorithm is performed in the xyz domain and should give well-smoothed elements but suffers from the grid departing from the geometry definition on curved regions (see Figure 2.35).

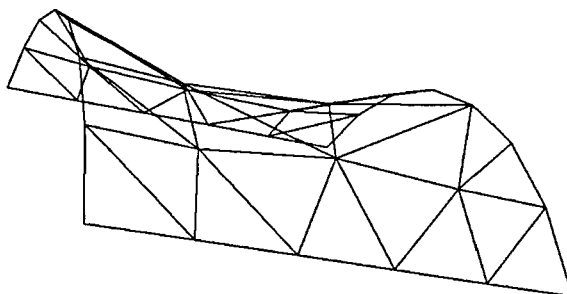


Figure 2.35 The grid on a cylindrical surface that has been smoothed resulting in separation from the geometry.

2.7. 3D Initial Results

3D grids generated using the original poor 2D surface grids as initial fronts, provided, at best very poor quality meshes and, usually failed. The grids produced were only possible with very large relaxations in the parameters and extensions of the search sphere (large values of $dstep$) around the best point. This resulted in large numbers of highly skewed and irregular elements with high variations in volume throughout the domain.

Using the improved 2D grids as boundaries for 3D tessellations resulted in more completed grids, however, the process could still not be regarded as totally robust. A set of tests (intersection, angle, etc.), similar to those used in the 2D case, were therefore required for the 3D process.

The first test requirement is a minimum distance between faces/points. This, although it may be small, is required to prevent the terminal case in three dimensions. This is the case where all the remaining faces cannot 'see' a vertex to tessellate to, because there are other faces in the way, and any new points would be too close. The simplest version of this scenario is seen in Figure 2.36, which shows a base face with three faces coming off it. The three new faces are each very close to an edge of another of the three faces, obscuring any existing or new vertices for the top point of a new tetrahedral.

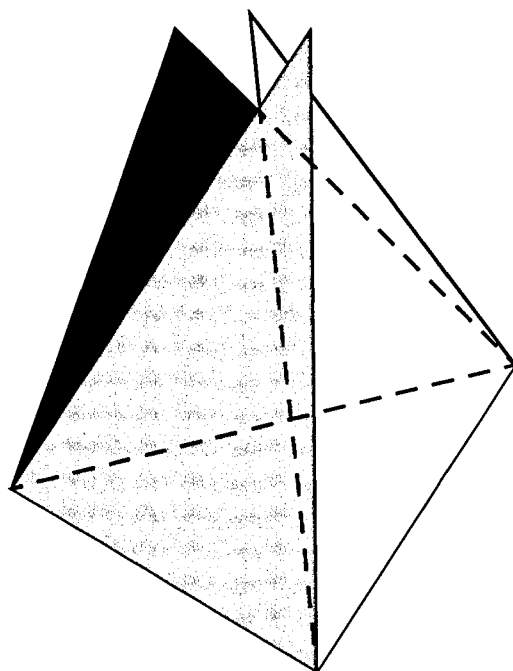


Figure 2.36 The problem of three faces that cannot see a point in front of themselves.

The second set of tests implemented were skewness and exterior angle tests between edges; these are exactly analogous to those in the 2D case. In addition, a test for angles between faces along any common edges was implemented. This is evaluated through a scalar product test on the two faces normals'. If these show that the angle between them is less than a preset figure, then the faces could either be overlapping or opposing (Figure 2.37). Furthermore, there is a combination of these two angle tests: a test of the angle between a face and an edge to ensure that one tetrahedral is not generated too close to another.

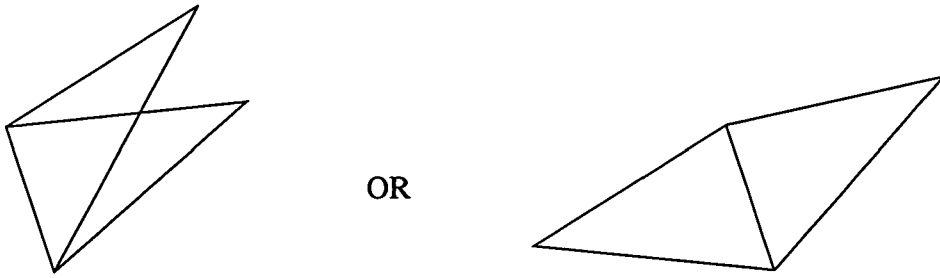


Figure 2.37 The possibility of an acute or an obtuse angle between faces producing the same scalar product.

A problem that is not easily detected is the possibility for a face to be completely inside a proposed tetrahedron as shown in Figure 2.38. This face, if generated, would cause the tessellation to fail, due to front faces folding back inside existing, already triangulated areas.

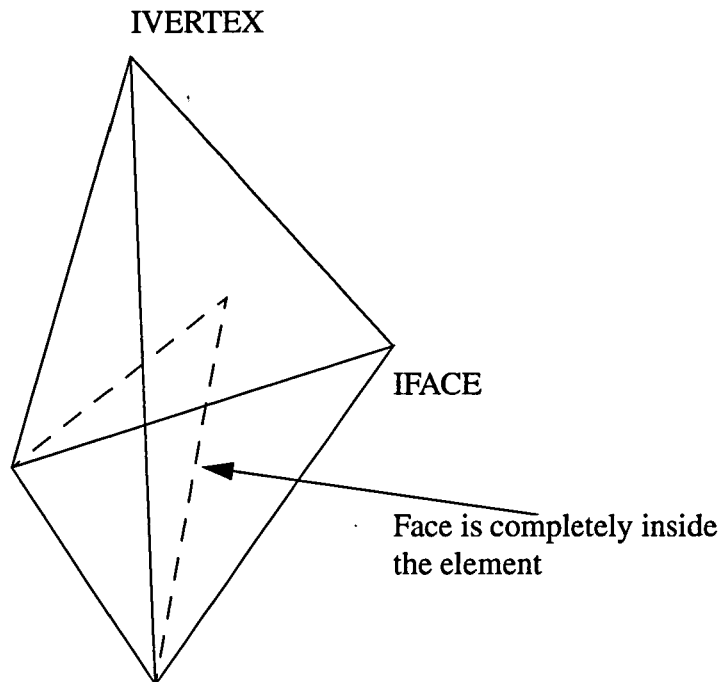


Figure 2.38 The case of a face being completely contained within an existing tetrahedron.

It is difficult to form (and therefore understand/repair) this type of problem, as all the faces must be fully connected. Even so, analysis using the following test shows it is possible. The test involves the comparison of the normals from both of the faces that share an edge with the normal of the face, that must also be in the

element. The distances along the normals should be less than the distance to the other face of the tetrahedral, if the case is to fail.

As in the 2D method, all faces that cannot be tessellated from are flagged, and when the front is empty, it is refilled with these faces. The parameters are then relaxed and the process restarted to try to fill in these holes.

This still leaves many failures of the kind illustrated in Figure 2.39, however. That is, three or more faces that combine to be part of a 'hole' and cannot see any points in front of themselves to tessellate to. As a solution to this problem the method described in the following section was proposed and implemented successfully.

2.8. Completion Step for the Advancing-Front Mesh Generator

As indicated earlier, the completion of both the 2D and 3D cases is often prevented by the incidence of faces that are too close to each other or of too great a difference in size. Whilst both can largely be prevented by careful selection of points for tessellation, the former can present a problem not before encountered in the literature: that of the inability of the individual faces in a tessellation to see a point in front of themselves, when there are three faces close to each other in a certain pattern.

There is of course a potential vertex at the end of the close face, however, if used, it would then create a cell that would intersect with the third triangle in the failed case (see Figure 2.39).

An alternative strategy to solve this problem is to use a new vertex somewhere in the centre of the collection of faces. This would succeed if all three faces could see this vertex, unfortunately no such vertex exists. Any other vertex would only serve to further worsen the case, by creating a new face that is even closer to the others.

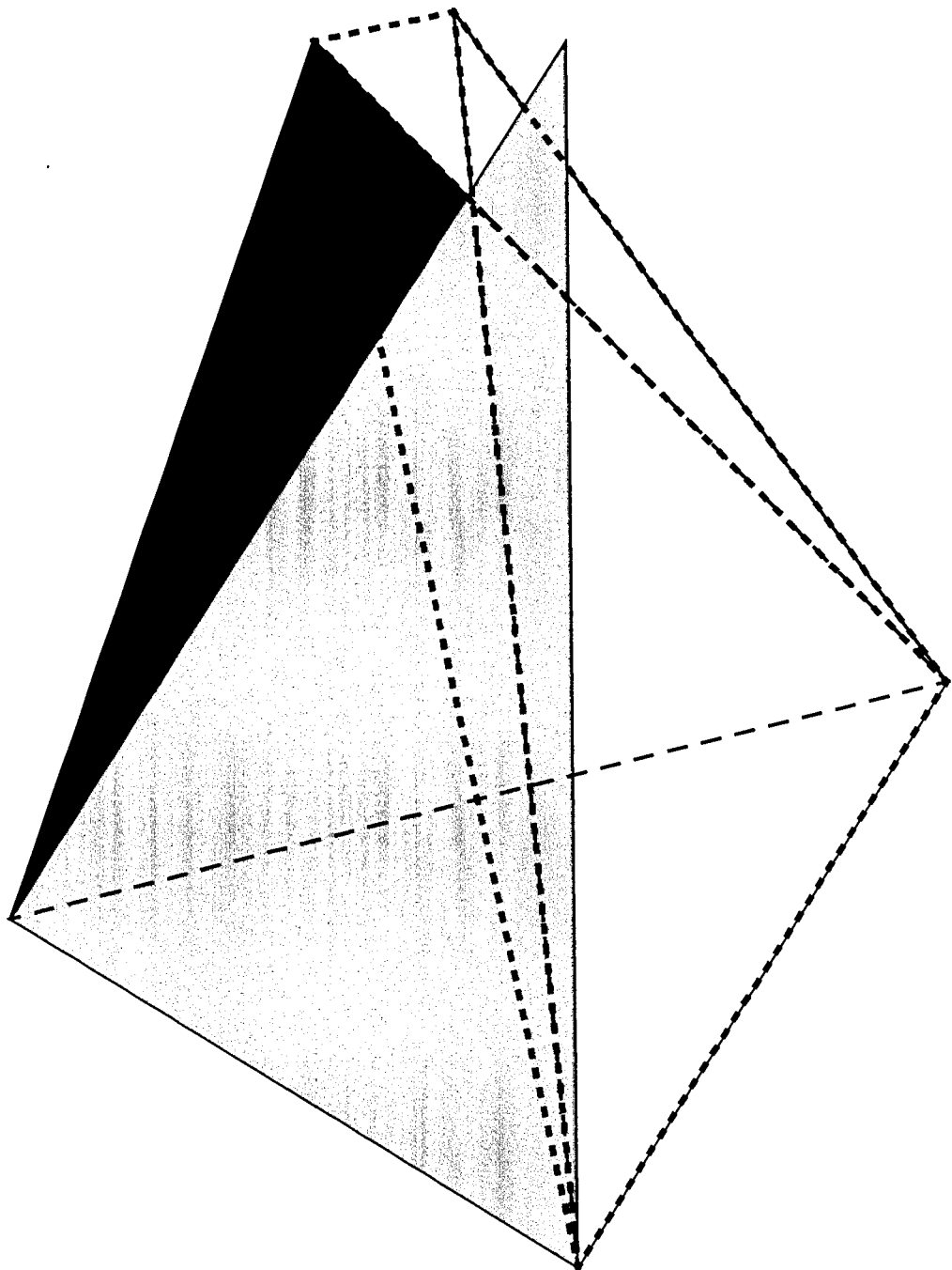


Figure 2.39 The proposed new element, note how it must intersect one of the other triangles.

The above case with only three faces (that could be turned into a proper 'hole' by the addition of three more outer faces, creating a total of seven faces) is the simplest example of this problem. There are any number of similar cases involving more faces. however, all face the same problem.

The solution developed involves the deletion of elements, faces and vertices that have already been tessellated from around the 'hole', until a convex hull is achieved. Having achieved this, the new 'hole' is filled with elements that consist of the outer faces of the hull and the vertex created at the geometric centre of the hull. A more elegant method, here, would be to re-tessellate the hull using the Advancing-Front method. However, for simplicity, it was decided to see whether the initial tests revealed elements that were too large or skew, in which case the method would be altered.

The procedure, therefore, (figures in 2D for simplicity), with this method in place for the generation of a grid on any pre-defined surface tessellation, is as follows:

1. Initiate the Advancing-Front grid generator with the parameters for grid quality set at a high level. For example: interior angles must be greater than 30° ; volumes of tetrahedra must be greater than a preset minimum; the range used to search for tessellation points in the algorithm is limited to the length scale of the background grid at that point.
2. This will leave a number of faces that are too close to other faces, or would form badly skewed or small tetrahedra. These will be locally connected. The parameters are relaxed (minimum angles are reduced, ranges are increased, etc.) and the Advancing-Front grid generator restarted on these faces.
3. The resulting set of faces will, again, be locally connected, however, the remaining clusters of faces will be even closer to each other. The next step is to try to connect up any pairs of faces that share an edge.
4. The remaining faces at this stage will all be of the degenerate case outlined above, that is, none of the faces can 'see' each other and the points that the Advancing-Front grid generator would like to put in are only visible to one of the faces in the cluster and, therefore, only serve to compound the 'closeness' problem.

The solution, as mentioned above, is to turn the non-convex hulls into convex hulls by deletion of faces and the elements that created them:

- a) Find the geometric centre point of all of the faces in the cluster formed by all of the locally connected faces. There may be more than one cluster, in which case, this method should be re-used for each cluster.
- b) Test all of the faces in the cluster with this point, to see if a positive volume is formed. If the volume is negative, then the face and the element that made it must be deleted. If all the volumes formed are positive, go to step (e) (Figure 2.40).
- c) If this element formed any of the other faces in the cluster, they must also be removed. Any not already in the cluster must be added to it.
- d) The resulting new cluster of faces is then passed back to the top of this algorithm, that is, return to point (a).
- e) The cluster is now a convex hull, and the tessellation is completed by tessellating

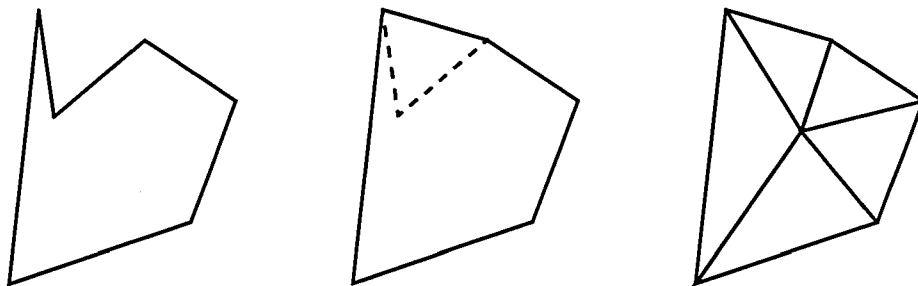


Figure 2.40 The deletion of a 'bad' element from the 'hole', and the subsequent re-triangulation.

all of the faces with the centre point of the convex hull.

- f) Move on to the next cluster of faces.

Care must be taken where two or more clusters coincide: a special routine must be added to remove the 'walls' between two clusters and turn them into one.

The resulting tessellation may contain vertices with very high degrees (number of edges coming off it), however, these will be reduced by the smoothing and swapping algorithms outlined later. If this is not the case, then the final step of tessellating the convex hulls to the centre point could be replaced with something more complicated, for example a restart of the Advancing-Front grid generator.

With this treatment the grid generator would now fully mesh any domain yet tested. An example is a cube of side length 1.0; the resultant surface tessellation is seen in Figure 2.41. The grid is reasonably regular but as Figure 2.42 illustrates, it will benefit from swapping and smoothing. The graphs show the number of cells versus a grid quality parameter, e.g. interior angle, volume or vertex degree. The figures demonstrate a substantial deviation from the normal distribution, in particular the tails are too long. The later application of face swapping and smoothing should improve these figures. It was, therefore, decided not to proceed further with the re-implementation of the Advancing Front grid generator to the convex hulls, as the quality of the method outlined above was satisfactory.

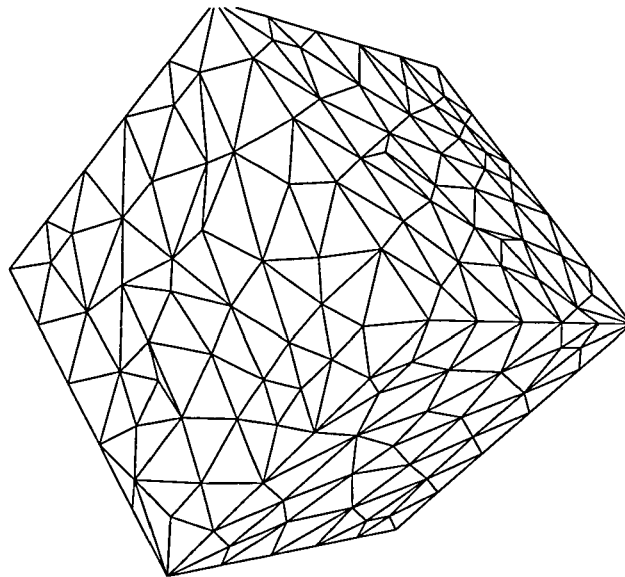


Figure 2.41 The initial grid (only the surface shown for clarity), unsmoothed and not utilising edge swapping

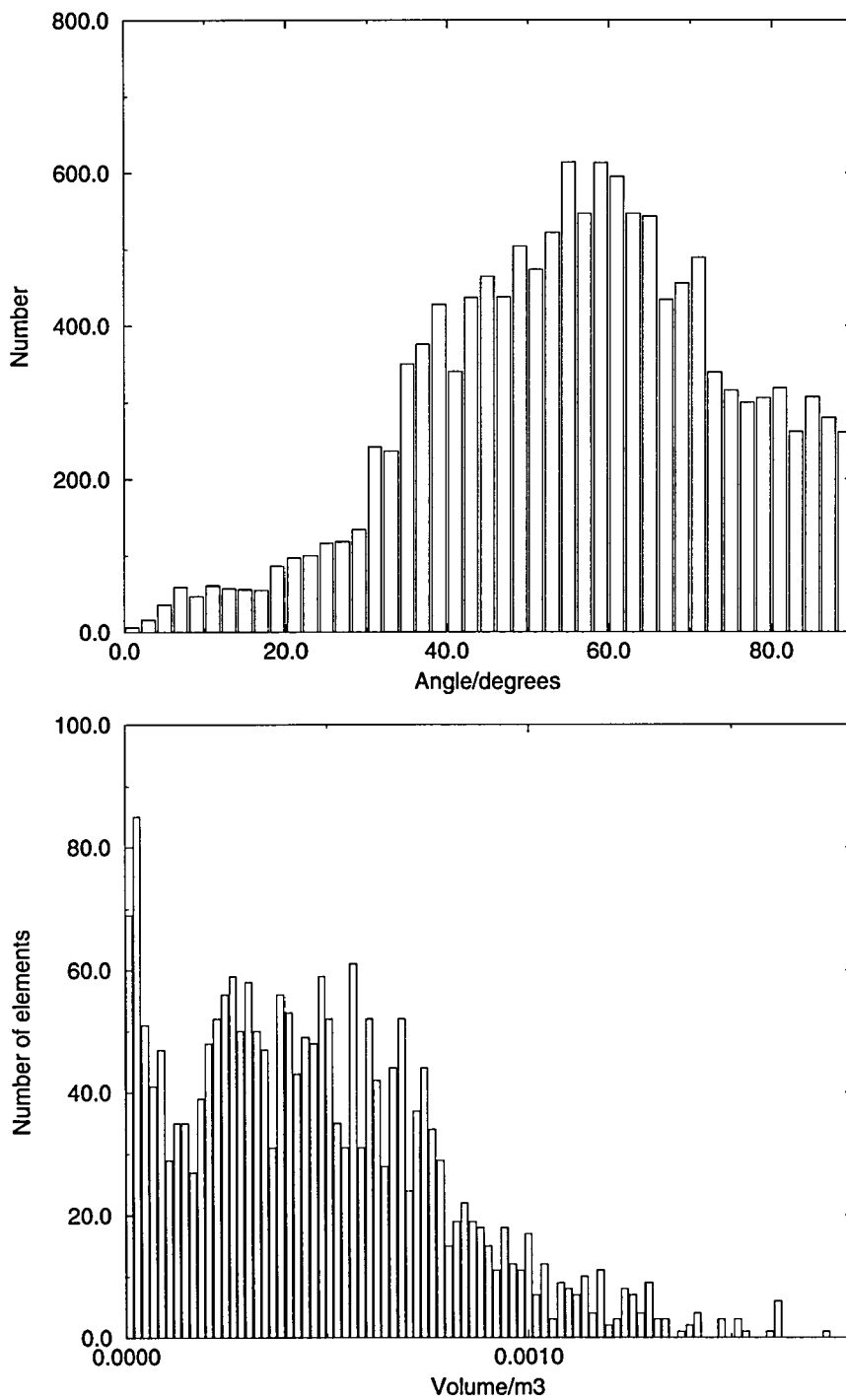


Figure 2.42 The distribution of internal face angles and volumes of tetrahedra for the above tessellation.

2.9. Smoothing

Grid quality is of paramount importance to the accuracy of any CFD calculation. The skewness of a cell is one measure of quality, as is the change in volume between cells. High skewness and large changes of cell volume will result in lower accuracy of the CFD solution. As illustrated in Figure 2.42, both of these are subject to considerable variation across the test cases domain. Another measure of grid quality is the vertex degree of the nodes within it. The high vertex degrees of the test case seen in Figure 2.43 are not, themselves, a problem. However, a vertex

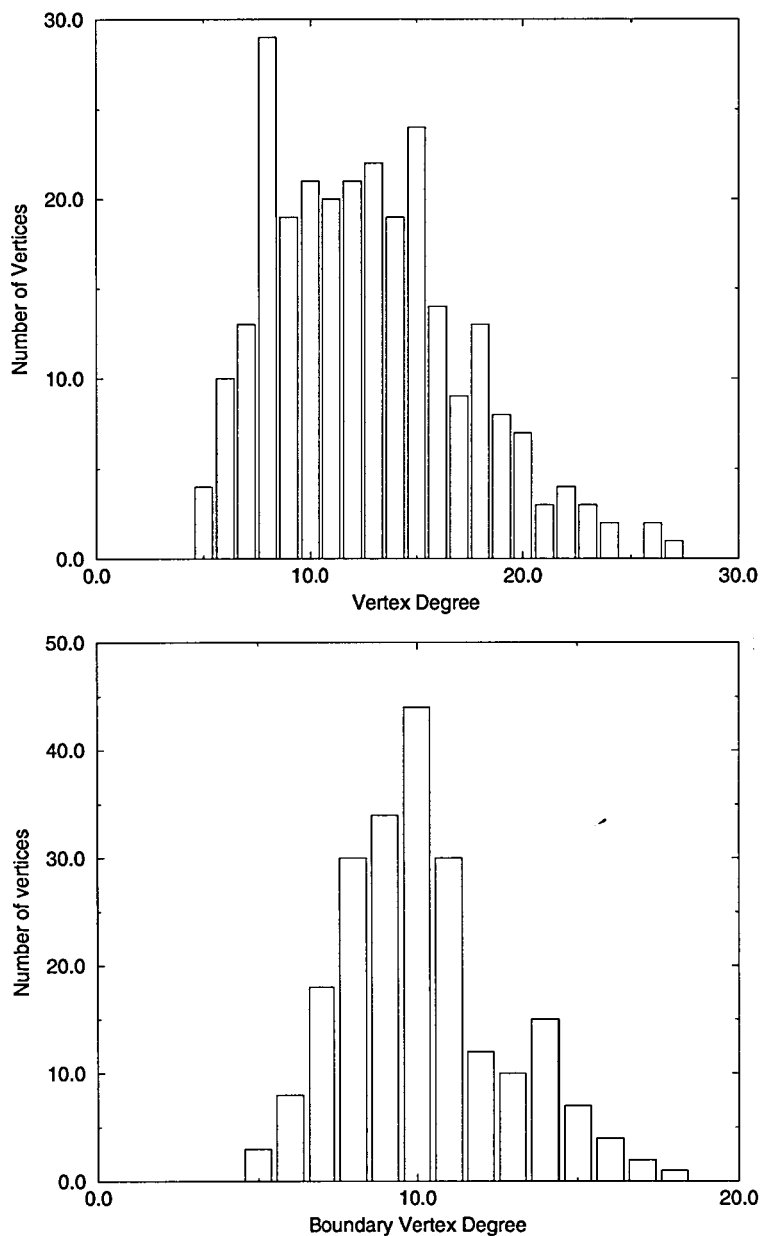


Figure 2.43 The degrees of the internal vertices (top) and the boundary vertices (bottom).

with a very high degree will give all of the elements connected to that vertex a very small interior angle, thereby, increasing the skewness.

To ensure high accuracy from the CFD solution, the skewness and rate of volume change must be minimised by the grid generation process, before the grid is submitted to the CFD solver. This minimisation is achieved via a combination of smoothing the nodes and swapping the faces and edges. This section describes the smoothing algorithm used. Section 2.10 focuses on the swapping procedure implemented for the code developed for this work.

The initial method used is a Laplacian smoother, where each vertex (i) is smoothed via the equation below:

$$\tilde{x}_i = \frac{\sum_{j \in k(i)} \alpha_j x_j}{\sum \alpha_j}$$

Where:

x_j = position of vertex j

\tilde{x}_i = new position of vertex i

α_j = optional weighting factor for each surrounding vertex

The vertices, j, are defined as all the vertices connected to vertex i by one edge

In 2D the results of using this gave good grid skewness levels, as can be seen when comparing the unsmoothed surface grid (Figure 2.41) with the smoothed surface grid (Figure 2.44). There is a regular distribution of points over the surfaces.

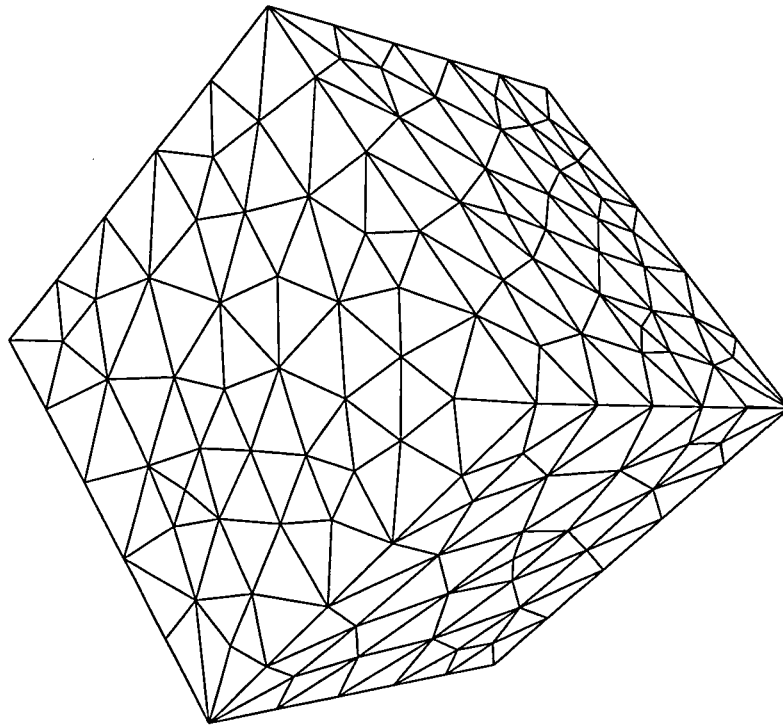


Figure 2.44 *The smoothed surface grid.*

In 3D, though, the method was less robust. The reason, however, is difficult to visualise in 3D. The analogue of the problem in 2D is seen in the convex hull problem shown in Figure 2.45.

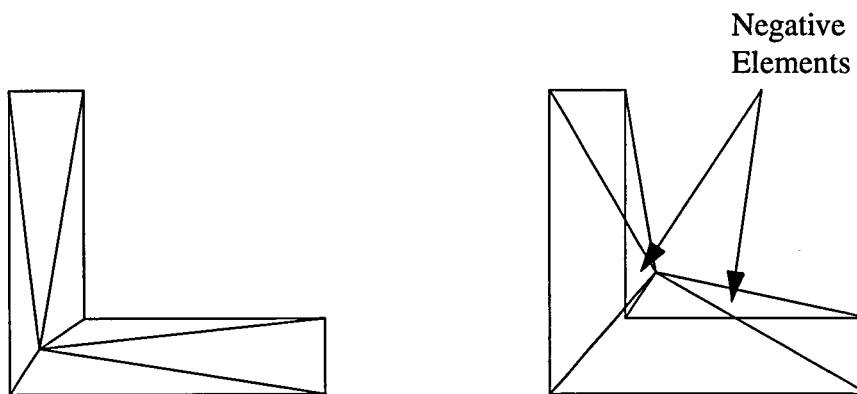


Figure 2.45 *The problem with Laplacian smoothing (The unsmoothed case is on the left).*

The vertex is being pushed outside of the volume that is being used to smooth it ('element reversal'). Incidentally, the algorithm used in 2D precludes this scenario, due to the order in which the vertices are smoothed and a relaxation in the process. In 3D, however, it is quite common due to the frequent occurrence of non-convex

hulls. There are two solutions to this problem. The first is to change the method of smoothing to a more intelligent one which prevents the occurrence of this situation. Several were considered including a variation on the above which pushes points away from it as well as attracts them and also a version which constrains the travel of any one point on each sweep [15]. These methods were rejected due to their inherent complexity. The second method is to remove the volumes seen in the above figure, which allow this kind of 'element reversal'. This can, as will be seen, be done using face and edge swapping. Unfortunately, this is not robust and does not guarantee the removal of all non-convex hulls.

The solution adopted was, therefore, a combination of face and edge swapping and Laplacian smoothing where the smoothing was altered to prevent the creation of negative volumes. By combining the two in this manner, an effective, robust solution was obtained. The modification to the smoothing may be considered simplistic, however, it provides the necessary improvement in grid quality without compromising the robustness of the grid generator.

2.10. Edge and Face Swapping

In 2D, edge and face swapping is used, here, to equalise the value of the vertex degree throughout the mesh. In addition, it helps to remove highly skewed elements from within the mesh. In 2D, the procedure identifies a vertex with too high a value of vertex degree and finds the two triangles connected to this vertex that share an edge and have the combined smallest interior angle at the vertex as shown (Figure 2.46).

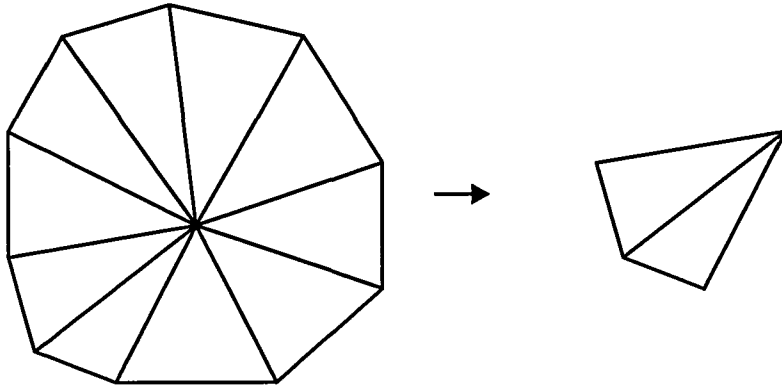


Figure 2.46 The two neighbouring faces with the worst skewness from a node with a high vertex degree.

The edge that is shared is then removed, and a new edge placed between the two vertices connected to the original vertex by one edge (Figure 2.47. Note: this is only done if the new edge crosses the old edge otherwise the resulting faces would overlap other faces). This lowers the vertex degree and after smoothing has been applied will help to equalise the internal angles throughout the mesh.

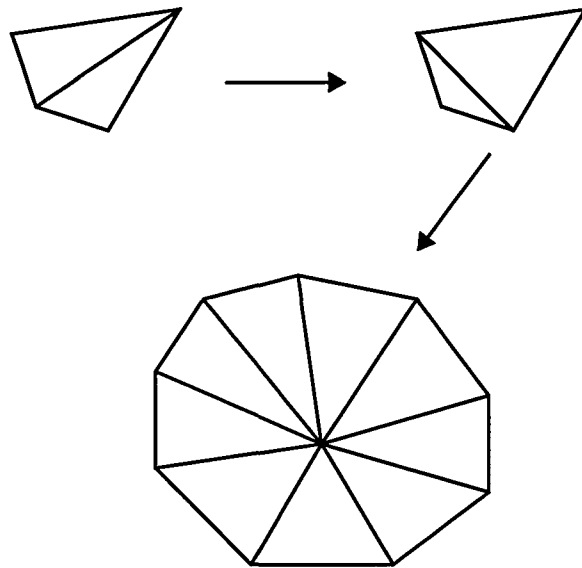


Figure 2.47 Edge swapping between two faces.

The problem with this method, as it stands, is that the decrease in degree of the above vertex has, in turn, increased the degree of two other vertices, which may now be over the threshold for edge swapping. If one of the edges is then swapped, we return to the original configuration and the process is repeated in a kind of eternal loop. To avoid this, a better method of deciding whether or not to swap an

edge could have been implemented following the work of Richter [73]. The method consists of carefully weighting the nodes during the smoothing and swapping operation, thus, giving an extra bias to one of the face pair configurations above. This was not completed in the work, as it was felt unnecessary; the loop cases outlined above were not encountered.

In 3D there are several types of face swapping:

1. Two tetrahedra sharing two faces go to three tetrahedra sharing three faces, (Figure 2.48).

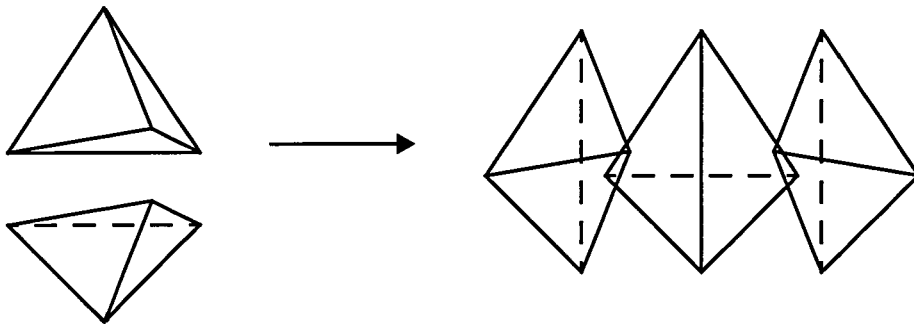


Figure 2.48 Two cell to three cell face swapping

2. Three tetrahedra sharing three faces go to two tetrahedra sharing two faces. This is the reverse of the first method (Figure 2.49).

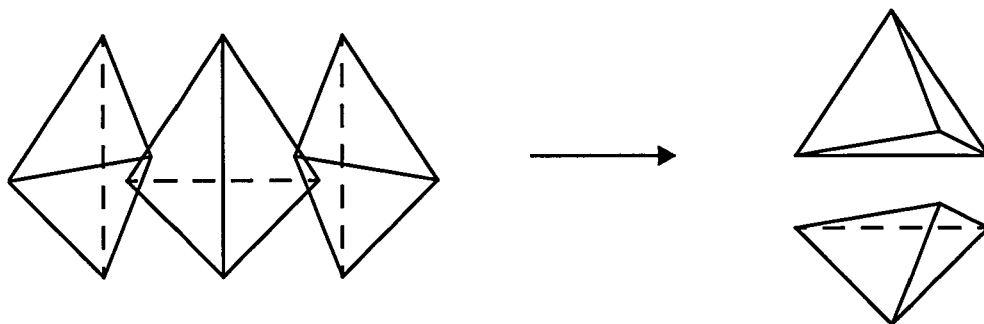


Figure 2.49 Three cell to two cell face swapping

3. Four tetrahedra sharing four faces go to four tetrahedra sharing four faces. This is the 3D analogue of the edge swapping, and can also be used on the boundary where two elements share a face. This type of boundary face swapping is, however, not implemented as it is adequately covered by edge swapping in 2D

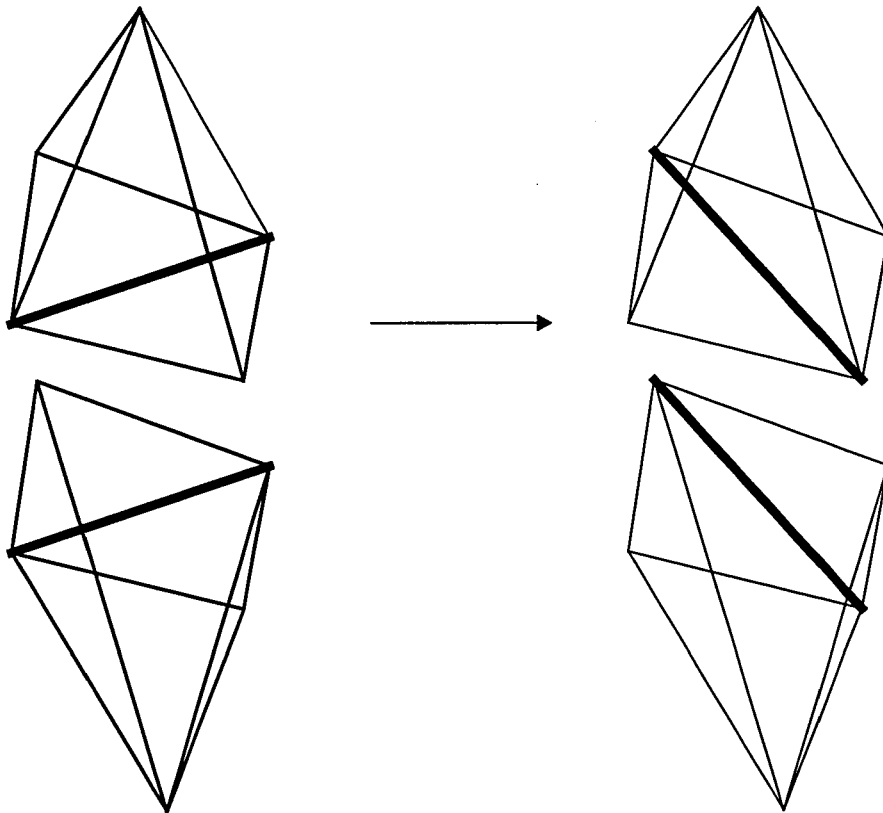


Figure 2.50 The four cell to four cell face swapping. If on the boundary it is analogous to 2D edge swapping.

The first of these cases, is the first in a series of tessellations where there are a number of cells surrounding one edge. The boundary faces for this collection of cells forms a hull of points, which can be filled with a different set of tetrahedra to the original 'faces round an edge' tessellation. The first case is where three elements can be replaced by two. It should be noted that, the 'new' face in this swap is at right angles to the faces that were removed. This pattern will be repeated for every case, the new faces will be at right angles to the replaced faces.

The three elements to two is the first of this class of swaps. The four elements to four elements (also documented above) is the second. The next case is five elements to six as shown in Figure 2.51 below.

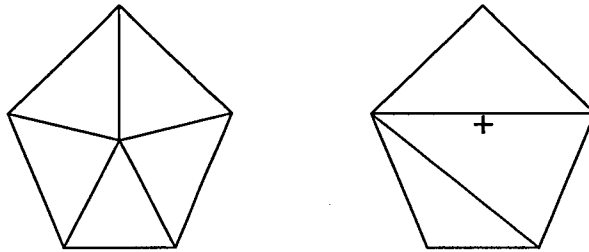


Figure 2.51 The replacement of five cells (left) with six by face swapping. The view here is looking along the common edge of the five cell case.

To understand the above, imagine looking at the five tetrahedra that share the edge from along the shared edge. The view seen is the one on the left. The new tessellation is viewed from the same perspective. The six new tetrahedra are formed by taking the three centre triangles and joining them to the other two vertices denoted by the point '+' on the diagram. These two points were the ends of the now deleted common edge. This is done for both sides of the tessellation, resulting in the six tetrahedra. This process can be reversed, however, the tests to establish that this can be done are very complex and, as such, were not implemented here. It was felt that the various swappings described above would be sufficient to improve the mesh over the original without this "reversed" scenario and this turned out to be the case.

The same process can be used for six to seven elements and so on. The last case considered here, though, is the seven to eight elements. This is because the number of occurrences of seven or more elements around one edge is small and, also, they tend to be removed by the other swapping and smoothing that takes place. These cases all share the same basic method with that of the 2D edge swapping.

The criteria of whether to swap the faces in 3D are based on elements' properties rather than those of the vertices. So, unlike the 2D case where the flip flopping case was found, the 3D set-up will suffer no such problems. The faces will either be swapped or not.

The criteria used are the same as suggested in a paper by Freitag et.al. [15]. The Delaunay-ness tests whether the circumsphere of any of the tetrahedra used in any of the above face swaps (i.e. 2, 3, 4, 5, 6 or 7) contains any of the other points used in the swapping. If none of the points lie inside any of the tetrahedra, then the tessellation is locally Delaunay and should be used. Should this test, compared with the result of the original element configuration, prove inconclusive (that is, both tessellations are Delaunay or both are not Delaunay), then a second test is used. This is to find the maximum and minimum dihedral angles of any of the tetrahedra used in the proposed and original cases. If the proposed formation is an improvement on the original, that is, the largest minimum angle seen is larger or the smallest maximum angle is greater, then it is used, otherwise the elements are left as they are.

2.11. Conclusions

It was possible to code the Advancing-Front grid generator in both 2D and 3D. The grids produced are of a reasonable skewness quality (before grid optimisation techniques are applied). The Advancing-Front grid generator was, however, found to be not as simple as other authors suggest. Neither 2D or 3D methods produced grids using the algorithm as described in the literature, without a considerable number of extra steps.

The 2D grid generator required several careful restrictions to the faces allowed to be generated. With these in place, the grid generator was a robust tool for producing 3D surface grids. The 3D grid generator suffered from more serious problems, which result in a degenerate front being formed that must be removed before the grid can be completed. These degenerate cases arise from the naturally heuristic nature of the Advancing-Front: it has no prior knowledge of what is in front of it. These degenerate cases were dealt with via the removal of sufficient cells to produce a convex hull which was subsequently re-tessellated. In addition to

this final step, several extra restrictions on cell generation were implemented which were similar in nature to those of the 2D method.

The quality of the grids was improved by use of edge swapping in 2D, and face swapping in 3D, coupled to an intelligent Laplacian smoother that would not produce negative elements.

Using this grid generator, the grids used in the following chapter were generated and evaluated. The formulation of an unstructured tetrahedral grid generator, developed with the express aim of evaluating better and more efficient grid strategies for analysing the flow over the Ahmed body, was an important part of this study. This chapter has highlighted the many and varied different approaches to unstructured tetrahedral mesh generation. The developed method will undoubtedly have an effect on the solution obtained using CFD. The purpose of the next chapter is to analyse these effects.

3 Initial Calculations Using Unstructured Grids

3.1 Introduction

Following the development of the unstructured grid generation algorithm described in Chapter Two a validation exercise was first performed. This involved running a series of calculations with grids generated from the Advancing-Front grid generator and, then, comparing them to the results of the calculations using grids from a commercial unstructured grid generation package. These calculations are an essential part of validating the tetrahedral grid generator proposed here for use on more complex bodies, such as the Ahmed body.

The commercial package used was the *FLUENT* [13] suite of programs. It consists of a preprocessor (*GEOMESH*), a volume grid generator (*TGRID version 3*) and a solver/postprocessor (*UNS version 5*). A brief description of the preprocessor and volume grid generator is included later in this chapter.

The two initial problems used to compare the two grid generators were selected from accepted and well-documented test cases. The first of these is the laminar lid-driven cavity [19] in which a simple cube has the uppermost side (lid) defined as a velocity boundary condition. The velocity is parallel to this surface and hence the flow within the box will be of a rotational nature. No quantitative data will be presented or compared for this case, it is included solely to evaluate qualitatively the quality of the grid. The second example is the laminar backward facing step [13,40] in which a flow in a duct is expanded on one side. The flow then re-attaches at a known (from experiments) distance from this step. The performance of the CFD prediction can be assessed by how accurately it predicts this reattachment point. Qualitative and quantitative data will both be included for this case.

Following this validation of the two unstructured grid generators for simple geometries they must be demonstrated as suitable on an automotive test case. The test cases discussed above, whilst commonplace, bear little or no relationship to the complex flow structures seen over the Ahmed body.

The Advancing-Front grid generator and the commercial Delaunay method will be used to generate a fully tetrahedral mesh between the Ahmed body and a rectangular outer domain. Only half of the flow over the body will be meshed and solved as the problem will be assumed to be symmetrical. The same surface grid will be used for both the meshes. In this case, the boundary grid will be generated using a Delaunay method in two dimensions. The two grids will be examined and a comparison of the solutions for the two grids made.

3.2 Description of Commercial Grid Generation Package

As with any CFD process the *FLUENT* package used here consists of a preprocessor to set up the grid and boundary/initial conditions, a solver and a post processor to interrogate the solution [13].

The preprocessor consists of two parts. The first is a basic CAD package, primarily intended to check the imported CAD from other packages. It does, however, provide some useful tools for the addition of extra geometry that may be necessary.

The second part of the preprocessor is a tool for “pasting” surface grid patches onto existing geometry. This allows the CFD engineer more control over the surface mesh than if every CAD surface had to be meshed separately. This part of the preprocessor also contains the algorithms for the surface mesh generation (Delaunay) and for the projection of the surface grid to the geometry.

Having obtained a surface mesh, a volume grid generator is used to form the internal grid using a Bowyer-Watson Delaunay type mesh generator as described in the

previous chapter. The surface mesh is used as the boundary grid, with which the tessellation must conform. The resulting volume mesh will, as discussed in Chapter Two, contain less elements than Advancing-Front grids for the same geometry. This results in less control over the spacing of the nodes of the volume mesh, therefore requiring localised refinement for improvement.

3.3 Lid driven cavity

An example of a surface grid from the FLUENT package can be seen in Figure 3.1. (examples of the Advancing-Front method for a cube have already been shown in the previous chapter). It depicts the fine surface grid for the lid driven cavity test case [13]. An example of the distribution of the cell skewness for the volume meshes generated by Delaunay and Advancing-Front methods can be seen in Figure 3.2. The face skewness is shown in Figure 3.3. Throughout these comparisons, the results from the Advancing-Front method are the left hand or top figure and the Delaunay the right or bottom. These two sets of graphs are the best measure of mesh quality. As indicated previously, the higher the level of cell skewness, the less accurate will be the solution. The face skewness helps understand the nature of the cell skewness. The face and cell skewness is measured in this work as:

$$\max \left[\frac{\theta_{\max} - \theta_e}{180 - \theta_e}, \frac{\theta_e - \theta_{\min}}{\theta_e} \right]$$

where:

θ_e = angle for an equiangular face or cell (i.e. 60° for a triangle)

θ_{\min} = smallest angle in the face or cell

θ_{\max} = largest angle in the face or cell

High face and cell skewness levels indicate that some of the cells will have to be long and thin, whereas low face skewness with high cell skewness indicates sliver or "flat" cells. All unstructured grids will have a mix of these. The aim should be for any grid

to contain a minimum of highly skewed faces and cells. Figure 3.2 and Figure 3.3 demonstrate that whilst the face qualities of the two grids are similar, the levels of cell skewness show a significant improvement in the Delaunay mesh.

Most of this improvement can be attributed to the Delaunay method's structure, whereby cells are added to regions that contain highly skewed cells. The Advancing-Front scheme is entirely heuristic, adding cells according to a preset field function until the domain is filled. The advantage of the latter scheme is that its adherence to cells of a certain size within the domain will improve the accuracy of the solution. This is demonstrated in Figure 3.4 and Table 3.1. The number of cells in the Advancing-Front mesh is higher than the Delaunay mesh. However, Figure 3.4 reveals the Advancing-Front mesh to have more cells with smaller volume compared to the Delaunay mesh that has more cells with larger volumes.

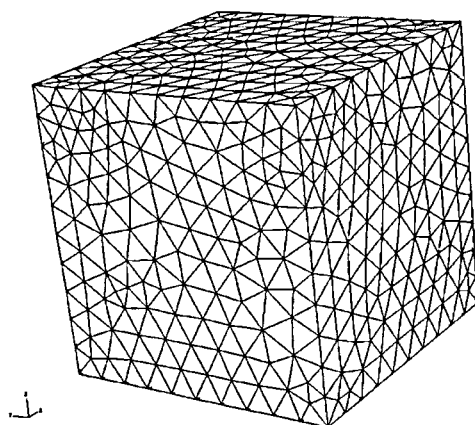


Figure 3.1 The fine boundary grid for the lid driven cavity (FLUENT package).

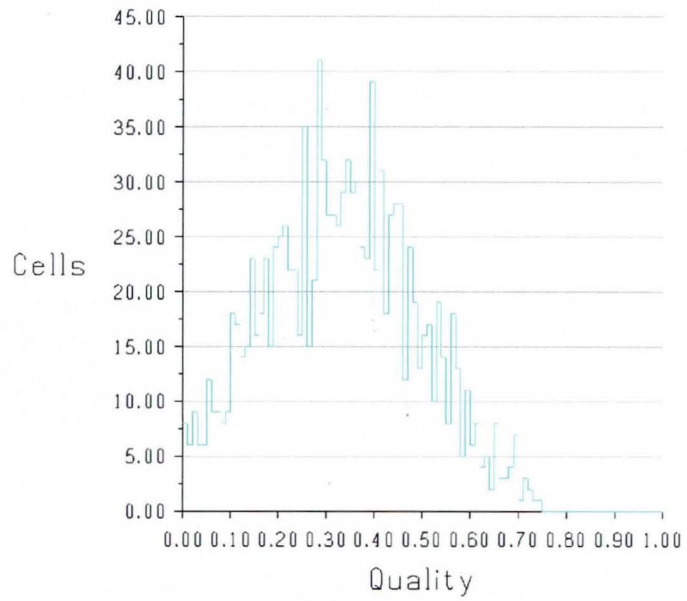
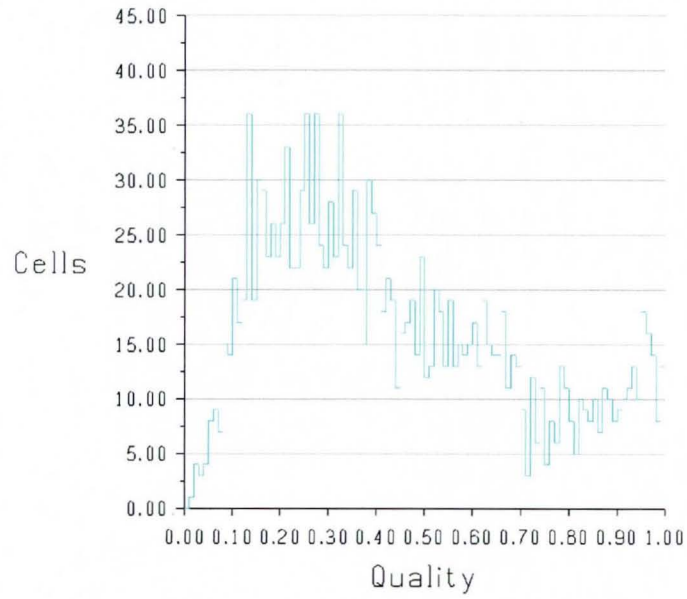


Figure 3.2 The cell skewness for the two coarse volume grids of the lid driven cavity. Advancing-Front on the top and commercial Delaunay method on the bottom.

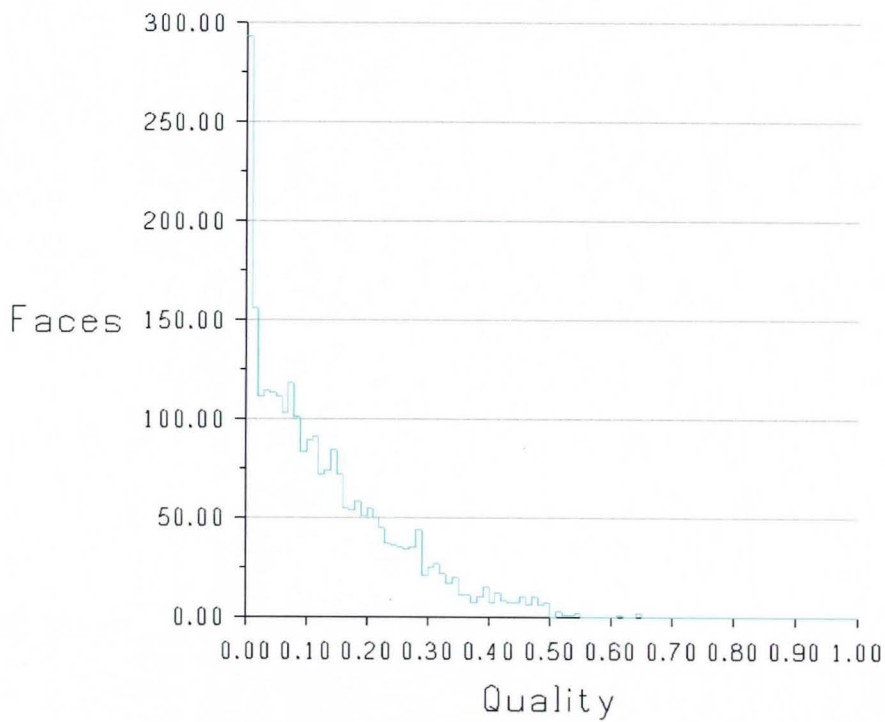
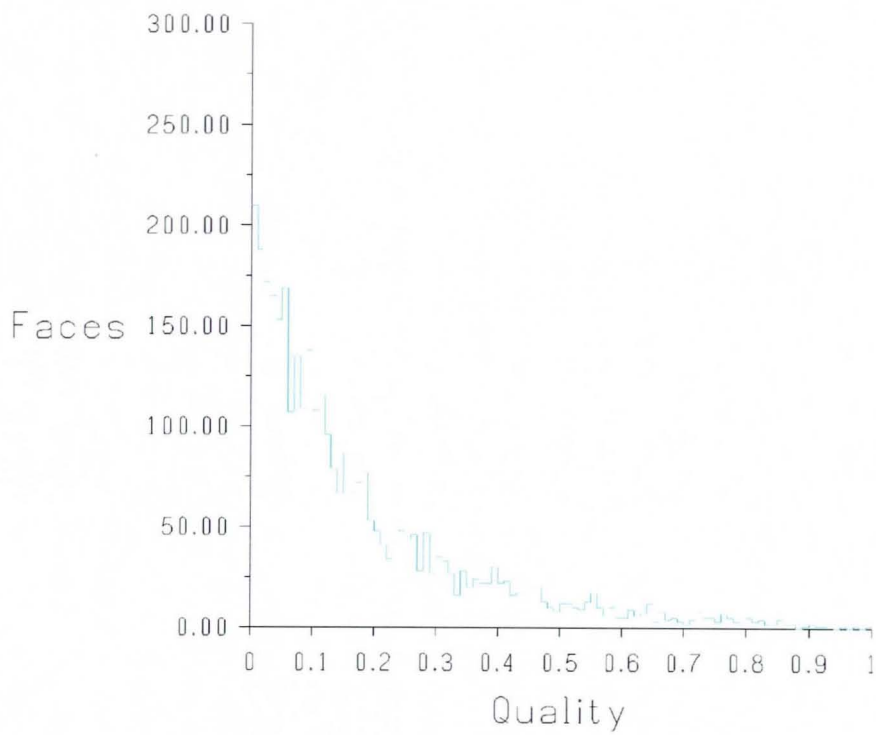


Figure 3.3 The face skewness for the two coarse volume grids of the lid driven cavity. Advancing-Front on the top and commercial Delaunay method on the bottom.

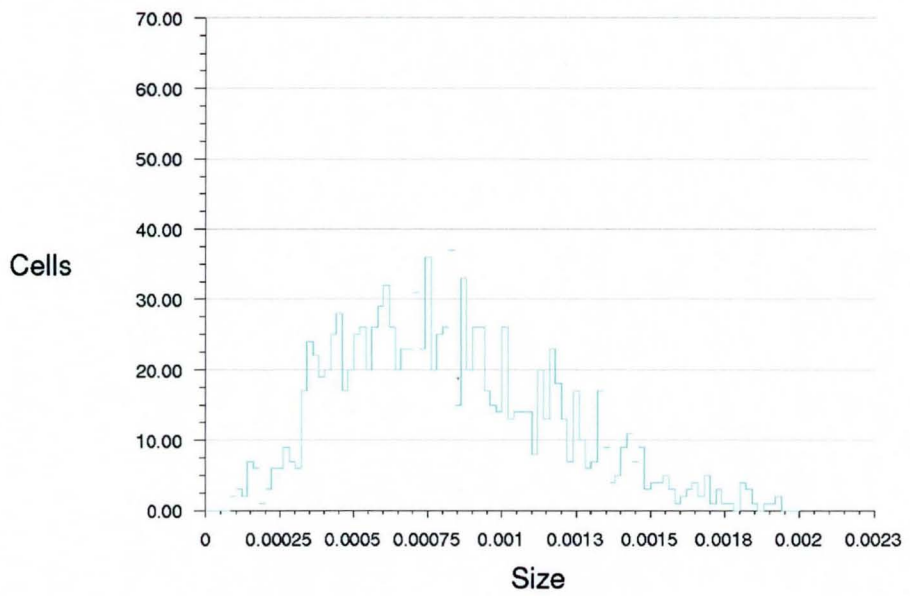
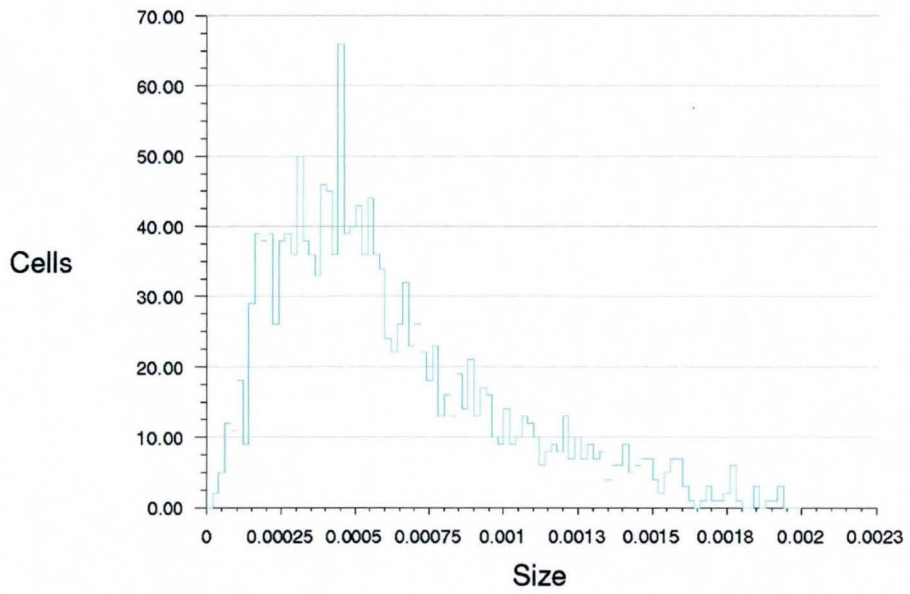


Figure 3.4 Distribution of cell volumes for the two grids. On the top, Advancing-Front and on the bottom, Delaunay.

The comparison of the grid sizes in number of nodes, faces and cells is seen in Table 3.1.

Grid type	Coarse Advancing-Front	Coarse Delaunay
Cells	1611	1217
Faces	3438	2650
Nodes	419	326

Table 3.1 The comparison of grid sizes from Advancing-Front and Delaunay methods.

In order to further compare the grid qualities, a slice through the centre plane of the domain (parallel to the symmetry planes and perpendicular to the inlet) was taken. The contours of cell volume and the mesh slice on this plane are illustrated in Figure 3.5. It is evident that at these coarse grid levels, the grid spacing is random with no pattern to the growth rate of cell volumes through the domain. However, as predicted, the cells in the centre of the Delaunay grid are larger than those on the boundary, whereas the Advancing-Front grid demonstrates similar grid spacing throughout.

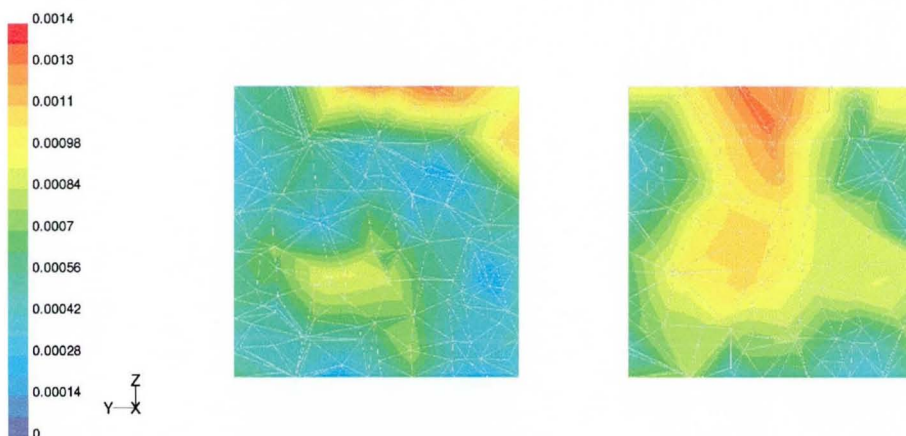


Figure 3.5 The 2D mesh slice on the centre plane through the domain, overlaid on the contours of cell volume on the centre plane of the lid driven cavity.

The next stage in the validation process is to use the above examples as the mesh for a CFD solution. The geometry of the cube above lends itself to the problem of a lid driven cavity flow. The boundary conditions for this type of flow are specified as follows and are illustrated in Figure 3.6. The top face is specified as a velocity condition parallel to that wall; the front and back as symmetry conditions and the remainder as walls. The resulting internal flow will be a re-circulation. As stated in the introduction to this chapter, no qualitative data will be presented for this test case.

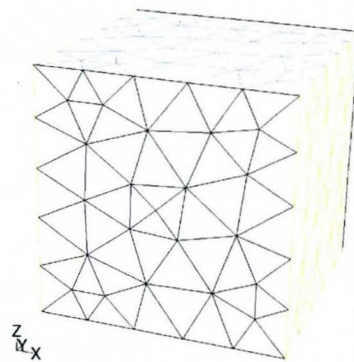


Figure 3.6 The boundary conditions for the lid driven cavity test case

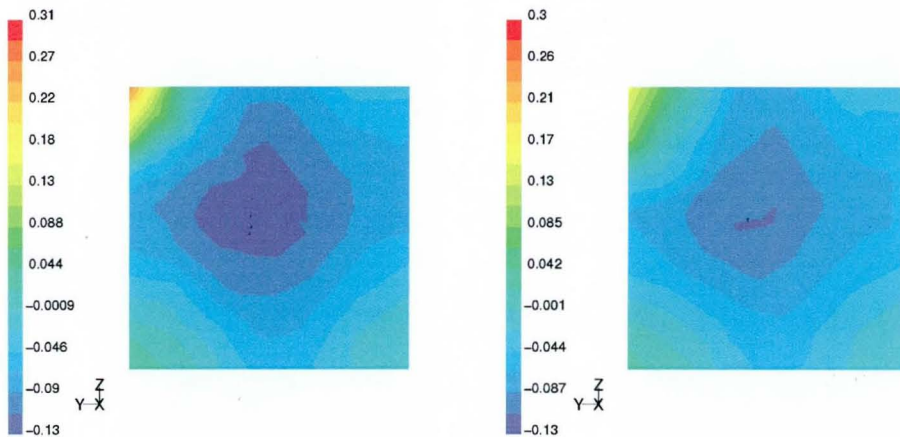


Figure 3.7 Contours of static pressure on the centre plane; Advancing-Front on the left and Delaunay on the right.

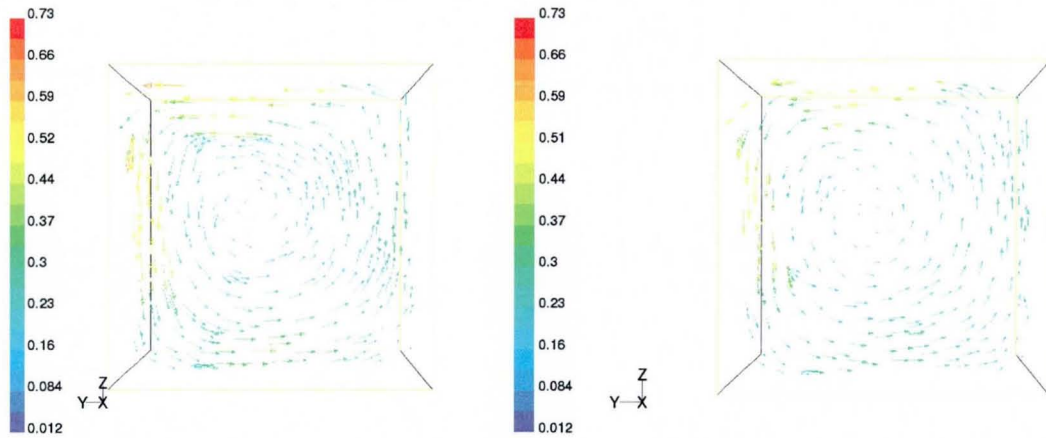


Figure 3.8 Velocity vectors coloured by velocity magnitude on the centre plane; Advancing-Front on the left and Delaunay on the right.

The contours of static pressure on the centre plane in the converged solution for both grids are shown in Figure 3.7. The two plots demonstrate the similarity of the results. The centre of rotation is the same for the two cases, the magnitude is similar and the velocity vectors seen (Figure 3.8) also demonstrate the similarities. However, a difference can be identified in the diffusion of the velocity between the walls and the centre of rotation. The Advancing-Front grid appears to be less "focused" than the Delaunay mesh. This is probably attributable to the numerical diffusion of the solution caused by the more highly skewed number of cells in the former mesh type.

Fine grids were used for the second stage of this test case and were significantly more refined than the coarse grids. The redefined mesh sizes are given in Table 3.2.

Table 3.2 The fine grid sizes for the lid driven cavity test case

Grid type	Fine Advancing-Front	Fine Delaunay
Cells	5819	6121
Faces	11363	12967
Nodes	1408	1417

The graphs of cell skewness for the two types of grid are shown in Figure 3.9. These again demonstrate the superior quality of the Delaunay generated grid. This can be attributed, in large part, to the refinement of unsuitable cells (highly skewed and large ones) by point insertion that is an integral part of the Delaunay method. The deficiencies in the Advancing-Front grids remain for the larger grid even allowing for the greater number of cells of this mesh. Figure 3.10 shows the quality of the faces within the two grids. The Advancing-Front grid has a greater spread of face skewness, even allowing for the difference in face numbers, Table 3.2. This greater spread will, as in the coarse grid, contribute to the lower cell quality of the Advancing-Front grid via the generation of new cells from existing faces, as used in this method.

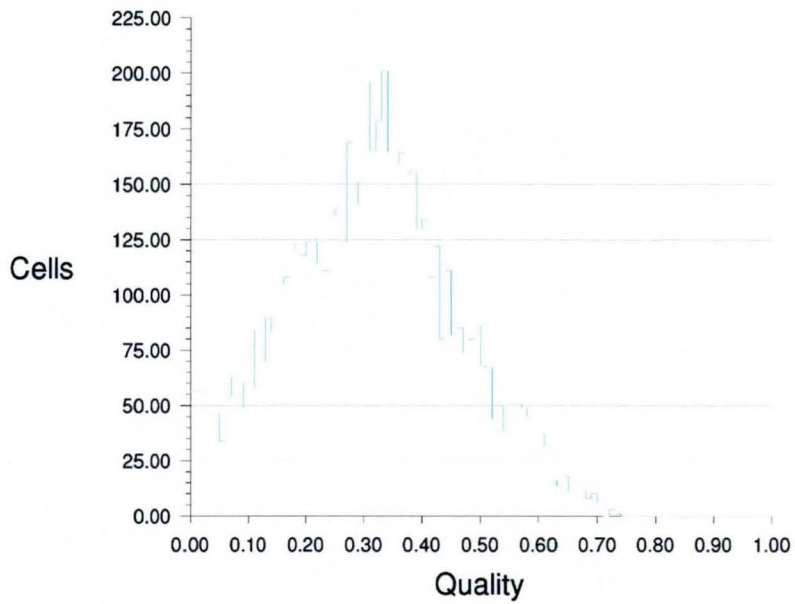
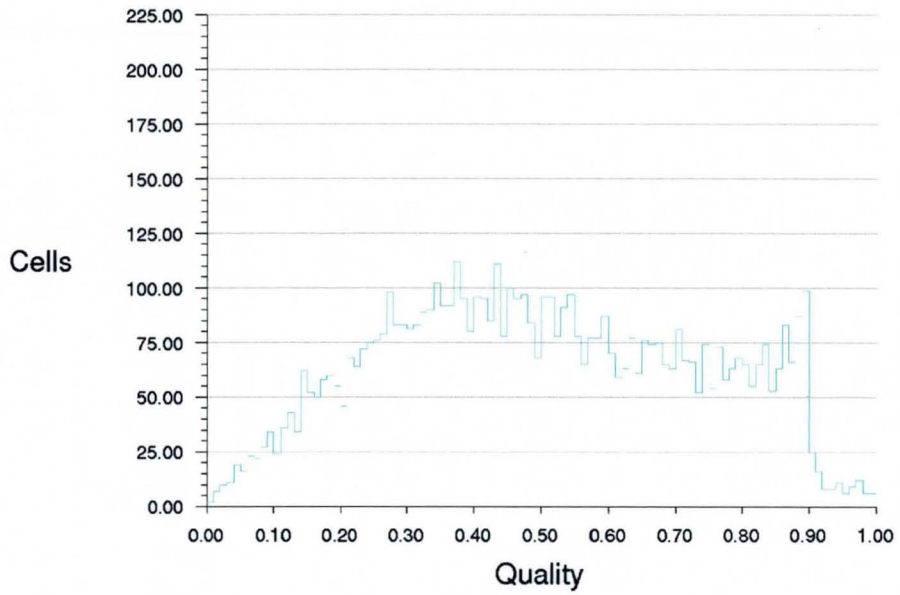


Figure 3.9 Cell skewness for the two fine grids on the lid driven cavity test case. The Advancing-Front generated grid is on the top and the Delaunay is on the bottom.

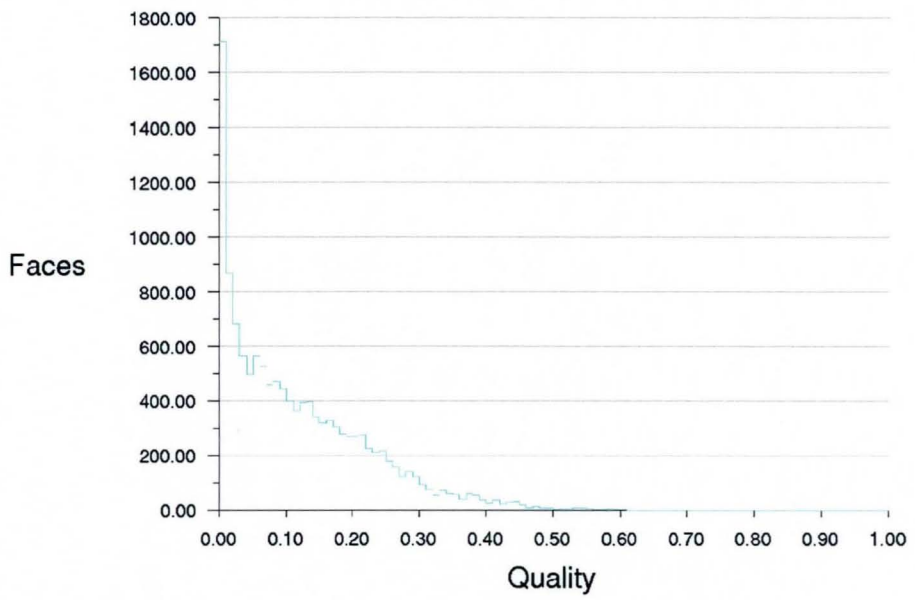
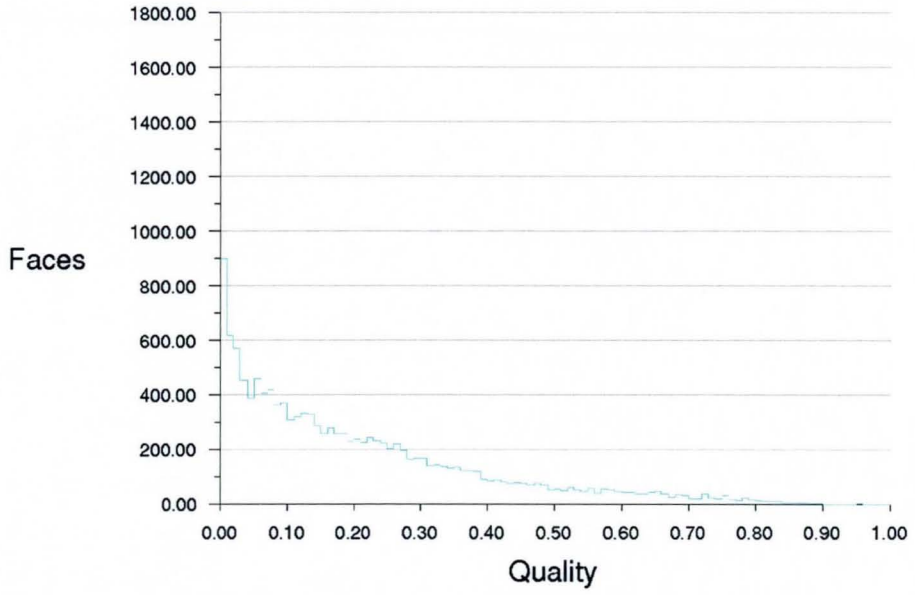


Figure 3.10 Face skewness distributions for the two fine grids on the lid driven cavity test case. The Delaunay case is on the bottom and the Advancing-Front on the top.

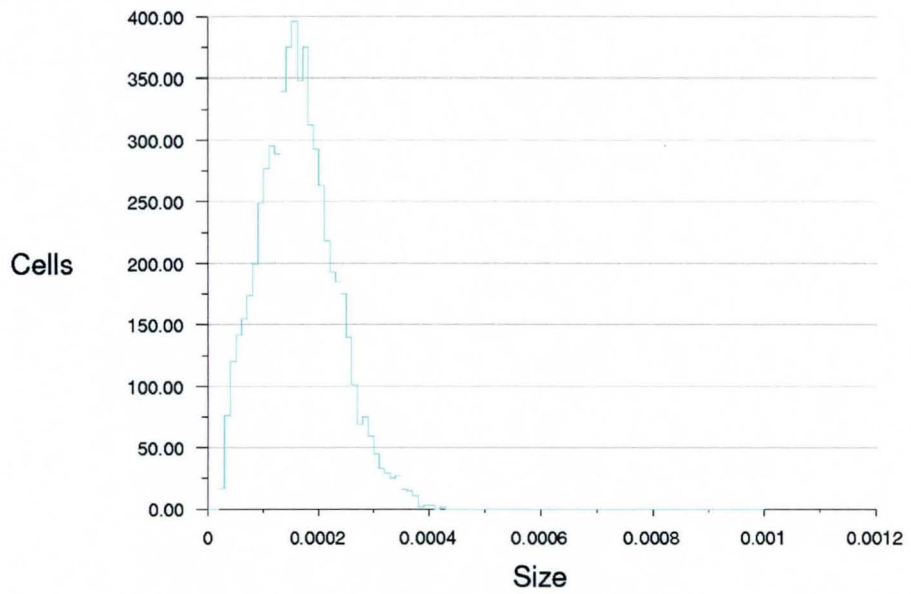
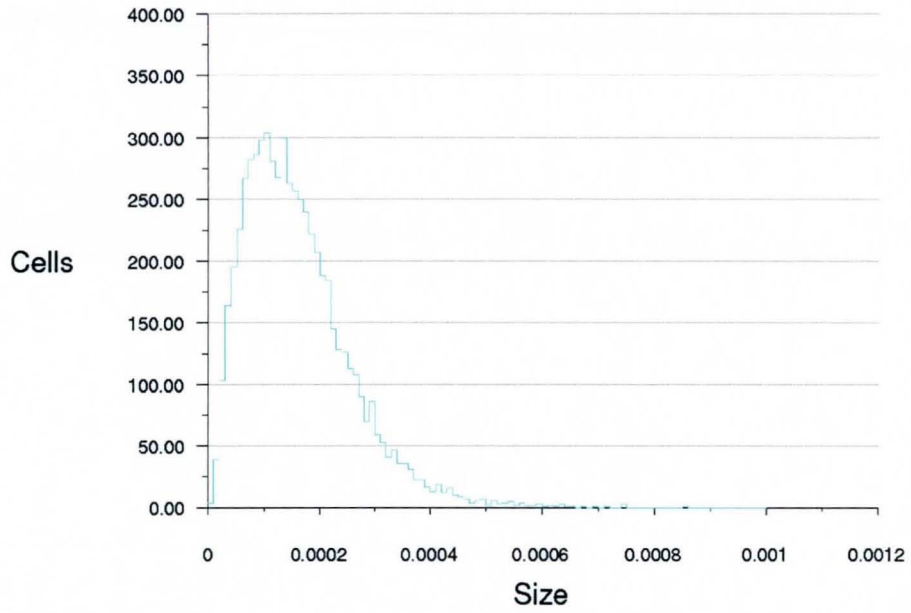


Figure 3.11 Cell volume distribution on the fine grids. Advancing-Front on the top and Delaunay on the bottom.

Figure 3.11, shows the Delaunay grid also to have a better distribution of cell volumes. However, the Advancing-Front grid has a lower maximum cell volume, that

will affect the resolution and accuracy of any solution. This suggests that the Advancing-Front grid may produce a more accurate solution in comparable tests. This is not a contradiction of the previous assertion that the Delaunay grid is of a higher quality, rather, that the Advancing-Front grid uses more cells within a given space. These extra cells will reduce the growth of cell size through the domain which will, in a CFD solution, increase the accuracy.

The contour plots of cell volume on the centre plane of the solution domain overlaid with the actual grid on the centre plane are contained in Figure 3.12. They show how well the Advancing-Front grid has graduated the cell volumes away from the boundary to the interior in comparison to the Delaunay grid. The only criteria used for cell volumes of a Delaunay grid is a global one, set without knowledge of the boundary grid. Consequently, there is no discernible pattern to the cell volumes. This has obvious ramifications for the accuracy of the CFD solution on the grid. By contrast, the Advancing-Front method uses a local function defined by the user to set the height of projection of any new cell and hence controls the volume, which gives this grid it's improved cell growth.

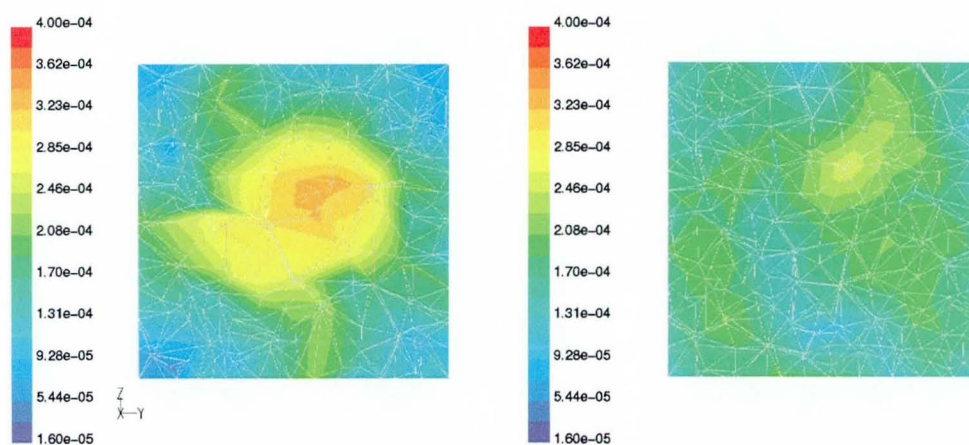


Figure 3.12 The contours of cell volume on the centre plane of the lid driven cavity test case for the two fine grid, overlaid with the grid slice on that plane. The Advancing-Front method is on the left with the Delaunay generated grid on the right. (Note: The long thin sliver cells here do not necessarily indicate highly skewed cells)

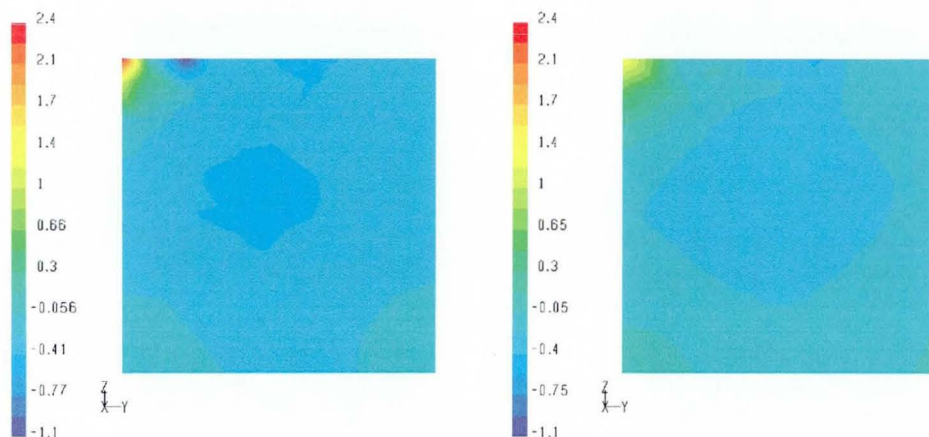


Figure 3.13 Contours of static pressure on the centre plane of the lid driven cavity test case for the two fine grids. The Advancing-Front method is on the left with the Delaunay generated grid on the right.

As can be seen from Figure 3.13 and Figure 3.14 the CFD solutions on the two grids give similar solutions. The centre of rotation is the same and the magnitude of the static pressure similar for most of the domain. However, the Delaunay grid solution has less variation of the static pressure than the Advancing-Front grid solution, and does not have a comparable peak of static pressure at the end of the driven lid where the flow stagnates. This is reflected in the velocity vectors, the peak velocity at the end of the driven lid is nearly twice the value in the Delaunay grid. These peaks are entirely dependent on the density of the grid at these points. This indicates that the Delaunay grid at this point is finer than the Advancing-Front grid.

To conclude, the effect of increasing the mesh refinement for both grid types increases the resolution of the recirculation. That is, the recirculations in the fine grid cases appear to be more central in the domain bear a greater resemblance to a recirculation pattern than the coarse grid cases. Both grid generators appear to be producing very similar flow fields for the fine grid predictions.

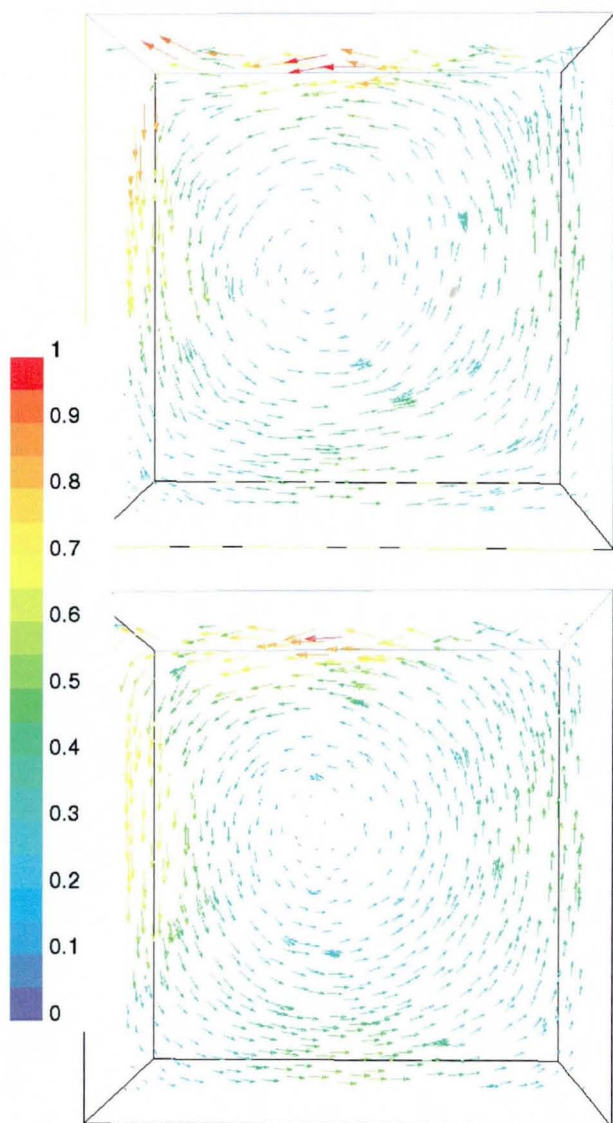


Figure 3.14 Vectors of velocity on the centre plane of the lid driven cavity test case coloured by velocity magnitude on the fine grids. The Advancing-Front method is on the top with the Delaunay generated grid on the bottom.

3.4 Backward Facing Step

There is a general lack of three-dimensional test cases with comparative quantitative data. However, some insight can be gained by using a three-dimensional version of the backward facing step [13,40].

The geometry for this test case is illustrated in Figure 3.15. The geometry consists of an internal flow, which contains an expansion of 1:2. The expansion takes the form of a step on one side of the domain. The inlet flow is allowed to develop for 20 step heights before the step and after this, the domain continues for 20 step heights. These are considered sufficient for the flow to develop before the step, and to then return to a non-re-circulating flow. As this study is concerned with the evaluation of a three-dimensional grid generator, the geometry will be projected in the third dimension by unit depth. This will allow a comparison of the results from the two grid generators with accepted results from experimental work.

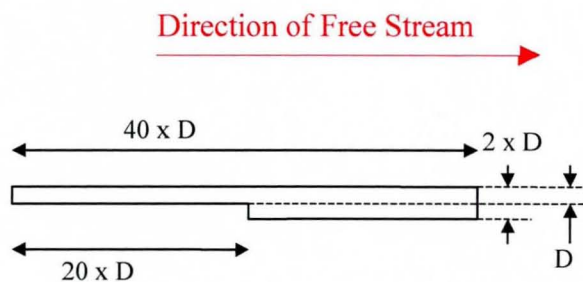


Figure 3.15 The dimensions for the backward facing step test case

The surface grid that will be used for this comparison is shown in Figure 3.16. The grid is the same for both of the internal grid generators tested here.

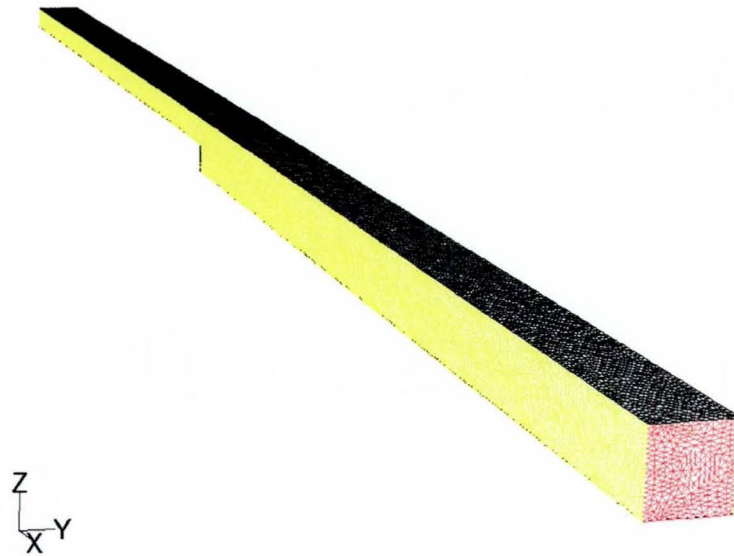


Figure 3.16 The surface grid on the backward facing step. The grid walls are coloured by boundary condition type: Black - wall; yellow - symmetry; red - outflow.

As defined previously, the measures of grid quality are the distributions of cell and face skewness. These indicators are presented in Figure 3.17 to Figure 3.19 for the two types of internal grids. Figure 3.17 shows the distribution of cell skewness for the two grids, the offset normal distribution of the Advancing-Front grid is clearly of a lower quality than the Delaunay grid. The distribution of cell sizes, Figure 3.18, however, shows the higher number of cells for the Advancing-Front grid and it's better distribution. The face skewness distribution, Figure 3.19, illustrates the lower maximum skewness in the Delaunay grid, it also shows the generally better distribution of the face skewnesses for this grid type.

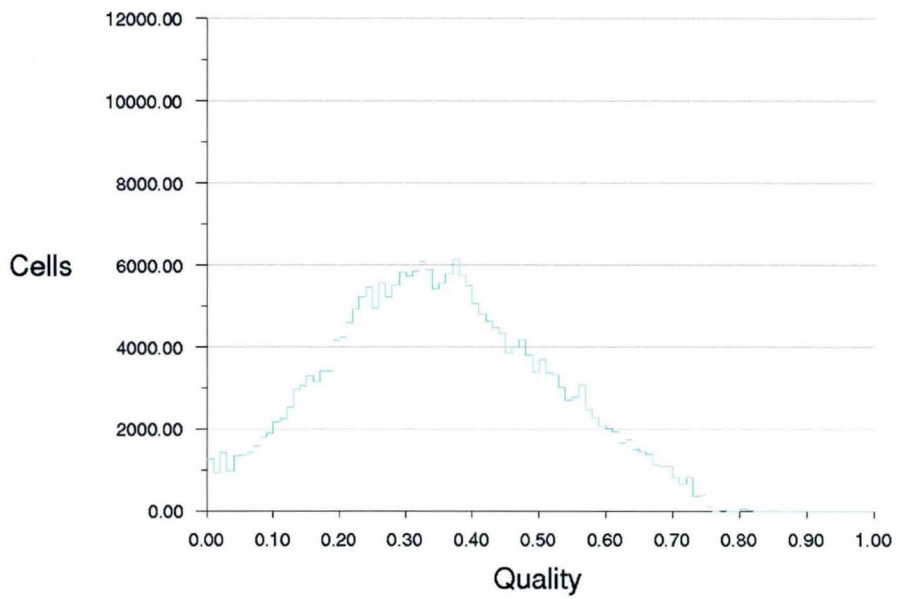
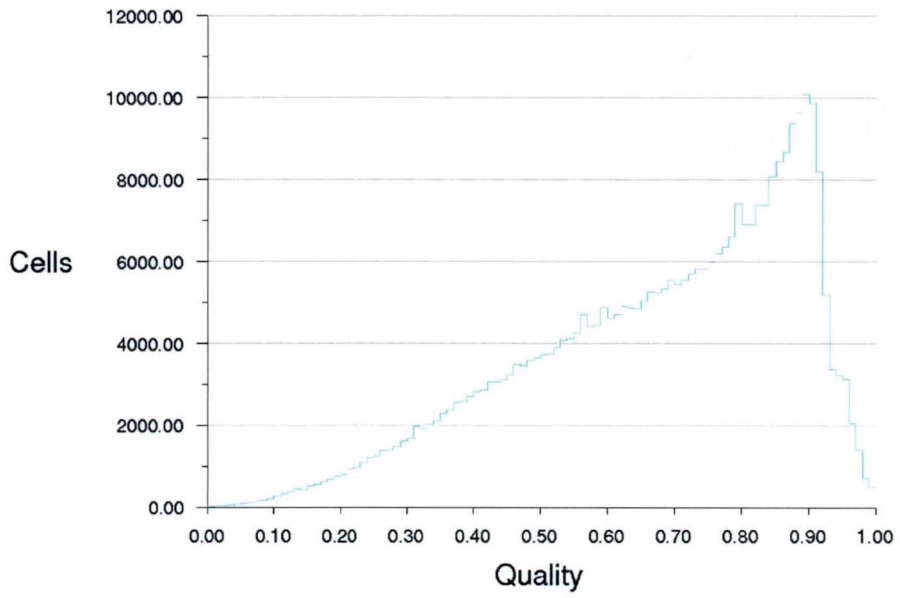


Figure 3.17 the distribution of cell skewness on the two grids for the backward facing step, the Advancing-Front grid is on the top and the Delaunay on the bottom.

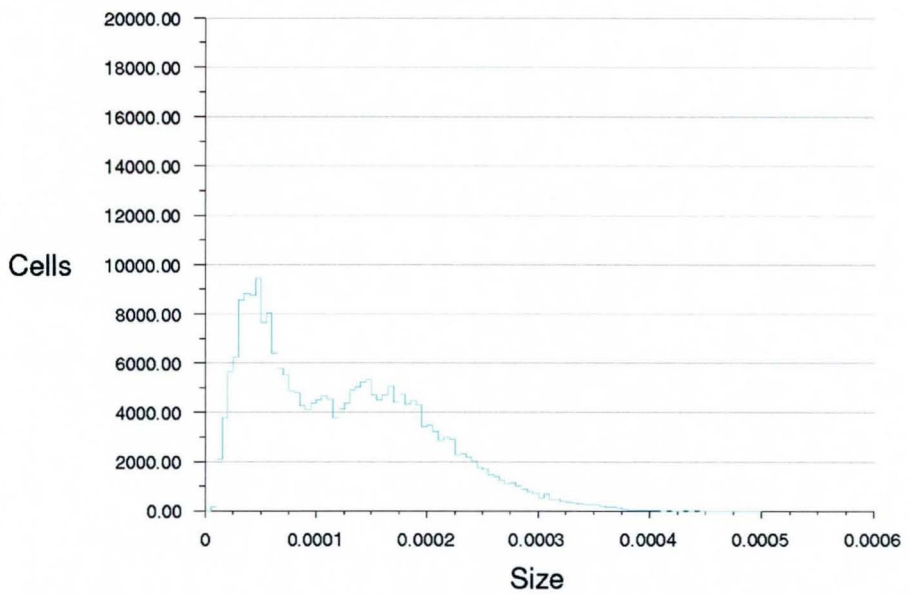
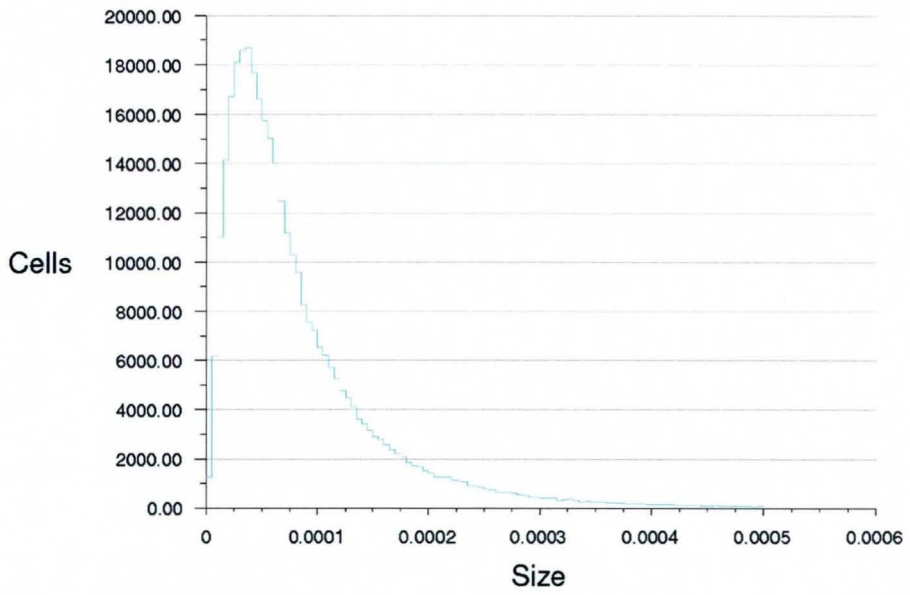


Figure 3.18 the distribution of cell volume on the two grids over the backward facing step. Advancing-Front on the top and Delaunay on the bottom.

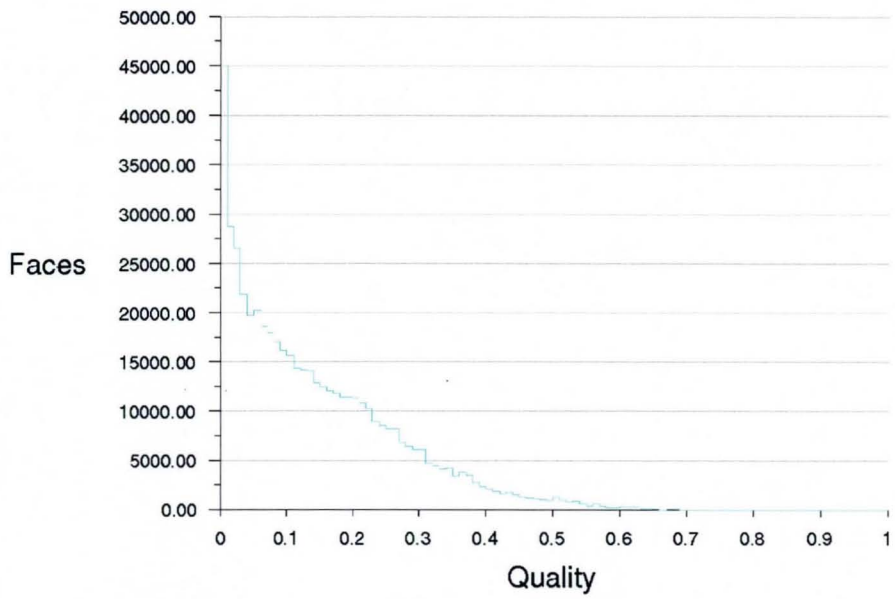
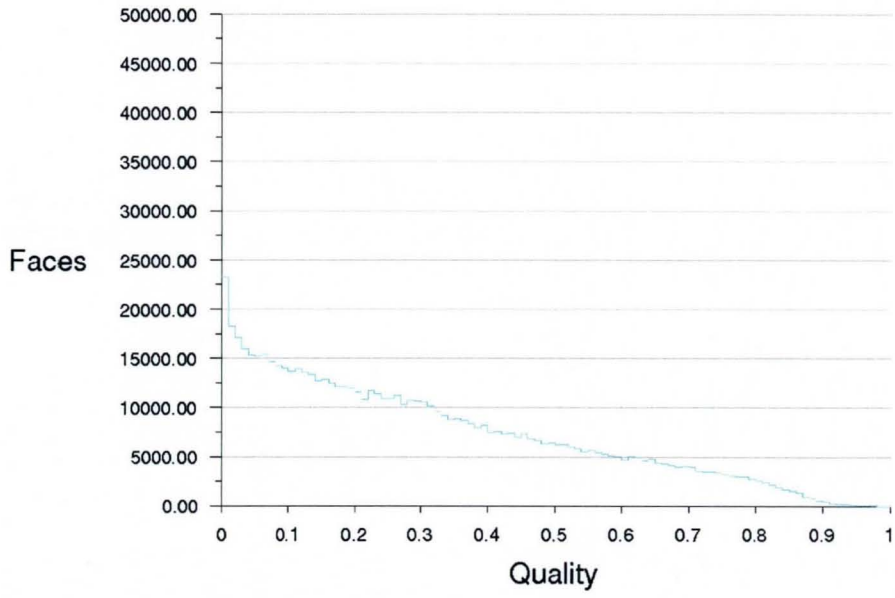


Figure 3.19 The distribution of face skewness for the two grids over the backward facing step. Advancing-Front on the top and Delaunay on the bottom.

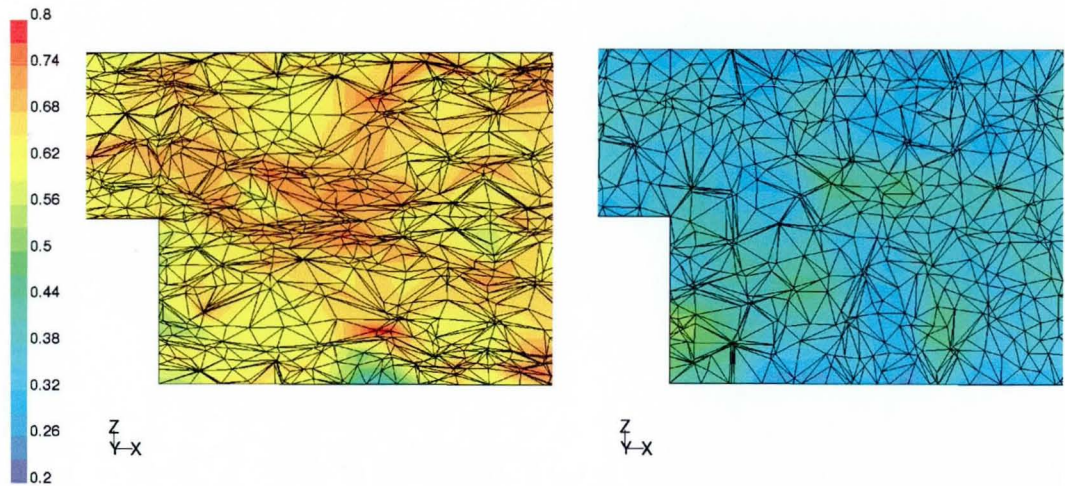


Figure 3.20 The contours of cell skewness on the centre plane overlaid with the grid itself (Advancing-Front on the left and Delaunay on the right).

The plots of centre plane contours of grid cell skewness overlaid with the grid slice are illustrated in Figure 3.20. The table of grid sizes is seen in Table 3.3. As can be seen, the two grids have important differences.

Table 3.3 The grid sizes for the backward facing step test case

Grid type	Fine Advancing-Front	Fine Delaunay
Cells	349140	242836
Faces	722404	509796
Nodes	73063	53047

The Advancing-Front grid is larger by some margin. The grid also has the largest cells, although the average cell size is smaller than in the Delaunay grid. In addition, the cell quality plot shows that the Advancing-Front grid has a greater number of lower quality cells than the Delaunay grid. This is supported by the plots of cell skewness contours on the centre plane near the step, (Figure 3.20) that are overlaid with the actual grid slice through the centre plane of the domain. The plots illustrate the higher skewness levels present in the Advancing-Front grid. The plot of cell volumes, Figure 3.18, however, shows the higher grid density over the domain for the

Advancing-Front grid, there are more small cells. The levels of face skewness are similar for both grids.

The boundary conditions for this case are as follows:

- Uniform velocity inlet corresponding to a Reynolds number of 500
- Pressure outlet condition (where the pressure is set to a reference value for the rest of the domain)
- Symmetry conditions along the sides
- Walls for the top and floor

This is primarily a two-dimensional test case, however, the symmetry condition on the sides allows for modelling in three-dimensions. The measure of the ability of the grid to solve the problem is the point of reattachment, which for a Reynolds number of 500 in the experiments of Kim et al [40] should be 10.1m after the step.

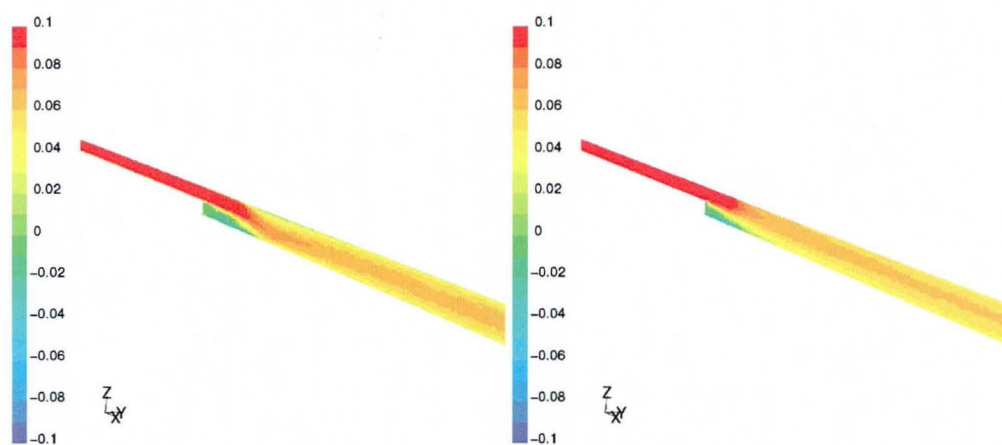


Figure 3.21 The contours of velocity magnitude on the centre plane of the three-dimensional backward facing step. The Advancing-Front grid is on the left.

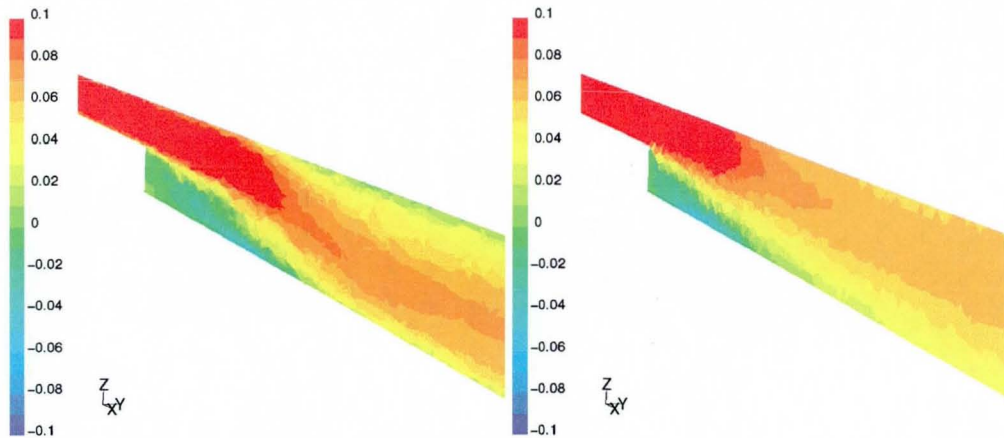


Figure 3.22 The close up of the contours of velocity magnitude on the centre plane of the three-dimensional backward facing step. The Advancing-Front grid is on the left.

Figure 3.21 and Figure 3.22 demonstrate that the flow patterns using the two grids are similar, although the re-circulation in the Advancing-Front grid would appear to be slightly larger.

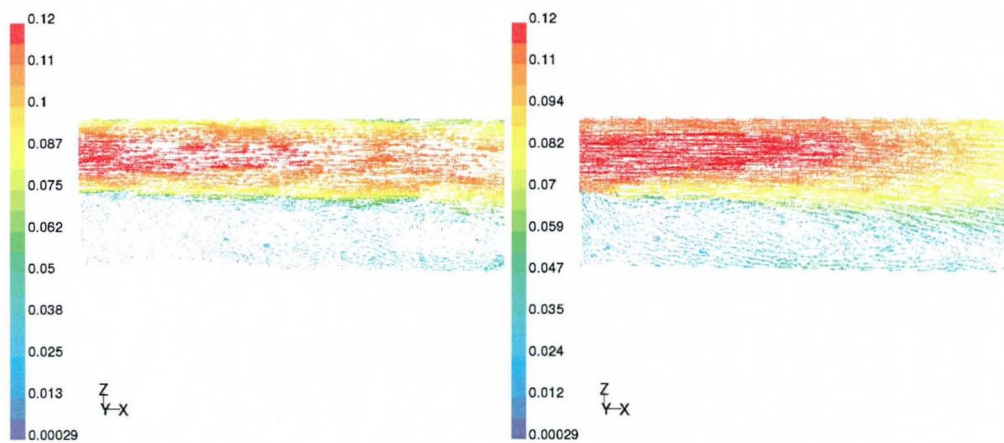


Figure 3.23 The streaklines coloured by velocity magnitude immediately after the step on the centre plane of the three-dimensional backward facing step. The Advancing-Front grid is on the left.

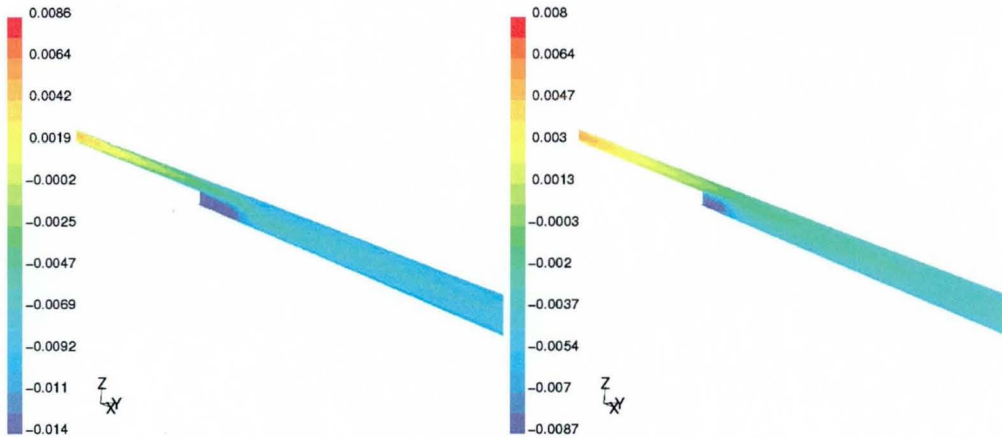


Figure 3.24 The contours of static pressure on the centre plane of the three-dimensional backward facing step. The Advancing-Front grid is on the left.

The larger re-circulation in the advancing grid case is more clearly seen in Figure 3.23 and Figure 3.24. The velocity vectors plots are similar for the two grids. The re-circulation in the Delaunay grid is, however, better defined in that there is one clear vortex, whereas the Advancing-Front grid solution has a less well defined flow pattern. It is possible that the latter flow pattern is increasing the separated region after the step through lower levels of diffusion there brought about by the increased grid density of the Advancing-Front grid. The velocity vector plots, Figure 3.23, also illustrate the secondary recirculation at the very bottom of the step. This is a feature of the experimental results and is also visible in Figure 3.25, the contours of x-velocity on the floor.

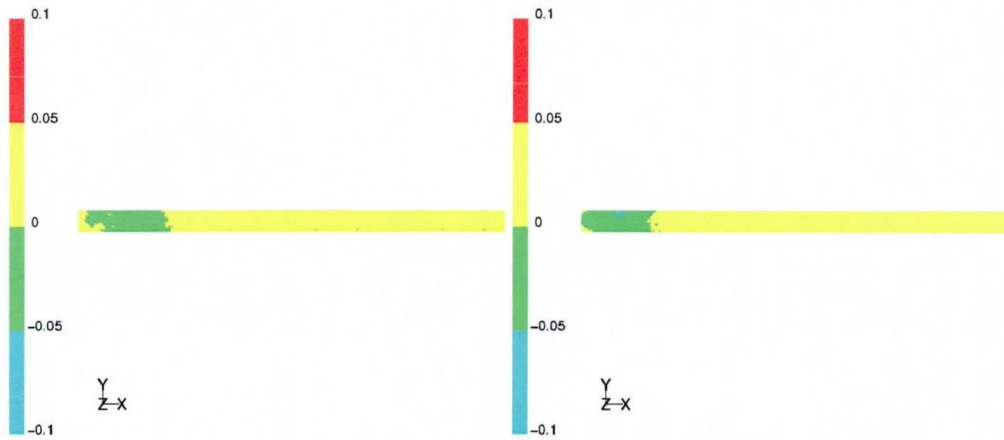


Figure 3.25 The contours of x-velocity on the floor of the backward facing step. The number of contours is reduced to give a clearer picture of where the flow reattaches after the step (experimental value is 10.1m).

In Figure 3.25, the contours of x-velocity on the floor clearly show the reattachment point via the use of a limited number of contours. The re-attachment position for the two grids is similar, with the solution on the Delaunay grid attaching slightly before the Advancing-Front grid solution. The reattachment length for the Delaunay grid was 8.2m and the Advancing-Front grid is 9.1m. This latter result is closer to that seen in the experiments (10.1m) and can be attributed to the better grid resolution of the Advancing-Front grid in the region around and after the step. More analysis could be made of these results and further comparisons made with experimental work, however, the main aim of these two test cases was not to perform calculations. This section of the project was intended to establish the similarities between the two grid generators and their range of applicability. To this end, the results of the work presented in this section (and the preceding one) have successfully compared the two grid generators. We can now, with some confidence in the expected results, apply both grid generators to more complex problems.

3.5 Ahmed Body

3.5.1 Comparison of the Delaunay and Advancing-Front grids

The comparison of the grid sizes is shown in Table 3.4.

Table 3.4 The breakdown of the grid sizes for the initial tetrahedral grid tests over the Ahmed body.

	Boundary nodes	Interior nodes	Boundary faces	Interior faces	Cells
Delaunay	4950	4588	9896	78276	41612
Advancing-Front	4950	33651	9896	391804	198376

The numbers of the internal nodes, faces and cells are much greater for the Advancing-Front generated grid than the Delaunay generated grid. This can again be attributed to the fact that the Advancing-Front grid generator has no method of increasing or decreasing cell size in regions where they are not required. It is entirely heuristic, relying on the previous cells for the new cell's size. By contrast, the Delaunay method will only introduce new cells where the cell quality conditions have not been met. This second approach is bound to use less cells as there is no constraint on volume size or growth rate, however, as discussed, this will reduce the potential accuracy of the flow solution. This may be interpreted as an unfair test of the two grid generators. A fairer test may have been to use similar numbers of cells, however, this would have given a much greater resolution of the surface (and thus the cells close to the surface) in the Delaunay generated grid.

In this section, the two grids will be compared in terms of quality. The breakdown of cell skewness seen in Figure 3.26 shows the higher quality of the Delaunay mesh. In comparison, the Advancing-Front mesh has more cells with skewness close to one.

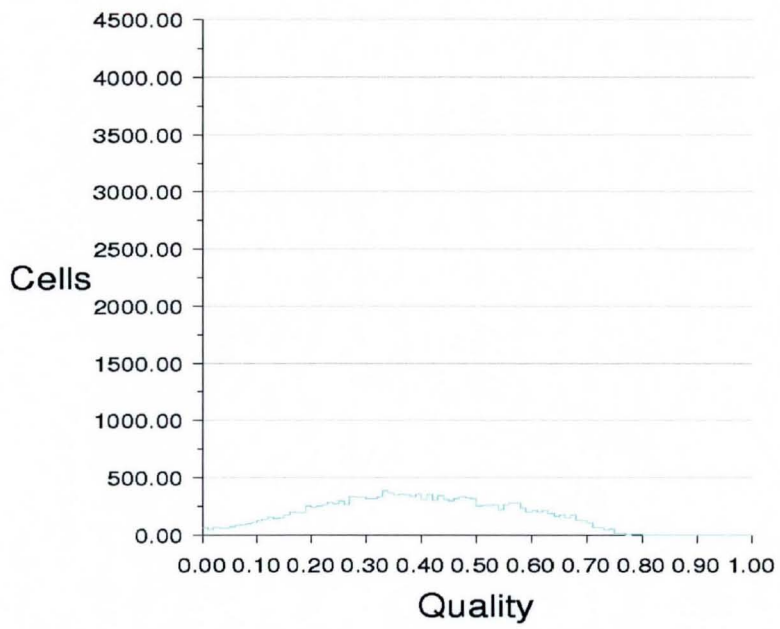
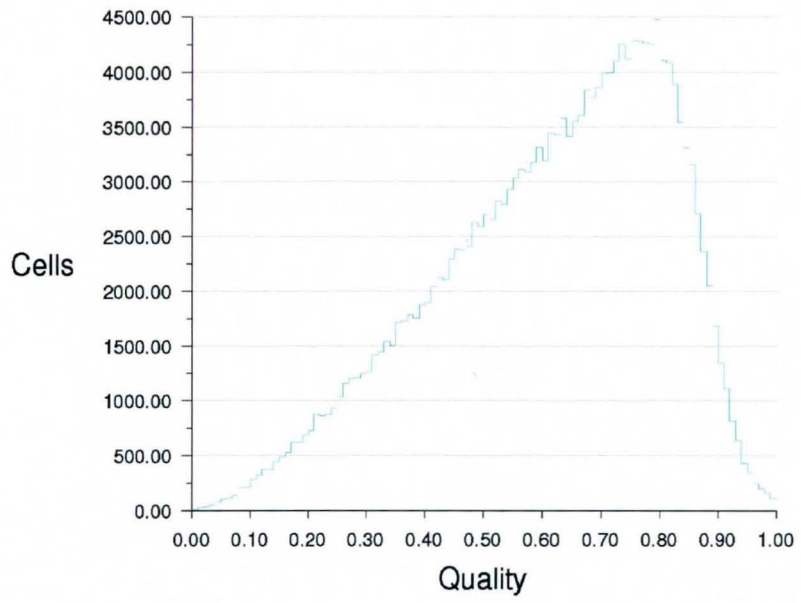


Figure 3.26 The breakdown of cell skewness for the two grids. Delaunay on the bottom, Advancing-Front on the top.

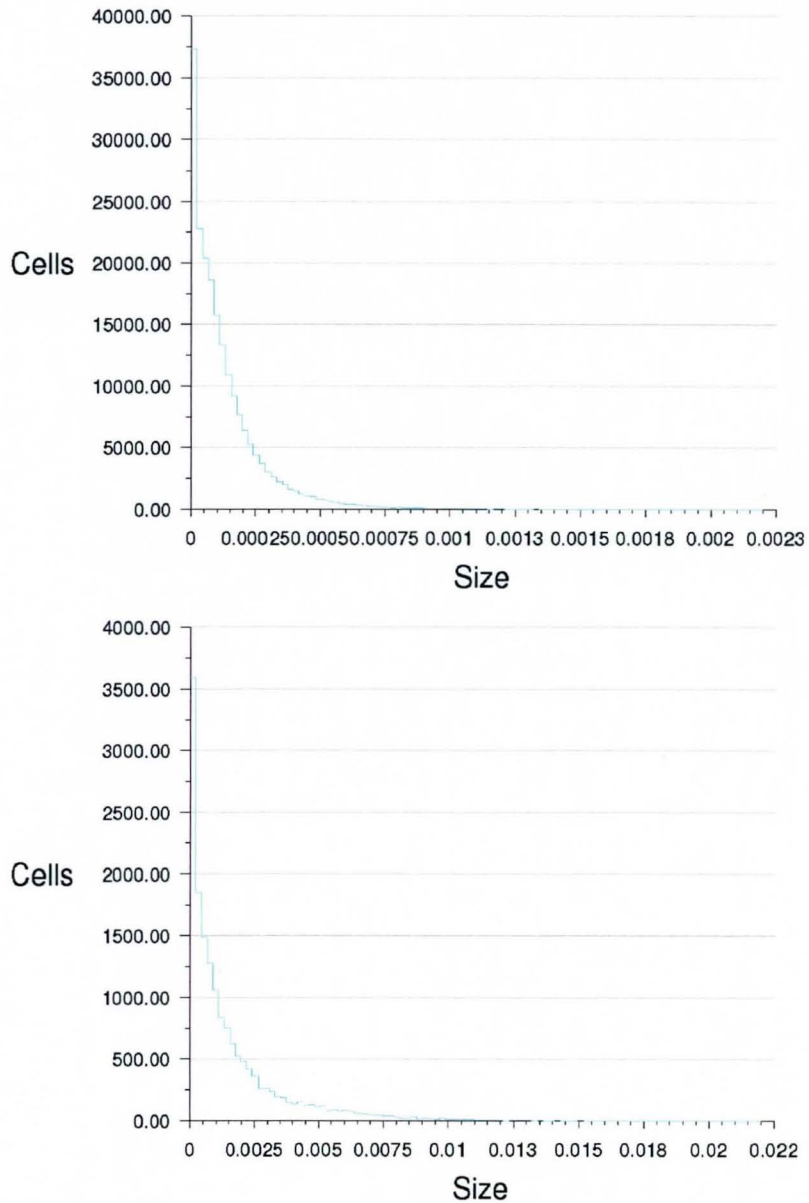


Figure 3.27 The breakdown of cell volume for the two grids. Delaunay on the bottom, Advancing-Front on the top. The range of volumes is from 0 to $0.022m^3$.

The breakdown of cell volumes (Figure 3.27) in the solution domain for the two grids shows the larger number of cells in the Advancing-Front grid. Generally, however, the spread of cells is similar. In Figure 3.28, the breakdown for the boundary and internal faces on the two grids is shown. The Delaunay grid, again, shows much lower skewness levels than the Advancing-Front grid when using the same boundary mesh.

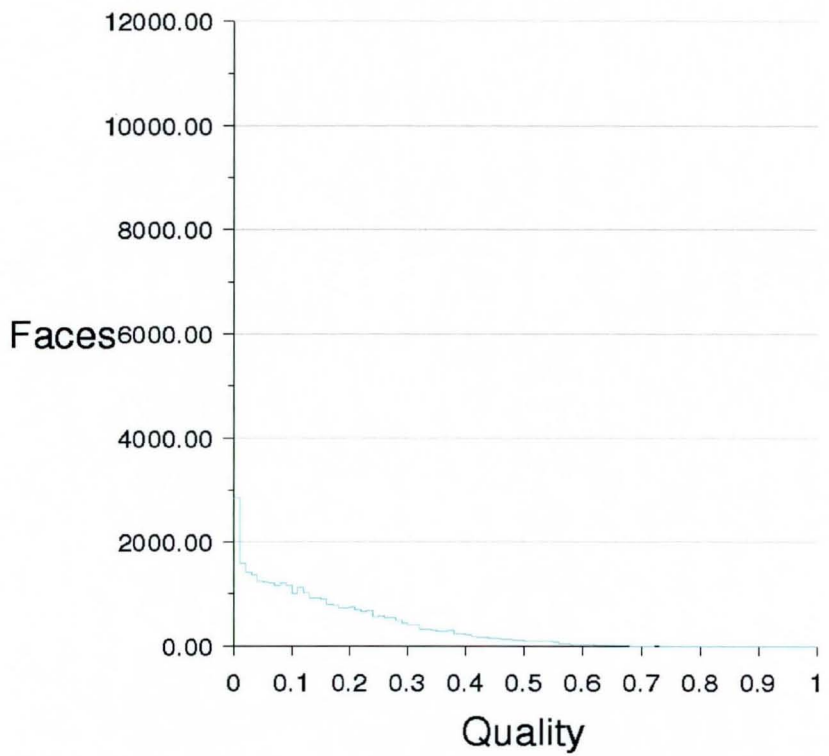
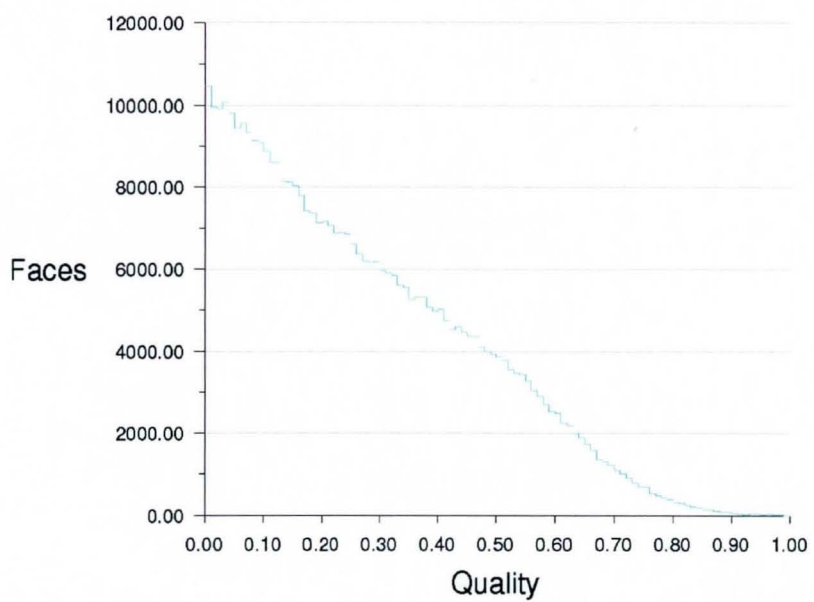


Figure 3.28 The breakdown of face (boundary and interior) skewness for the two grids. Delaunay on the bottom, Advancing-Front on the top.

The mesh quality measures clearly indicate the Delaunay mesh to be the more efficient, with lower levels of skewness for both cells and faces whilst using fewer cells. The extra number of cells for the Advancing-Front grid are as mentioned before due to the ideal grid cell size not being increased away from the geometry. This would be improved by the use of a background grid.

The quality of the meshes from a solution accuracy point of view can be tested through a CFD solution on these meshes. This was done and the solutions are compared to each other in the rest of this chapter.

The wall average wall y^* values on the Ahmed body in the calculations below are 2000 for the Advancing Front mesh and 4000 for the Delaunay mesh.

3.5.2 Comparison of solutions for Delaunay and Advancing-Front grids

The contours of velocity magnitude (shown in Figure 3.29) illustrate the general flow pattern for the geometry. The general patterns of the velocities around the body are consistent with those seen in other reported calculations (see Chapter 1). The static pressure contours, (Figure 3.30) show the similarities of the two results.

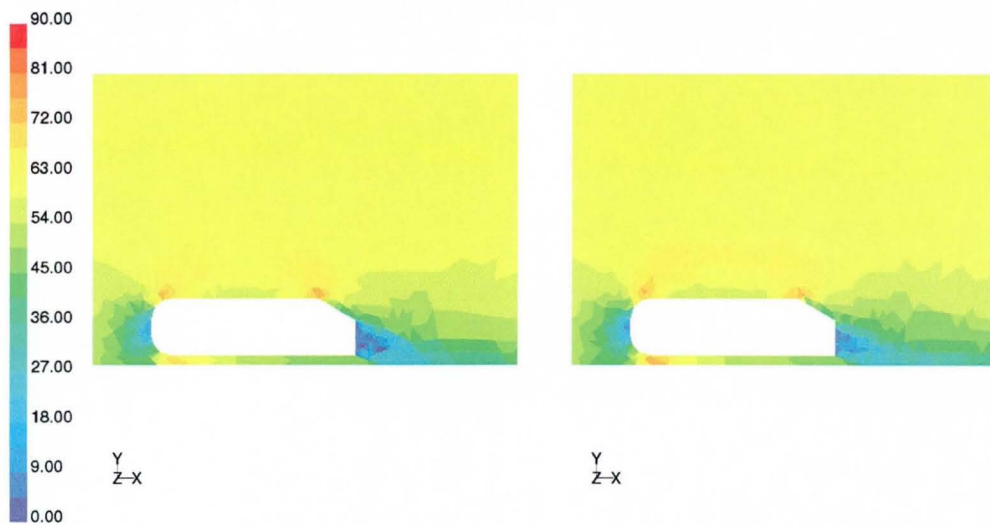


Figure 3.29 The velocity magnitude contours for the two grids on the symmetry plane.
Delaunay on the right, Advancing-Front on the left.

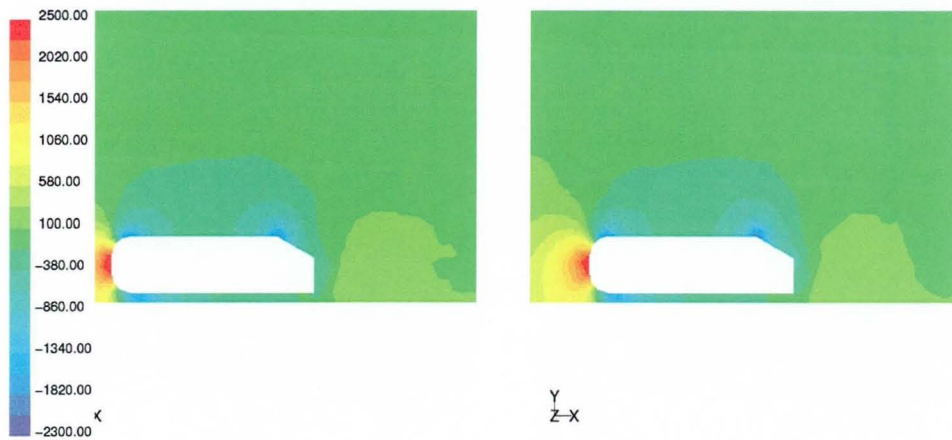
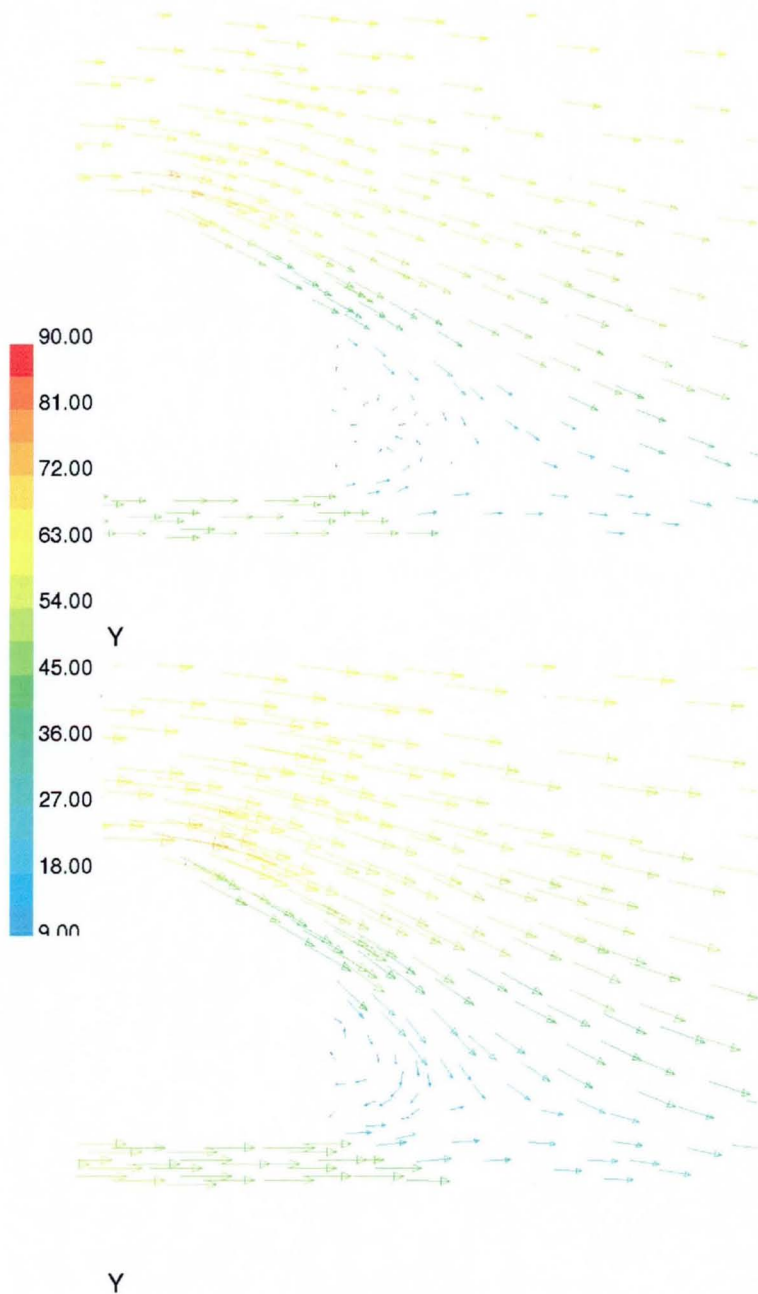


Figure 3.30 The contours of static pressure for the two grids on the symmetry plane.
Delaunay on the right, Advancing-Front on the left.



*Figure 3.31 The velocity vectors for the two grids coloured by velocity magnitude.
Delaunay on the bottom, Advancing-Front on the top.*

In Figure 3.31, the velocity vectors indicate that the Delaunay predicts a single large vortex in the region after the body. By contrast, the Advancing-Front grid predicts two counter rotating vortices of near equal strength. The latter is closer to the "real-life" flow field demonstrating the superior resolution of the flow field by this grid.

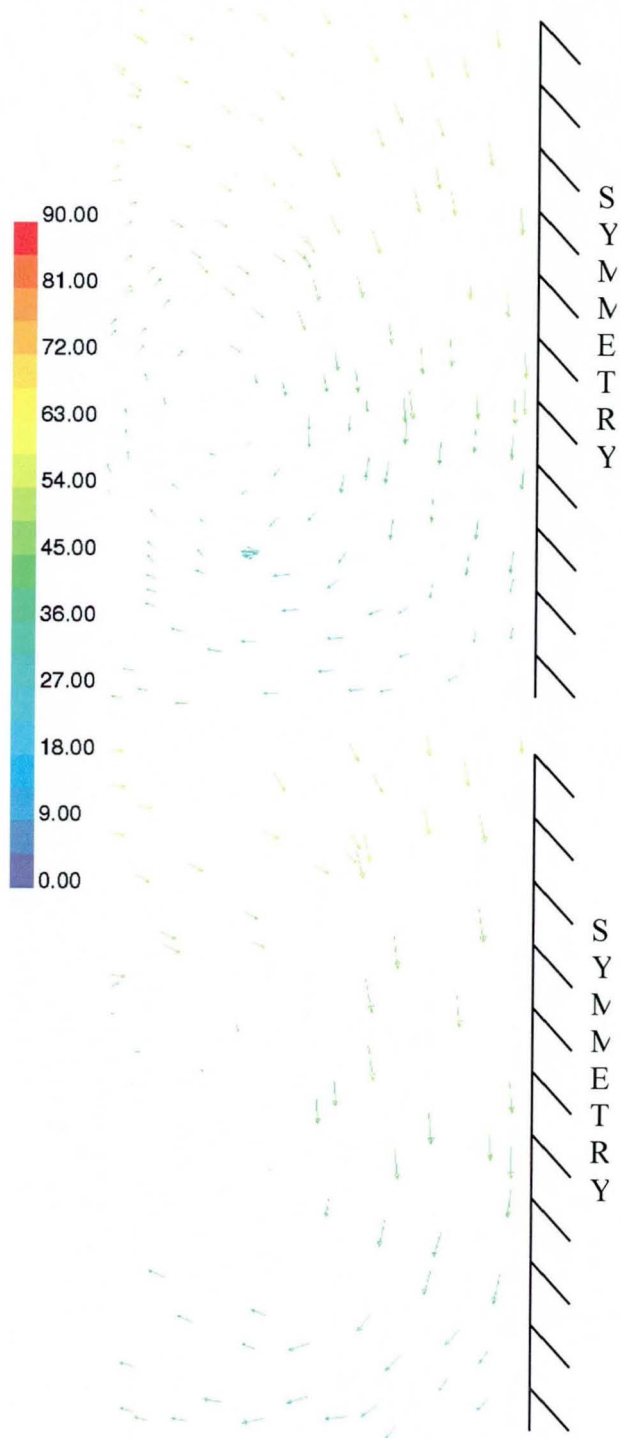


Figure 3.32 The velocity vectors for the two grids coloured by velocity magnitude on a vertical plane 0.5m behind the end of the body. Delaunay on the bottom, Advancing-Front on the top.

It is evident from Figure 3.32 and Figure 3.33 that the Advancing-Front grid has resolved the counter rotating longitudinal vortices, in comparison to the Delaunay grid, which has not. This can be attributed in large part to the Delaunay grid's rapid expansion of cell volume away from the body. Although this is clearly a superior result for the Advancing-Front grid, it is mainly due to the extra number of cells introduced into the grid by the lack of a background grid. This could be viewed as a flaw in the usual spacing seen in unstructured grids, which is not sufficiently refined to pick up the flow features of the problem.

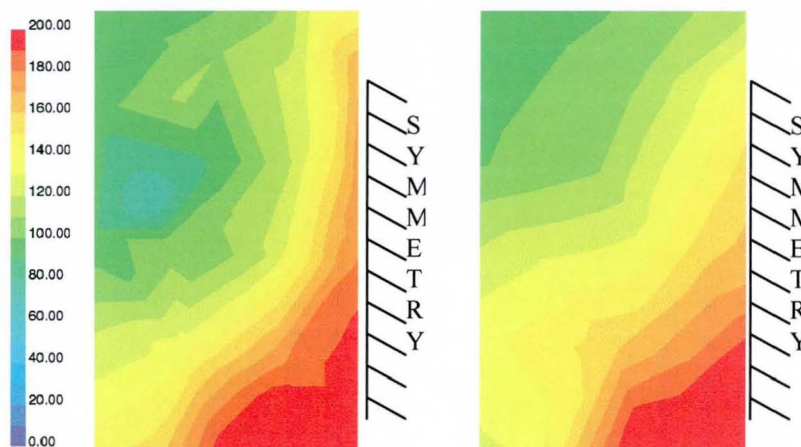


Figure 3.33 The contours of static pressure for the two grids on a vertical plane 1.5m behind the end of the body. Delaunay on the right, Advancing-Front on the left.

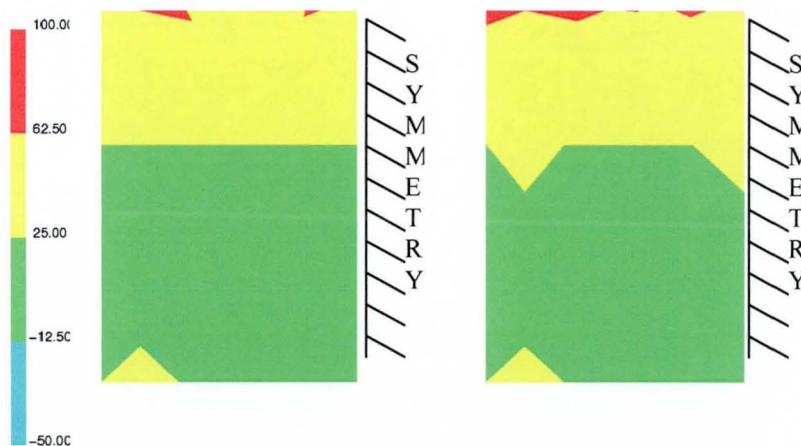


Figure 3.34 The contours of velocity magnitude for the two grids on the rear surfaces of the body. Delaunay on the right, Advancing-Front on the left.

The plots of velocity contours on the rear surfaces of the body are shown in Figure 3.34. The number of contours has been reduced to 4 to display the areas of flow reversal on the slant surface. The plots show that, as expected, the flows are both attached on the rear slant surface.

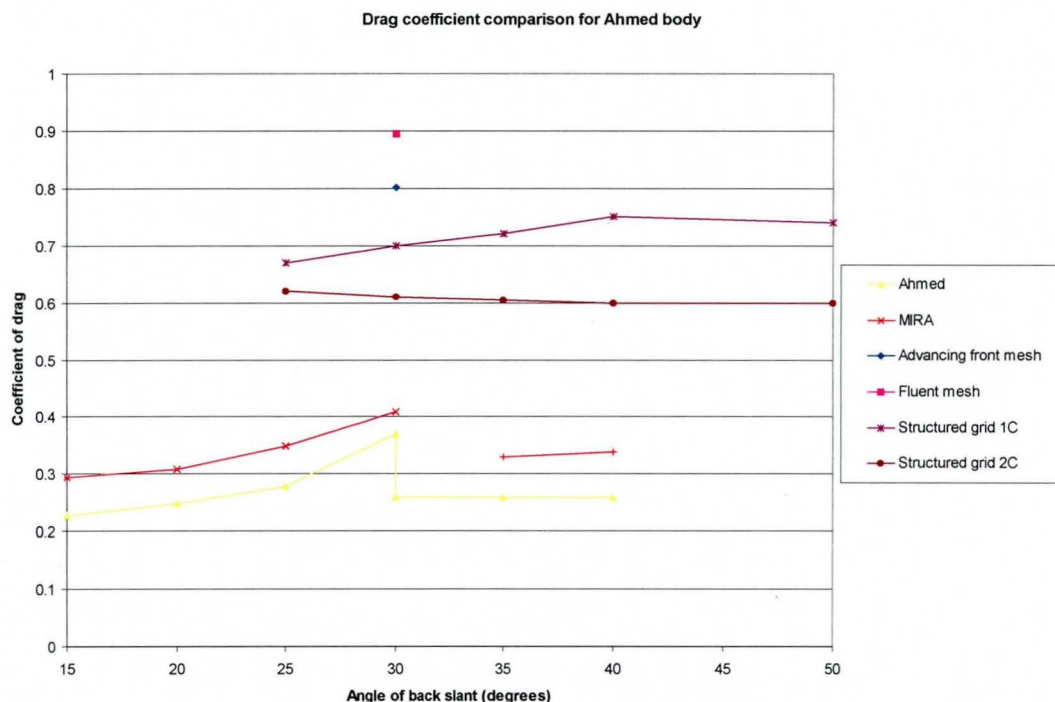


Figure 3.35 The drag forces on the Ahmed body for the two grids. Also shown are the experimental results from Ahmed and MIRA.

The drag results for these grids are included in Figure 3.35 together with the experimental results and some of the structured mesh results from Chapter 1. They are again much higher than the experimental results. This can be attributed to several factors, which will be considered in subsequent chapters.

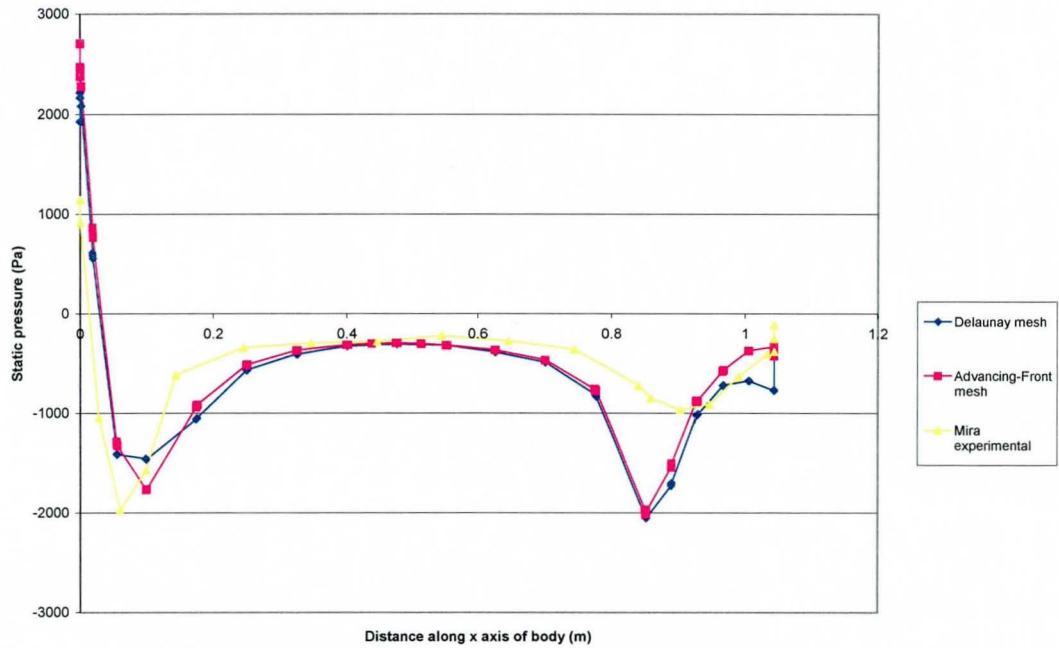


Figure 3.36 The static pressure values on the upper body centreline for the two grids.

The static pressures on the upper surface centreline of the body show very similar results. The lack of surface grid resolution for this level of mesh suggests that any further analysis of these plots would only be valid as part of a mesh refinement study.

3.6 Conclusions

This chapter has demonstrated the similarities between the two grid generators, which were both tested on two general test cases and a specialised automotive problem. The first of the general cases was a lid-driven cavity to be evaluated in a purely qualitative manner, the second a backward facing step, with a known experimental reattachment length. The automotive problem was the Ahmed body in close proximity to the ground.

Overall, the two grid generators have produced similar grids. The flow solutions on the two grids are also very similar. All the test cases show comparable flow structures with minor differences. The position of the reattachment point in the backward facing step case is predicted to be similar to the experimental value in both test cases, reinforcing the similarity of the grids.

The Delaunay grid typically generates fewer cells than the Advancing-Front grid starting from the same boundary discretisation. Those cells are of a higher quality due to the intelligent nature of the point placement algorithm used, as seen in all the test cases in this chapter. The Advancing-Front grid has no method of “realising” the benefits of various point placement options in a global sense. This leaves the Advancing-Front method the difficult task of “filling in the gaps” at the end of any grid generation. Consequently, skewness levels are higher. However, the advantage of the Advancing-Front method is the ease in which points can be clustered and the grid density increased, in desired areas, which results in a higher number of cells. This is demonstrated by the results of the backward facing step test case. The reattachment length is close to the experimental value for the Advancing-Front grid. This is a direct consequence of the better resolution of the flow, which reduces the numerical diffusion. The corollary to this extra cell clustering is that the grid has a more progressive change in the cell size through the domain. This can be attributed to the Advancing-Front algorithm using a typical cell projection height to form the next element. The Delaunay algorithm is designed to use the maximum size element permissible within the refinement bounds set in the program.

The addition of a background grid to the Advancing-Front algorithm would allow increase of the grid spacing away from the walls (or decrease it as necessary). It would also reduce the size overhead for the Advancing-Front algorithm. Another problem identified in the previous chapter is the failure of the Advancing-Front algorithm to produce a mesh due to the difference in cell spacing seen on different parts of the surface mesh. This problem would also be prevented by the use of a background grid.

The Ahmed body results will be examined in terms of the questions posed in the introduction. Firstly, the was the flow field similar to those suggested by the wind tunnel experiments. The two grids produced very similar results with the same pressure and velocity distributions on the symmetry plane. The Delaunay grid predicted a single large re-circulation after the body whilst the Advancing-Front grid produced two counter rotating vortices of near equal strength. Both these features are seen in wind tunnel experiments on the Ahmed body within an angle sweep of the back slant. The Advancing-Front grid is known to be more refined away from the body, therefore, we can conclude that the Delaunay grid employed here was insufficiently refined. The rest of the flow field is as can be expected over the Ahmed body with a back slant angle of less than 30° . The flow over the slant surface is attached. This is consistent with the 30° slant surface calculations in Chapter 1, which used structured grids that were "bent" over the back/slant edge. The flow field and the effect of the grid on it need further investigation and they will be tackled in Chapter 4.

The second question to be considered is whether the bulk drag levels are of the same magnitude as the experiments. The values for the two grids are not only larger than the wind tunnel experiment values, but are also larger than the structured grid values in Chapter 1. This is unacceptable and will be considered further in Chapter 4. The value for the Advancing-Front grid is higher than the Delaunay grid value, which suggests that the level of grid refinement is affecting the drag.

The third question concerning the change in the drag values with the back slant angle cannot be answered here, as only one angle was tested. However, it should be noted that the flow field results of these CFD calculations are consistent with those seen in the experimental results at lower values of back slant angle.

The final question to be considered is whether the prediction can be, or has been, improved by these calculations. The size of the Delaunay grid over the Ahmed body is certainly smaller, however, the accuracy has decreased. The counter rotating vortices were not sufficiently resolved by this grid. The Delaunay grid prediction can (as will be discussed in Chapter 4) be improved by the use of finer meshes. The Advancing-Front grid did not suffer from this lack of resolution, as the grid spacing does not significantly increase away from the body. However, it is worth noting here that the background grid, which is not featured in this implementation of the Advancing-Front grid, would reduce the number of cells, but not reduce the number of cells in this wake region. It is known to be an important area for the flow, and the background grid would be set up accordingly.

4. Ahmed Body Calculations Using Unstructured Tetrahedral Grids

4.1 Introduction

The initial structured grid and tetrahedral calculations from the previous chapters indicated a need for higher resolution in the region behind the body. Whilst more cells and, thus, greater resolution of the flow detail is always important, it is usually the case that to resolve the flow to this detail for the whole domain results in massive grid sizes for most test cases. With structured grids, the increases in grid refinement close to the body also result in increases in the number of cells away from the body, that is, the overhead is too high. To avoid this problem, unstructured grids are used.

The objective of this chapter are twofold. Firstly, to investigate fully the effect of mesh resolution on the predicted results, and secondly, to investigate further the effect of mesh topology over the top/slant edge of the body. The results will be compared to each other, as well as the Ahmed [2] and MIRA [22] wind tunnel results. The CFD prediction shares the same Reynolds number as the Ahmed results, however, the MIRA results, although at half the Reynolds number, can still be referred to. The comparisons will focus on three areas: force results; symmetry plane upper surface static pressure values; and plots of velocity and pressure. This thorough analysis attempts to capture all grid-related effects on the solutions and provide an insight into the minimum mesh requirements for a body of this type, thereby addressing the principle objective of this study. The progressive increase in the refinement of the mesh will permit more substantiated conclusions concerning the success of these types of grid generator to predict the flow over this type of body.

The Ahmed body is seen in Figure 4.1.

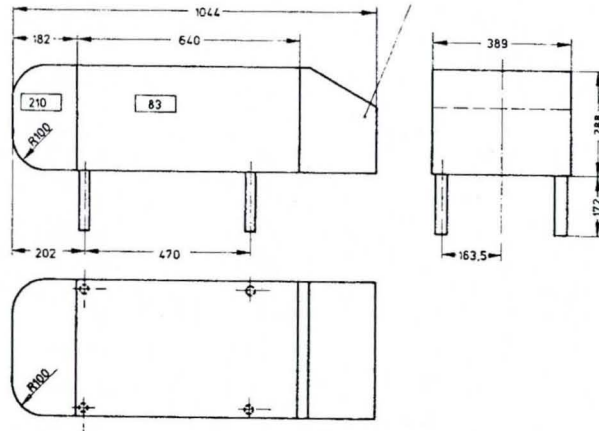


Figure 4.1: Geometry of the Ahmed body (copy of Figure 1.17, included here for ease of reference)

The geometry has a rounded front section leading to a square cross-section. At the rear, the body has an upper slant surface that varies between 20° to 50° . The CFD calculations presented here cover this range in 5° increments.

Recalling, from the discussions provided in earlier chapters, that the flow over the slant surface of the body shows three distinct patterns as the angle of the back slant is increased. The first is fully attached flow over the whole of the surface. This flow structure is maintained up to around 25° . Between 25° and 30° , the flow separates from the top/slant edge although only around the symmetry plane. This separation is small and the flow re-attaches to the slant surface before separating again from the slant/base edge. This separation contains very low-pressure fluid which increases the drag on the body. This flow pattern becomes unstable at 30° and to maintain this flow pattern Ahmed placed a splitter on the symmetry plane just after the body. The third flow pattern, the stable flow pattern at 30° and for higher angles of slant surface, separates from the top/slant edge and does not re-attach to the slant surface. This complete separation reduces the effect of the mixed flow from the sides and top of the body. This reduces the strength of the counter-rotating longitudinal vortices, which were up to this point increasing in strength, considerably. This, combined with the

disappearance of the separation bubble seen on the slant surface for angles of slant surface lower than 30° , reduces the drag appreciably.

4.2 Coarse Grid Calculations

The smallest grid size used in this chapter is given in Table 4.1.

Table 4.1 The grid size for the coarsest cases.

Cells	24469
Faces	46083
Nodes	2727

The grid on the surface of the body and the symmetry plane is represented in Figure 4.2.

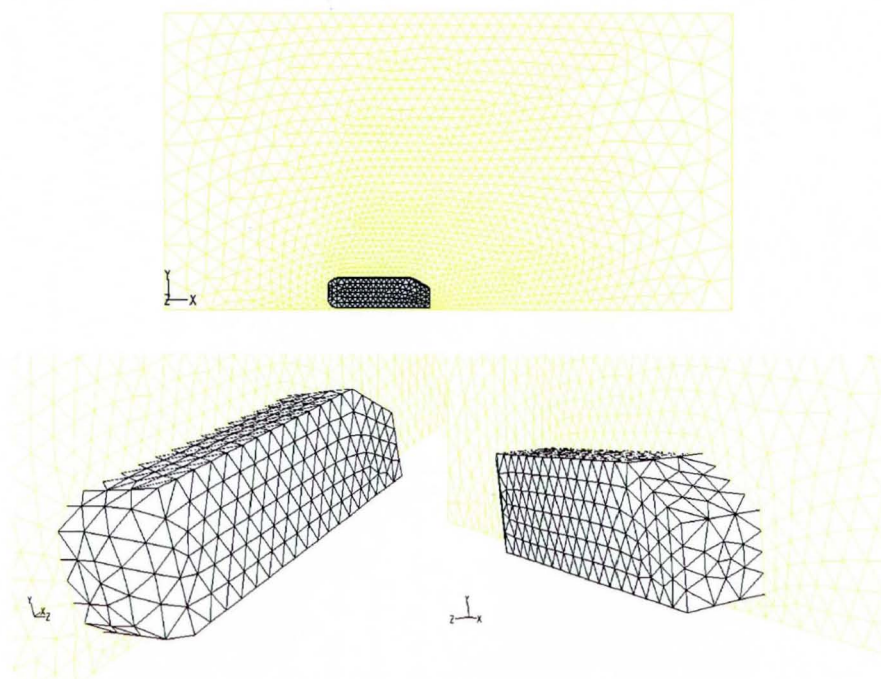


Figure 4.2: Coarse tetrahedral grid over Ahmed body

The quality of these grids is illustrated (Figure 4.3) as histograms of the skewness of the faces and cells respectively. The cell skewness quality, here, has a normal distribution. This fact demonstrates that the bulk of the cells in the domain are of good quality, with a few cells having high skewness up to a maximum of 0.75. In this case, the face quality distribution shows the majority of the faces to be close to equilateral, ruling out long thin cells. Thus, it can be surmised that there are few if any sliver cells.

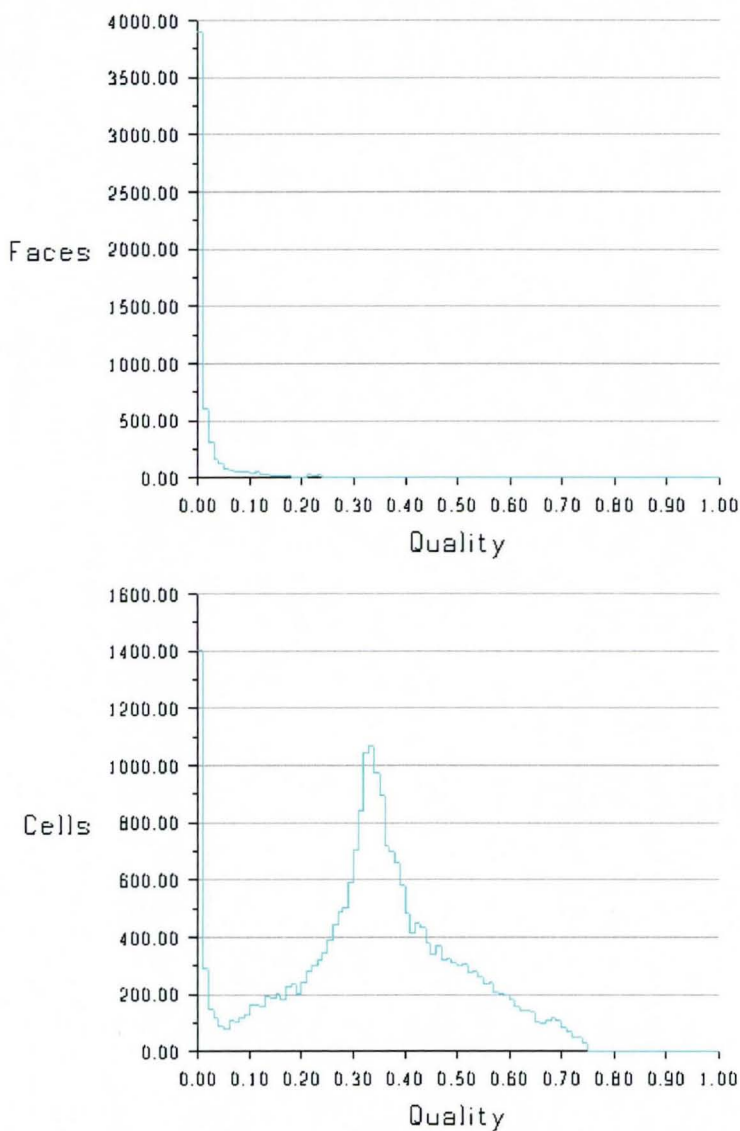


Figure 4.3: Quality of coarse tetrahedral grids

The cases were assembled using the Delaunay mesh generator outlined in the Chapter 3; the comparison of results from mesh generation packages, namely, the surface mesh

generator, *PCUBE*, and the internal mesh generator, *TGRID*. As the two types of grid generator have been compared in the initial tests chapter, and the results found to be similar, it appeared that the commercial package would allow a quicker and more efficient investigation into the effects of the mesh on the flow. The average wall y^* value on the body for this grid was 3200.

Once the grids had been generated, the boundary and initial conditions were applied using the pre-processor part of the commercial *FLUENT/UNS* program. The boundary and initial conditions for the flow problem are outlined in Table 4.2.

Table 4.2 The boundary conditions used for the Ahmed test cases.

Grid type	Tetrahedral only
Fluid material	Air @ Standard day: Density = 1.225 kg/m ³ Viscosity 1.75x10 ⁻⁵ kg/ms
Inlet	60m/s 2% inlet turbulence based on a length scale of 1.044m (body length)
Turbulence model	K-ε
Outlet	Outflow
Outer domain	Walls
Differencing scheme	1 st order upwind (unless specified)
Centre plane	Symmetry

These conditions are exactly the same as used in the initial calculations in Chapter 1 and therefore as in the experimental work. The differencing scheme and the turbulence model are also identical to those used in Chapter 1.

The force results of the first calculations are presented in Table 4.3:

Table 4.3 The drag and lift on the Ahmed body for the coarse grid results. Also shown is the breakdown of the forces into skin and pressure components.

angle	Pressure drag	Skin Drag	Total drag	Pressure lift	Skin lift	total lift
20	79.18	7.06	86.24	34.24	0.08	34.32
25	76.94	6.90	83.84	40.40	-0.03	40.37
30	75.78	6.78	82.56	51.32	-0.02	51.30
35	82.11	7.16	89.27	69.77	-0.08	69.68
40	79.18	6.92	86.09	44.17	0.04	44.21
45	82.62	6.55	89.18	36.90	0.14	37.04
50	85.95	6.78	92.73	42.59	0.00	42.59

The comparison of the total drag levels to those of the experimental work is graphically represented in Figure 4.4. The results show no similarity to the results from the experimental values seen in either the Ahmed results [2] or the MIRA work [22]. The general levels of the forces are too great, being double those expected, furthermore the results demonstrate no drop in drag at the critical angle of 30°-35°, whereas the wind tunnel results show a large one. It is in this range of angles in the wind tunnel results where the flow in the wake of the body changes, which gives rise to the reduction in the drag. It is also noteworthy that the drag levels of these coarse tetrahedral calculations are similar in level to the drag results from the structured grid predictions, the results of which were presented in chapter 1.

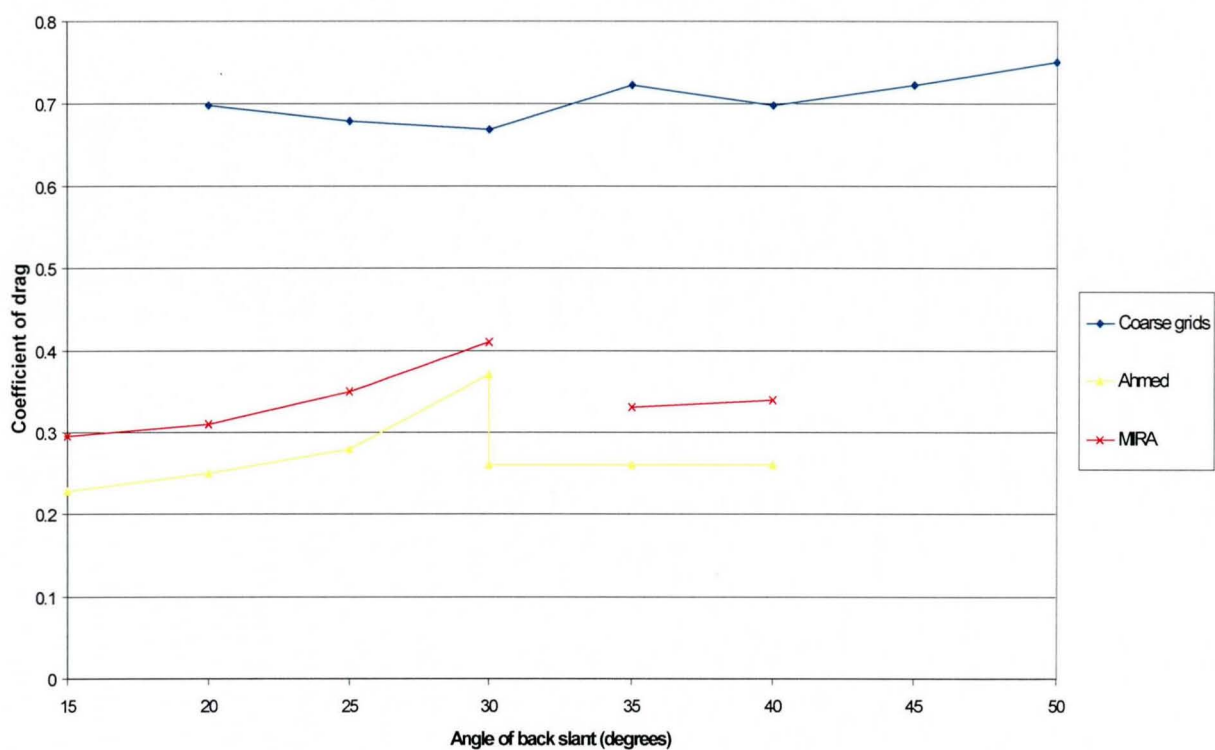


Figure 4.4: Comparison of drag force versus back slant angle for coarse tetrahedral grids. Also shown are the experimental values for MIRA and Ahmed results.

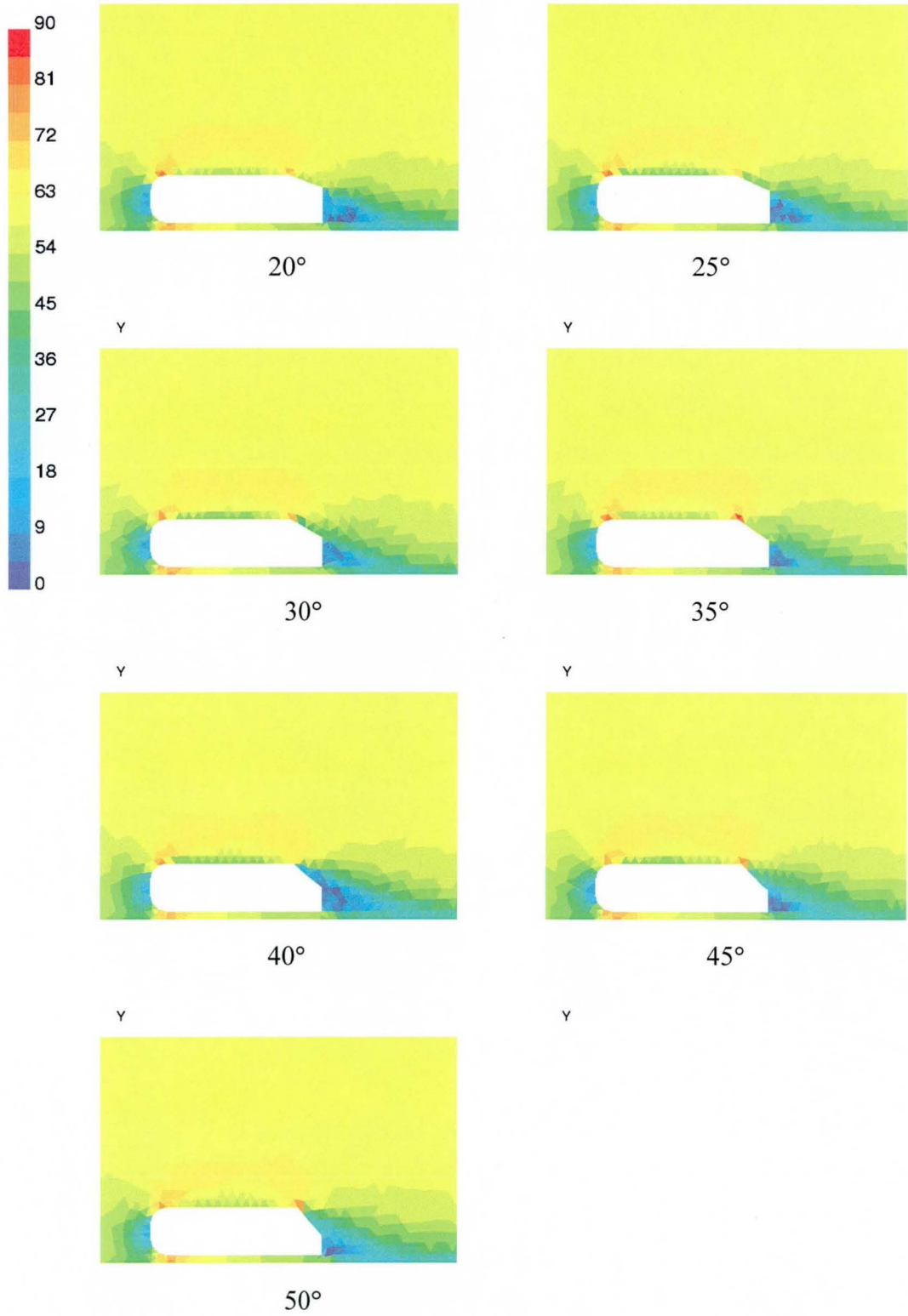


Figure 4.5 The contours of velocity (m/s) on the symmetry plane

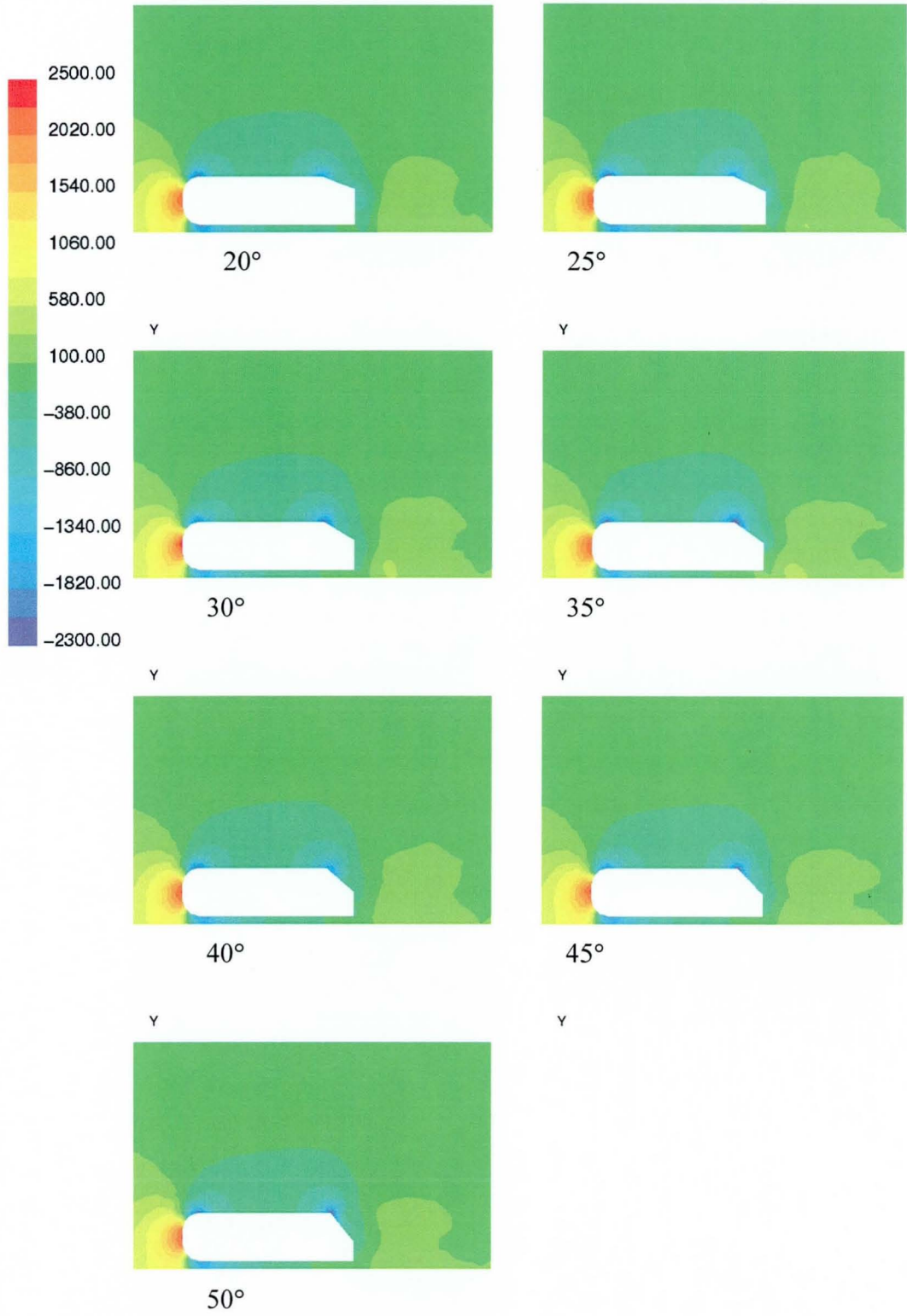


Figure 4.6 The contours of static pressure (Pa) on the symmetry plane.

The velocity and pressure contour plots in Figure 4.5 and Figure 4.6 clearly show the inability of this grid to pick up the expected flow pattern behind the body. There is no sign of the complex twin vortices behind the body. This can be mainly attributed to the lack of resolution in that region.

As is evident from these two sets of plots, the flow remains attached to the surface over the top/slant edge for all flow angles. What happens further along the slant surface is dependant on the angle of the slant surface. The drop in static pressure over this corner is similar for all angles of the backlight. The flow in the 20°, 25°, 30° and 35° cases then continues along the slant surface remaining attached until the sharp corner at the very rear of the body, where it separates and does not re-attach. The flow in the 40°, 45°, 50° cases separates somewhere along the slant surface after (but not immediately) the top/slant edge, again without re-attaching. The separation point moves progressively up the slant surface as the angle of slant surface is increased. The separation from the top/slant edge and subsequent re-attachment to the slant surface, seen in the wind tunnel experiments at around 30°-35°, is not reflected in the CFD results. This type of separation should be accompanied by a lower magnitude of pressure trough over the top/slant edge as the flow no longer has to accelerate around the edge.

The second set of plots (Figure 4.6) illustrates the large increase in static pressure on the front of the body. In addition, the plots for 20° to 35° of back slant surface demonstrate the increasing drop in static pressure over the top/slant edge as the angle increases. After this as the slant surface angle is increased further the static pressure decreases (40°) and then increases again (45°). This suggests that the flows for these higher angles of slant surface are not a true reflection of the physics of the problem.

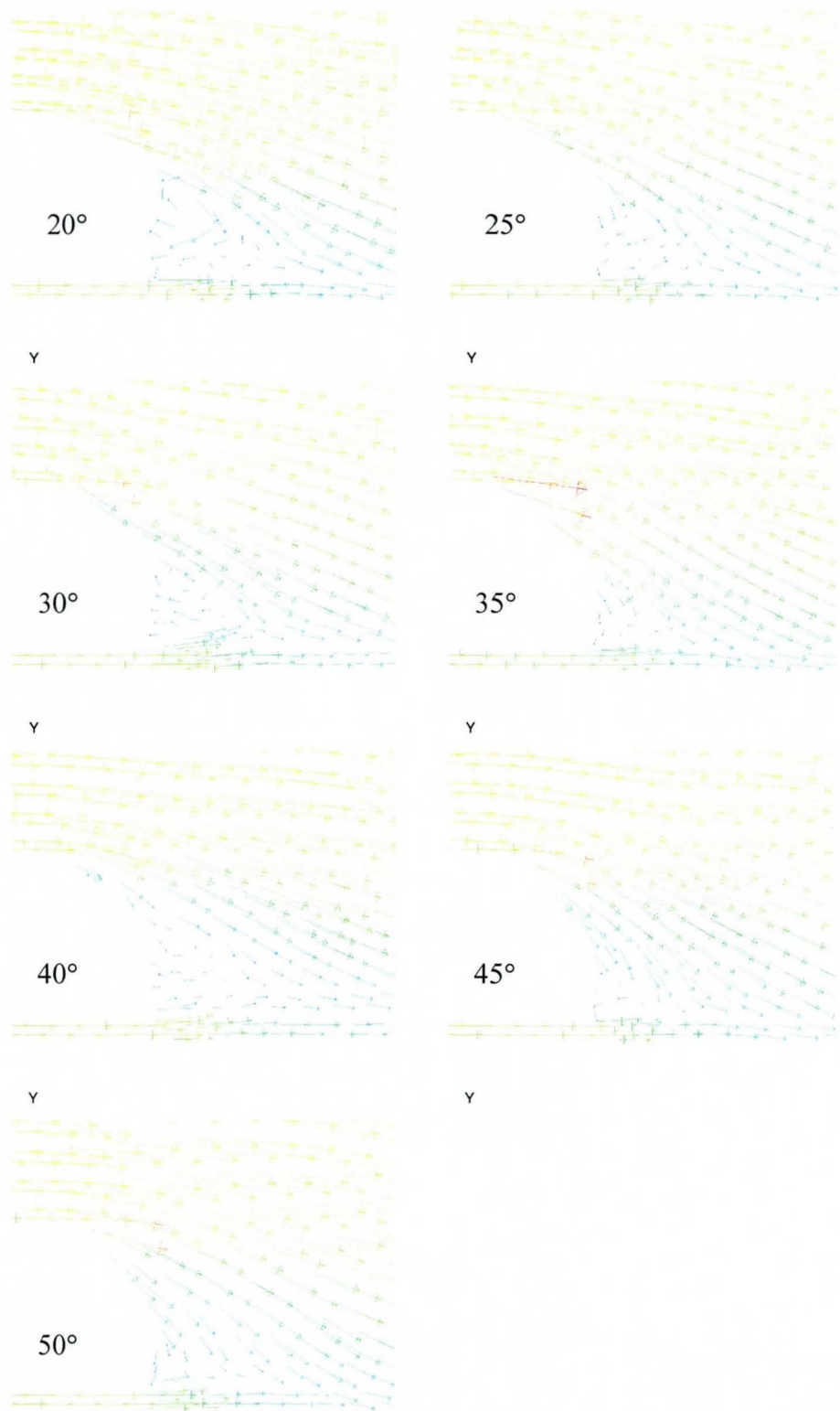
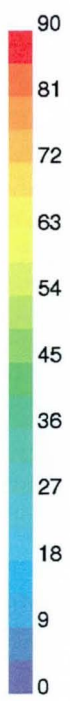


Figure 4.7 The streaklines on the symmetry plane coloured by velocity magnitude (m/s).

The plots of velocity vectors over the top/slant edge coloured by velocity magnitude (Figure 4.7) illustrate more clearly what is happening on the slant surface. For the lower angles (less than 40°) the flow remains attached to the surface over the top/slant edge. For slant surface angles of around 40° , the flow separates, however, only after being forced around the edge. The flow separates due to the adverse pressure gradient that exists on the slant surface. For slant surface angles higher than 40° , the flow is, again, forced over the edge. However, it does not appear to separate due to the pressure gradient. This can be attributed to the increased pressure drop over the top/slant edge that will, in turn, reduce the pressure gradient along the slant surface (See Figure 4.6).

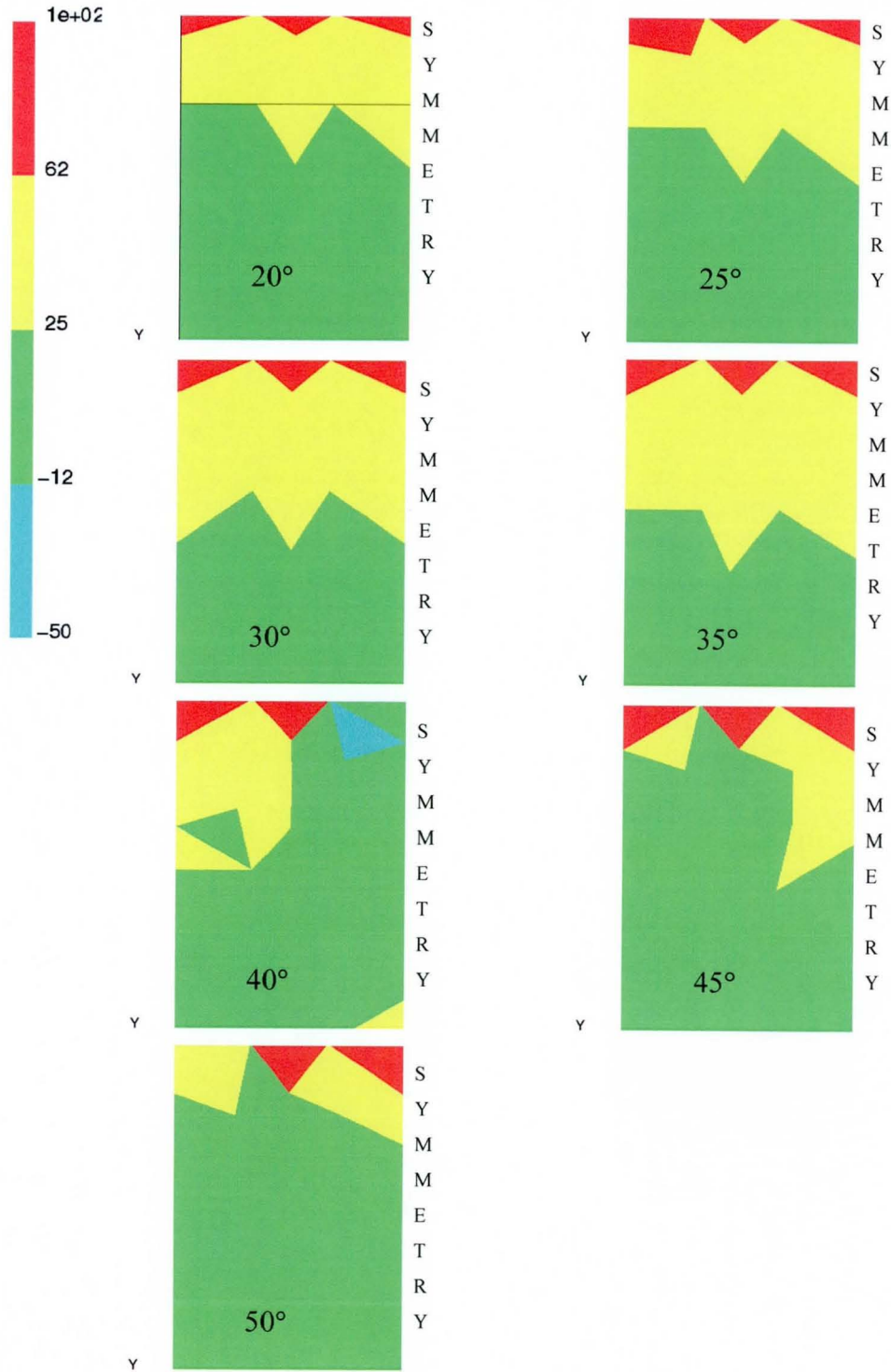


Figure 4.8 The contours of velocity on the slant and rear surfaces of the body, reduced to 4 levels so as to give an impression of separation on the body. The symmetry plane is on the right side.

Figure 4.8 shows the contours of x-velocity on the rear of the body. There are only four contours spanning a large range in order to highlight where the flow reverses on the slant and back surfaces of the body. As Figure 4.8 demonstrates, the flow is not separating in the 20°, 25°, 30° and 35° cases. The 40° case separates from just after the top slant edge on the symmetry plane. Further from the symmetry plane the flow remains attached. This is similar to the flow witnessed for the slant surface angle around 30° in the experimental data although, in that case, the flow separated at exactly the top/slant corner on the symmetry plane. Subsequently, in the 45° and 50° cases, the flow appears to separate close to, but not at, the top/slant edge and does not reattach. This, in addition to the rest of the evidence, leads to the conclusion that the flow is separated over the majority of the slant surface, yet the bulk flow movement after the top/slant edge is down wards parallel to the slant surface. This bears little similarity to the anticipated flow field.

In order to explain the flow behind the body the plots of velocity vectors and static pressure contours are taken at 0.5m after the x position of the nose of the body. These plots are pictured in Figure 4.9, Figure 4.10 and Figure 4.11.

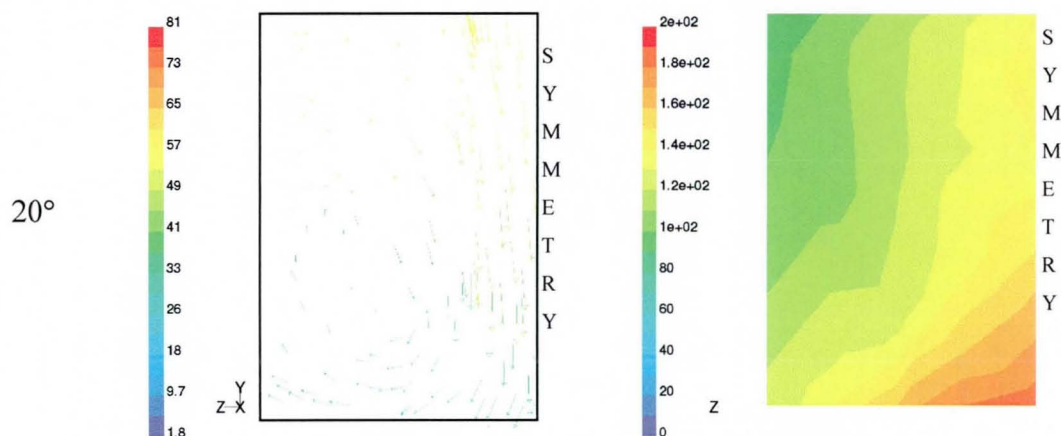


Figure 4.9 The velocity vectors (coloured by velocity) on the left and static pressure contours on the right for the plane $x = 0.5m$ (body is 0 to 1.044m). 20°.

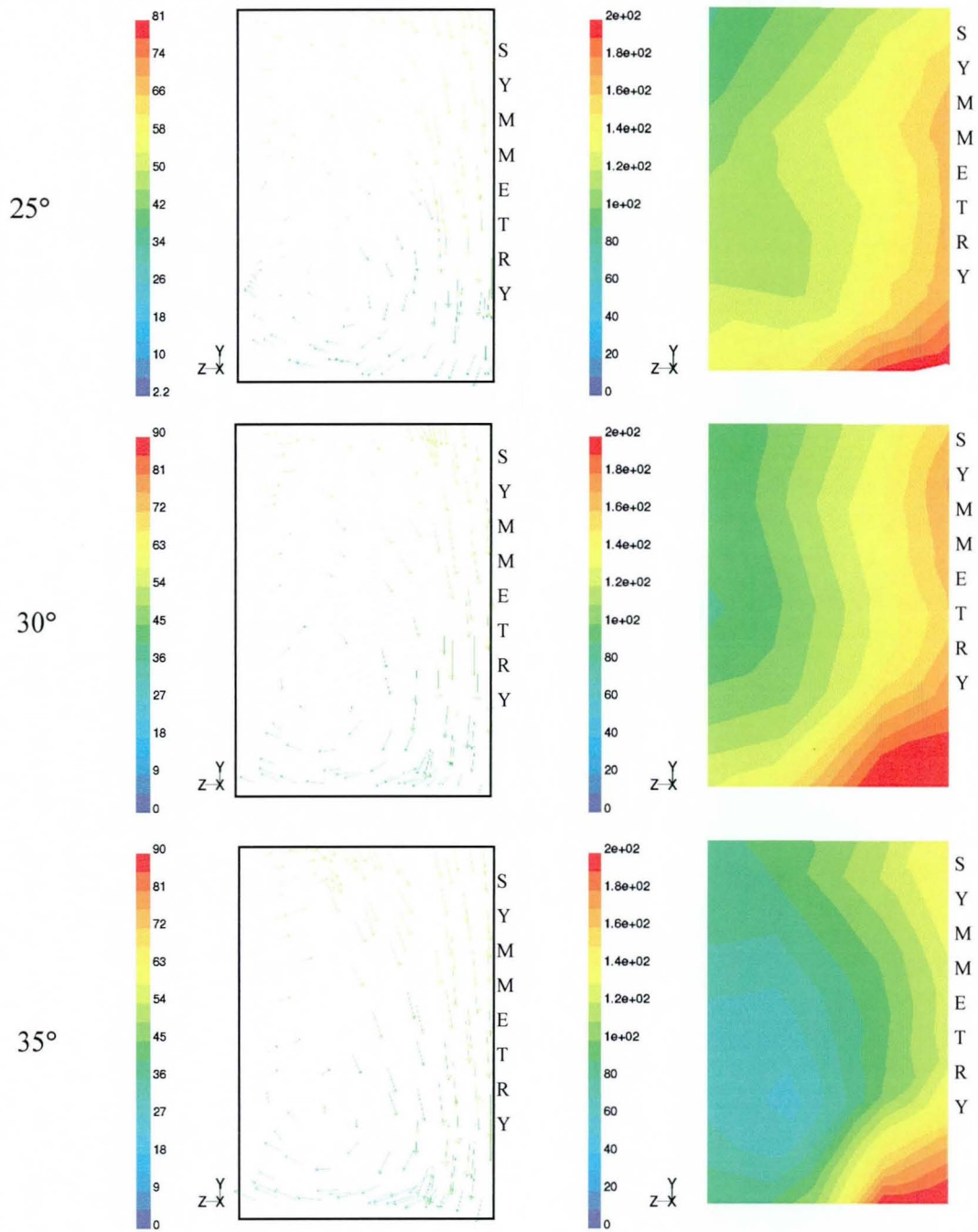


Figure 4.10 The velocity vectors (coloured by velocity) on the left and static pressure contours on the right for the plane $x = 0.5\text{m}$ (body is 0 to 1.044m). 25° to 35° .

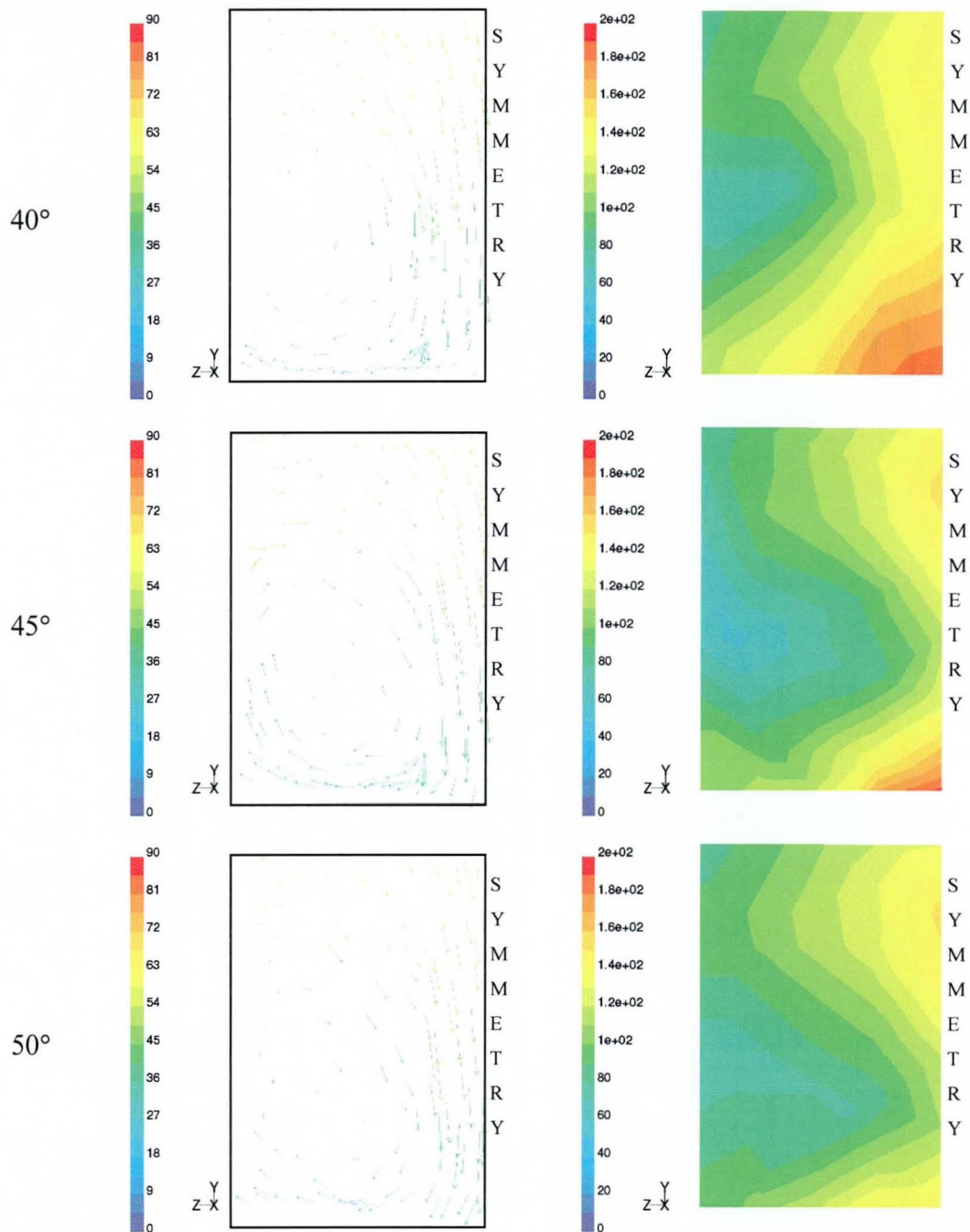


Figure 4.11 The velocity vectors (coloured by velocity) on the left and static pressure contours on the right for the plane $x = 0.5m$ (body is 0 to 1.044m). 40° to 50° .

Figure 4.9, Figure 4.10 and Figure 4.11 illustrate two factors: firstly, the increasing intensity of the counter-rotating vortices after the body and, secondly, the development of the down-wash. The lower angles (20° - 35°) show recognisable

counter-rotating vortices in the velocity vector plots, whilst the static pressure contours suggest there to be no obvious low-pressure centre to the vortices. This suggests that they are very weak. As the angle increases the magnitude of the velocity vectors in the vortex increases slightly and the rotation appears to “tighten” to a centre. Indeed, the static pressure contours show a low-pressure region in the centre of rotation. As the angle increases further the centre of rotation seems to move inwards, towards the symmetry plane and downwards slightly. This is consistent with the experimental data.

The graphs in Figure 4.12 and Figure 4.13 show the plots of static pressure on the upper and lower surfaces of the Ahmed body centerline. The upper surface plot depicts the rise, and then drop, in static pressure, as the flow first stagnates on the nose of the body and subsequently accelerates towards the top. The flow remains attached over the length of the top surface, before flowing over the top/slant edge. In all cases, here, the flow remains attached until the slant/rear edge. The flow does not separate as mentioned above. Evidence supporting non-separation can also be identified in the large drop in static pressure as the flow goes over the top/slant edge. The flow on the underside, again, produces the increase and decrease in the static pressure over the nose followed by a gradual increase in static pressure. This increase is attributable to the flow decelerating in the axial direction, as more flow is slowed by the interaction with the non-moving ground.

Clearly, the levels of diffusion caused by the low accuracy of the large cells over the body are greatly influencing the flow field, and in this sense the unstructured mesh results are similar to the structured results presented earlier.

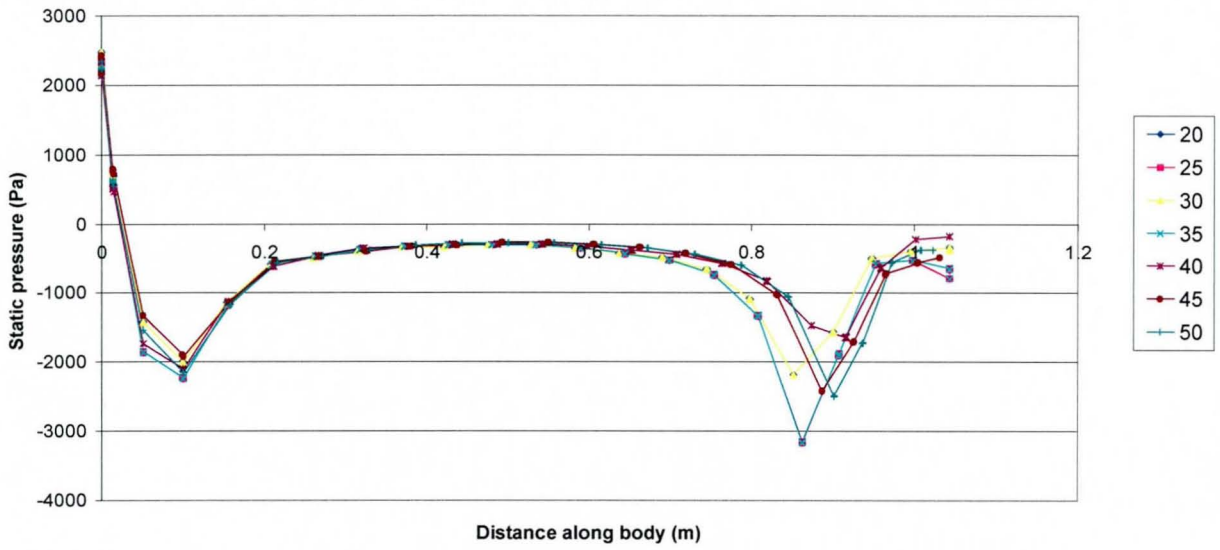


Figure 4.12 The plot of static pressure on the upper surface centre line of the Ahmed body for the coarse grids.

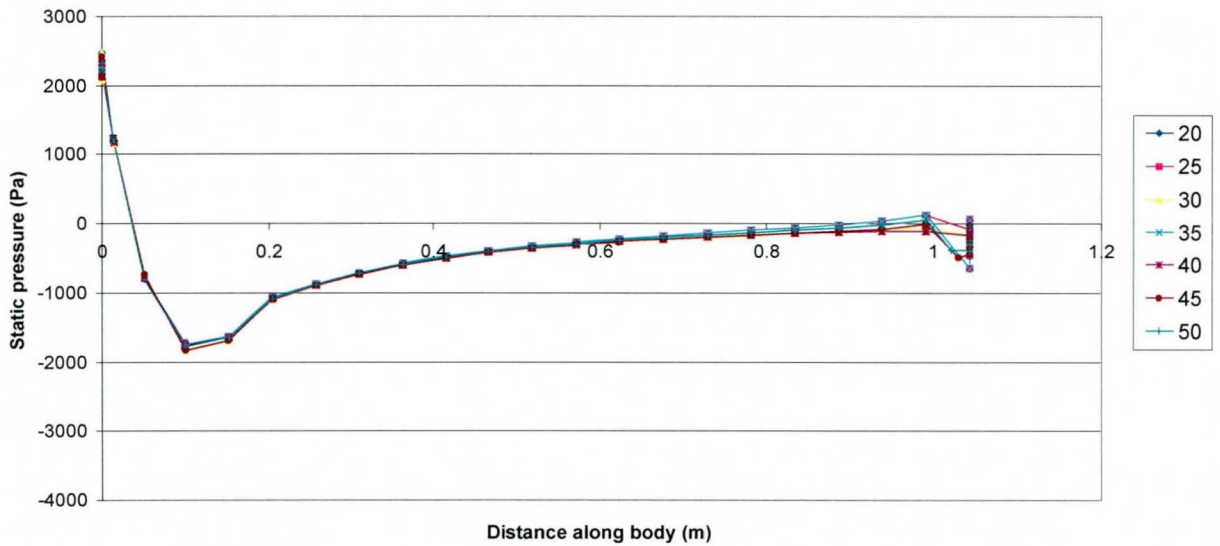


Figure 4.13 The plot of static pressure on the lower surface centre line of the Ahmed body for the coarse grids.

4.3 Fine Grid Results

The coarse grid results implied that the flow over the Ahmed body is not being resolved accurately. This was suggested by two factors. Firstly, by the bulk motion of the flow behind the body following the slant surface; and secondly, by the static pressure drop over the top/slant edge being fairly constant for all angles of that surface. Increasing the grid density should help increase the accuracy of the results and improve the prediction and resolution of the flow-field. The grid sizes for the coarse and fine grids, Table 4.4, illustrate the increased number of nodes, faces and cells for the fine grids. The discrepancy in the number of cells between the fine grids in the unstructured grids (114,000) and the structured grids from Chapter 1 (350,000) is due to the more efficient cell placement of the unstructured mesh generator. As described in Chapter 1, the structured grid is wasteful of cells in the far-field. A better measure of the grid density is possibly the density of the surface grid on the Ahmed body. These are comparable for the medium grids from Chapter 1 and the fine grids presented here. The average body surface wall y^* value for this grid was 1560.

Table 4.4 The grid sizes for the coarse and fine grids.

	Coarse grids	Fine grids
Cells	24469	113290
Faces	46083	215761
Nodes	2727	13732

The plots of velocity magnitude contours (Figure 4.14) indicate the basic flow pattern over the symmetry plane of the car. For all the cases, the majority of the flow field is independent of the slant surface angle. The similarities include the stagnation point and the subsequent increase in the velocity as the flow accelerates around the nose of the body. As is evident from Figure 4.14, for the lower angle cases (20°, 25°, 30° and 35°), the flow over the back slant remains attached all along its length. For the slant surface angles above this, the flow separates at some point along the slant surface (after the top/slant edge).

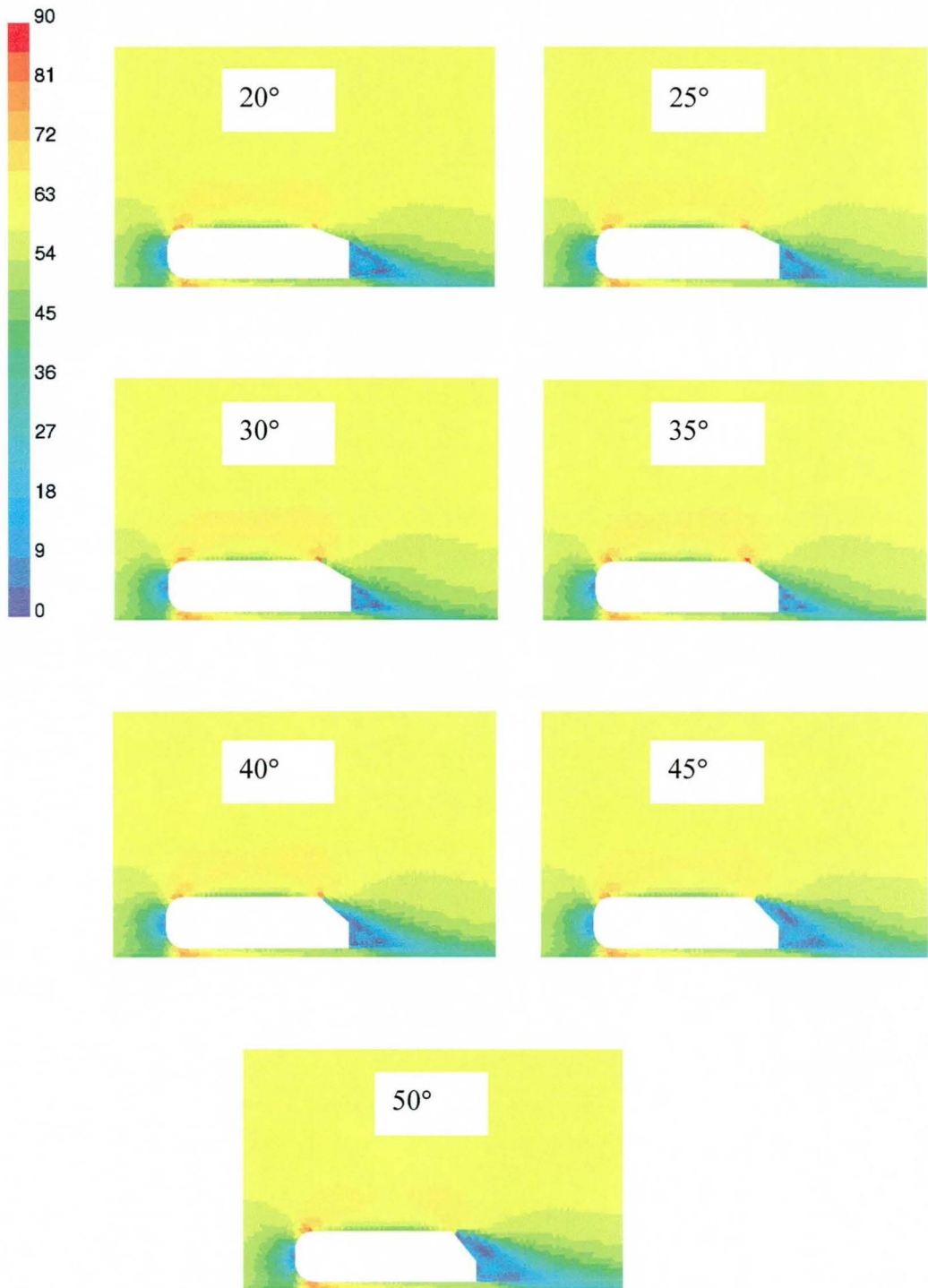


Figure 4.14 The contours of velocity magnitude (m/s) on the symmetry plane of the fine grid over the Ahmed body for the 20°, 25°, 30°, 35°, 40°, 45° and 50° cases.

The velocity magnitude plots are insufficient to fully analyse the flow (as seen in the above coarse grid cases). The plots of static pressure on the symmetry highlight (see Figure 4.15) the most important feature, with respect to the flow over the slant surface, is the drop in pressure over the top/slant edge. As noted in the previous section, if this pressure is low it indicates an acceleration around this edge. If this acceleration is large enough, the flow will remain attached to the slant surface, or at least, the upper part of it. The plots shown for the fine grids indicate that the low-pressure increases in magnitude from 20° to 35° , and then decreases (the pressure rises again). It can, thus, be deduced that the flow is not accelerating as strongly around this edge as the angle increases. That is to say, the flow may be more inclined to separate.

The actual nature of these re-circulations can be seen in the plots of velocity streaklines coloured by velocity magnitude on the symmetry plane of the body in Figure 4.16. These plots are limited to the rear portions of the body where the major differences occur in the solutions.

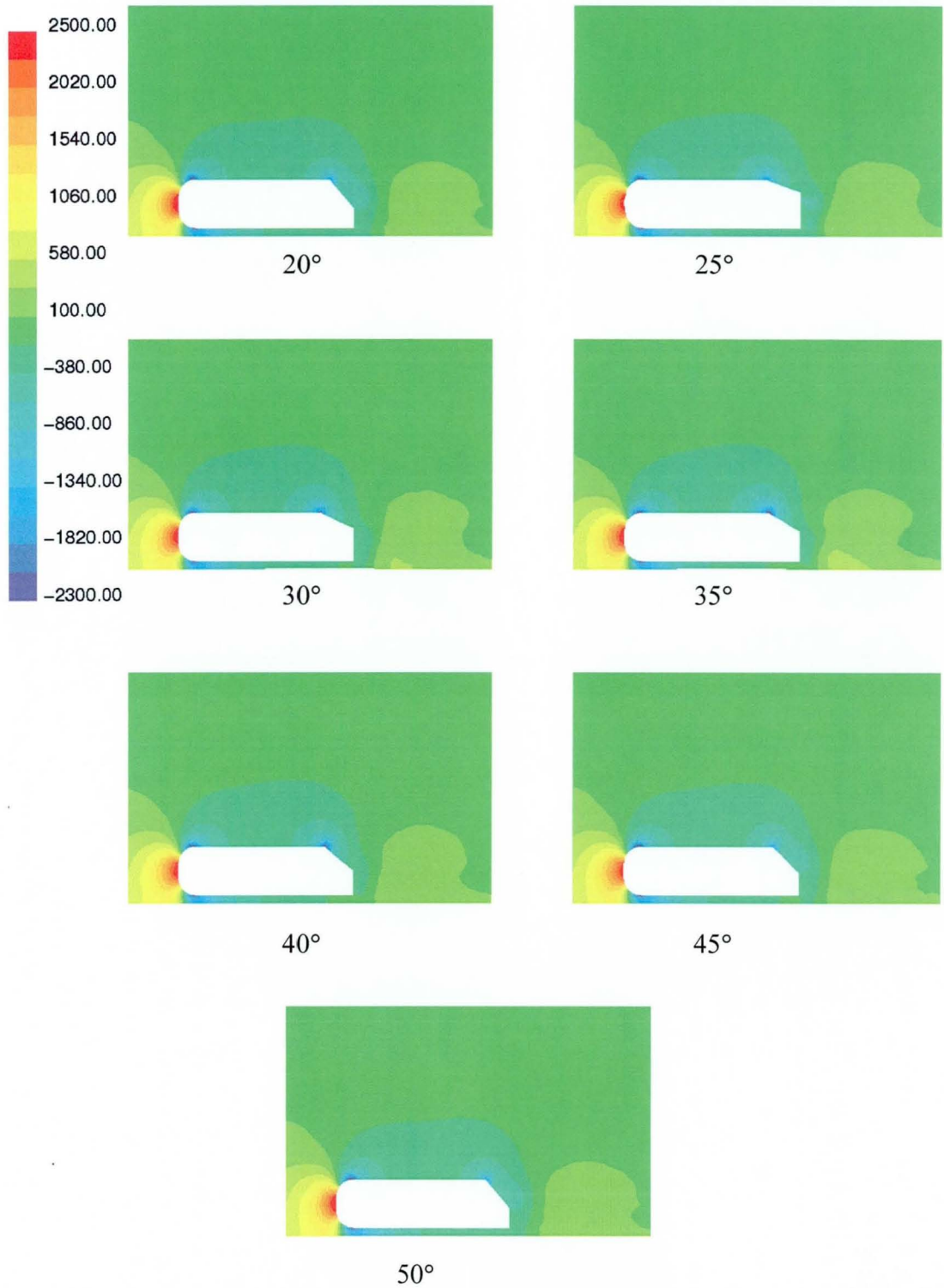


Figure 4.15 The contours of static pressure (Pa) on the symmetry plane of the Ahmed body.

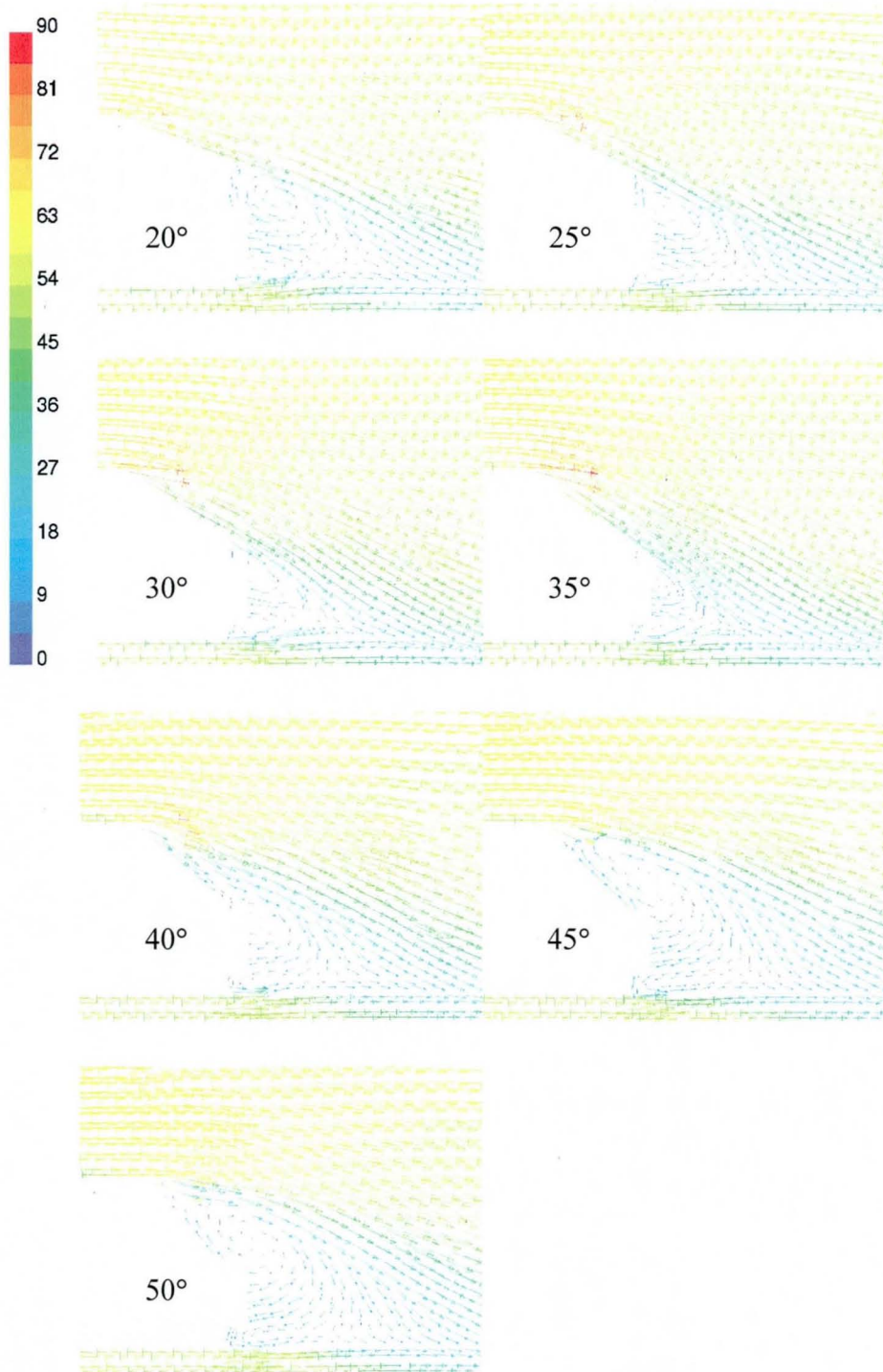


Figure 4.16 The velocity vectors (m/s) on the symmetry plane of the Ahmed body for the fine grid calculations.

For the first four back slant angles (20° , 25° , 30° and 35°), the flow can be seen to follow the shape of the body until the slant/rear edge, with a pair of lateral vortices

formed behind the base surface. This vortex pair is the symmetry plane slice through the horseshoe ring vortices that are discussed in the experimental work by Ahmed [2]. As the angle of slant surface increases, the upper vortex becomes dominant over the lower.

The case with the 40° angle of back slant shows the flow separating on the slant surface after the flow has gone over the top/slant edge. After the edge, the adverse pressure gradient on the slant surface slows the flow sufficiently for it to separate. The twin vortex structure mentioned above now develops into a larger structure, still containing two counter-rotating lateral vortices, however, with the upper vortex now much greater in strength. The flow in the 45° and 50° cases appears to have separated abruptly from the top/slant edge. However, further examination reveals that this is not the case. Closer examination shows that the flow is turning downwards after the edge. There is also evidence that the flow is subject to a general down wash after the body; that is, the wake is closing early. Further evidence to suggest that the structure of this separation is incorrect will be discussed later.

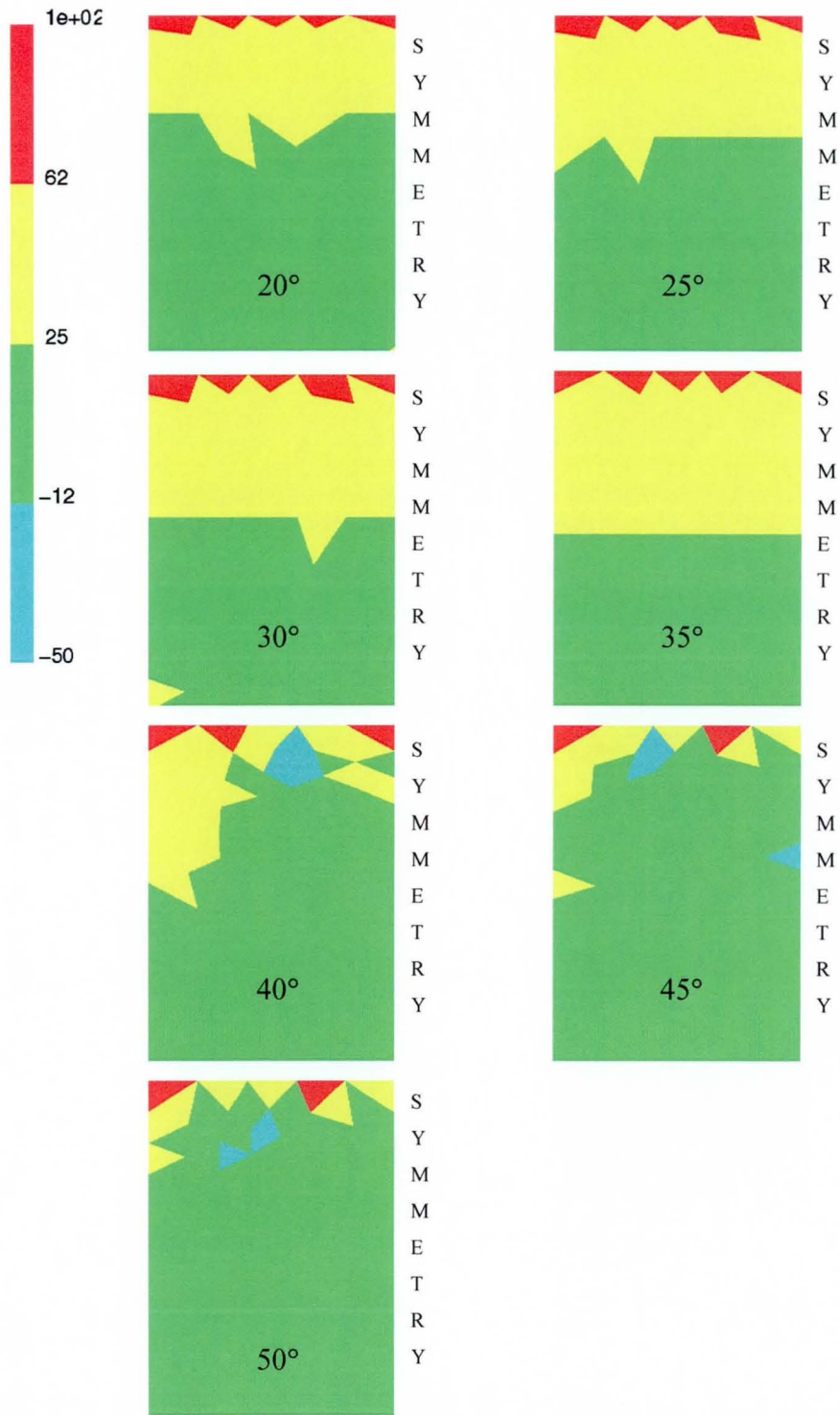


Figure 4.17 The contours of x velocity (m/s) on the slant and rear surfaces of the Ahmed body for the 25 to 50 back slant cases. The number of contours is reduced for clarity.

The flow on the surface of the slant and base surfaces of the body (Figure 4.17) indicates the nature of the separation there. For the 20°, 25°, 30° and 35° cases, the flow can be seen to come off the top edge at above 60m/s and to follow the shape of the body until the end of the slant surface, where it separates cleanly. The flow, in the 40° case, is attached on the outer edge of the body slant surface, where the flows coming from the side and top mix to produce the counter-rotating longitudinal vortices. These vortices were already present but are increased in strength, as the angle of slant surface is raised, due to the increased down wash. On the symmetry plane, the flow is attached as it comes over the top/slant edge and separates just afterwards. It remains separated over the rest of the rear of the body exhibiting no inclination to re-attach as in the high drag flow field witnessed in the wind tunnel results. In the 45° case, this behavior is exaggerated with the flow only just remaining attached on the outer edge of the body slant surface. In the 50° case, the flow may be attached for only the upper part of the outer edge of the slant surface. The most important feature of these plots, for the 40°, 45° and 50° slant surface angles, is that they show that none of these cases separates completely from the top/slant edge. This type of sharp edged body should produce almost immediate separation from the edge, if not for small angles of surface change, then certainly as the angle increases.

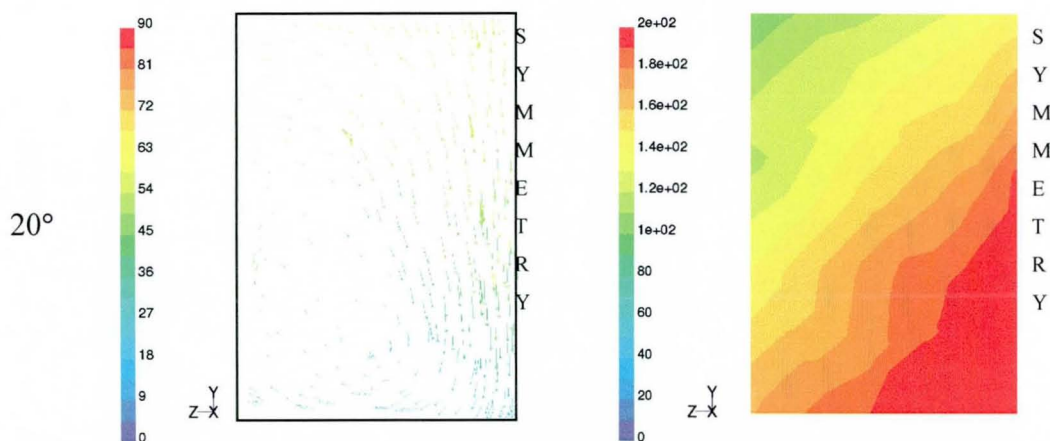


Figure 4.18 The combined plots of in plane velocity vectors (coloured by velocity magnitude, m/s) with the contours of static pressure (Pa). Both are situated 0.5m down stream of the start of the body. 20°.

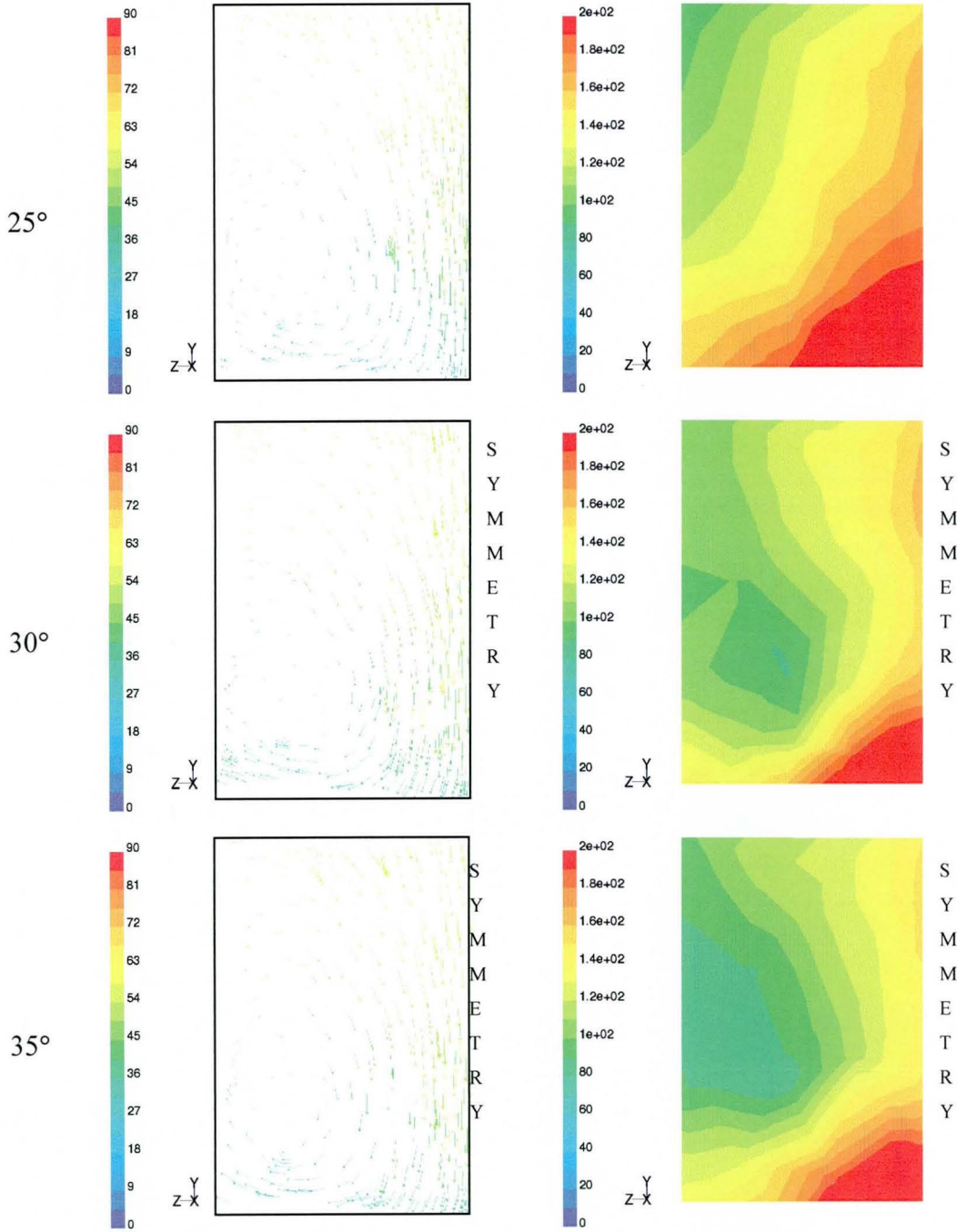


Figure 4.19 The combined plots of in plane velocity vectors (coloured by velocity magnitude, m/s) with the contours of static pressure (Pa). Both are situated 0.5m down stream of the start of the body. 25° to 35°.

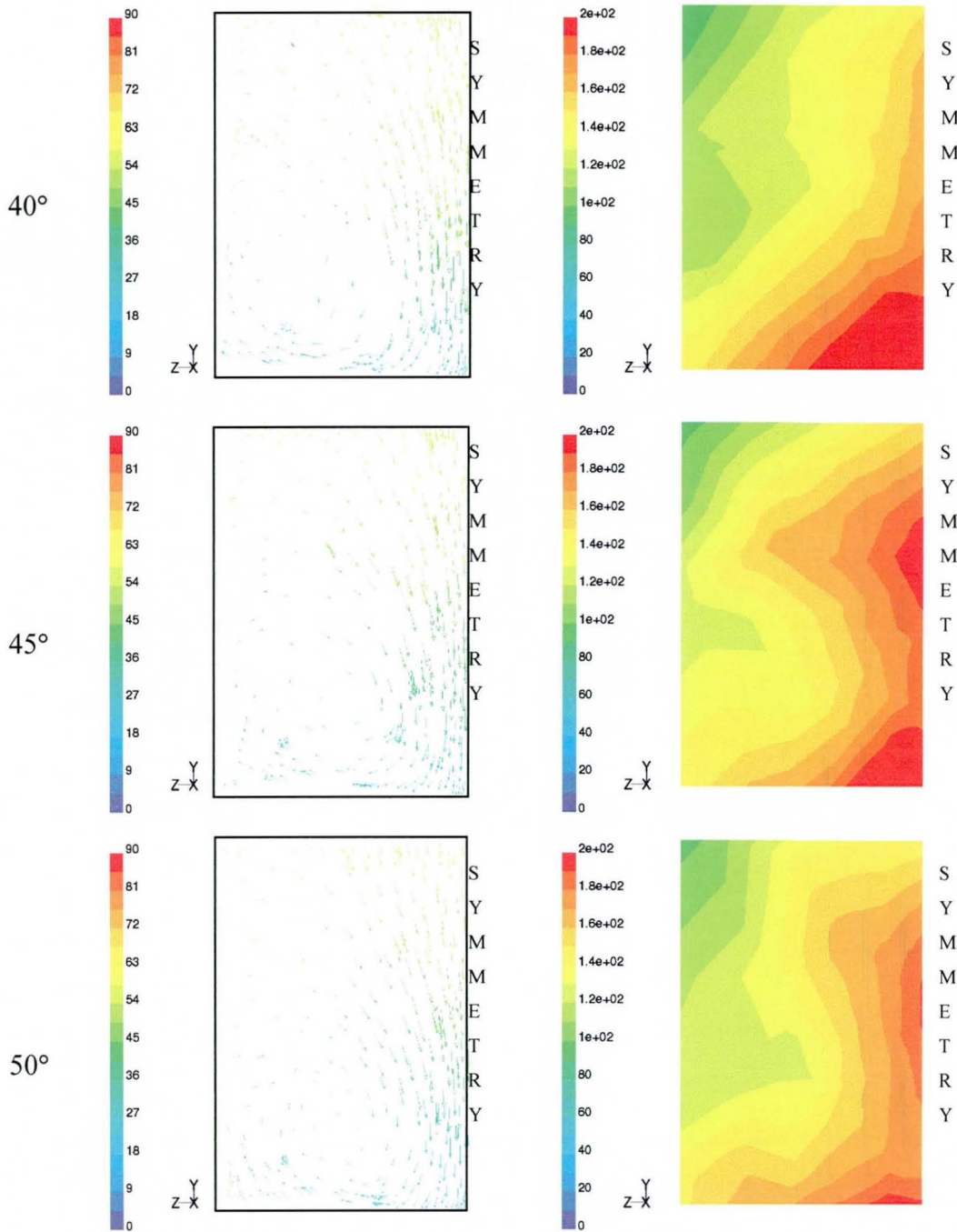


Figure 4.20 The combined plots of in plane velocity vectors (coloured by velocity magnitude, m/s) with the contours of static pressure (Pa). Both are situated 0.5m down stream of the start of the body. 40° to 50°.

Figure 4.18, Figure 4.19 and Figure 4.20 illustrate the in-plane velocity vectors (coloured by velocity magnitude) and the static pressure on the plane, 0.5m behind the

start of the body. As with the coarse grid calculations, these demonstrate the increasing intensity of the counter-rotating longitudinal vortex up to the 35° case. After the 40° case, the strength of this vortex appears to weaken, supporting the evidence that the flow has either separated, or partially separated, from the rear slant surface of the body.

The plot of static pressure distribution on the body centerline upper surface (Figure 4.21) clearly shows the problem with the separation point for these cases. The pressure peak and trough at the front of the body are as expected. However, at the rear, the pressure distributions do not correspond to the expected trends. The cases up to and including 35°, show an increasing pressure drop as the flow follows the shape of the top/slant edge. The cases above that (40°, 45°, and 50°) show a decrease in the depth of that trough, signaling a lower pressure being required to force the flow over the top/slant edge. This would appear incorrect. If the flow were attached, the pressure drop should increase (deeper trough); and if it separates, there should be no pressure drop (no trough). These results will be explained in section 4.4.

Figure 4.22 compares the drag coefficients for the two grids and the experimental values. Evidently, the drag now decreases slightly after the 35° case. This is an improvement over the coarse grid results, however, the drop is insufficient when compared to the experimental data. Furthermore, the level of drag is less, which indicates that the higher accuracy of the fine grid is better at resolving the pressure gradients of the problem than the coarse grids.

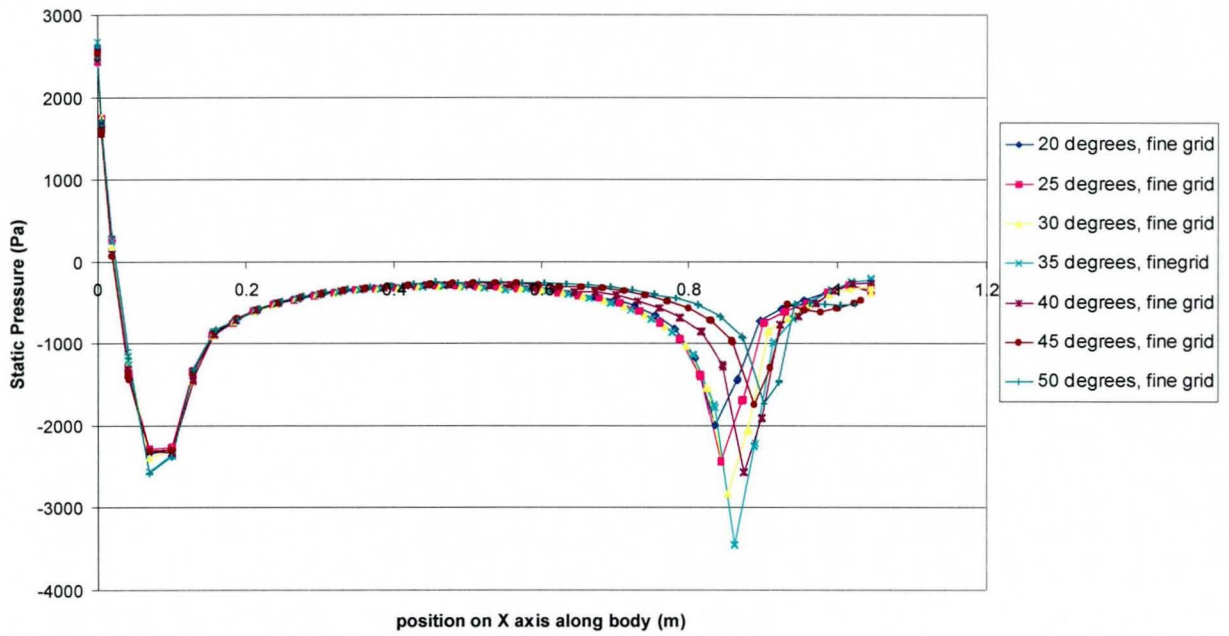


Figure 4.21 The static pressure (Pa) distribution on the centre line of the Ahmed body for the fine grid calculations.

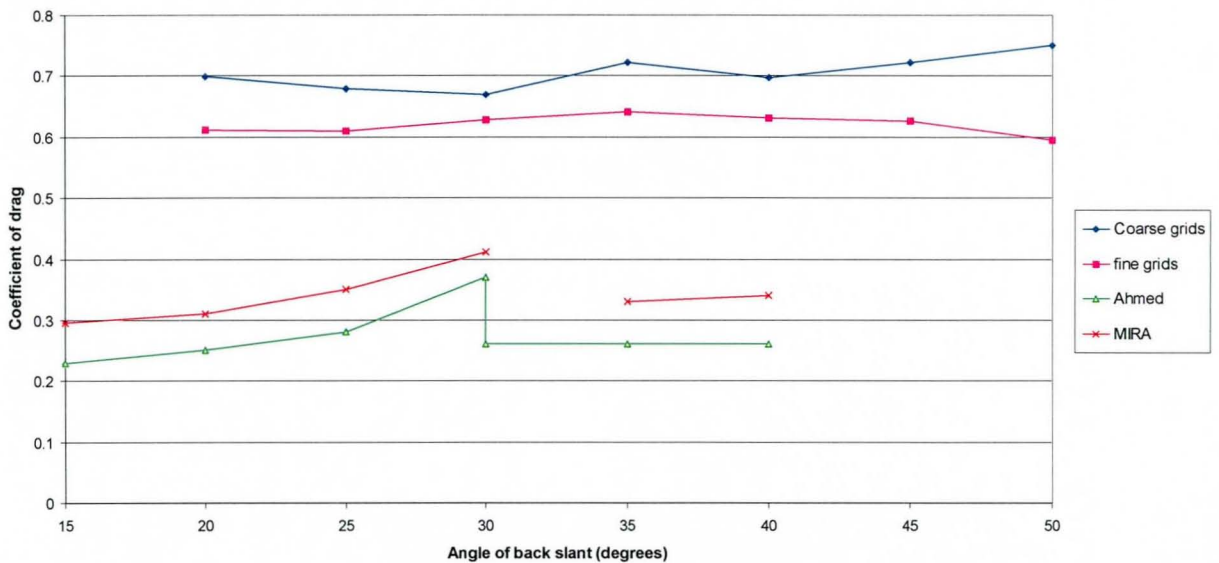


Figure 4.22 Coefficient of drag for the coarse and fine grid results on the Ahmed body.

4.4 Alternative Fine Grid Calculations

Section 4.3 suggested that the fine grids are inaccurate when attempting to resolve the high gradients of pressure seen over the body. One possibility is that too much of the axial flow over the top/slant edge is being artificially forced around the corner by the topology of the grid in that region. This is explained in diagrammatic form in Figure 4.23.

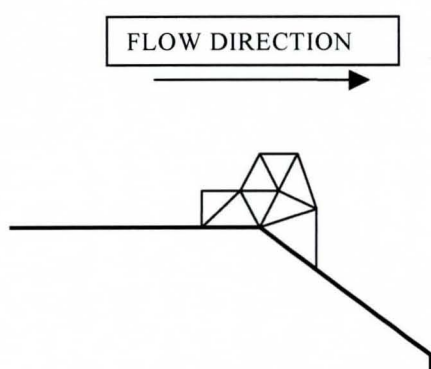


Figure 4.23 The diversion of axial momentum by the coarse grid

The diagram shows the topology of the grid at the junction between the top and slant surfaces at the rear of the Ahmed body. This type of topology was also seen in the initial calculations in the introduction. By referring to Figure 4.2, it can be seen that this topology is implemented in the initial grids. The important area is the number of cells sharing a node at the corner and the angle that any internal faces come out from it. In the case above, where there are several cells over the corner and the faces come away from the surface as shown, the following occurs. As the flow comes over the top/slant edge, some of the momentum is passed from the cell just before the edge to the one after it, via the flow through the face between them. This is not a true representation of the physics of the problem for high angles of slant surface where the flow can be expected to separate. The cell after the edge is partially behind the body and, should the flow separate at that point, a portion of the cell would be in the separated region and the rest in the free stream. For a single cell to model this "split flow" correctly is impossible. Therefore, in the separated flow regime some of the free stream momentum is passed into the first cell after the corner. This increases the pressure drop (greater negative pressure) that could be expected as the flow goes over

the slant (Figure 4.21) and thereby delays separation until a higher angle. In addition, when separation does occur in this grid, it is initiated further along the slant surface than in the wind tunnel experiments. This is due to the increased momentum in the cell just after the top/slant edge. The separation will be of the type associated with pressure gradients along curved surfaces, as opposed to the sudden separation seen in sharp edged bodies. It can be summarised that this type of grid topology will, at these grid levels, not predict the correct type of flow over the Ahmed body for the full separated ($>35^\circ$) case. This problem will occur with any level of grid refinement. However, as the grid is successively refined the resolution of the flow in this region should be able to reproduce more increasingly accurate separation at, or just after, the top/slant edge. The difference between the true separation and the CFD one at this point will diminish with increasing grid resolution, culminating in separation occurring at the same point to within the bend radius of the wind tunnel model.

With reference to the plots of static pressure distribution on the centre line upper body surface discussed in section 4.3 (Figure 4.21), it is evident how, for all angles of slant surface, there is a pressure trough over the back/slant edge. This trough is not seen in the wind tunnel results for angles greater than 30° . Indeed, after 35° , the pressure trough becomes smaller in magnitude as less of the flow goes around the top/slant edge. This pressure trough is being maintained by the flow around the top/slant edge remaining attached due to the grids influence. If the flow were to remain attached at these high angles of slant surface, the pressure trough would increase in magnitude for every increment in the angle. This type of grid dependent behaviour was also seen in the structured grid calculations.

Clearly, if this theory is correct it will remain a problem for all the grids proposed here, whilst the grid above the top/slant edge is of the type of construction seen in Figure 4.23. An alternative topology, similar to that used in the structured calculation seen at the beginning of this study is proposed later in this chapter.

4.5 Grid Modification

A test to further examine the effect of grid topology consists of altering the grid at the rear slant surface such that some of the internal faces lie in the horizontal plane directly after the corner (see Figure 4.24). Thus, if the flow should separate none of the axial momentum is artificially presented to the flow on the slant surface by the grid.

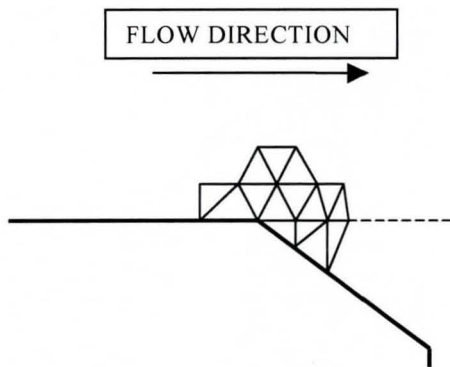


Figure 4.24 The modified grid over the rear of the Ahmed body. Altered to allow the separation of the flow to be aligned with the grid.

Applying this technique to the rear of the Ahmed body, the fine grid calculations are repeated. The results are presented below. The topology of the original and the modified grid can be seen in Figure 4.25.

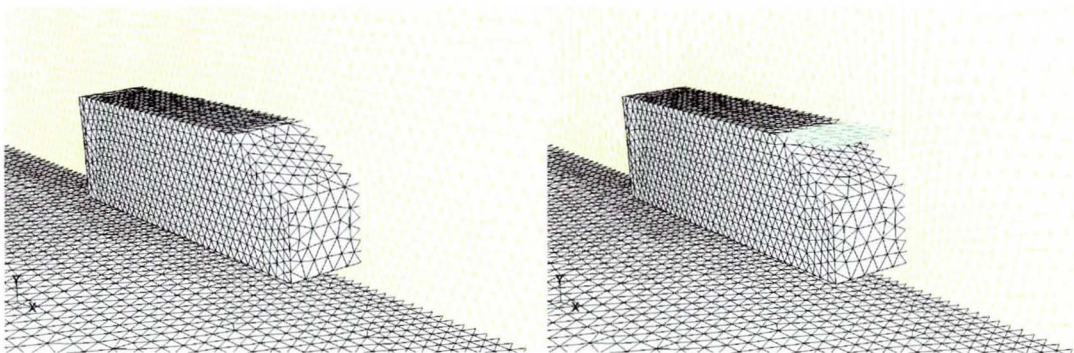


Figure 4.25 The two fine level grids. Original on the left and modified on the right. The plot of the modified grid also shows the interior plane on the back of the body that ensures the shape of the cells leaving the back/slant edge.

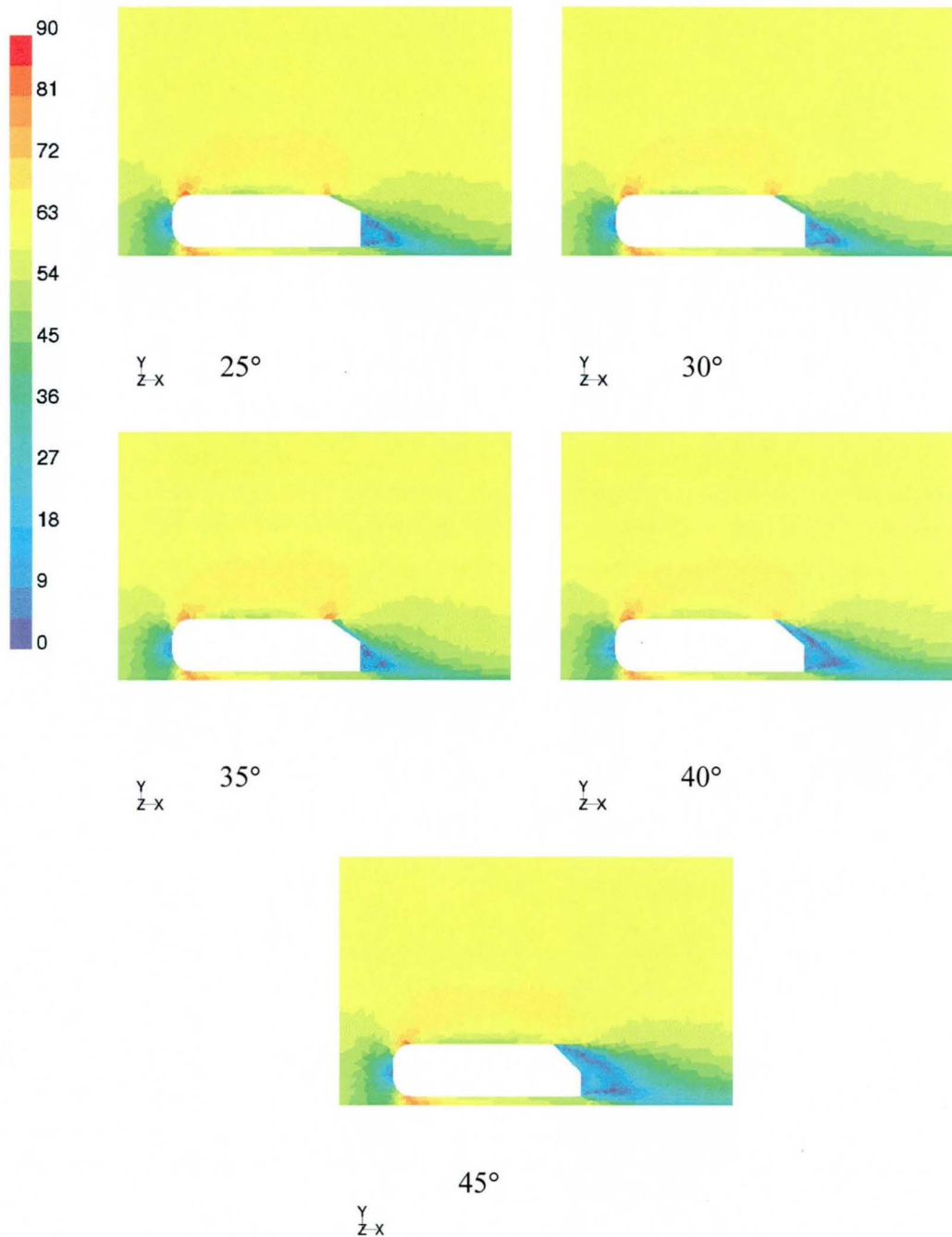


Figure 4.26 The contours of velocity magnitude (m/s) on the symmetry plane for the modified fine grid cases.

The plot of velocity magnitude contours on the symmetry plane for this type of grid on the 25°, 30°, 35°, 40° and 45° cases is shown in Figure 4.26 and can be directly compared with Figure 4.14 for the original fine grids. These show how the flow in the

25° case remains attached over the entire extent of the slant surface. The 30° and 35° cases appear slightly separated from the surface, however, they still generally follow the shape of the surface. The 40° case is separated behind the slant surface of the body. The flow is still being pulled down within half a body length of the base surface. The 45° case is much more separated than any of the cases so far seen in this chapter, with the flow clearly separating at the top/slant edge. The flow after the body is pulled downward in the wake region but not to the extent of the unmodified grid solutions.

The plots of static pressure on the symmetry plane (Figure 4.27) illustrate the development of this separation more clearly. The 25°, 30°, 35° and 40° cases all exhibit the low-pressure zone on the top/slant edge, that occurs when the flow accelerates around it. The 45° case is different. There is no low-pressure above the top/slant edge, indicating that the flow is separating cleanly at this edge, as in the experimental results.

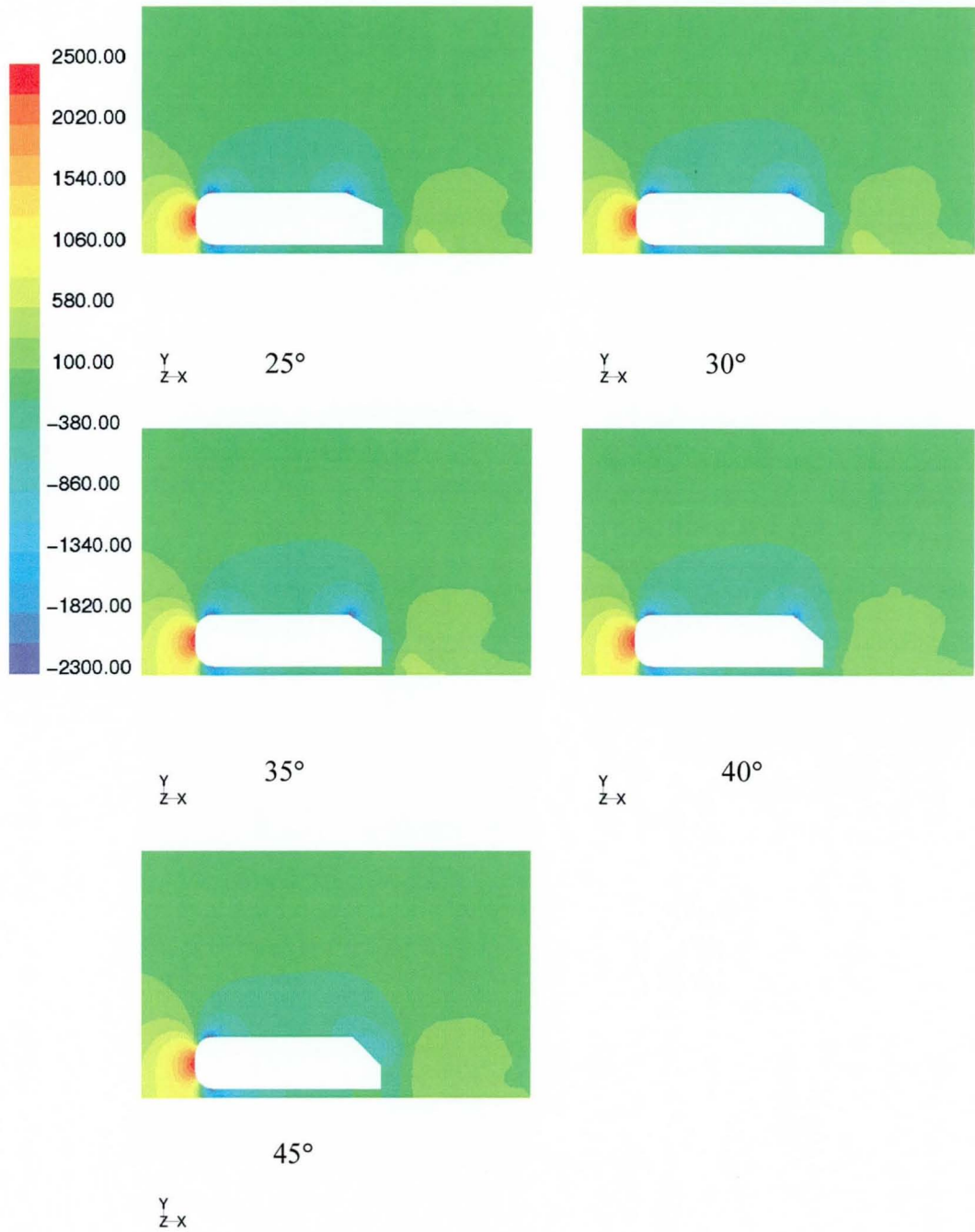


Figure 4.27 The contours of static pressure (Pa) on the symmetry plane of the modified fine grid calculations.

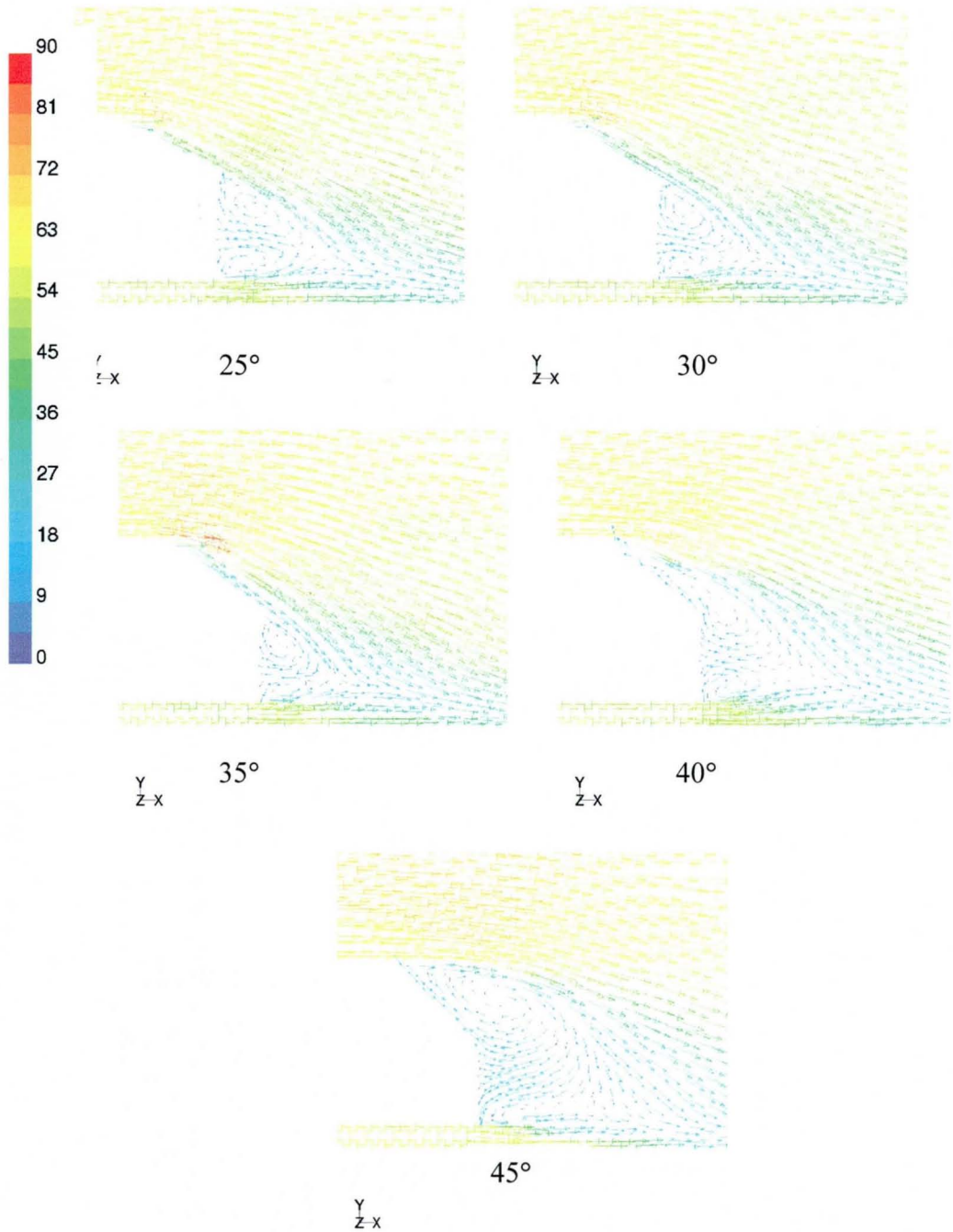


Figure 4.28 The velocity vectors on the symmetry plane of the modified grids on the Ahmed body. Coloured by the velocity magnitude (m/s)

The plots in Figure 4.28 illustrate the vortex structure behind the body developing with increasing angle of back slant. The 25°, 30° and 35° cases all demonstrate the flow to be attached until the end of the slant surface, albeit with some slowing-down

of the flow next to the surface. This can be attributed to the grid now being optimised for the separated flow regime. Consequently, the flow over the top slant edge in the attached cases is being presented to a cell that has one face perpendicular to the flow into it. This makes it very difficult for any of the momentum out of the cell to leave via this face (only possible through diffusive fluxes) and therefore down the slant surface. All these three cases demonstrate the twin vortices after the body that are the slice through the horseshoe vortex ring that follows this body (not to be confused with the counter rotating longitudinal vortex pair).

The 40° slant surface angle case in Figure 4.26, Figure 4.27 and Figure 4.28 identify the flow to be fully separated from the slant surface. The upper part of the after body horseshoe vortex merging with the recirculation on the slant surface. In the 45° case, this merging is complete, leaving a large vortex on the slant surface and a smaller one below this.

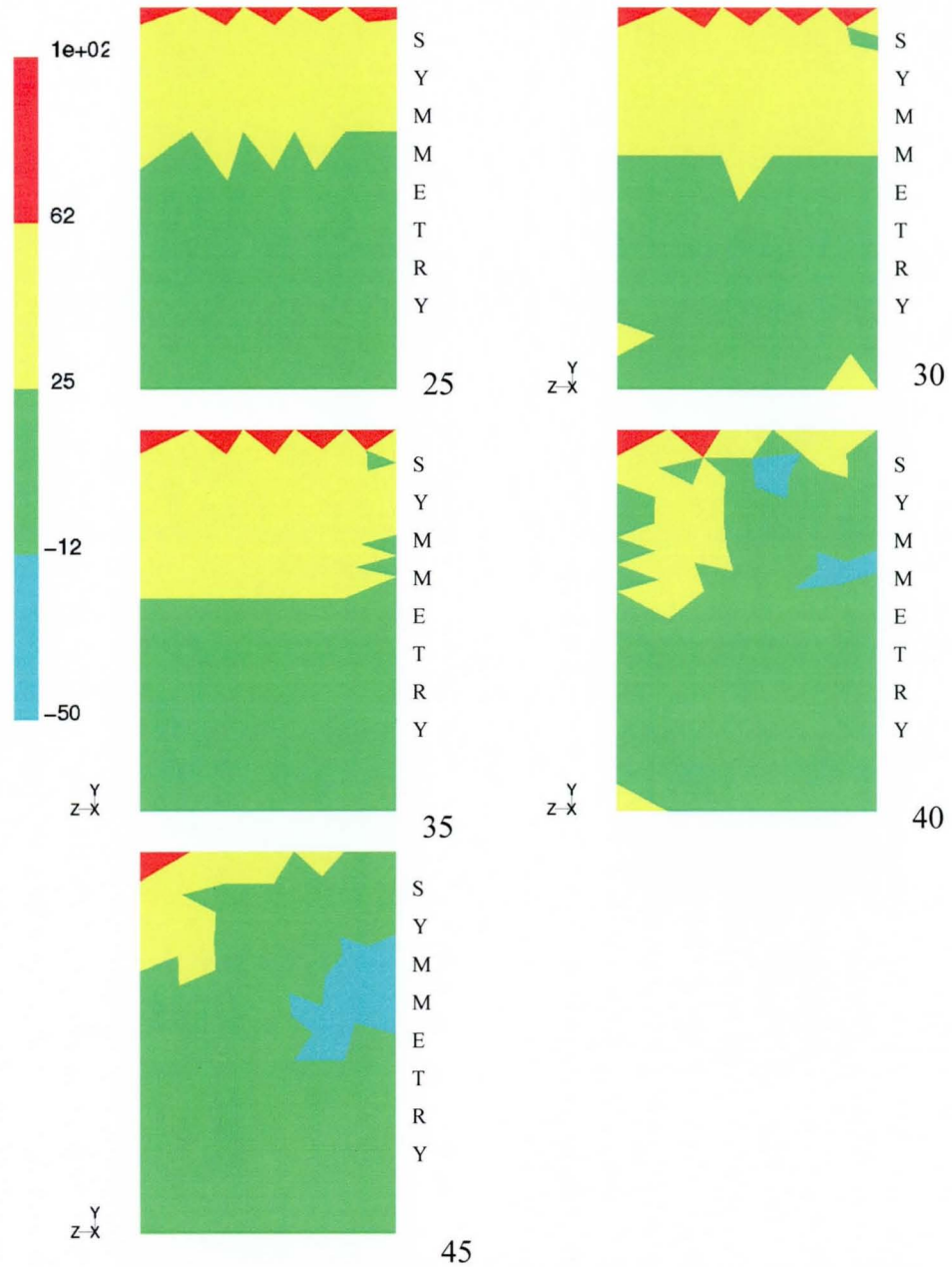


Figure 4.29 The contours of x -velocity (m/s) on the rear surface of the body.

Figure 4.29 shows the contours of x -velocity on the rear surface of the body. The number of contours have been reduced for clarity. The 25°, 30°, and 35° cases show the attached flow over the entire slant surface as expected. The 40° case shows partial separation on the slant surface. The 45° case exhibits the same flow pattern with a larger separated region. The separation begins as expected from the outer edge. This differs from wind tunnel experiments, in which the separation began at the top of the

slant surface along most of the top/slant edge, and reattached to the slant surface gradually from the sides inwards. The resulting separation region resembles a U shape when looking from behind the body.

The flow is expected to separate over the whole of the top/slant edge and then reattach starting from the outer bottom edge of the slant. A possible conclusion from this is that the grid is not sufficiently fine over this part of the body.

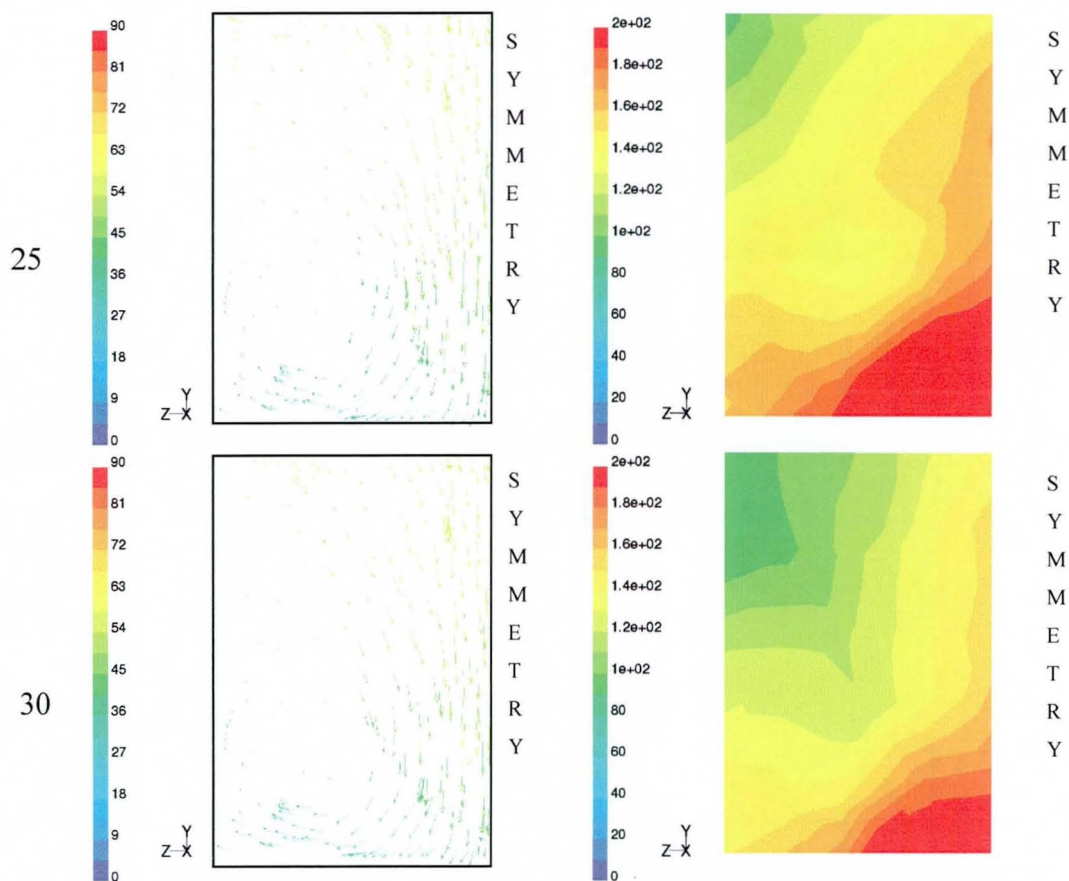


Figure 4.30 The combined plots of in-plane velocity vectors (coloured by velocity magnitude m/s) with the contours of static pressure. Both are situated 0.5m down stream of the start of the body. 25° and 30°.

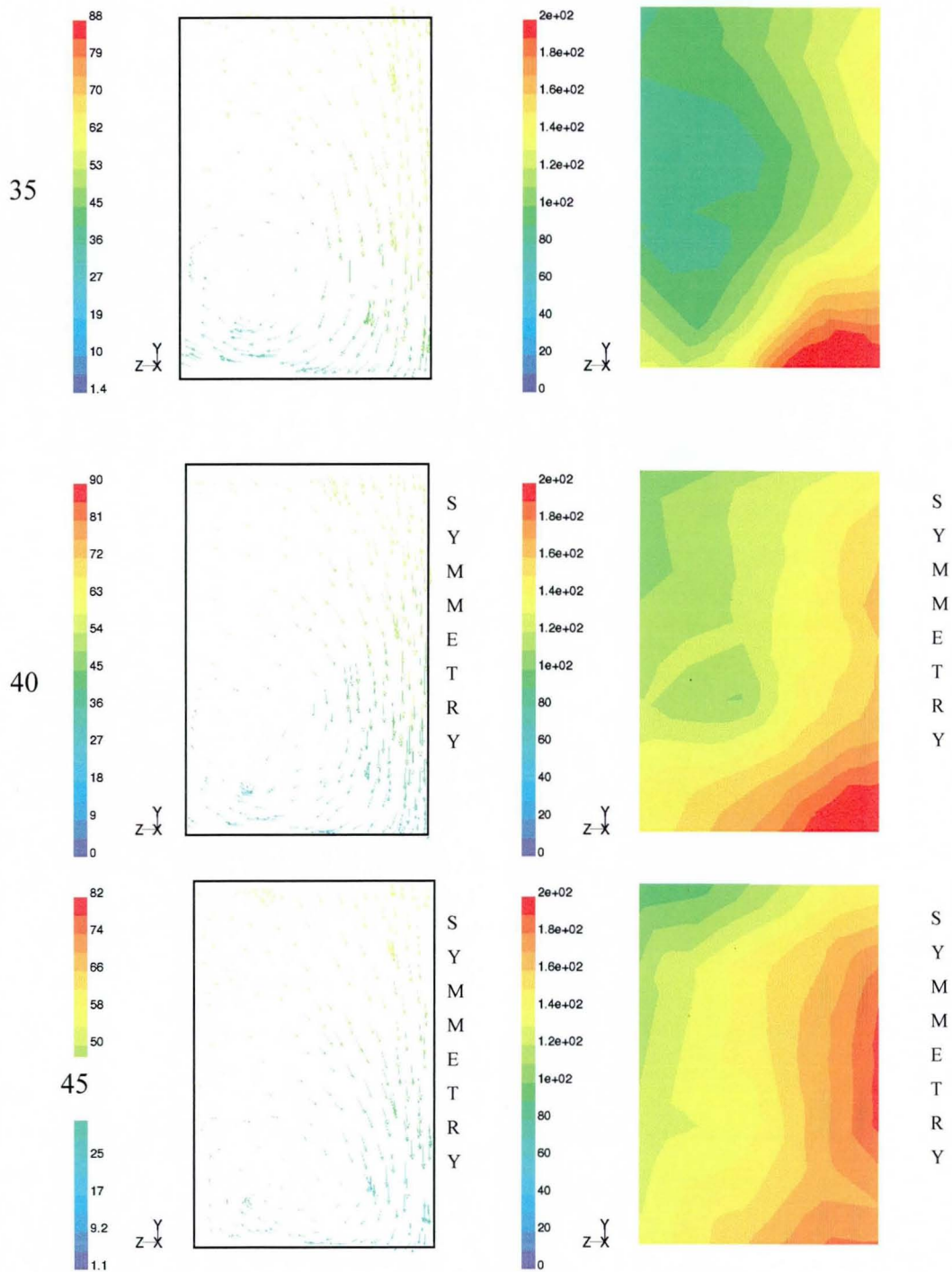


Figure 4.31 The combined plots of in-plane velocity vectors (coloured by velocity magnitude m/s) with the contours of static pressure. Both are situated 0.5m down stream of the start of the body. 35° to 45°.

Figure 4.30 and Figure 4.31 illustrate the combined static pressure contours and velocity vectors in the plane 0.5m behind the start of the body. These show the increasing strength of the counter-rotating longitudinal vortices behind the body, until the 40° and 45° slant surface angle cases where the strength tails off. This tailing off is more rapid than in the unmodified grids indicating the change in the nature of the separation.

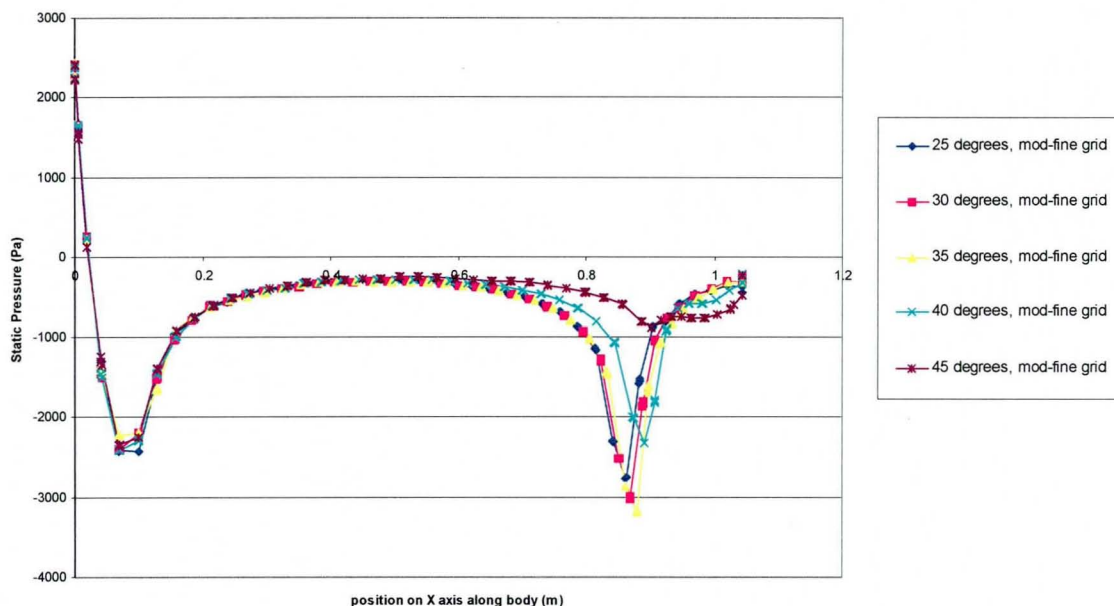


Figure 4.32 The static pressure distribution on the centre-line upper surface of the Ahmed body for the modified fine grid.

The plot of static pressure distribution on the centre-line upper surface (Figure 4.32) shows the same trends at the rear of the body as the previous fine grid, with the exception of the 40° and 45° slant surface angle case. The 40° case demonstrates a lower magnitude of pressure trough after the body, whilst the 45° case shows no

trough at all. This is similar to the behaviour of the experimental data, and should result in a decrease in the drag for this case.

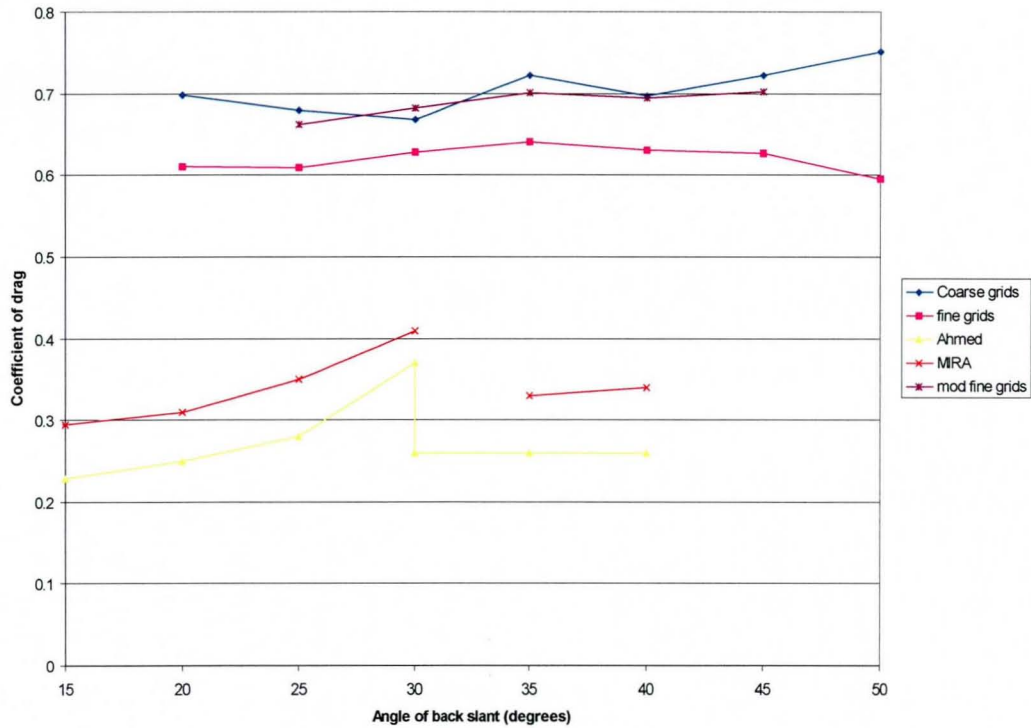


Figure 4.33 The comparison of the drag coefficients for the Ahmed body over a range of back slant angles.

With reference to Figure 4.33, it is evident that the expected bulk drop in drag from the original fine grids does not occur. In fact, the drag figures for the original fine grids are lower than the figures for the modified fine grids. There are several possible explanations for this:

- The drop in pressure is on surfaces that affect the lift more than the drag (that is, upwards).
- The levels of drag are generally too high, masking any drop in the figures.
- The levels of induced drag associated with the twin counter rotating longitudinal vortices may not be as high as seen in the experimental results.

Alternatively, the grid density maybe insufficient to adequately resolve the flow and, thus, the solution is being affected by this change in the internal mesh structure. Further investigation into the cause of this drag rise would be necessary if this effect were seen for subsequent successive mesh refinement. This mesh refinement will form the next section.

4.6 Second Level Fine Grids

In order to further determine the grid dependencies, an additional level of refined grid was tested for the range of critical angles. These cases were run in original and unmodified grid topology form. The grids will be referred to as fine-fine and mod-fine-fine. The cases chosen, based on the results of the previous sets of calculations, were for the 30°, 35°, 40° and 45° slant surface angles. The results are presented and discussed below. The sizes of these new grids are defined in Table 4.5. The average body surface wall y^* value for these grids was 872.

Table 4.5 The grid sizes for the fine-fine grids.

	Fine fine grids	Modified fine fine grids
Boundary nodes	24455	24562
Boundary faces	48906	49120
nodes	32410	33376
faces	504145	516616
cells	264299	270588

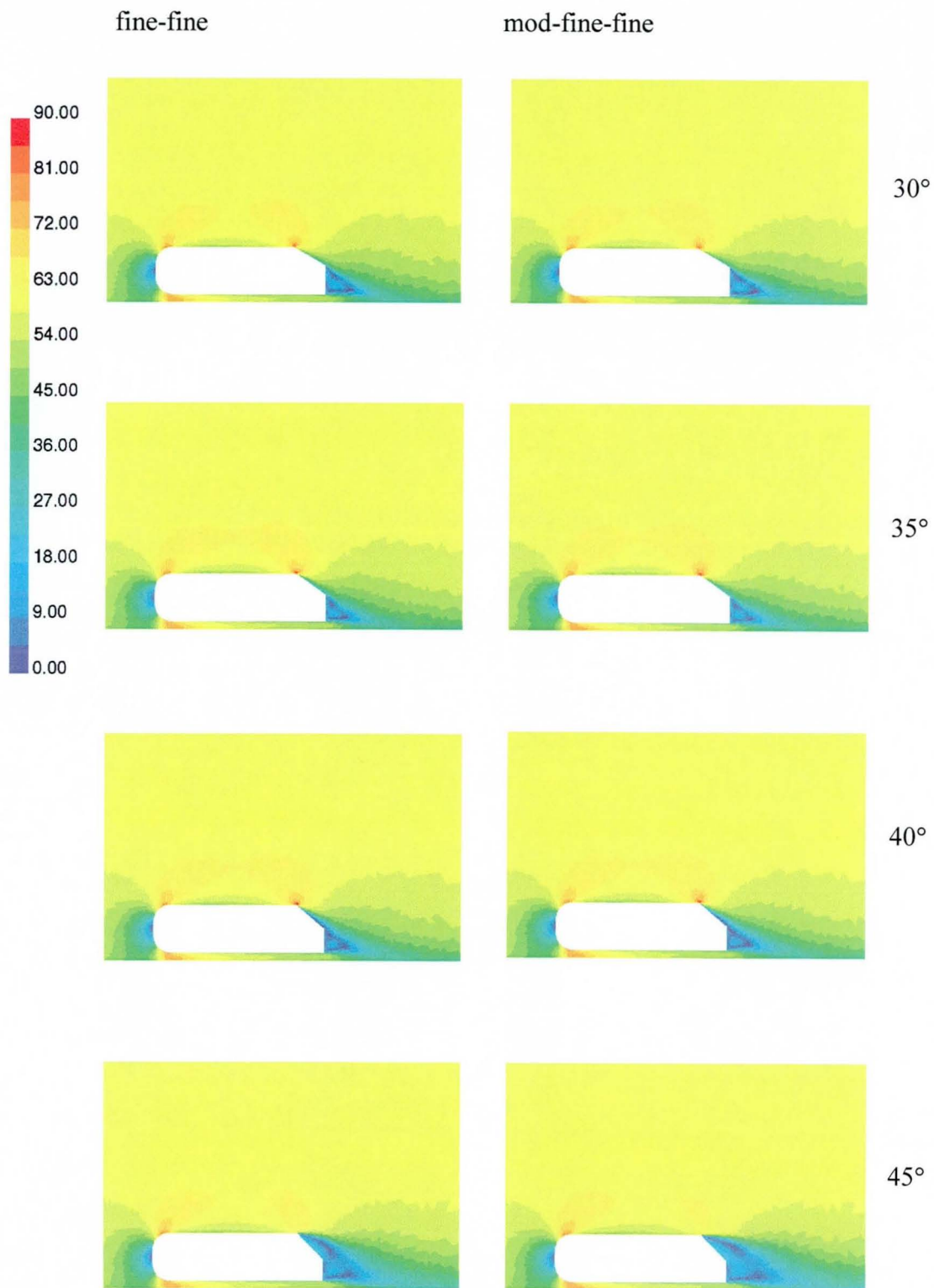


Figure 4.34 The contours of velocity magnitude (m/s) on the symmetry plane for the fine-fine grids (left) and the modified fine-fine grids (right).

The contours of velocity magnitude on the symmetry plane represented in Figure 4.34 reveal the similarity of the flow patterns for the two grids at this level of refinement. All three angles have major similarities for the two grids, with the only noticeable difference being seen in the 45° case, which has a slightly more extended wake region for the modified grid. The 35° case is attached over the slant surface, whilst the 40° and 45° cases are separated, at least on the symmetry plane. In addition, the contours of static pressure on the symmetry plane (Figure 4.35) demonstrate the similarities.

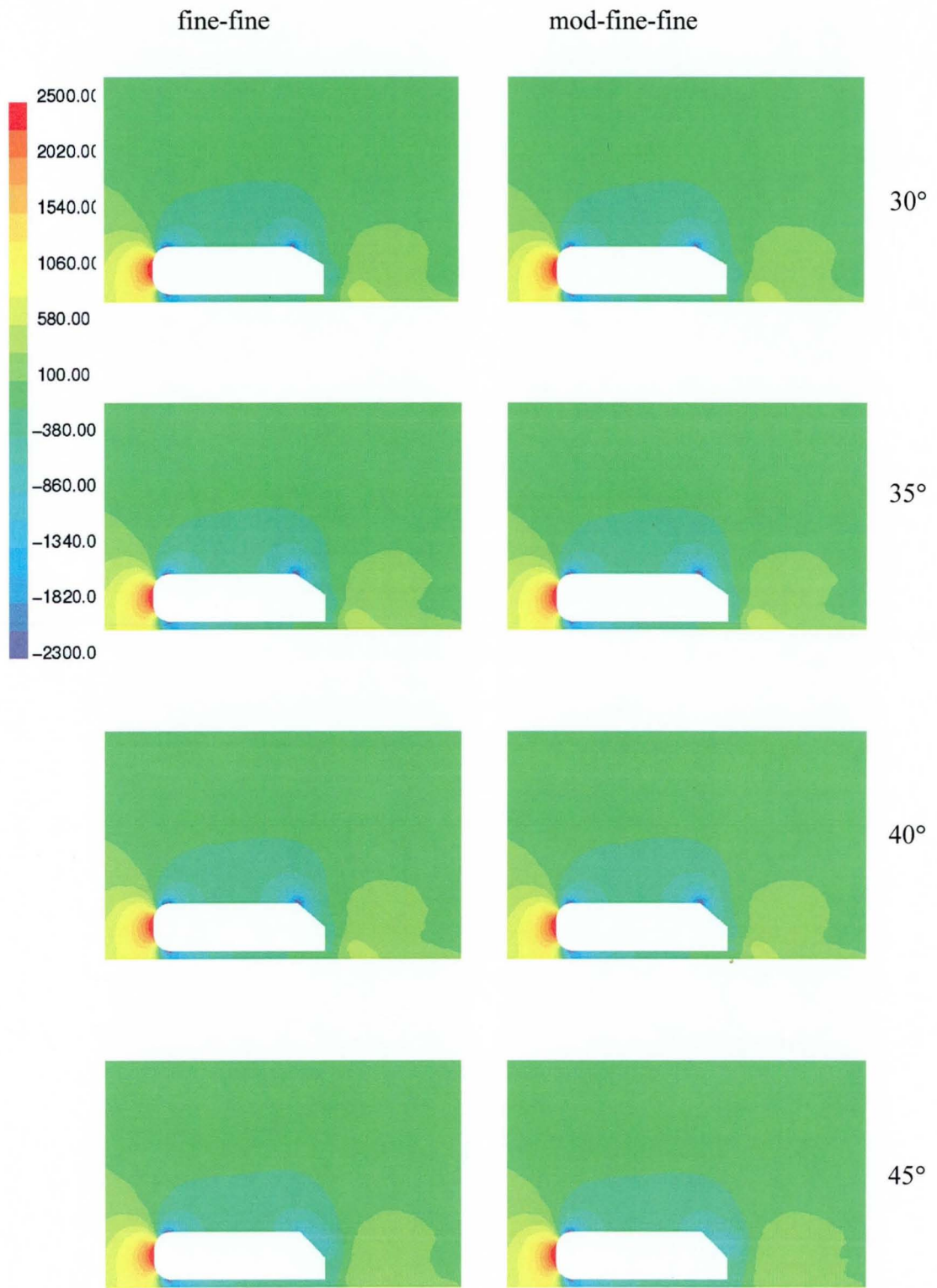


Figure 4.35 The contours of static pressure (Pa) on the symmetry plane for the two types of grid. The modified grid is on the right.

fine-fine
mod-fine-fine

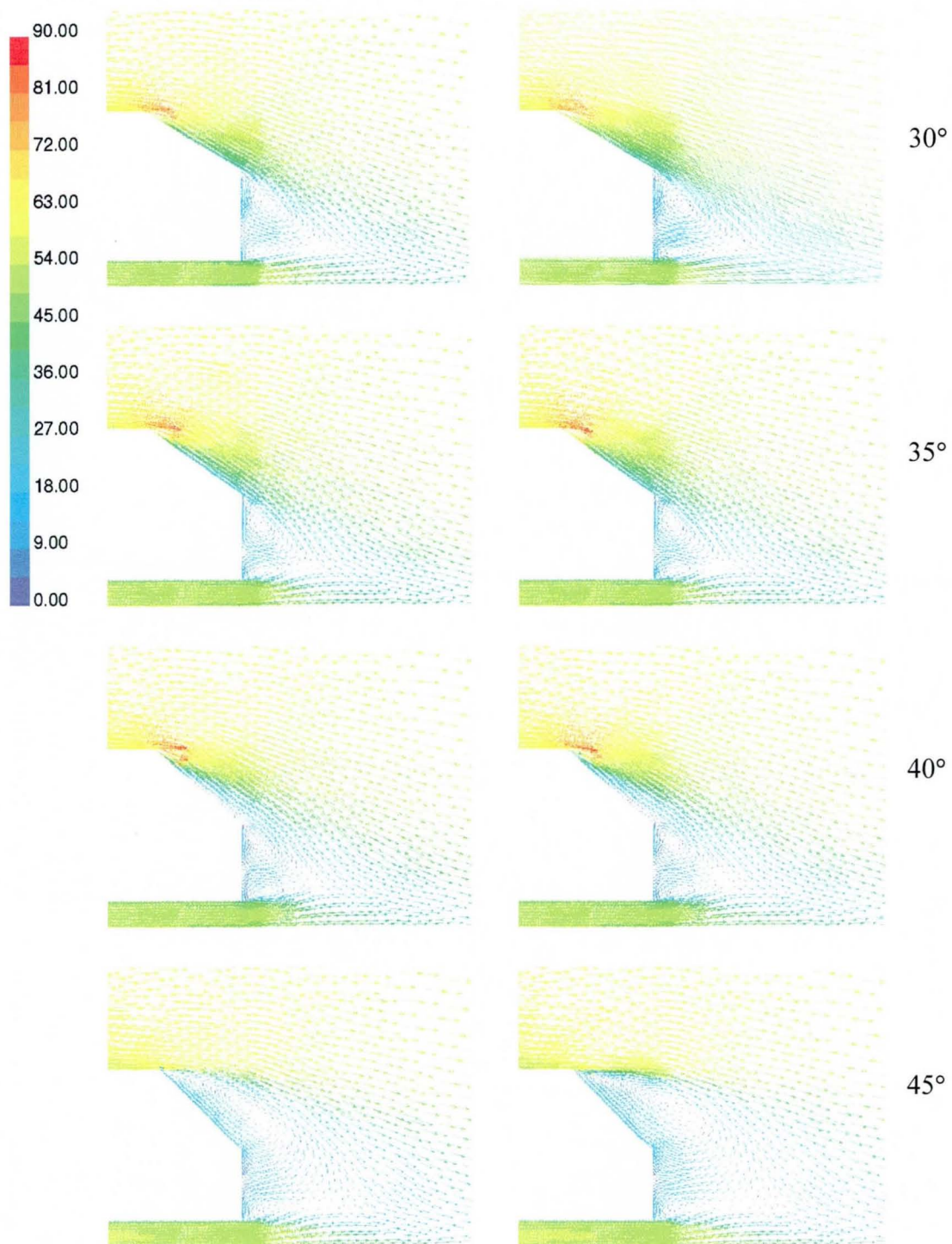


Figure 4.36 The velocity vectors coloured by velocity magnitude (m/s) for the two grids (modified grids is on the right).

The velocity vectors on the symmetry plane demonstrate little that is conclusive, except that the centre of rotation for the vortex after the slant surface (40° and 45°

cases) appears to be slightly further to the rear for the modified grids. The contours of x -velocity on the rear surface of the body (Figure 4.37) show the nature of the separations on those surfaces. The 35° case is largely attached with a slight separation at the end of the slant surface at the symmetry plane. The 40° case shows this separation extending to most of the slant surface; and the 45° case is fully separated with a large magnitude reversed flow on the lower part of the slant surface near the symmetry plane. It is noticeable that in all three cases, the separation is slightly larger for the modified case. This can be attributed to the tendency of the unmodified grid to divert flow along the slant surface. Despite this, however, it is reasonable to say that the solutions seen here are largely independent of the precise grid topology.

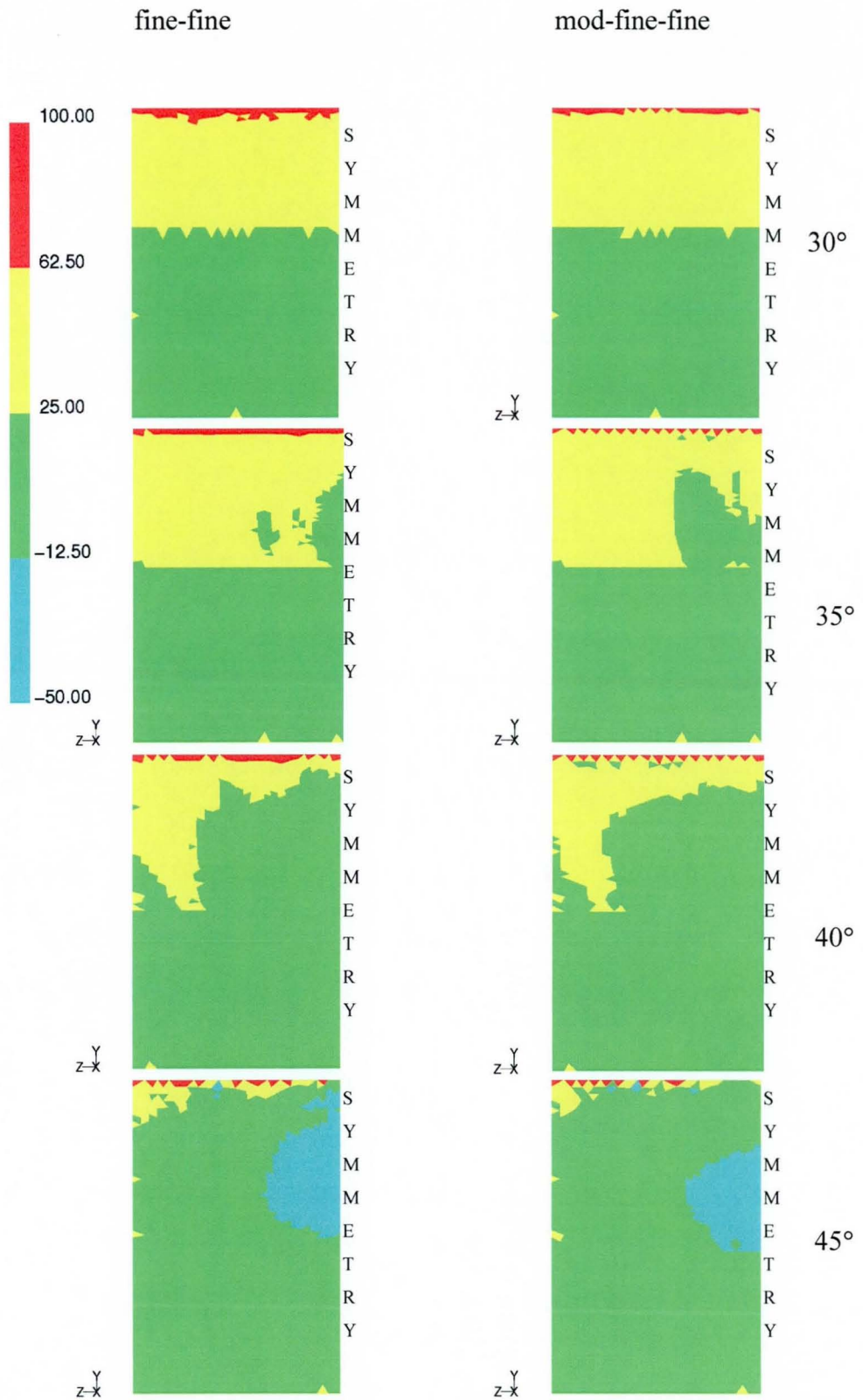


Figure 4.37 The contours of x-velocity (m/s) on the surfaces of the body (the modified grid is on the right).

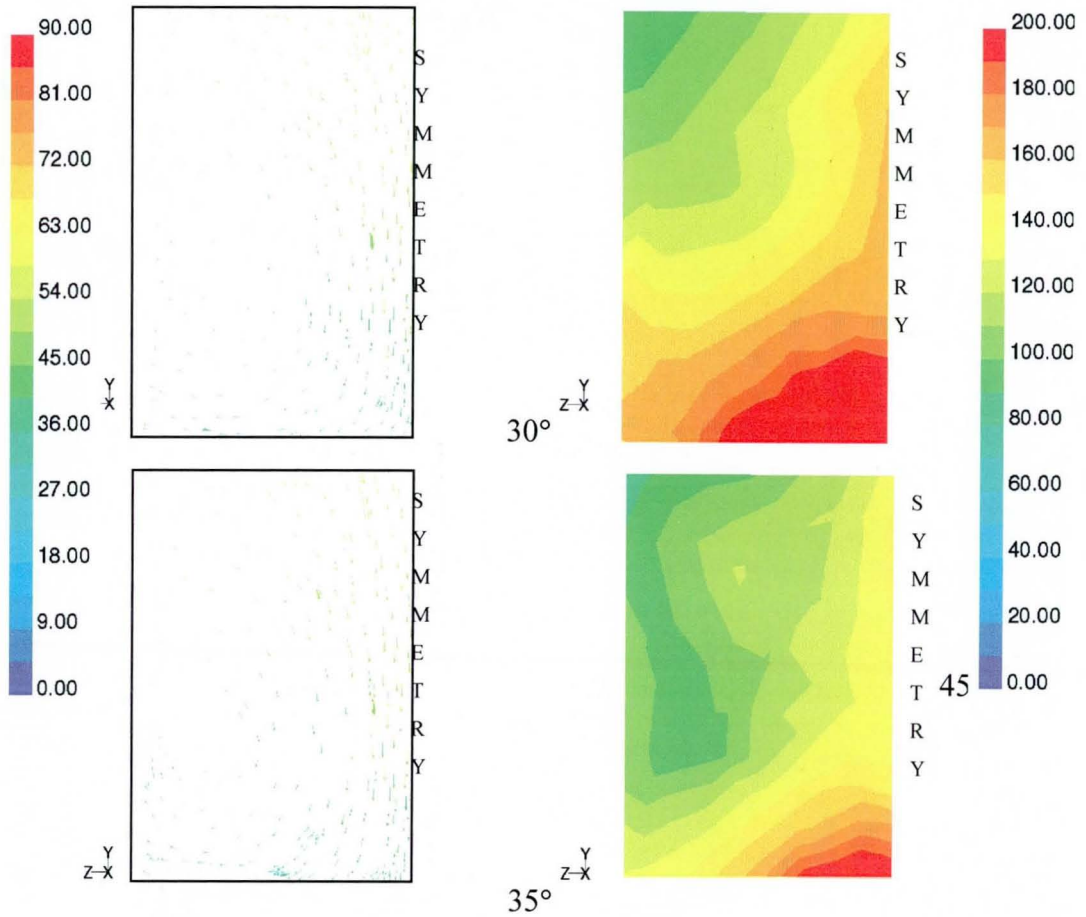


Figure 4.38 The combined plots of in-plane velocity vectors (coloured by velocity magnitude) with the contours of static pressure. Both are situated 0.5m down stream of the start of the body. For the fine-fine grids. 30° and 35° slant surface angles.

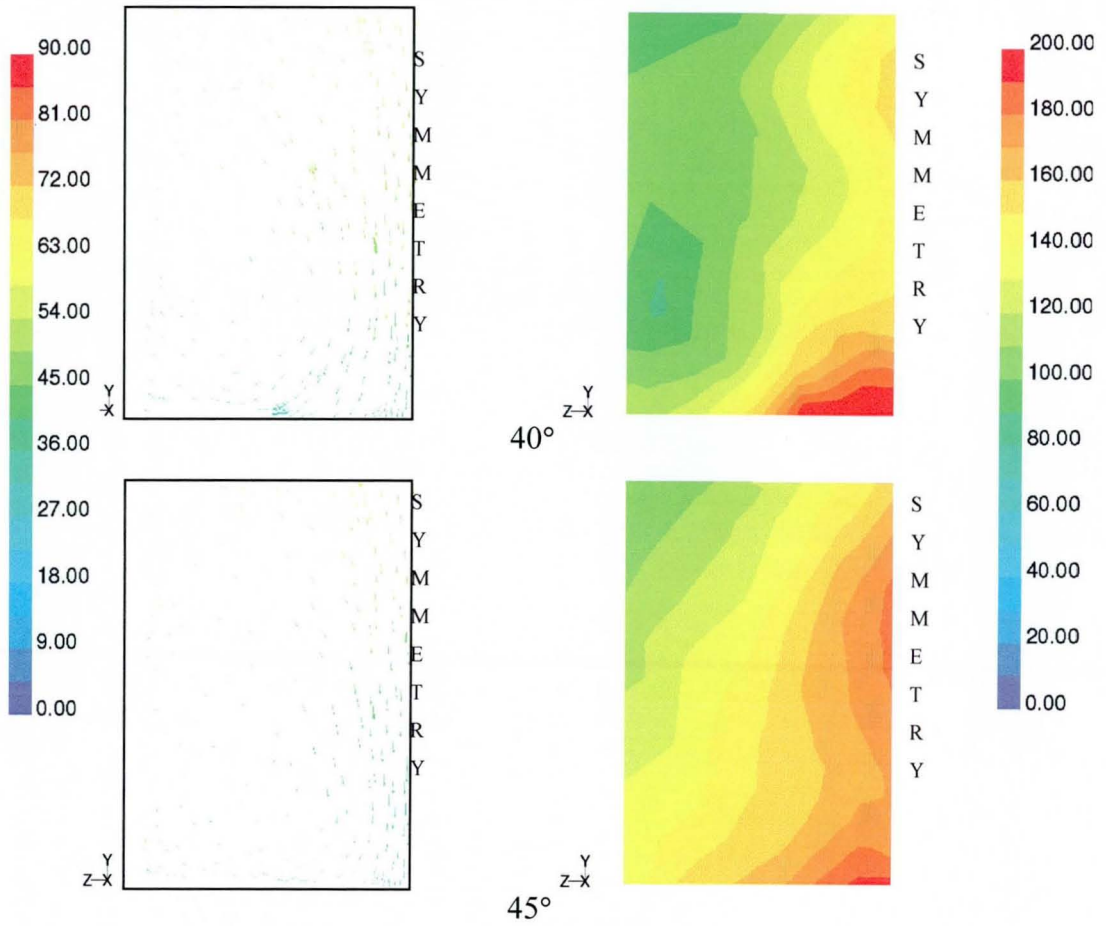


Figure 4.39 The combined plots of in-plane velocity vectors (coloured by velocity magnitude) with the contours of static pressure. Both are situated 0.5m down stream of the start of the body. For the fine-fine grids. 40° and 45° slant surface angles.

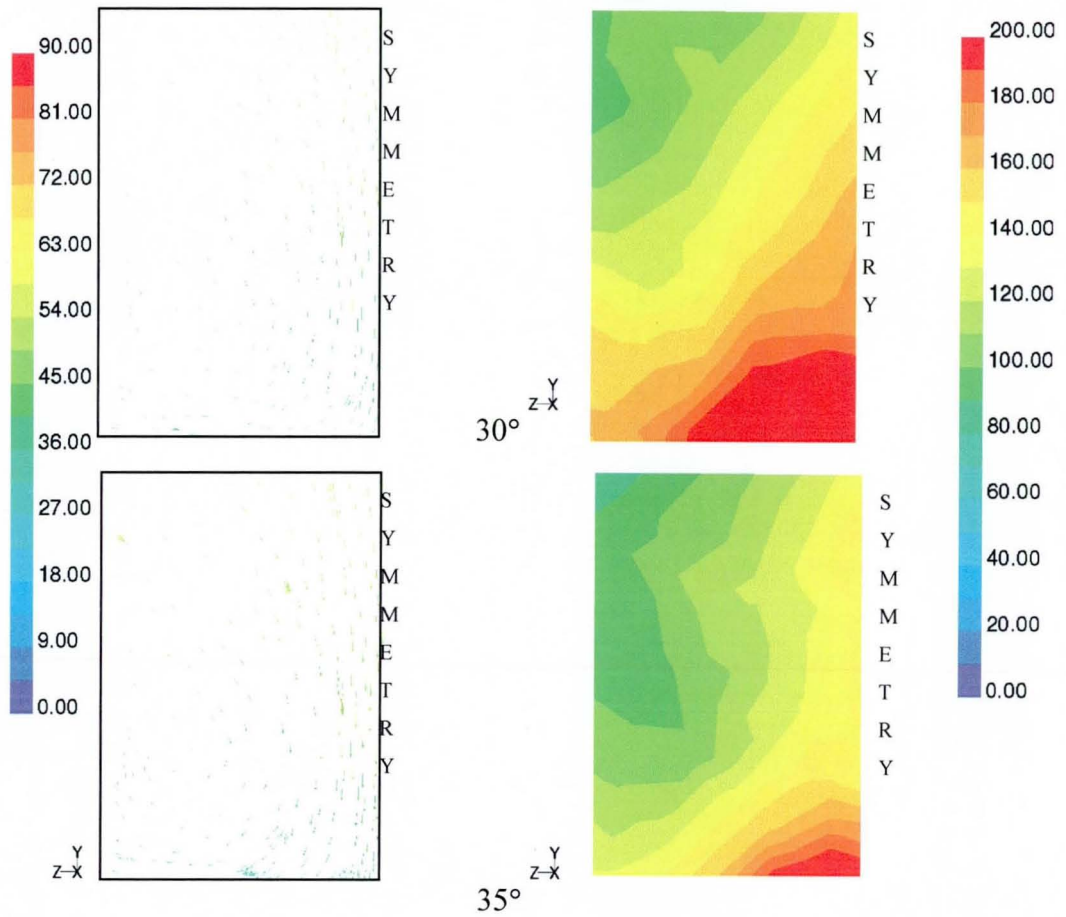


Figure 4.40 The combined plots of in-plane velocity vectors (coloured by velocity magnitude) with the contours of static pressure. Both are situated 0.5m down stream of the start of the body. For the mod-fine-fine grids. 30° and 35° slant surface angles.

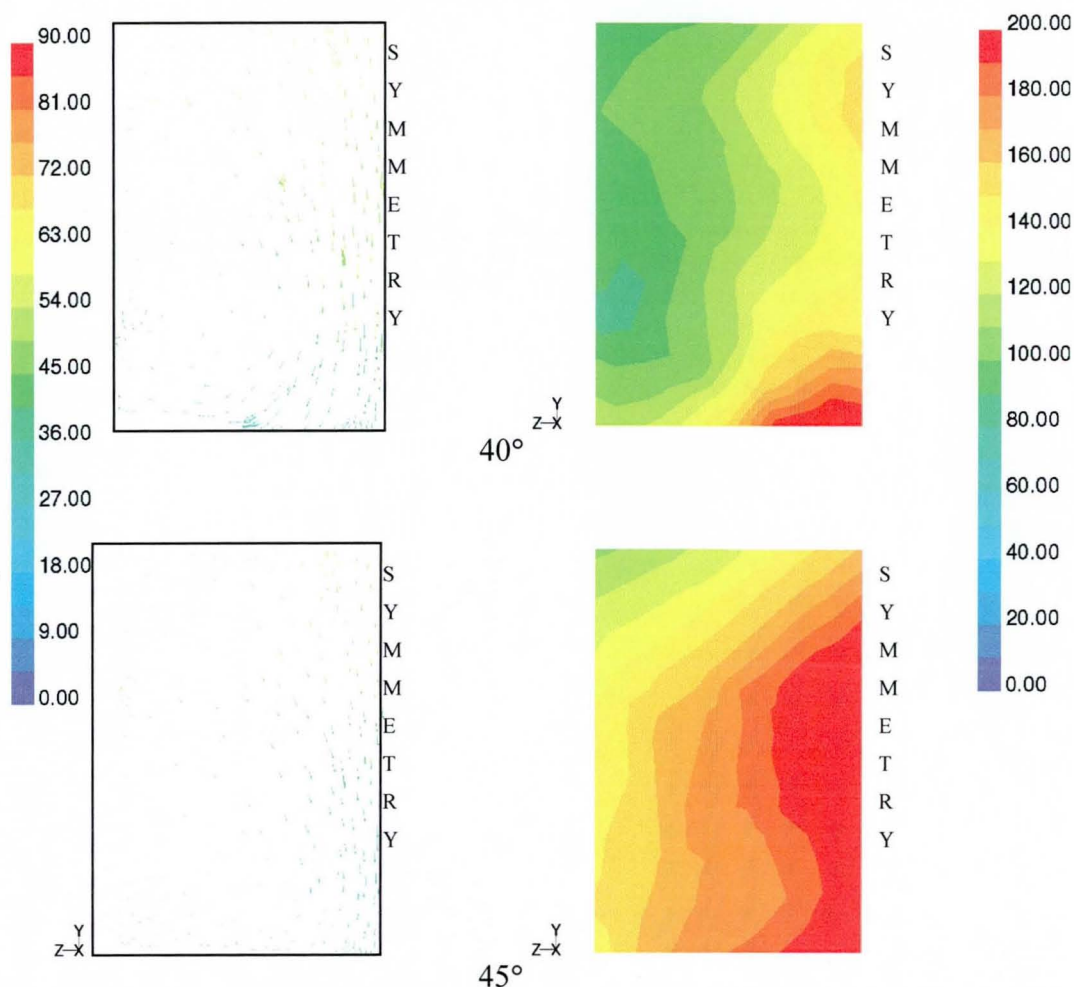


Figure 4.41 The combined plots of in-plane velocity vectors (coloured by velocity magnitude) with the contours of static pressure. Both are situated 0.5m down stream of the start of the body. For the mod-fine-fine grids, 40° and 45° slant surface angles.

The characteristics of the counter-rotating longitudinal vortices are illustrated in Figure 4.38 and Figure 4.39 for the fine-fine grids, and Figure 4.40 and Figure 4.41 for the mod-fine-fine grids. The two grids show similar re-circulations in the 35° and 40° cases. The 45° cases show the increased strength of the down wash in the modified grid results. This is attributable to the increased size of the separated region at this slant surface angle, for this grid topology.

In addition, the upper surface centerline static pressure distributions (Figure 4.42 and Figure 4.43) demonstrate the similarities for the grids. The 35° and 40° cases are nearly identical. The 45° case shows a slightly extended low-pressure region over the top/slant edge in the unmodified grid, due to the diversion of the axial momentum in this area. In both sets of results, the pressure distributions are largely as expected, with the separated case having a lower pressure drop after the top/slant edge, as in the wind tunnel results. However, the separation should have occurred at 30° to 35° degrees not 45°.

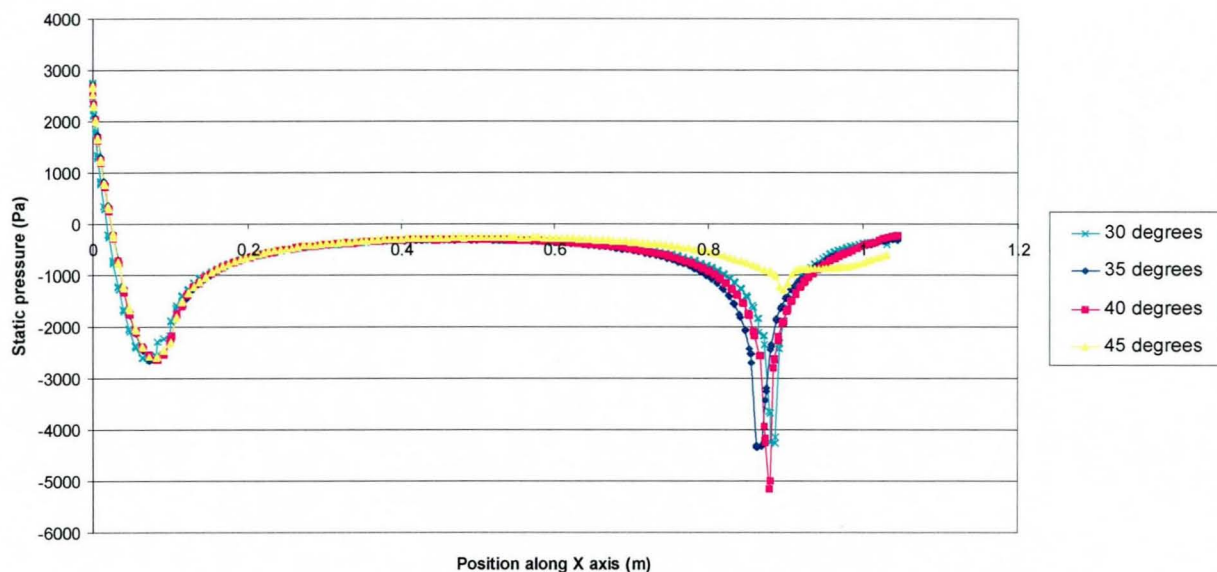


Figure 4.42 The static pressure values seen on the upper side symmetry plane centreline of the Ahmed body for the fine-fine grids.

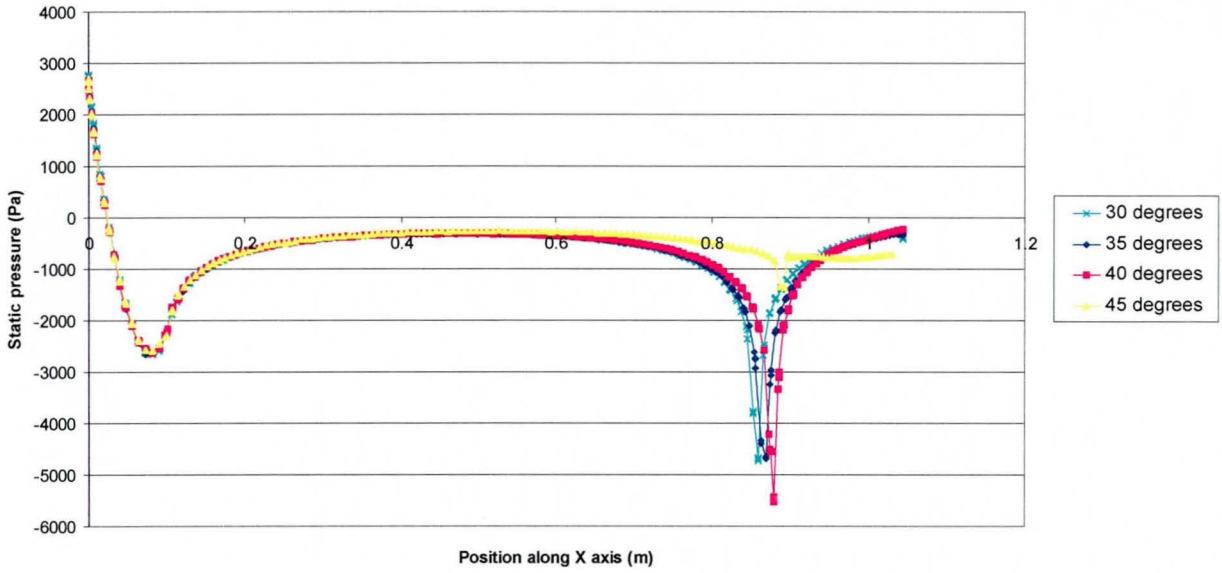


Figure 4.43 The static pressure values seen on the upper side symmetry plane centreline of the Ahmed body for the modified fine-fine grids.

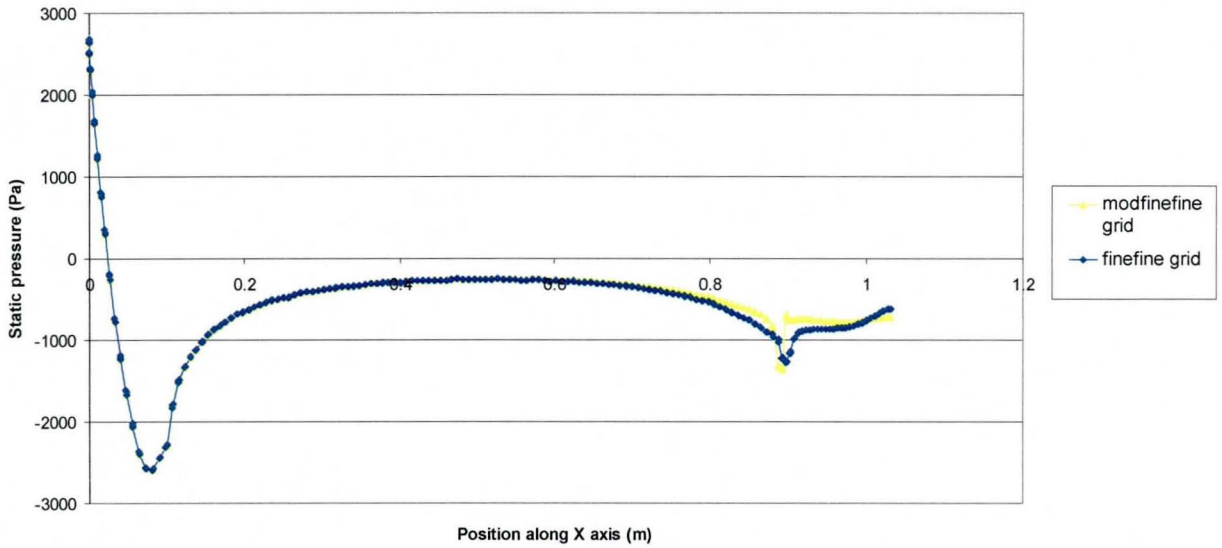


Figure 4.44 The static pressures on the upper surface centreline of the Ahmed body for the 45° case with both mesh types.

The direct comparison of the static pressures on the upper surface centreline for the 45° case is illustrated in Figure 4.44. The pressures are the same for the majority of the body. The only differences occur, as expected, at the rear of the body. The modified grid still indicates a pressure drop at the top/slant edge. However, it is confined to the actual corner. The normal grid shows that low-pressure extending along the first part of the slant surface, indicating that it has not properly separated.

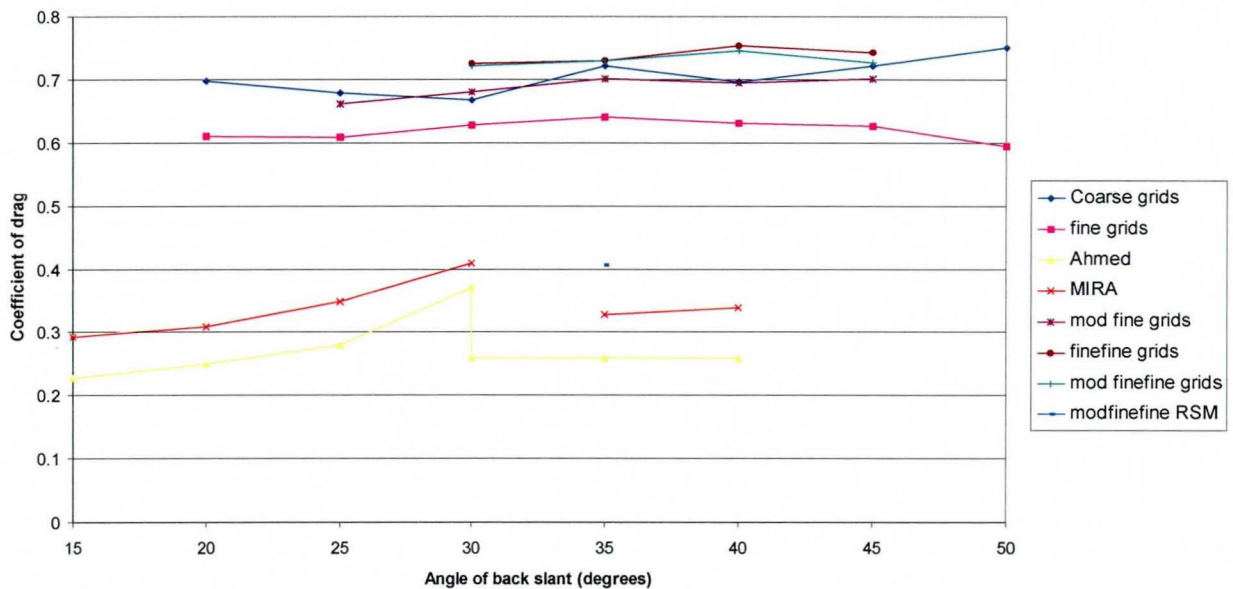


Figure 4.45 The drag coefficients for the various grids compared to the experimental values.

The drag coefficients for these cases are shown in Figure 4.45, along with the other grid results and experimental values. The level of drag is slightly higher than in the other grids, however, there is now a slight change in drag as the flow regime changes, particularly in the modified grid results. The change, however, still takes place at about 10° higher than in the wind tunnel experiments.

4.7 Results of Second Order Differencing Scheme

The two grid topologies at their most refined level were used in conjunction with a higher order differencing scheme. The QUICK differencing scheme as used in the structured grid calculations is not available for tetrahedral grids in the *FLUENT/UNS* solver, due to the complexity of determining the upwind cells. There is, however, a second order scheme available both for the continuity and the momentum equations details of this scheme are given in the introduction.

The second order scheme was applied to angles of back slant 35° , 40° and 45° . The results for the two grids are presented in this section. Figure 4.46 illustrates the contours of velocity magnitude, and Figure 4.47 the static pressure on the symmetry plane, for the fine-fine and mod-fine-fine grids. The separation region on the symmetry plane can be seen forming on the 40° mod-fine-fine grid, but not, however, on the fine-fine case. This is the expected difference between the modified grids and the unmodified grids. The less diffusive nature of the second order differencing scheme is reducing the smearing of the velocity around the top/slant edge in the modified grids. This has the effect of increasing the mesh dependent nature of the flow solution in this area.

The static pressure contours (Figure 4.47) clearly illustrate the differences between the grids. Both 45° grids are fully separated on the symmetry plane, and both 35° cases are fully attached. The 40° unmodified grid is attached with the associated low-pressure over the top/slant edge being seen. The modified grid, by contrast, displays no low-pressure there, and consequently is separated.

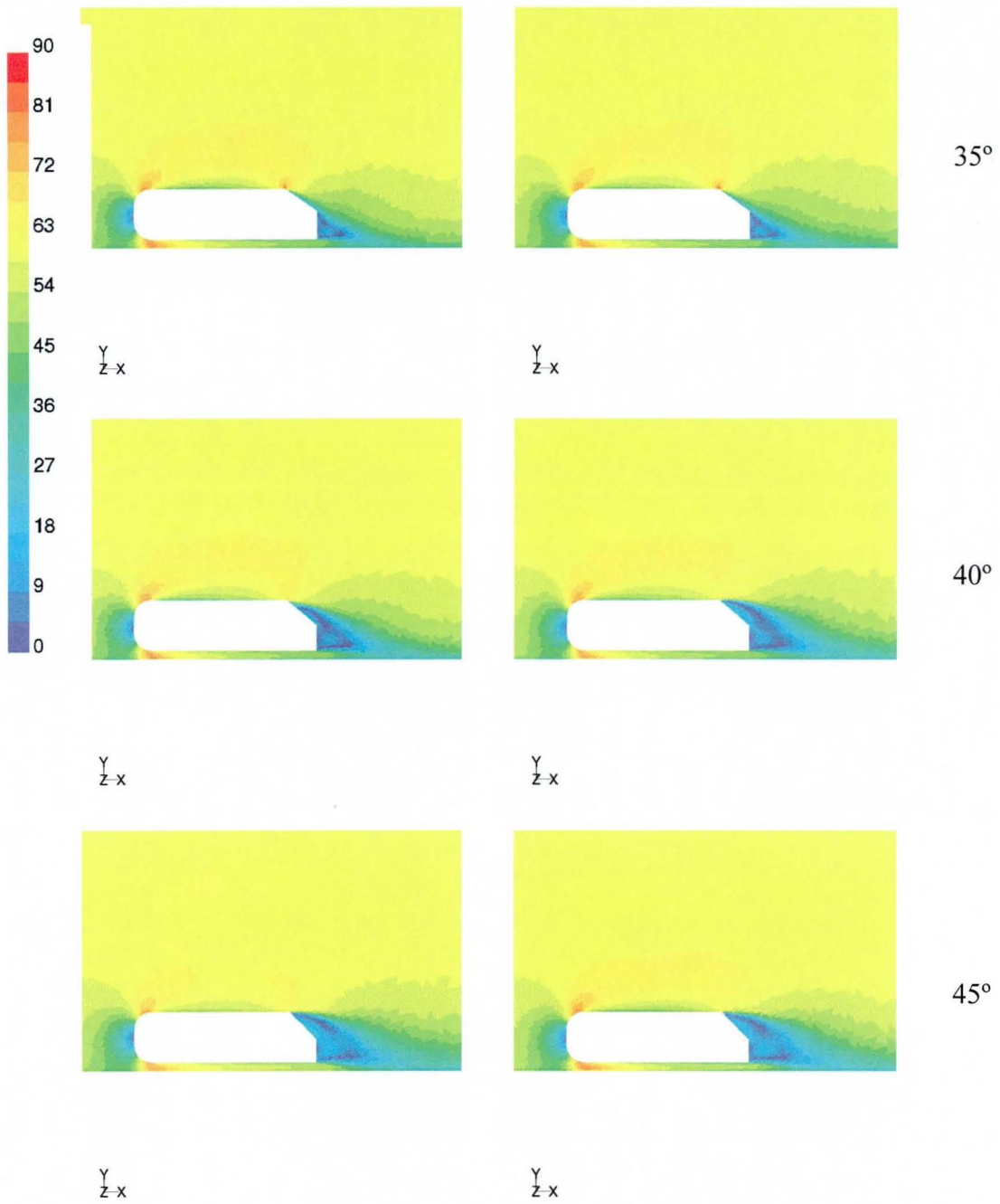


Figure 4.46 The velocity contours on the symmetry plane for the second-order calculations. (The fine-fine grids are on the left and the mod-fine-fine grids on the right)

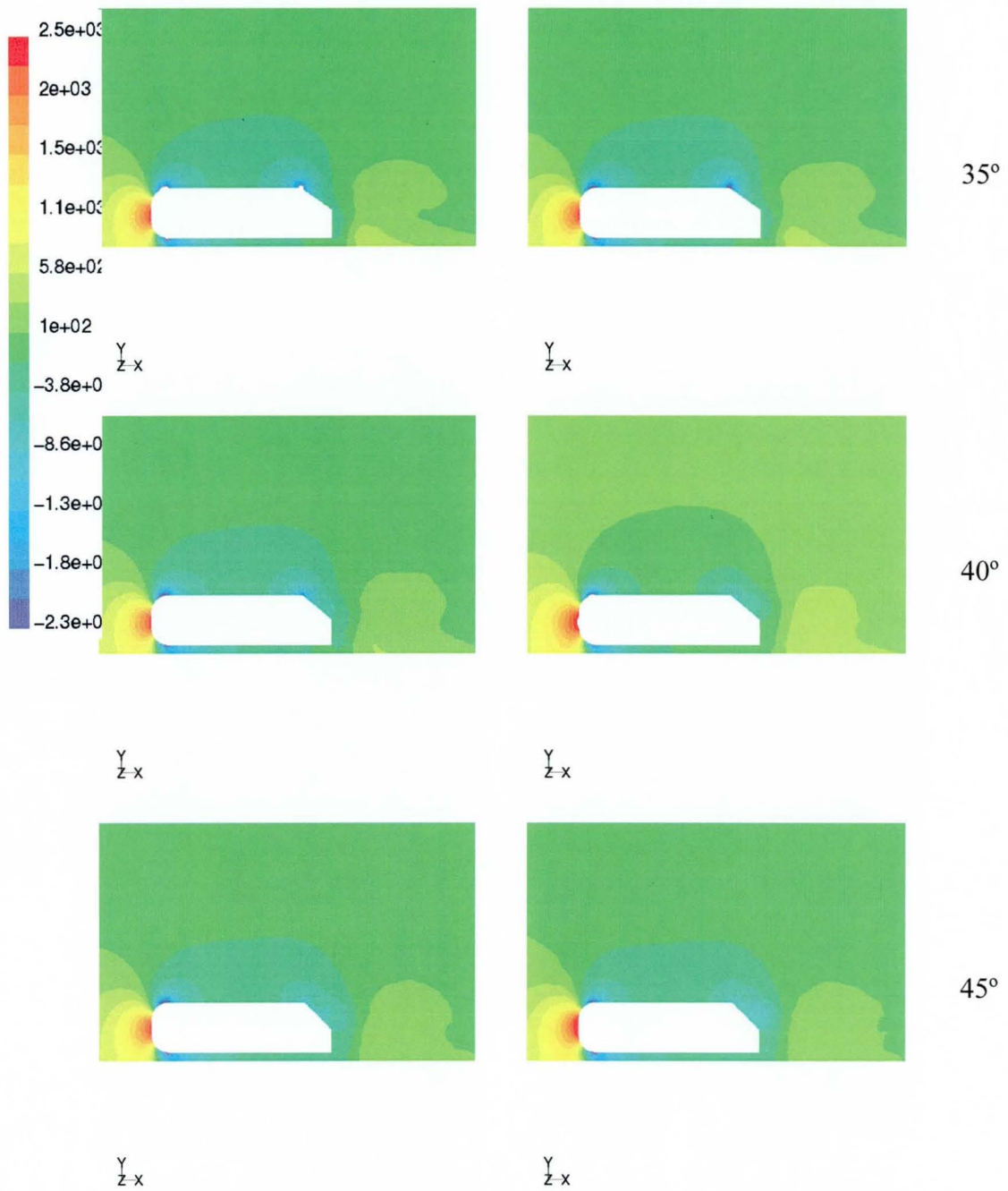


Figure 4.47 The static pressure contours on the symmetry plane for the second-order calculations. (The fine-fine grids are on the left and the mod-fine-fine grids on the right)

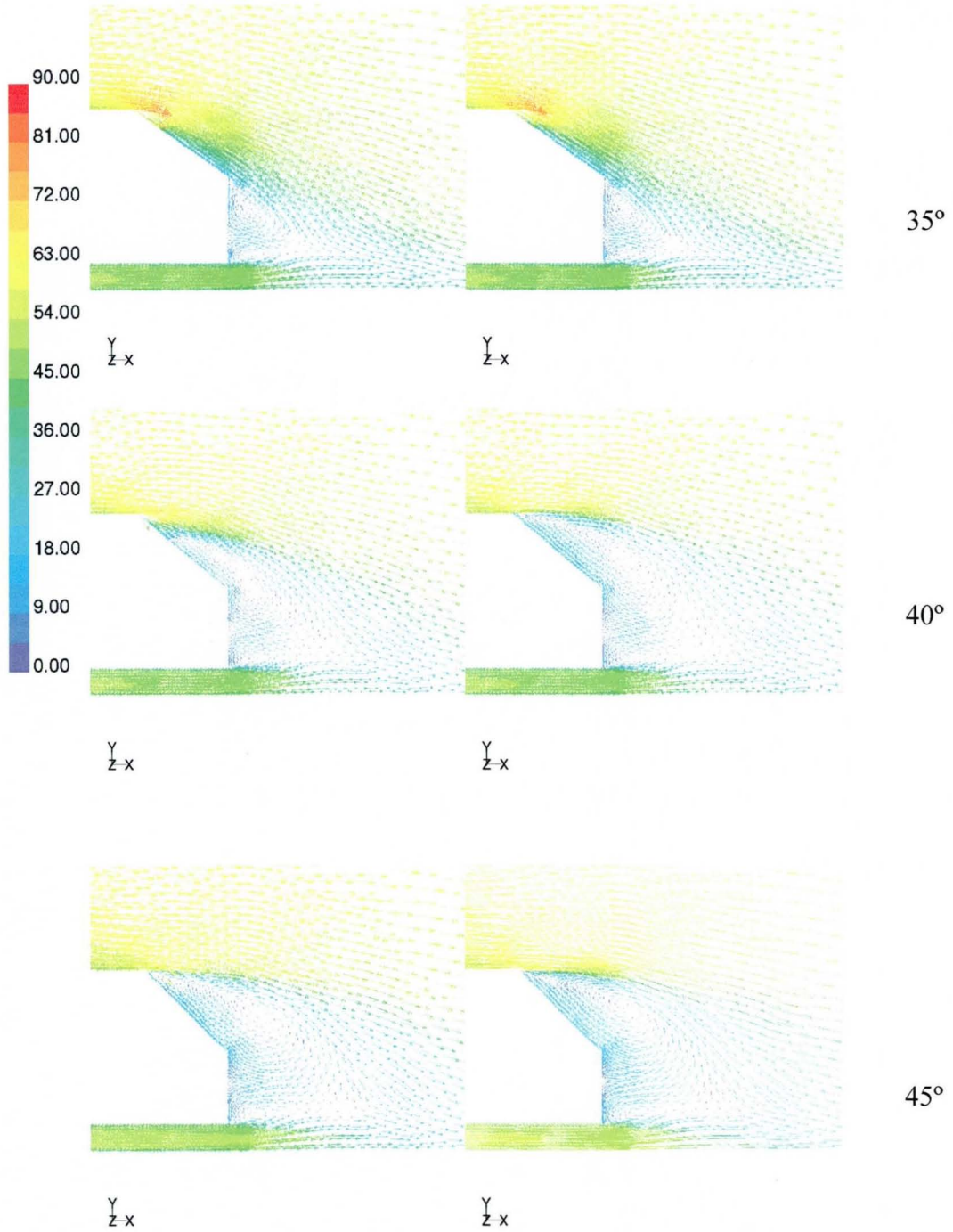


Figure 4.48 The velocity vectors coloured by velocity magnitude on the symmetry plane for the second-order calculations. (The fine-fine grids are on the left and the mod-fine-fine grids on the right)

The velocity vectors on the symmetry plane shown in Figure 4.48 provide more information about the various flow patterns over the body. The two 35° cases are, as mentioned above, fully attached. The 45° cases are, similarly, both fully separated. These two sets of flow solutions are very similar, which shows the small mesh dependency of these grids. The modified 40° case is fully separated, as seen in the 45° grids above. Indeed the solutions are very similar. The unmodified grid is almost fully separating, however, crucially, it has first directed the flow around the top/slant edge causing an area of attachment there. This flow subsequently separates, due to the adverse pressure gradient seen on this surface.

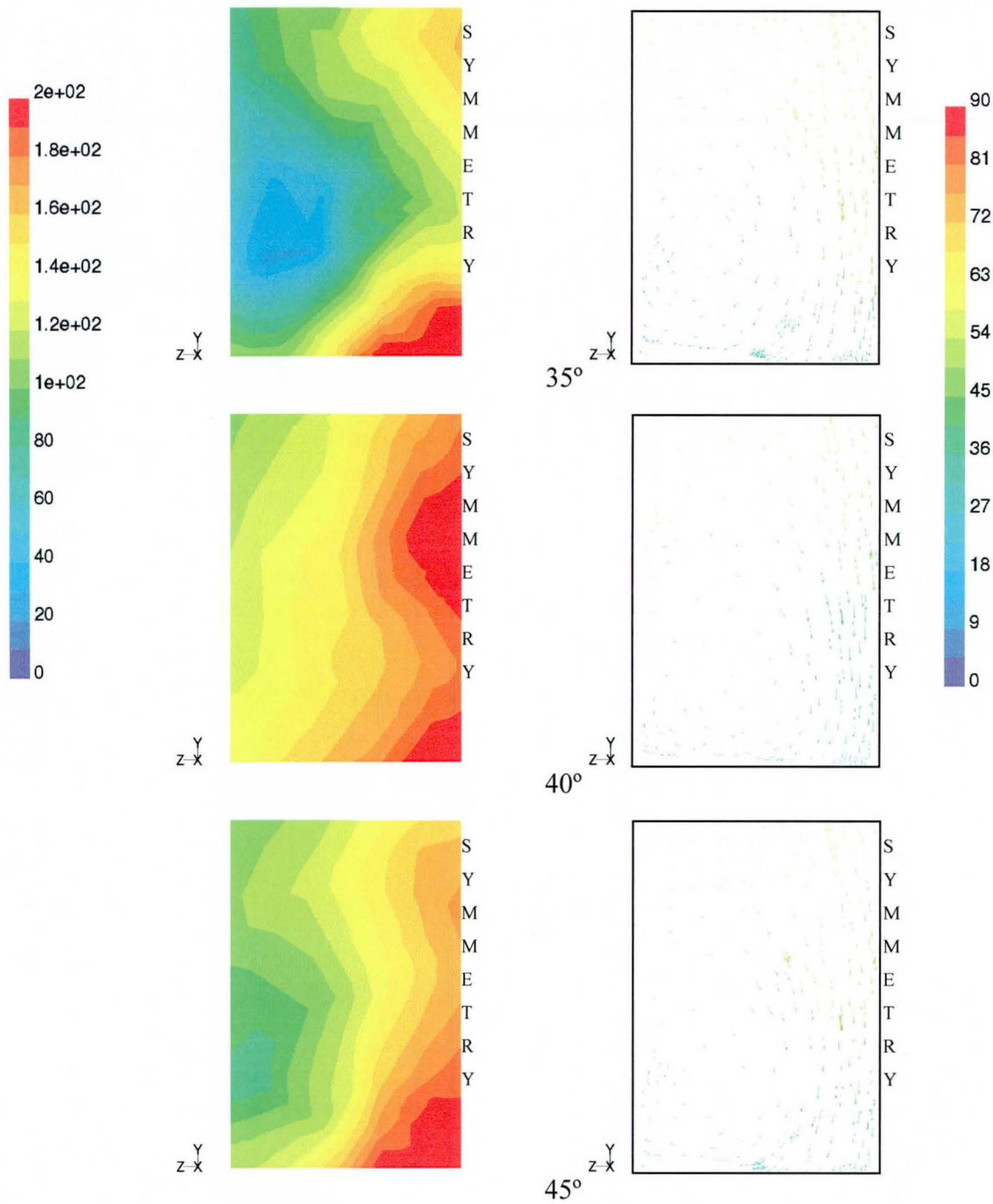


Figure 4.49 The static pressure contours and velocity vectors coloured by velocity magnitude on the plane 0.5m behind the body for the second-order calculations. (The fine-fine grids are shown here)

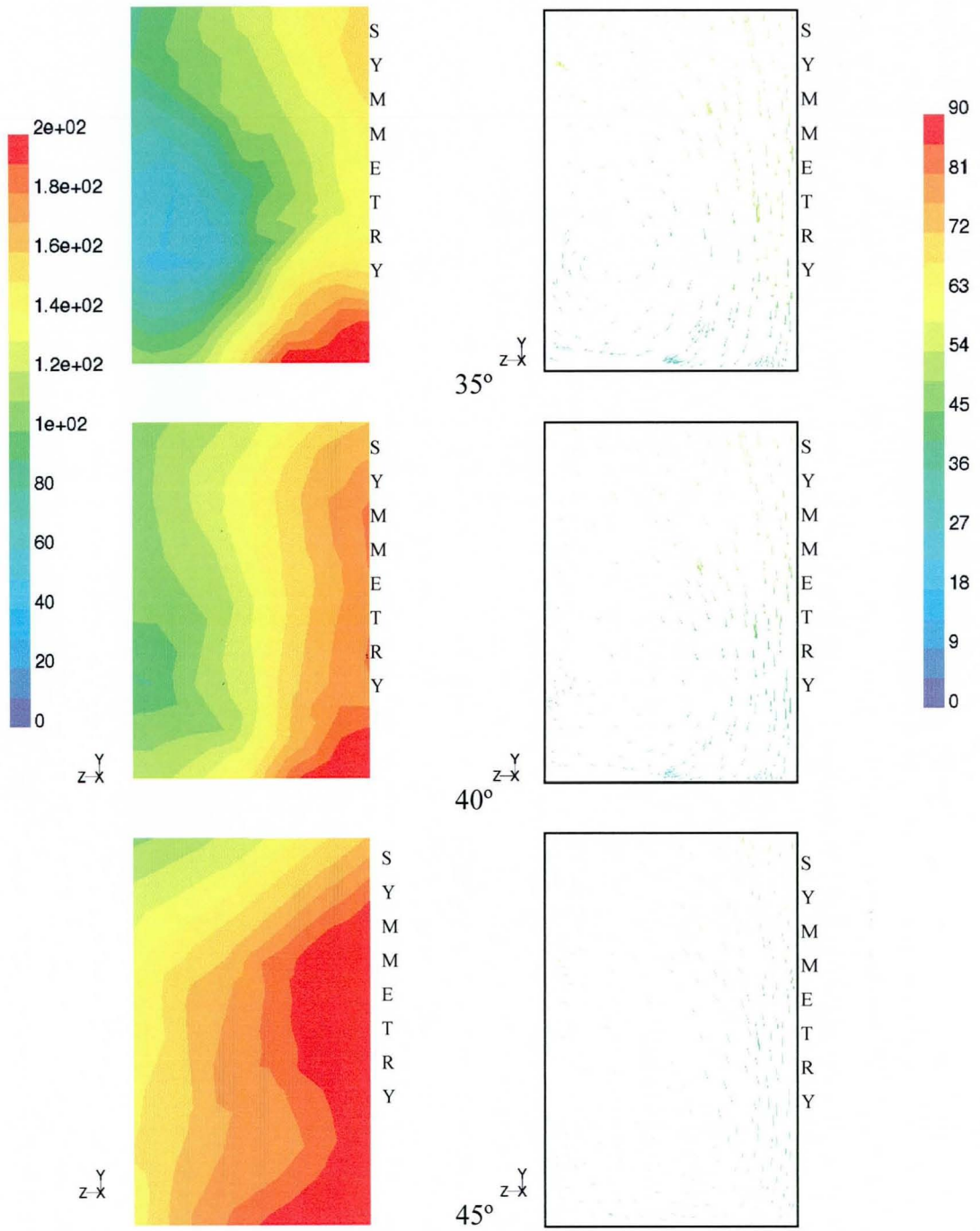


Figure 4.50 The static pressure contours and velocity vectors coloured by velocity magnitude on the plane 0.5m behind the body for the second-order calculations. (The modified fine-fine grids are shown here)

The two sets of combined far field plots, seen in Figure 4.49 and Figure 4.50, illustrate the static pressure contours and velocity vectors in a plane 0.5m behind the end of the body. These plots help to identify the presence and strength of the longitudinal vortex structures behind the body that are started by the interaction of the flows around the top and sides of the body. The 35° and 45° cases, again, demonstrate the same behaviour for the two grids, the former body producing strong re-circulations and the latter, none at all. The 40° cases show a change between the grids; the unmodified grids show evidence of weakened versions of these vortices. The modified grids show no longitudinal vortices.

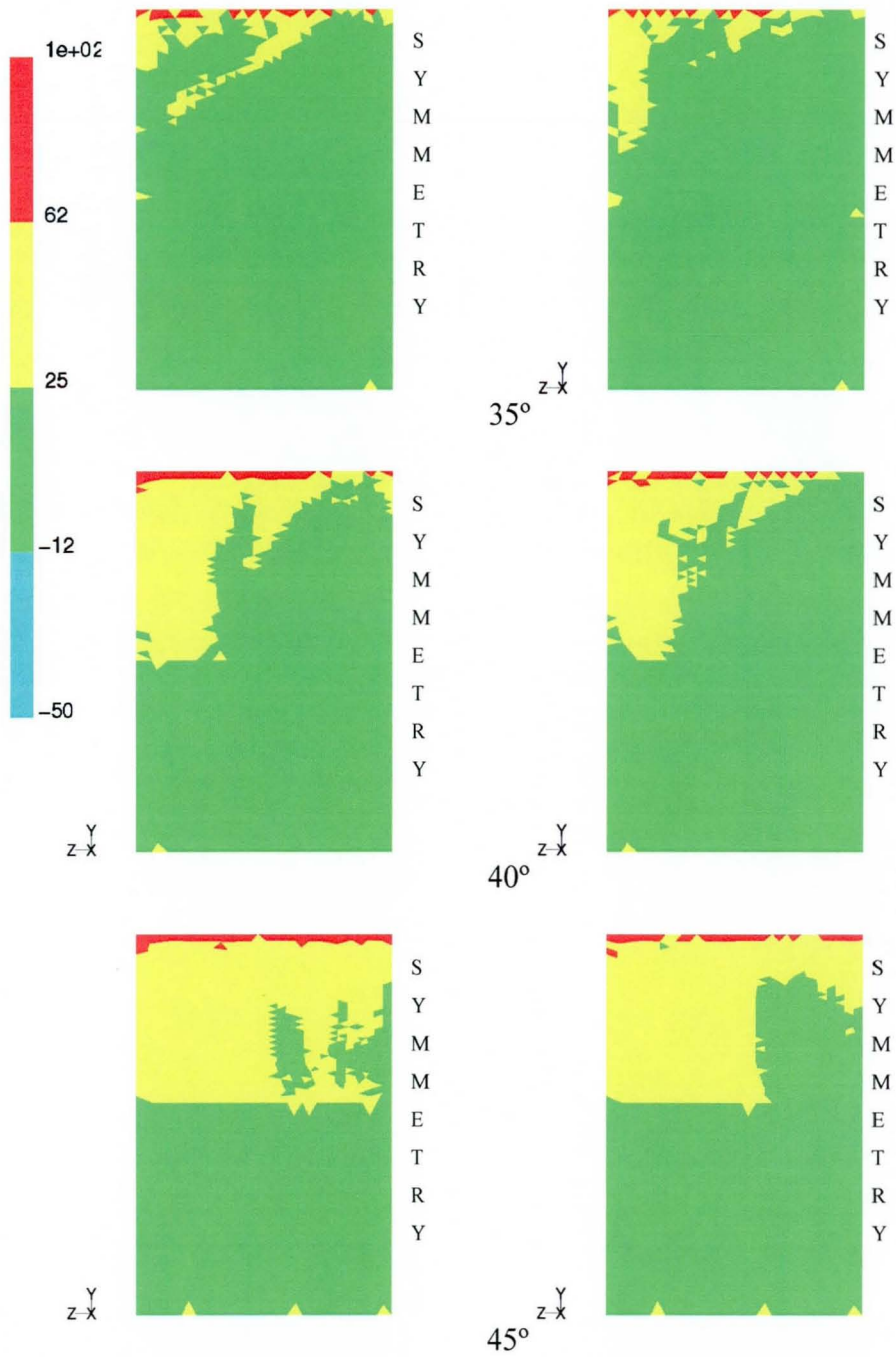


Figure 4.51 The contours of velocity on the rear of the body reduced to 4 levels to emphasize the separated region. (The fine-fine grids are on the left and the modified fine-fine grids on the right)

The contours of velocity on the slant and rear surfaces of the body for these cases are shown in Figure 4.51. The number of contours has, again, been reduced to four for

clarity. The plots show the virtual absence of attached flow on the slant for the entire surface in the 45° cases. The 35° cases, by contrast, show only slight separation starting from the bottom of the centre-line. The separation in the modified grid is slightly larger, however, still close to the unmodified grid result. The 40° cases are remarkably similar to each other, especially when considering the differences in the separation from the slant surface on the symmetry plane seen previously. The crucial difference is the fully separated region at the top of the slant surface next to the symmetry plane on the modified grid that is not present in the other grid case. If this separation were to re-attach later in the slant surface, this would be the correct flow field (albeit 10° higher than in the wind tunnel results). However, there is no sign of this. The static pressure plots on the upper body centre-line seen in Figure 4.52, Figure 4.53 and Figure 4.54 reinforce the evidence of the types of flow behaviour witnessed. The low angle cases are fully attached, the high angle fully separated, and the 40° case attached in the unmodified grid and separated in the modified grid.

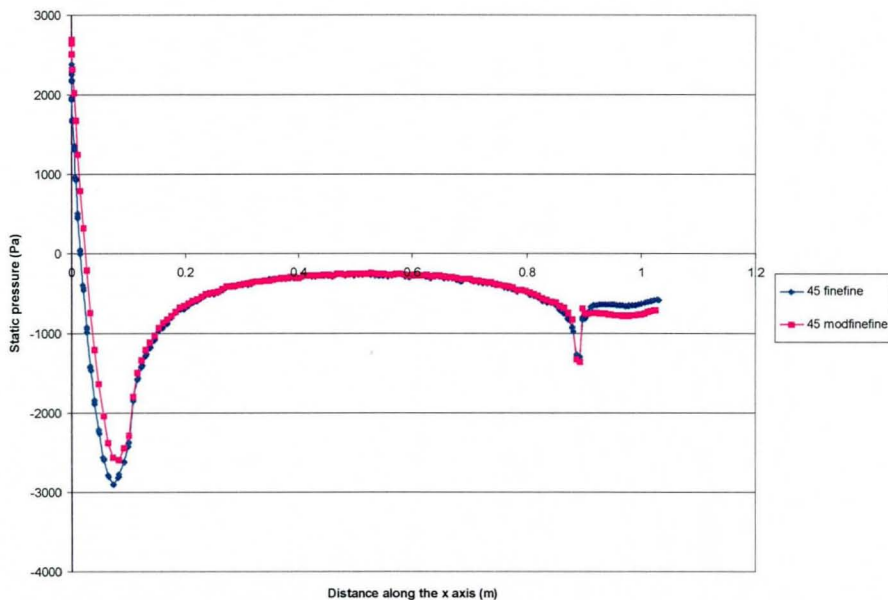


Figure 4.52 The static pressures distribution along the upper body centreline for the 45° angle case on both grids.

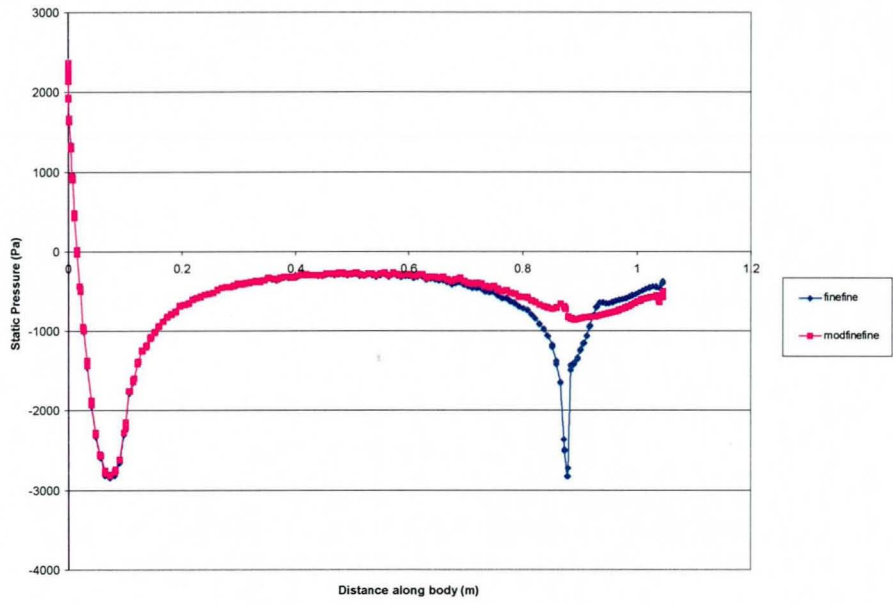


Figure 4.53 The static pressures distribution along the upper body centreline for the 40° angle case on both grids.

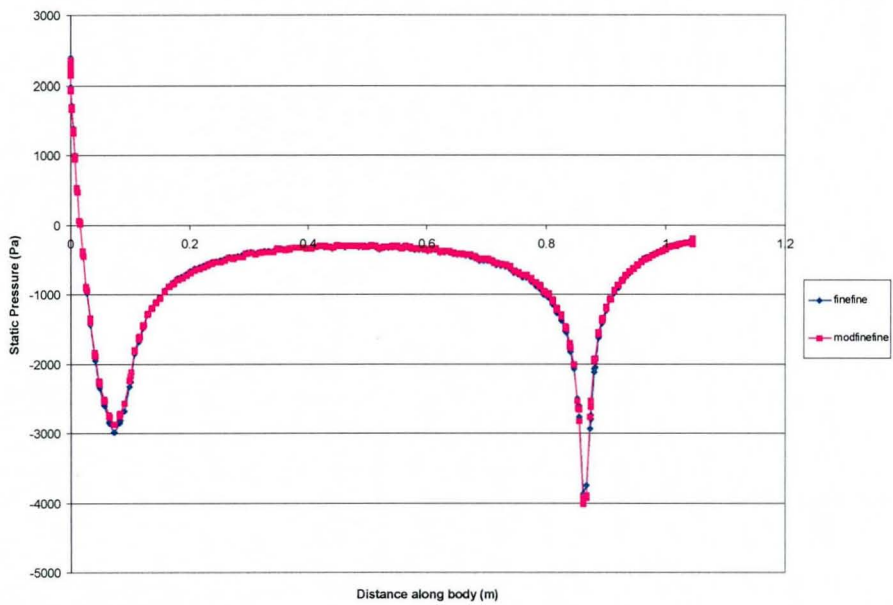


Figure 4.54 The static pressures distribution along the upper body centreline for the 35° angle case on both grids

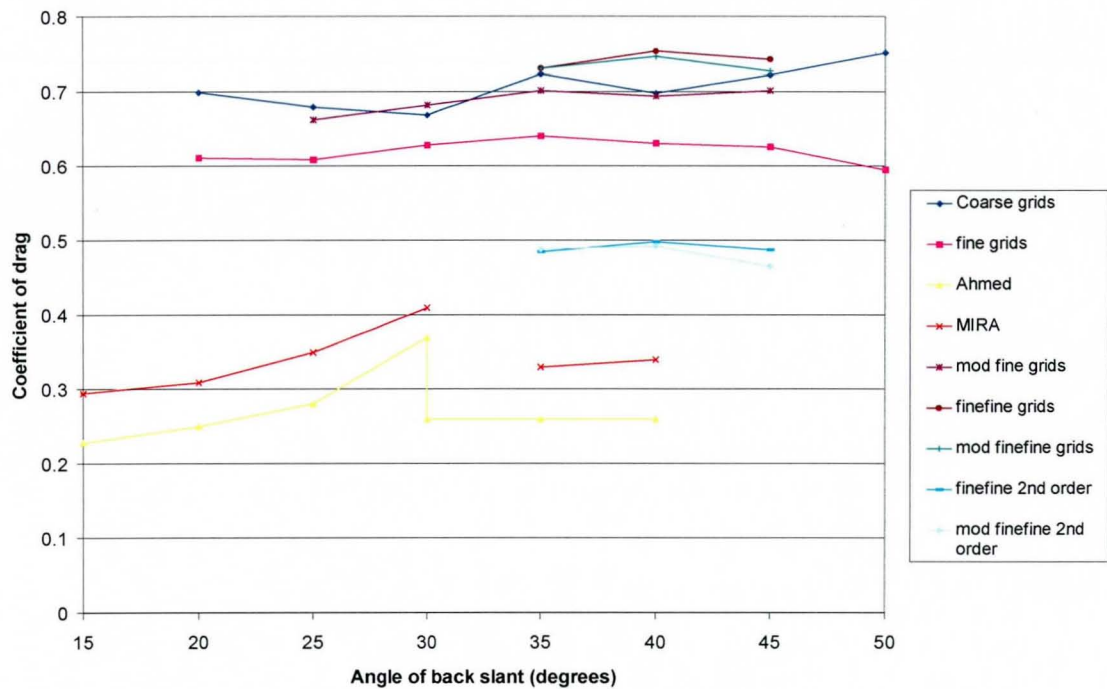


Figure 4.55 The drag results for the second order calculations on both grids.

The drag values, Figure 4.55, for these calculations shows significant improvements over the hybrid differencing cases seen earlier in the chapter. The levels of drag are significantly lower than previously. Also, due to the changes in the flow field, there is a small change in the drag values with the variation in back/slant angle. However, it is much smaller than in the wind tunnel experiments. It is also notable that the modified grid shows a greater drop after the 40° case peak than the unmodified grid. For the unstructured tetrahedral grid work presented here, the drag results for this grid were the closest to the experimental data.

The drag values above can also be compared with the CFD predictions produced by MIRA for this body [6] using a k-ε turbulence model and second order differencing. The comparison of these results from the work done here with the experimental and CFD results from the MIRA calculations are included in Figure 4.56. The results of the MIRA fine grids (162 000 cells) show a large rise at around 30° of slant surface and a slight drop thereafter. The very fine grids (224 030 cells), whilst only for the

higher slant surface angles, show a large drop in drag at around 30° which is consistent with the experimental results. It is interesting to note the similarity in the drag results from the MIRA CFD fine grids and the finefine grid results (both topologies) from the work presented here when used in conjunction with the second order differencing scheme. The number of cells in the work presented here is higher than that of the MIRA work, which is also fully tetrahedral. This highlights the importance of the numerical method in attaining the correct results for the drag over this type of body.

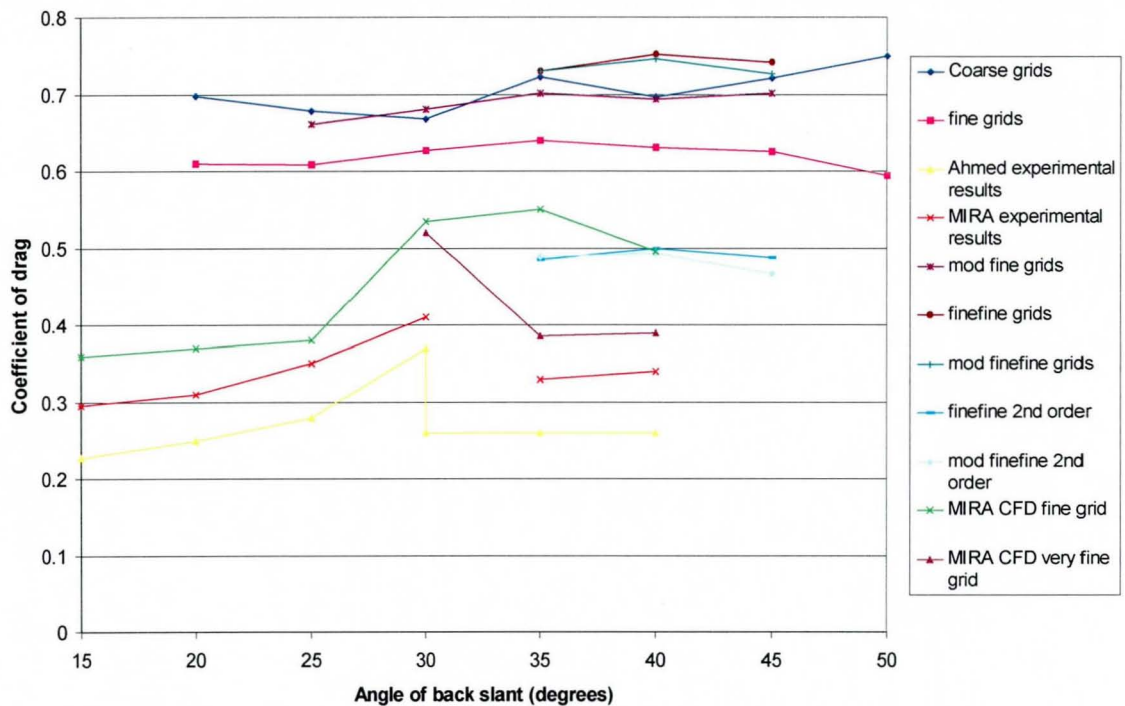


Figure 4.56 The drag values for the calculations from this work and the experimental and computational work from MIRA [6].

4.8 Conclusions

In this chapter several sets of unstructured grid calculations have been performed using a range of topologies and refinement levels. The geometry used was an Ahmed body in close proximity to the ground, with a set of rear back slant angles that varied from 25° to 50° . The results have been studied and comparisons made between the different grid types.

- **Flow Field Structure**

The flow fields for all the grids in this chapter resembled the expected structure from the wind tunnel results. The coarse and fine grids did not sufficiently resolve the twin longitudinal counter rotating vortices that follow the body. These were better predicted by the second level refined grids and particularly with the second-order accuracy discretisation. The flow around the nose and mid-section of the body was attached, as in the experiments. The flow over the rear of the body was also, apart from the exceptions outlined below, correctly predicted for both extreme cases of slant angle; the fully attached and fully separated flow patterns.

- **Drag Levels**

The drag levels seen for all calculations in this chapter are too high. The drag coefficients for the fine grids are higher than those for the coarse grid, which is surprising. The drag levels for the fine-fine grids are higher still. The modified fine grid drags were higher than the fine grid drags, which were unexpected. The modified fine-fine grids gave very similar drags to the fine-fine grids. The calculation using the Second Order Differencing scheme reduced the drag levels by around 30%. However, these levels still remain substantially higher than the levels seen in the wind tunnel results

- **Non Prediction of High Drag Flow Regime**

None of the calculations showed any indication of the high drag flow regime, observed in the wind tunnel results. between the fully attached and fully separated flow regimes.

- **Variation of Drag With Slant Surface Angle**

The drag did show signs of small variations as the angle of slant surface was increased. This change was smaller than seen in the wind tunnel, owing to the non-prediction of the high drag regime. The changes were attributable to changes in the strength of the twin longitudinal counter rotating vortices, as the slant surface angle was increased. The changes experienced with the coarse grid results, could not be associated with the changes in body shape due to the poor resolution of the grid.

- **Prediction of Change From Attached to Separated Flow**

The change from attached to separated flow was not predicted until around 10° after the slant surface angle at which the wind tunnel results changed. The angle at which the flow separated was also dependent on the grid topology, for all but the second level refined grids for the first-order differencing scheme results. The use of the Second Order Differencing scheme, with these highly refined grids, reintroduced some of the dependency of the solution on the grid topology. The fine-fine grids were attached, and mod-fine-fine grids were separated, for the 40° angle of slant surface.

- **Separation Starting From Top/Slant Edge**

The original grid topology forced the flow around the top/slant edge artificially, which prevented flow separation from the top/slant edge. The separated regions in the higher slant surface angles of the original grids all originated from part way down the slant surface. These separations were all attributable to adverse pressure

There are still areas for further work.

- The very high drag levels seen in these results - despite the lowering effect of the second order schemes. This is probably due to the still high levels of numerical diffusion in these calculations.
- The high drag regime seen in the wind tunnel results are not being reproduced.

The final question posed was whether each new piece of work had improved the results, and whether any pointers to further improvements had been found. The grids here allowed rapid change of size of cells from small to large, which permitted small overall grid sizes. However, the resolution of the flow field away from the geometry is less than in structured grids, introducing more numerical diffusion and less resolution into the predictions. It was felt that, in order to reduce this numerical diffusion of the solutions, and hence the accuracy of the solution, the grid away from the body should be more refined in areas of high change in the flow. These areas are above, to the sides, and behind the body. In addition, it was felt that the solution accuracy had suffered, due to the use of tetrahedrals over the body. If the faces of the computational cells can be aligned with the flow, to the extent that they are perpendicular or parallel to it, the accuracy of the solution will be higher. This is because of the way in which the equations governing the flow are discretised over the grid. To achieve this alignment it is desirable to use blocks of hexahedral cells in the areas required and tetrahedrals elsewhere. This type of grid is termed, a mixed grid. This type of grid structure will be applied to the flow over the Ahmed body in the next chapter.

5. Calculations Using Mixed Meshes

5.1 Introduction

The techniques used for generating the structured grids and unstructured grids described in earlier chapters are combined here to produce mixed element meshes. These meshes use different types of elements to produce what is currently felt to be, the optimum type of grid for this application. The orthogonal nature, regularity and gradual growth of the elements provided by the structured grids allow for high accuracy and resolution of flow in regions of high change (for example, near bodywork). By contrast, the unstructured tetrahedral grids allow rapid change of element size and reduce the total number of cells used, whilst also reducing the user overhead in mesh generation. This chapter will include a description of these methods and the results of the application of this type of grid to the Ahmed body test case. An example of a mixed mesh consisting of triangles and quadrilaterals can be seen in Figure 5.1 below. This method represents an improvement over the modelling techniques so far used in this study for the problem of a bluff body in close ground proximity. In this respect, this chapter addresses part of the overall objective for this study.

5.2 Grid Generation

There are three parts to any mixed mesh: the structured part, the unstructured part, and the interface between them. These will be examined in turn.

5.2.1 Structured Mesh

Structured meshes, as discussed in Chapter One, consist of blocks of hexahedrals glued together to form larger blocks. These groups of blocks can be fitted into the simpler parts of the solution domain. The groups of blocks must retain a largely cuboid shape, therefore, the range of spaces that can be filled using this type of block is limited. This reduces their applicability in the majority of large and complex problems.

The advantages of blocks of hexahedrals are that the accuracy of the discretisation over them is of a high order due to the high orthogonality and smoothness of volume change of the cells. This improves the accuracy of the solution. They also have other advantages. Firstly, the size of cells in any domain filled using hexahedral blocks can be more closely controlled than in other types of mesh. Secondly, whenever the cell sides are aligned with the flow direction, they provide even higher accuracy. This second advantage is important and requires careful attention from the user of the grid generator. If the grid cells are not aligned with the flow in regions of high change, the results of the CFD solution can be little more accurate than the results of the unstructured grids.

The structured or hexahedral part of the mesh is generated using the usual structured mesh generation techniques. This involves the "fitting" of blocks of hexahedrals to the surface of the geometry. These blocks are, typically generated initially using algebraic

methods. These methods place points regularly on the Non Uniform Rational Bezier Spline (NURB) surfaces of the blocks and join the points on the known surfaces to form the interior cells of the blocks. These initial faces and cells will be highly skewed and often result in non-valid (negative volume) cells. These poor quality cells are repaired using elliptical grid smoothers that ensure the maximum orthogonality of the blocks and faces is achieved, whilst giving a smooth and regular 3D grid. A detailed discussion of this is given in Anderson [3].

Following the generation of the hexahedral grid, it must be re-formatted into a data structure suitable for the unstructured solver. This is achieved by removing the *ijk* addressing data from the grid that describes it in a global environment, and replacing it by the local indexing of the type used in the unstructured grid. This uses the point and face data that describe a cell to identify the neighbouring cells. By identifying one cell, the remaining cells in the domain and their relationship (distance, etc) with the initial cell can be calculated.

This type of grid allows for a tight, regularly spaced, and orthogonal grid to be placed in regions where this is considered necessary. This requires some prior knowledge of the flow field, however. This information is fortunately available in the present problem from the previous calculations.

5.2.2 Unstructured Mesh

As mentioned previously, tetrahedrals are easily generated using one of the algorithms described in Chapter Two. The drawback of this type of grid is its comparatively low accuracy compared to a hexahedral grid. However, if the clustering of the cells (where there are high concentrations of smaller cells or low numbers of larger cells) is carefully controlled, they can provide good results.

The unstructured, or tetrahedral, part of the grid is generated in the same manner as the whole tetrahedral grids used earlier in this thesis. In this case, the Delaunay grid

generator is used. This type of grid allows for the transition from different parts of the structured grid domain, or to the boundary, using fewer cells than the structured grids. This type of grid is easier to implement, as it does not require the careful placement and matching of blocks, as in the hexahedral grids.

5.2.3 Pyramidal Mesh:

Pyramid cells are used as the interface between the hexahedral elements and the tetrahedral elements. One of the faces of the pyramid is square, which is butted up to the outside face of the hexahedral element. The other four faces of the pyramid are triangular and provide part of the boundary for the initial condition of the tetrahedral grid generator. As can be deduced from the previous statement, the grid generation follows the following order: structured hexahedrals, pyramids and then unstructured tetrahedrals.

The pyramids are generated in a similar manner to the Advancing-Front algorithm used in tetrahedral mesh generation described in Chapter Two. The quadrilateral face surface elements of the structured mesh are taken in turn, and a pyramid of perfect height constructed in the direction away from the structured mesh. The pyramid height is calculated using a factor of the average side length of the quadrilateral face. The top of the pyramid is found by taking the intersection of the diagonals of the base quadrilateral and constructing a new point along the outwards face normal through it.

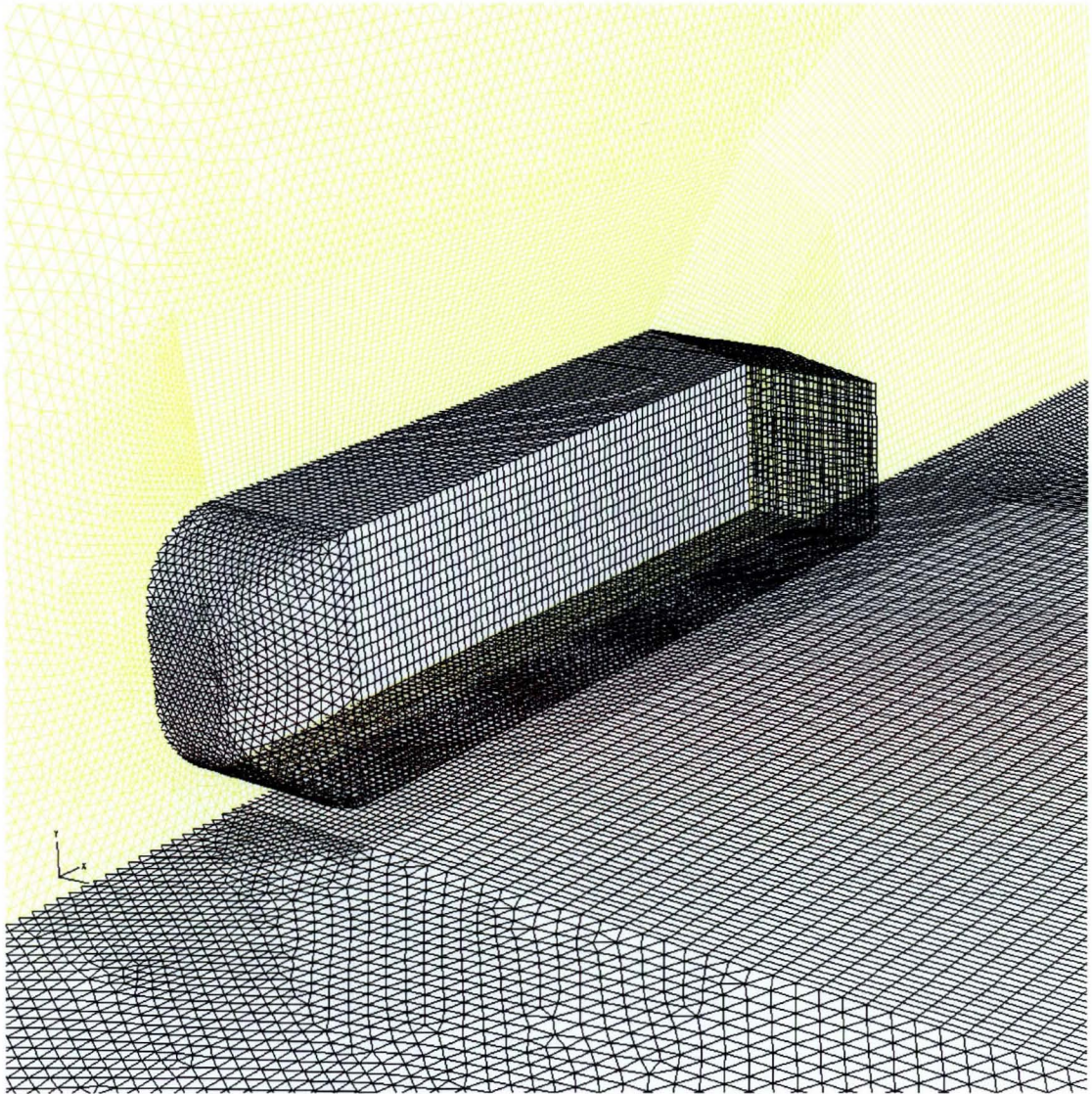


Figure 5.1 The close up of the surface mesh over the Ahmed body for the mixed meshes.

The boundary of any 3D mixed mesh will consist of triangles and quadrilaterals. The boundary grid of the mixed mesh over part of the Ahmed body can be seen in Figure 5.1. It shows the concentration of cells around the body, as well as how the hexahedral cells have only been used along and behind the body, and not in front of it. Hexahedral cells around the node of the body may have improved the resolution of the high flow gradients in that area. However, as can be seen in Figure 5.3, the cell volumes expand very slowly in this area due to the influence of the hexahedral cells on the unstructured mesh generator.

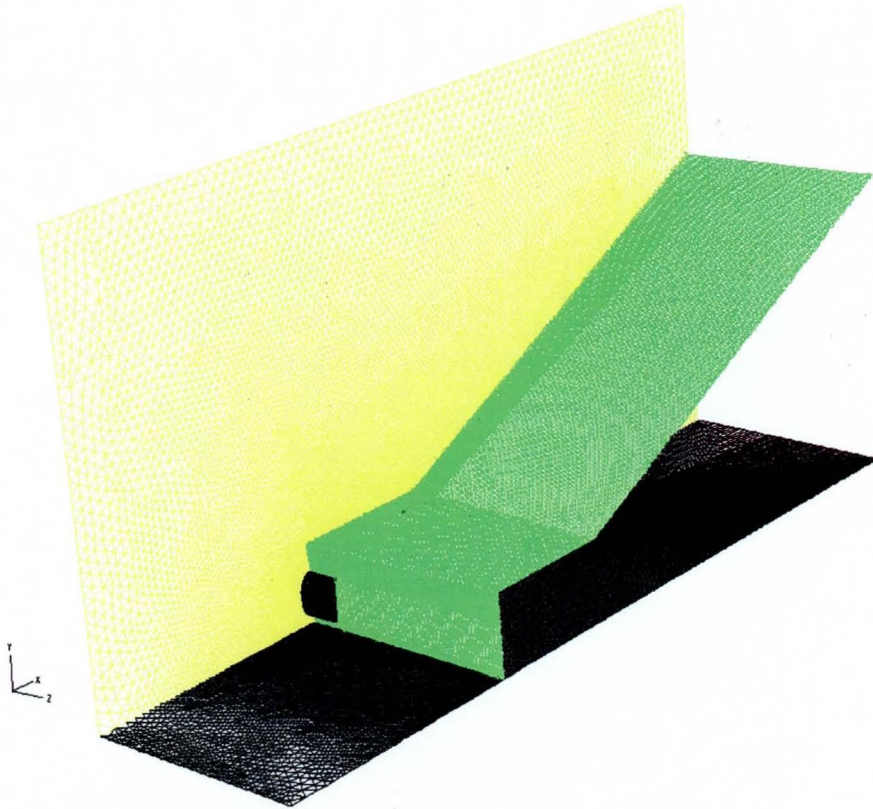


Figure 5.2 The boundaries of the hexahedral mesh over the Ahmed body. The region behind and below the green surface is hexahedral the rest tetrahedral.

Figure 5.2 illustrates how the mixed mesh is divided. The region below and behind the green “face” consists of hexahedrals, whilst the region above it is made up of tetrahedrals. The green face, itself, is made up of the pyramids that form the interface between the hexahedrals and the tetrahedrals. This figure demonstrates the type of mixed grid used in this study. The regions of hexahedrals and the tetrahedrals are not mixed up, that is, they are contained in entirely separate zones. There is a second type of mixed grid that has the different element types mixed in together in one zone. This type of grid is not used here.

The cells in the domain are clustered around the body and, to a lesser extent, the wake. The variation of the volume of the cells close to the body can be seen in a plot of cell volume on the symmetry plane (Figure 5.3). The hexahedral cells close to the body can be seen providing a uniform cell size, that gradually grows away from the surface. After this, the tetrahedral cells provide a more rapid change to the cell size.

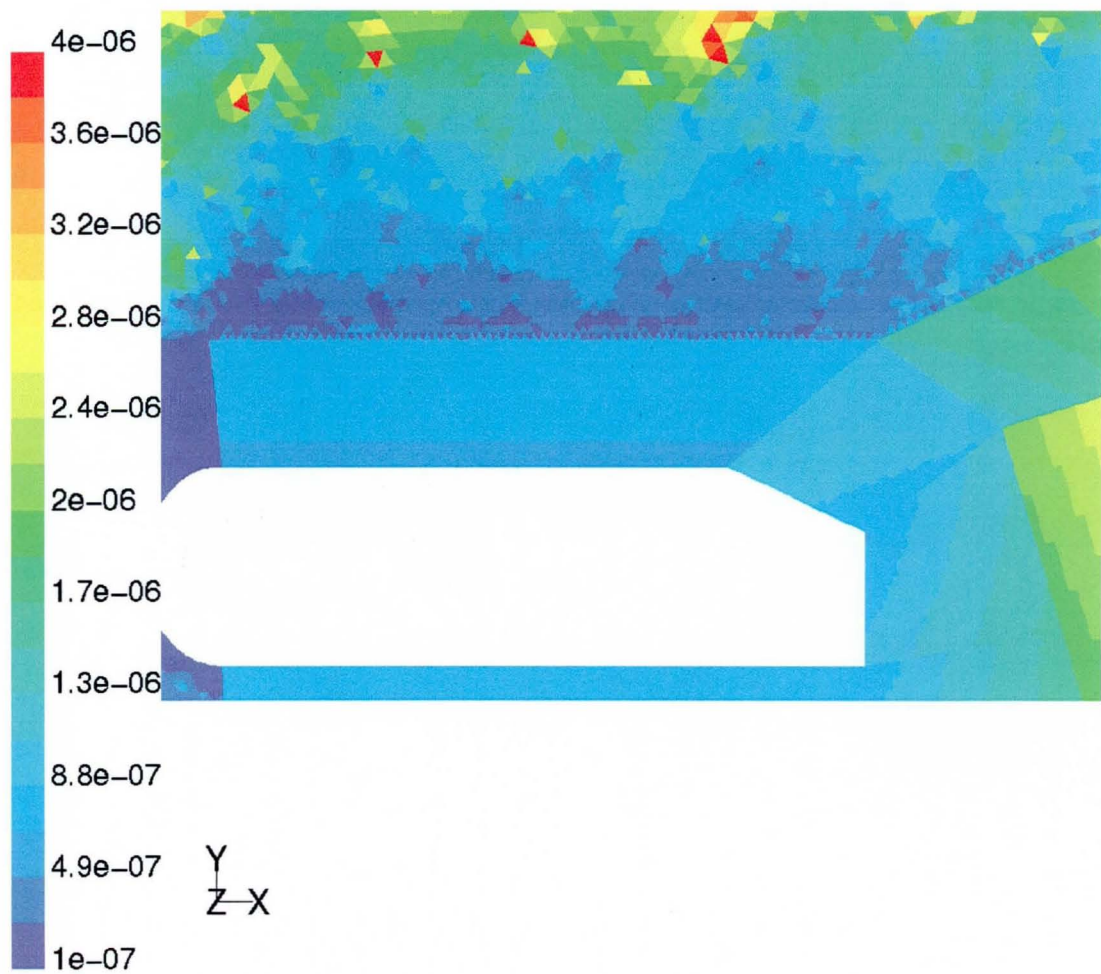


Figure 5.3 the contours of cell volume (m^3) on the symmetry plane close to the Ahmed body.

The actual size of the meshes produced using this method is given in Table 5.1.

Table 5.1 The size of the mixed mesh

	Total
Nodes	1176979
Faces	4377891
Cells	1640927

The mixed meshes are considerably more refined than the grids used in previous chapters (Chapters One and Four). This change reflects the increase in size of calculation possible on a typical desktop workstation over the period of study. The new mesh size should increase the accuracy of the solution and help to better resolve the flow field. The average body surface wall y^* value was 3000 for these grids.

5.3 Calculations

The mixed mesh technique described is applied to the Ahmed body over the range of back angles 25° to 45° . The variation between grids is minimal as the topology is maintained for the five cases investigated.

The turbulence model used was, as in the previous calculations, the $k-\epsilon$ two-equation model. The calculations presented in the following section used the first order differencing scheme. A calculation using the higher order schemes was performed on the 30° case. The higher order scheme used was dependent on the type of cell. The hexahedral cells allow the use of a third order QUICK scheme, however, the tetrahedral and pyramidal cells can only be used in conjunction with the second order scheme as described in [14].

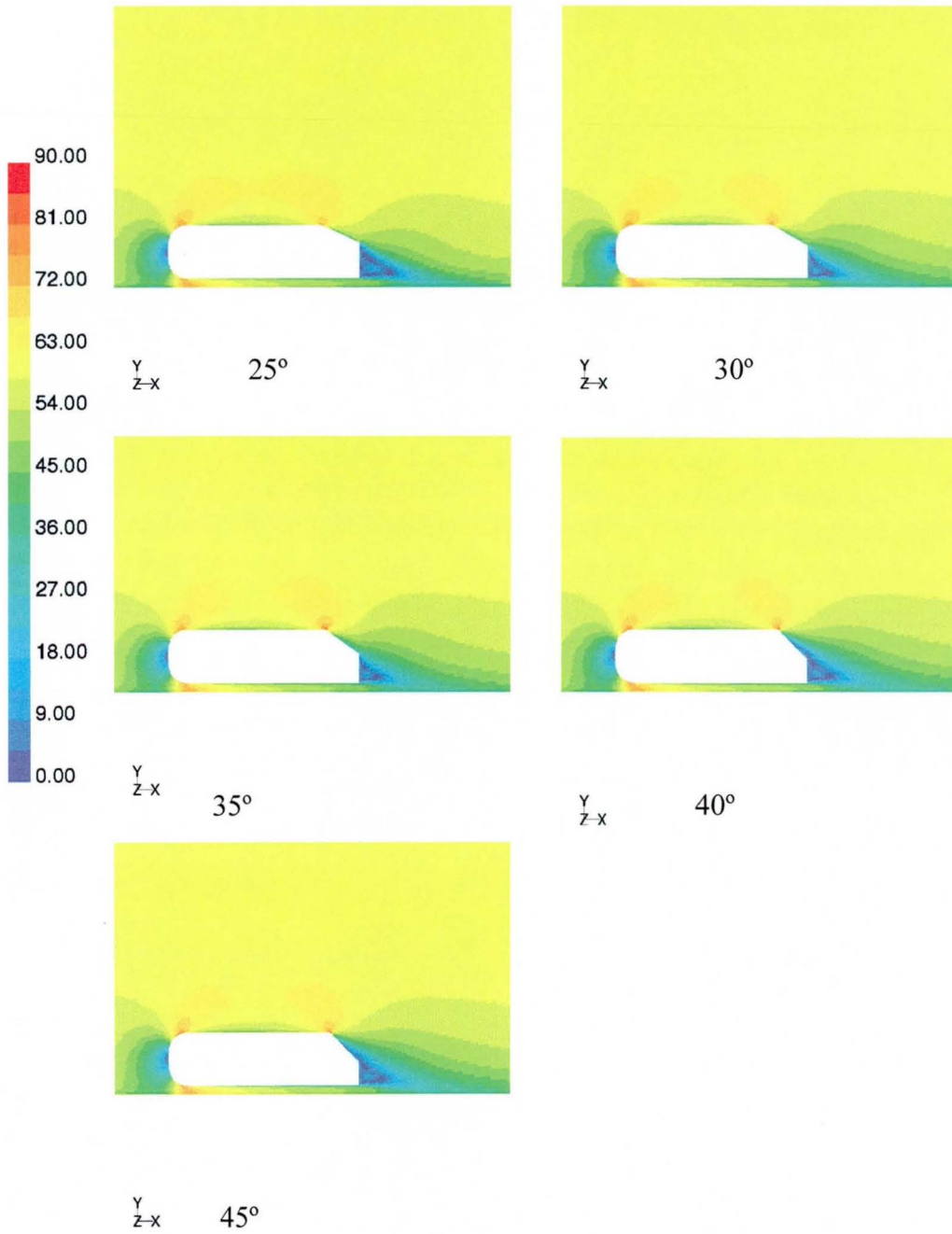


Figure 5.4 The contours of velocity magnitude (m/s) on the symmetry plane for the mixed mesh calculations.

The contours of velocity magnitude on the symmetry plane are illustrated in Figure 5.4. They indicate the flow to be attached until the back slant angle reaches 40° . This is, as expected from the work in Chapters One and Four, 10° later than seen in the experimental evidence. As shown in Chapter Four, this is attributable to the shape of the grid over the top/slant edge. The cells here follow the shape of the body in this area, which, as previously described, makes it easier for the flow to attach. The improved resolution of the grid in around the body has not removed the grid dependency of the solution. This is despite the higher number of cells for these calculations than in the fine-fine grids in Chapter Four, where the grid dependency was greatly reduced. The area around the top/slant edge is of particular importance with structured grids (as seen in the Chapter One, the initial structured calculations done on the Ahmed body), as there is no randomness to the cells, as could be expected in an unstructured grid. This amplifies the effect of the grid shape on the solution.

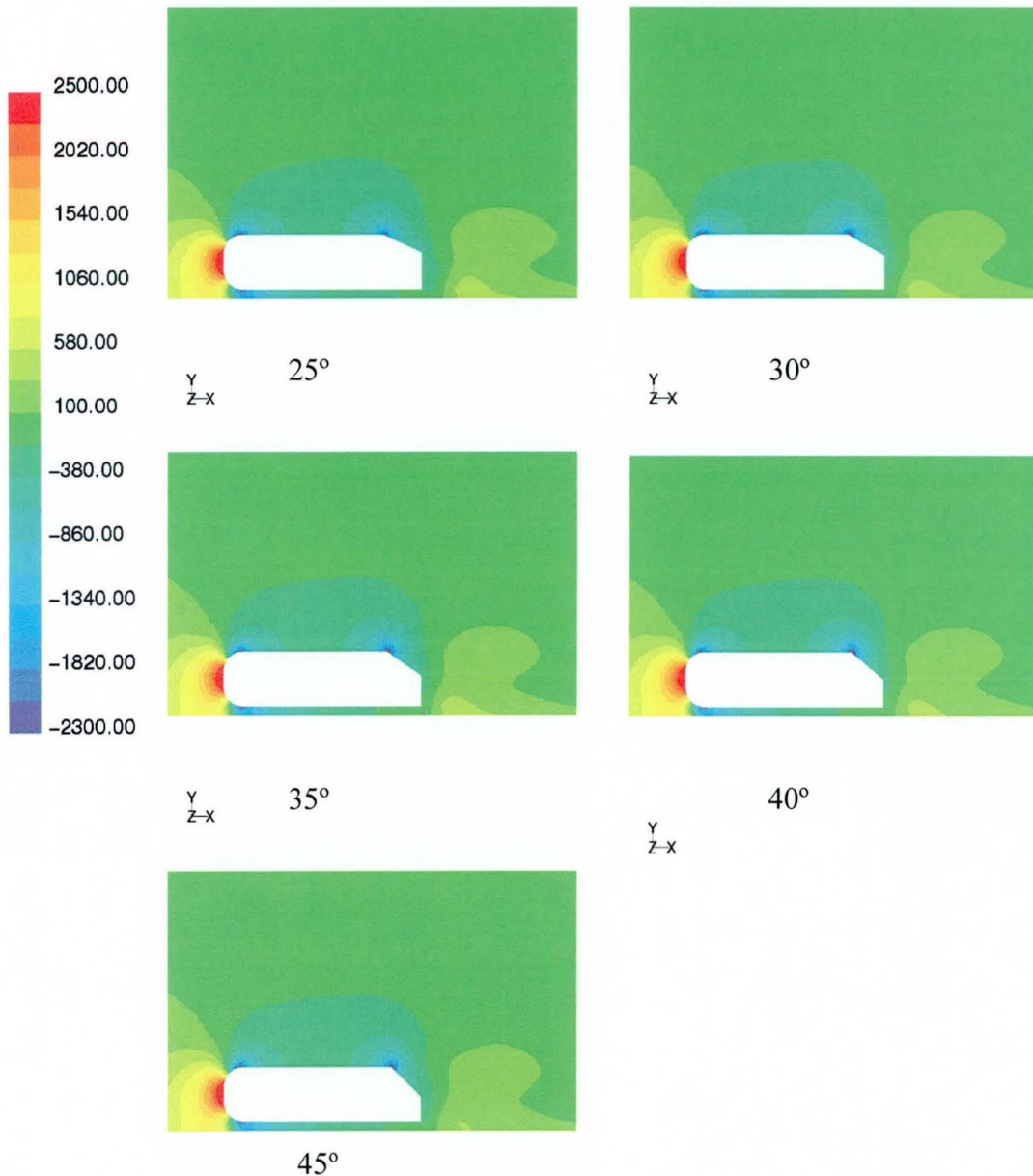


Figure 5.5 The contours of static pressure (Pa) on the symmetry plane for the mixed mesh calculations.

The contours of static pressure on the symmetry plane of the geometry reveal the very gradual progression to separation through the angle sweep. It also demonstrates the drop in static pressure over the back/slant edge for large angles of back slant. This trend was also seen in the unmodified grid structures used in Chapters One and Four. At these large angles of slant surface, the wind tunnel results indicate no static pressure trough.

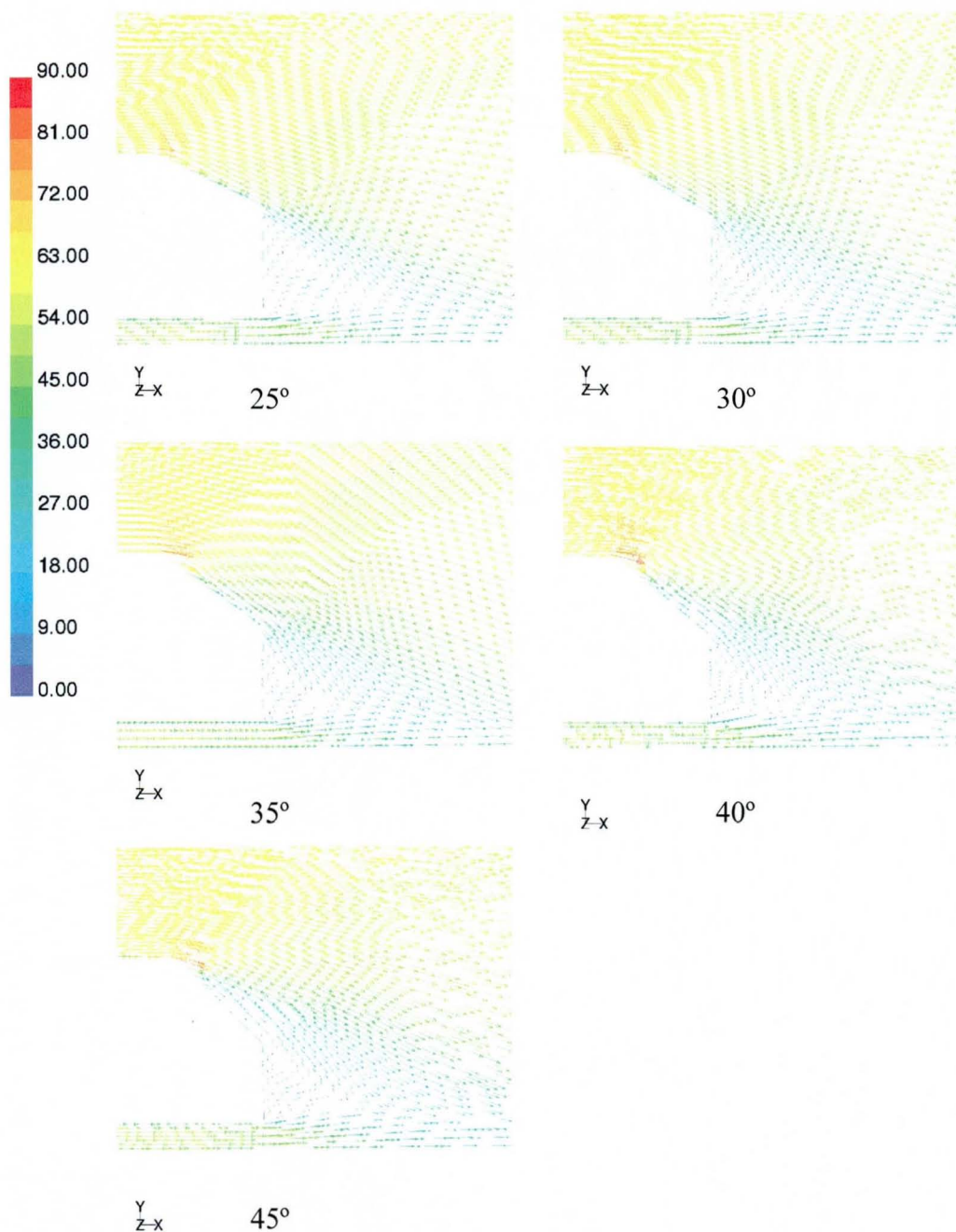


Figure 5.6 The velocity vectors over the rear of the body on the symmetry plane for the mixed mesh calculations (coloured by velocity magnitude, m/s).

The velocity vectors on the symmetry plane, shown in Figure 5.6, illustrate more clearly the development of the separation. Rather than the sharp separation expected for this type of body, the flow remains attached at the top/slant edge for all angles of slant surface. Subsequently, there is a gradual reduction in the velocity along the slant

surface due to the adverse pressure gradient seen there. These plots also show the symmetry plane slice through the counter rotating vortices behind the base surface of the body, that are part of the horseshoe vortex structure that follows it (not to be confused with the twin longitudinal counter rotating vortices). As the angle of the slant surface increases, the relative strengths of the upper and lower of these vortices does not change dramatically, highlighting the failure of the flow to separate from the slant surface in the correct manner. The structure should, for high angles of slant surface, exhibit a stronger upper vortex directly after the slant surface. The wake of the body appears to be closing up more quickly in the CFD results than expected, as demonstrated by the size of this vortex structure. For the fully separated result, this vortex structure should occupy the region after the slant and base surfaces of the body completely. These figures are a good example of the better resolution of the region behind the body than the tetrahedral grids.

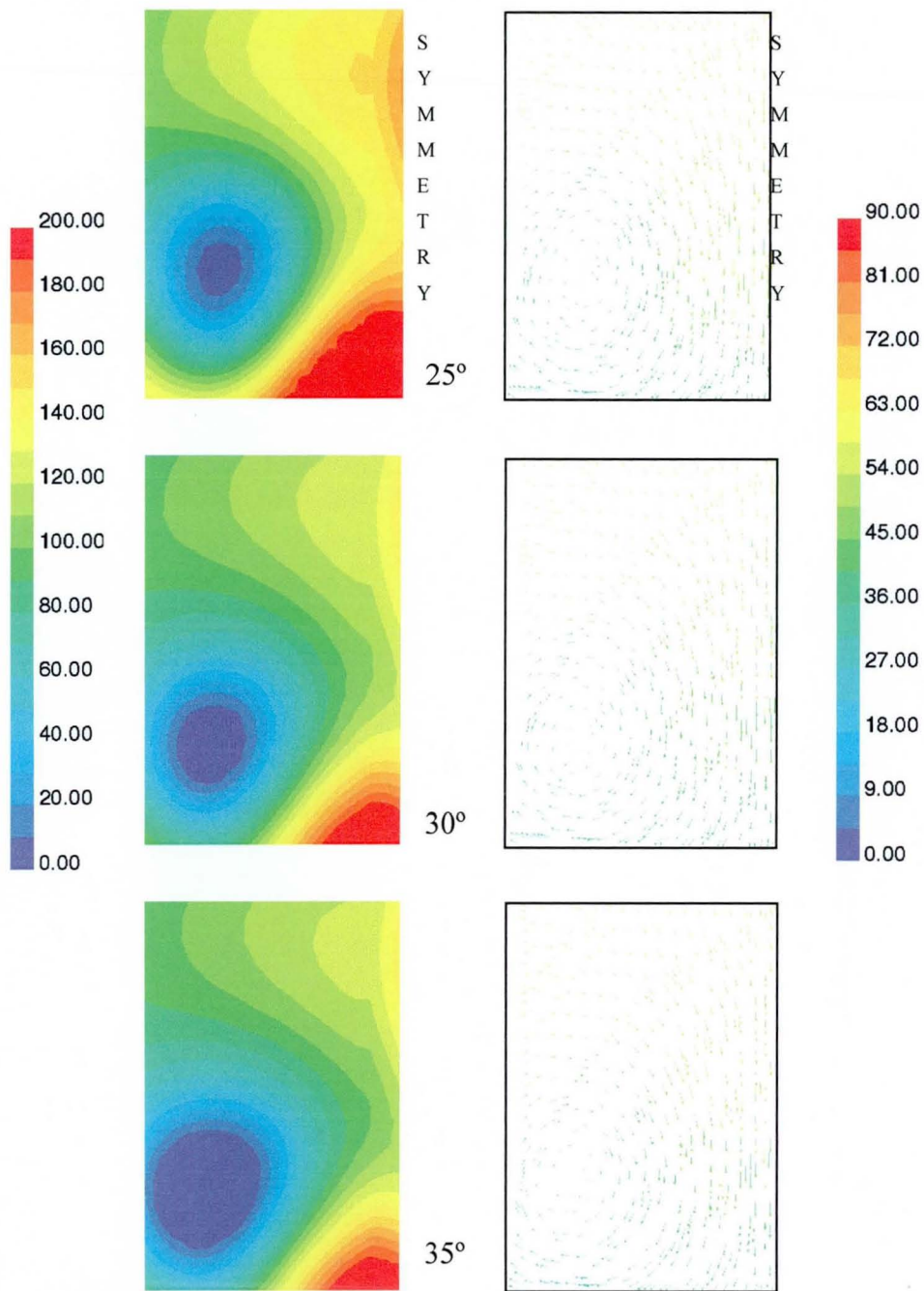


Figure 5.7 The contours of static pressure (Pa) on the left and the velocity vectors coloured by velocity magnitude (m/s) on the right. Shown here on the vertical plane 0.5 metres behind the body for the 25°, 30° and 35° cases. The symmetry plane is on the right of each picture.

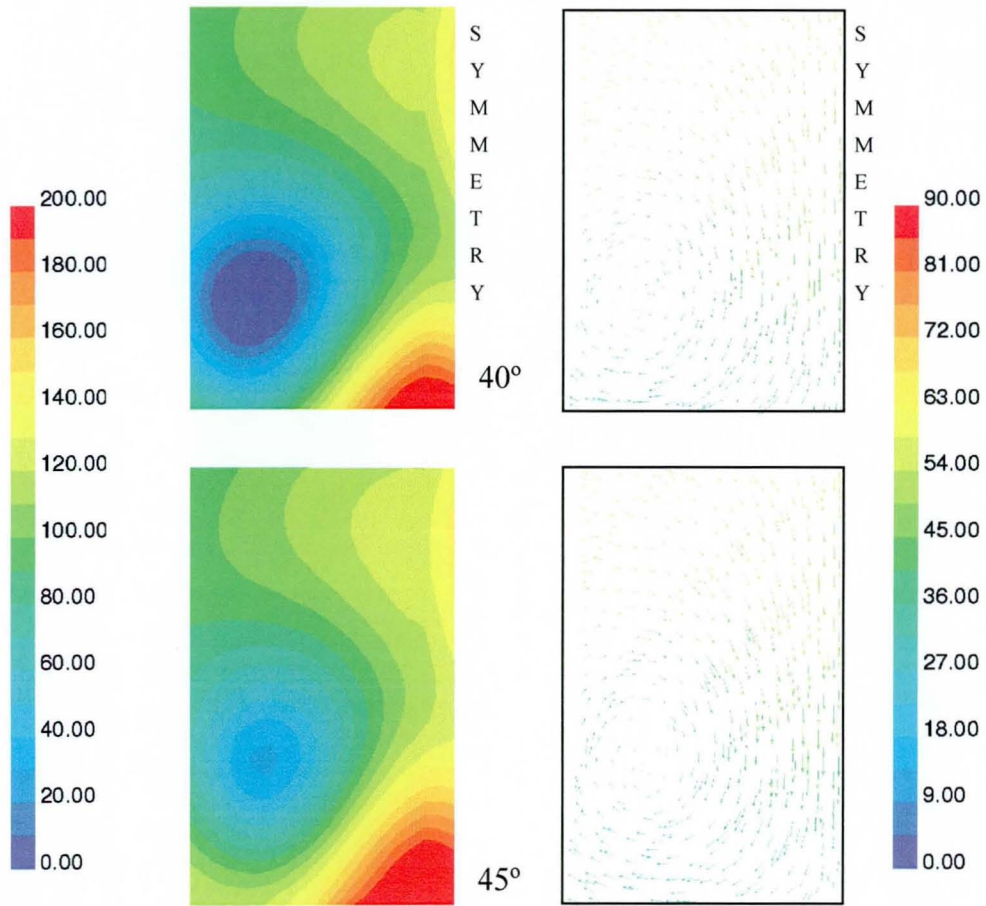


Figure 5.8 The contours of static pressure (Pa) on the left and the velocity vectors coloured by velocity magnitude (m/s) on the right. Shown here on the vertical plane 0.5 metres behind the body for the 40° and 45° cases. The symmetry plane is on the right of each picture.

The plots of velocity vectors and velocity vectors on the plane 0.5 metres behind the body (Figure 5.7 and Figure 5.8), show the high resolution of the flow field there, in contrast to the tetrahedral grids. They can be directly compared to the plots of velocity vectors (Figure 1.27) and pressure contours (Figure 1.29) for the 30°, high and low drag regime, experimental results. The plots show clearly how the flow pattern changes between 40° and 45°, as the flow separation from the slant surface increases in size, resulting in the lower strength of the longitudinal counter rotating vortices. This increase in separation can be seen in Figure 5.9. Note how the separation grows from the end of the slant and not the top, as is the case in the wind tunnel experiments.

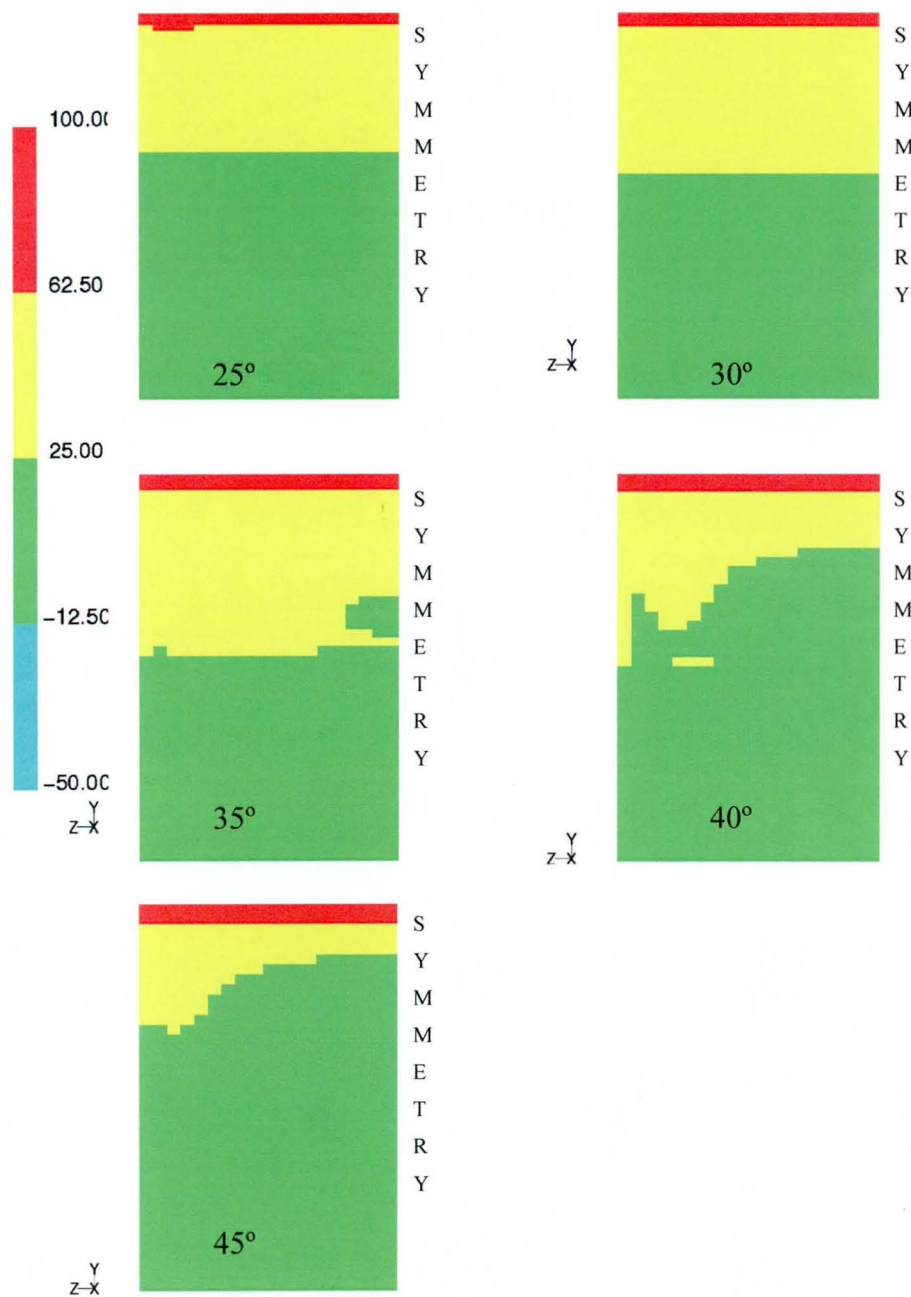


Figure 5.9 The contours of velocity (m/s) on the rear of the Ahmed body for the mixed meshes. A lower number of levels are shown to give a clearer picture.

The drag values are given in Table 5.2 and Figure 5.10. As can be seen, the values are higher than the tetrahedral grids and much higher than the wind tunnel results. The value for the 25° case is lower than the rest of the results. This is reflected in the

lower strength longitudinal counter rotating vortices seen in Figure 5.7 and Figure 5.8. There is, then, a small rise in the drag between 30° and 35° and, again, between 35° and 40° before a slight drop to 45°. These are, again, reflected in the strengths of the longitudinal counter-rotating vortices. Also included in Figure 5.10 is the drag result from the 30° case using the higher order differencing scheme. This change has significantly lowered the drag level as expected. It is reasonable to expect the drag values for the other angles of slant surface to be equally reduced.

The breakdown of the drag for the 40° slant surface angle (Table 5.3) gives a more detailed analysis of which parts of the body are producing the correct drag results, when compared to the wind tunnel results. These numbers can also be compared to the results of the structured grid tests from the introduction. It is interesting to note that the majority of the drag is being generated on the front of the body for the CFD models, particularly the mixed mesh result. The values for the shear drag are, as in the structured grid calculations, in reasonably good agreement. The slant and base surface pressure drags for the mixed mesh are in good agreement with the measurements from the high drag result from the wind tunnel, and represent a significant improvement over the structured grid results. It is interesting to note, therefore, that the effect of the mixed meshes has improved the drag prediction on all parts of the body, bar the front.

Table 5.2 The table of lift and drag values for the mixed mesh calculations.

Angle	Drag (N)
25	84.849
30	96.767
35	98.003
40	98.399
45	97.073

Table 5.3 The break down of the drag over the Ahmed body for the 40° slant surface angle. Also shown (for 30°) are the wind tunnel high and low drag values [2] and the results of the structured grid tests from Chapter 1.

	Shear	Front	Slant	Base	CD
Mixed grid	0.062	0.403	0.291	0.040	0.797
Structured grid 2C	0.046	0.278	0.132	0.163	0.619
Structured grid 2M	0.071	0.205	0.126	0.176	0.578
Ahmed high drag	0.057	0.016	0.213	0.092	0.378
Ahmed low drag	0.051	0.019	0.089	0.101	0.260

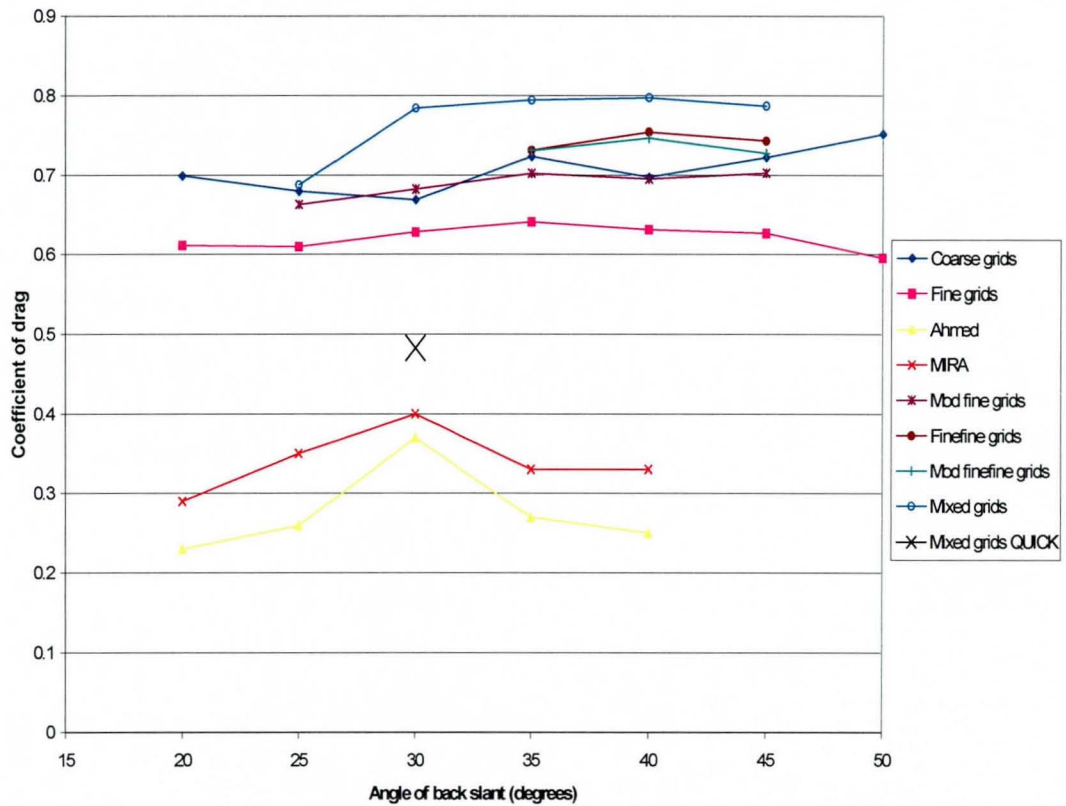


Figure 5.10 The comparison of the drag coefficient variation with angle of back slant for the various types of grids.

The plots of static pressure on the upper body centreline (Figure 5.11) show the increasing strength of the pressure trough around the top/slant edge until the 40° case, after which, there is a slight reduction as the separation increases in size.

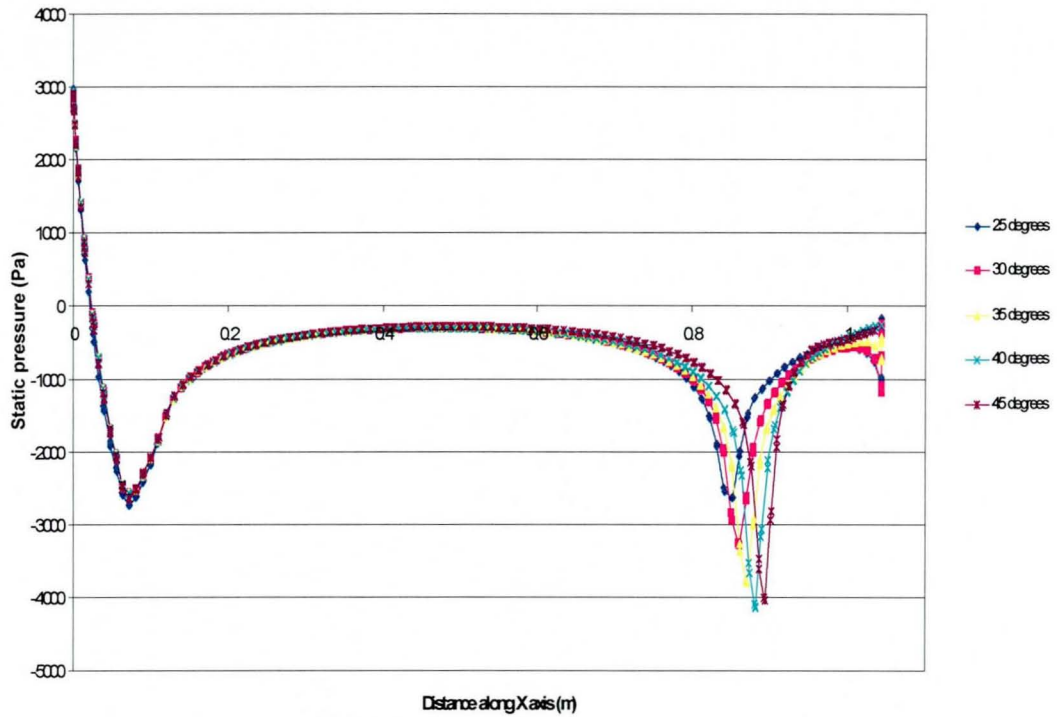


Figure 5.11 The static pressure on the upper body surface centreline for the mixed grid calculations.

5.4 Conclusions

The mixed grid was developed to bring together the best elements of the two existing types of mesh. That is, the high accuracy brought about by the orthogonality and gradually changing properties of a structured mesh and the more computationally efficient mesh usage from the tetrahedral grids. By combining these methods, a mesh that was of high quality where it was needed, and less cells where it was less important, could be generated. This allowed a higher possible mesh size and reduced the high numerical diffusion levels seen in the fully tetrahedral grid results. In addition, the meshes produced were of a clearly higher quality close to the body, than the tetrahedral meshes.

In considering the objectives of this thesis, the results of this work showed encouraging signs that the solution of the flow over the Ahmed body has been improved by the use of this type of grid. In particular, the flow behind the body has been resolved much more clearly than in the corresponding fully tetrahedral grid calculations. This is a direct consequence of the use of regular, orthogonal, high quality hexahedrals in this area. The flow still shows a resistance to separation, which is, as in previous grids (Chapters One and Four), due to the shape of the grid over the back/slant edge. When the separation does occur, it is again of the wrong kind, being driven by a pressure gradient on the slant surface rather than the sharp edge. Consequently, the separation begins at the rear of the slant surface rather than the top. There is evidence of the separation beginning on the symmetry plane and growing outwards from there with increasing angle of back slant. However, as the separation starts from the bottom of the slant and not the top, as in the experiments, it is difficult to relate this pattern to the wind tunnel results.

The complete separation from this surface is not predicted at all for this type of grid over the range of slant surface angles tested in this study. Despite this, the drag results, although too high throughout the range of angles, do show some slight

evidence of a rise, and subsequent drop, around the 40° angle. This is attributable to the increasing strength of the longitudinal vortex structure behind the body up to the 40° case, and the subsequent weakening of this structure due to the changes to the separation from the slant surface. The mechanisms of this change in drag are similar to those that create the changes seen in the wind tunnel, but, due to the incorrect separation growth, not as pronounced.

Despite these problems it is clear that the method outlined in this chapter is better at resolving the flow field within the wake and potentially, with increased refinement levels, more accurate when predicting the correct flow pattern of separation.

6. Conclusions And Recommendations For Further Work

The main objective of this study was to assess the application of CFD methods to the flow over a bluff body in proximity to the ground. In addition to this main objective, the following questions were posed in order to provide a framework for the study:

- Are the flow fields produced in the CFD predictions similar to the ones suggested by experiments?
- Are the bulk levels of drag in the CFD model similar to those seen in experiments?
- Can the CFD calculations reproduce the rise and sudden drop of the drag factor observed the experiments?
- Can the CFD results be improved upon - in terms of either accuracy or efficiency?
- Can this type of flow problem be represented by time-averaged CFD predictions or can some aspects only be captured by unsteady CFD?

The bluff body used throughout the study was the Ahmed body. By varying the back slant angle, this is capable of reproducing all the significant flows patterns relevant to road vehicle aerodynamics, most importantly, attached flow over the front portion, a streamwise trailing vortex pair of varying strength, and quasi-2D turbulent wakes. The overall drag characteristic of this body exhibits the classic rise in drag coefficient, as the vortex strength increases, up to a critical angle of 30° , at which point the vortex system bursts and the drag drops significantly. This drop in drag coincides with the merging of the separation bubbles on the slant and base surfaces.

The work completed in this study can be briefly summarised as follows:

Chapter 1. The problems surrounding the prediction of the external flow around passenger automobiles were investigated and discussed; an initial parametric assessment of the ability of a structured grid to predict flow over the Ahmed body was completed. The parameters varied were grid topology, grid size, turbulence model and differencing schemes. These calculations were instrumental in defining the objectives for the thesis.

- Chapter 2.** An unstructured tetrahedral grid generator for use on bluff bodies in close proximity to the ground was developed based on the Advancing-Front technique.
- Chapter 3.** The above developed method was demonstrated using test cases with known results and shown to be capable of generating grids which could be used in a current unstructured grid solver (FLUENT).
- Chapter 4.** Several unstructured tetrahedral grids over the Ahmed body, using three levels of successive refinement and two grid topologies, were generated. The results of the CFD solutions with these grids were compared against wind tunnel and structured grid results.
- Chapter 5.** A high resolution mixed grid over the Ahmed body was generated and CFD solutions obtained. The results were, again, compared to wind tunnel and previous results.

The significant points made in the discussions of the results in each chapter are summarised below:

Chapter 1.

Two levels of refinement using a structured type grid were employed on two different topologies. In addition the computational experiments evaluated a higher order differencing scheme and two turbulence models. None of these calculations was able to capture all three flow modes. The results can be summarised as follows:

- The separation or attachment of the flow to the slant surface depended on the grid topology over the top/slant edge.
- Separation from the slant using an initial topology with grid lines wrapped around the body was later than seen in wind tunnel results, and was of a type associated with an adverse pressure gradient rather than a sharp edge.
- The second type of grid topology produced solutions which separated at earlier angles of slant surface than the first.
- No calculation captured the high drag flow (separation on slant surface) regime.
- All separations began from the bottom of the slant surface rather than the top, in contrast to the wind tunnel results.
- Drag levels integrated from surface pressures over body were too high.

- The fine grids and/or QUICK differencing method did not alter the flow pattern significantly, however, drag levels were reduced. This can be attributed to lower levels of numerical diffusion.
- The Reynolds Stress turbulence model had a similar effect on the flow field and drag values. This was due to the reduction of the turbulent energy predicted on the front of the body which is carried along the body.
- None of the grids and/or methods used in this first chapter captured the jump in drag, as the angle of the back slant was increased.
- The difference in the drag level between the two grid topologies was consistent with that seen between the high and low drag regimes for the wind tunnel model.

Chapter 2.

The development of a 2D and a 3D unstructured mesh generator in this work can be summarised as follows:

- The Advancing Front and Delaunay mesh generator families were researched and discussed
- The Advancing Front grid generator was chosen for development due to its better resolution of the flow field through a more rigorous adherence to a specified grid size within a given domain.
- Due to the non-availability of an unstructured tetrahedral grid generator, the Advancing Front based method was developed first in 2D then in 3D.
- The quality of the grids generated by this method were found to be initially of a low quality due to the heuristic nature of the algorithm, resulting in poor cells towards the end of the triangulation phase.
- A smoothing and swapping algorithm at the end of the main grid generation stage vastly improved the cell quality.

Chapter 3.

As an initial validation exercise, the Advancing Front grid generator was applied to three-dimensional versions of two well-known flow problems: the lid driven cavity and the backward-facing step. The Advancing Front grid generator was used to generate grids for these two geometries. As a control experiment, the same geometries

were meshed using a commercial Delaunay grid generator. The results can be summarised as follows:

- The results of the lid driven cavity calculations demonstrated faithful representation of the flow field.
- The Advancing front results gave greater resolution of the recirculation that is the main feature of the flow, however, at the cost of more cells in the computational domain.
- The re-attachment point of the turbulent backward-facing step was accurately predicted. The Advancing Front grid was, again, marginally closer, at the expense of many cells than the Delaunay grid

These results made it evident that the grid generator proposed here was at least as good as existing commercial grid generators. However, there was a penalty in terms of grid size. The next stage was to assess the applicability of the two grid generators to the problem of the flow over a bluff body in close proximity to the ground. The results of the comparison demonstrated that:

- Both the grid generators were applicable to the problem.
- The flow field was better resolved in the Advancing Front grid.
- The number of cells was much lower in the Delaunay grid.
- The overall geometric quality of the Delaunay grid was higher.
- The drag values for the two grids were too high.

Chapter 4

Having developed and validated the methods involved, a set of unstructured meshes were generated over the Ahmed body for a back slant angle sweep:

- Higher density grids were used than the validation grids used in chapter 4.
- The drag levels were still much too high, approximately twice those seen in the experimental values, and similar to the level seen in the structured grid predictions.
- No meaningful change of drag force with increasing slant surface angle was found.
- The flow fields, whilst being substantially correct, showed no separation from the slant surface for any angle.

A second set of grids was developed using considerably more cells (the edge ratio used to define the boundary edges of the 2D grid was halved) The results using this grid to predict the flow over the Ahmed body were much improved:

- The flow now separated from the slant surface at angles above 40° .
- The drag levels were also reduced
- A slight peak in the drag was seen for the angle of slant surface at which the flow separated.

Despite these improvements, several problems remained:

- The separation occurred too late in the angle sweep, and it was not a separation of the type associated with a sharp corner.
- As detailed in Chapter Four, the topology of the grid around the top/slant edge was believed to influence the momentum flux from the flow over the top of the body onto the slant surface, regardless of the angle of the bodywork.
- The flow then separated from the slant surface due to an adverse pressure gradient, explaining the late separation seen in the angle sweep.

A third set of grids was developed using an alternative topology of grid over the top/slant edge designed to align the grid and the expected flow direction around this edge. This was achieved by producing meshes that had faces aligned with both flow patterns. The results are summarised as:

- The separation from the slant surface was now occurring at a lower angle of back slant, 40° as opposed to 45° before. Still higher than the wind tunnel result.
- The separation that occurs in the modified grids WAS complete from the slant surface. In addition IT was the correct type associated with a sharp edge.
- Disappointingly, the drag levels were now higher. This served to demonstrate the grid sensitivity of the results; despite similar grid sizes and qualities the drag has risen considerably.
- The slight drag peak was still present although, again, too small compared to the wind tunnel results.
- The modified grid did not capture the high drag flow regime seen in the wind tunnel results at around 30° .

The higher drag levels, and the fact that the two grid topologies were giving different drag levels, indicating that there was still grid dependency in the solutions. With this in mind, a further two sets of grids were generated, one for each topology. These grids were even finer, using an edge length of half that used previously. These grids produced improved results:

- The drag predictions for the two grid topologies were now similar to each other for all the angles tested, implying greatly reduced grid dependency.
- The flow patterns were now similar between the grids for all angles of back slant.
- The drag levels were still too high compared to the wind tunnel observations.

As determined in the structured mesh study (Chapter One), the level of drag on a given grid was reduced by the use of a higher-order-differencing scheme. The tests using the finest two unstructured grids were therefore repeated with A 2nd order differencing method.

- The drag levels were reduced substantially but still not to the levels seen in the wind tunnel results.
- The flow pattern for the 40° cases indicated attached flow for the modified grid, and separated for the modified grid. This was, however, only on the centreline. The rest of the slant surface showed substantially similar velocities for the two grids, at all angles of slant surface.

Chapter 5

The high levels of drag predicted may be attributable in part, to the high levels of numerical diffusion known to occur in tetrahedral grids used in complex flows where substantial grid/flow misalignment can occur. Hexahedral elements, as used in Chapter One, are known to reduce these levels. In the introduction, hexahedral meshes were discounted, due to their wastefulness of cells away from the body. This remains true. However, if the regions of hexahedrals are kept to areas of interest and important flow features, their benefits can be exploited and efficiency problems negated. This argues for the use of mixed grids.

The mixed grids in this study have hexahedral blocks of cells near the body and in the wake region. A layer of pyramids then completes the boundary grid for the tetrahedral grid used to fill the rest of the domain. The results can be summarised as follows:

- The separation is not of the correct type when compared to the wind tunnel results. As in previous calculations in this study, the grid topology has affected the flow over the join at the top and slant surfaces of the Ahmed body.
- The intermediate flow regime of a separate separation on the slant surface is not predicted.
- The change in slant surface angle does produce a slight change in drag in line with that seen in the wind tunnel experiments.
- The levels of drag seen are too high, mostly attributable to the first order discretisation scheme and basic turbulence model.
- The flow resolution is greatly improved.

The greater accuracy of the solution of the flow in the wake is important, however, the hexahedral cells over the top/slant edge of the body have, as in the introductory structured grid work, influenced the flow pattern there. The unstructured grids reduced this problem by increasing the grid resolution at that point. It must be concluded that many more cells are required in the area over the top/slant edge, even than in the current mixed mesh. It is important to note that, over four times the number of grid line were used in the axial direction over the body in the mixed grids, than in the fine structured grid from the introduction.

The various approaches to the meshing structure clearly have a large effect on the results seen. The refinement of the mesh also is of great importance to the accuracy of the result. To conclude the work the following points can be made:

1. Fully attached and fully separated flow fields were well predicted
2. Grid dependency can be reduced by grid refinement
3. Flow patterns are grid dependent until very fine grid levels are reached
4. High drag flow regime not predicted
5. Drag levels reduced by higher order differencing schemes
6. Drag levels still too high

The main objective of the study, to assess and improve the use of CFD to predict the flow over the Ahmed body, has been completed. A wide range of methods and algorithms has been tested. The results indicate that the full separation from the rear

of the slant to be highly grid sensitive, especially when hexahedral cells are used in that region. The use of unstructured grids reduced this grid dependent effect. However, the high drag flow field has not been reproduced by any calculation in this study. The levels of drag were found to be highly dependent on the choice of turbulence model and differencing scheme.

The results in this thesis suggest that with careful application of the various types of grid, the correct flow field can be achieved for some slant angles. , however, the solution method used in this study (ie steady state RANS solutions) is clearly not capable of capturing any unsteadiness of the flow. Whilst for most slant angles this is not too serious, it is felt that unsteadiness is at least in part responsible for the sudden switch of flow mode seen at 30° of slant surface on the Ahmed body. It is therefore recommended, as further work, that some effort be directed to applying unsteady CFD solution algorithms to this problem. This may take the form of A time-accurate CFD approach, retaining a statistical turbulence model, or as a Large Eddy Simulation (LES). The geometry of the Ahmed body is sufficiently simple to allow both these methods to be applied and contrasted. This would do much to establish whether the flow mode switch, which is an important feature of ground vehicle aerodynamic flows, can be captured by an unsteady CFD approach.

1.10 References

1. Adey, P.C. & Greaves, J.R.A., "The Application of a 3-D Aerodynamics Model to the Sterling 825 Body Shape and Comparison With Experimental Data", SAE Paper 880456, 1988.
2. Ahmed, S.R., Ramm, G. & Faltion, G., "Some Salient Features of the Time-Averaged Ground Vehicle Wake", SAE paper 840300, 1984.
3. Anderson, J.R., "Computational Fluid Dynamics: basics with applications", ISBN 0-07-001685-2, McGraw Hill, 1995.
4. Aurenhammer, F., "Voronoi Diagrams: A survey of a fundamental geometric data structure.", ACM Computing Surveys, 23:345-405, 1991.
5. Baker, T.J., "Three dimensional mesh generation by triangulation of arbitrary point sets.", AIAA paper 87-1124, June 1987.
6. Baxendale, A. J., Graysmith, J. L. & Howell, J., "Comparisons between CFD and Experimental Results for the Ahmed Reference Model", Royal Aeronautical Society Conference on Vehicle Aerodynamics, Loughborough, July 1994.
7. Bonis, B., Cogotti, A. & Vitali, D., "Numerical and Experimental Flow Field Survey of an Aerodynamically Efficient Passenger Car", 3rd International Conference on "Innovation and Reliability in Automotive Design and Tests", (1993).
8. Bowyer, A., "Computing Dirichlet Tessellations", The Computer Journal, Vol. 24, No. 2, pp162-166, 1981.
9. Carr, G.W., Motor Industry Research Association, Private Communication.
10. Carr, G.W., "Validation of CFD Codes for Predicting Aerodynamic Performance", Automotive Engineering, 921001, Oct/Nov 92.
11. Corral, R., Barroso, J. M. & Burgos, M. A., "Automatic Mesh Generation by a Mixed Advancing-Front Delaunay Approach", ASME 97-GT-91, 1997.

12. Craft, T.J. & Launder, B.E., "Computation of Impinging Flows using Second-Moment Closures", 8th Symposium on Turbulent Shear Flows, Munich, 9th-11th Sept., 1991.
13. Driver, D.M. and Seegmiller, H.L., "Features of a Reattaching Turbulent Shear Layer in Divergent Channel Flow," AIAA Journal, Vol. 23, No.2, pp. 163-171, 1985.
14. Fluent Inc., Reference Manuals, 1999.
15. Freitag, L. A. & Ollivier-Gooch, C., "A comparison of Tetrahedral Mesh Improvement Techniques", 5th International Meshing Round Table, Pittsburgh, October 1996.
16. Frey, P. J., Borouchaki, H. & George, P., "Delaunay Tetrahedralisation using an Advancing-Front Approach", 5th International Meshing Round Table, Pittsburgh, October 1996.
17. Gaylard, A.P., Baxendale, A.J. and Howell, J.P., "The Use of CFD to Predict the Aerodynamic Characteristics Of Simple Automotive Shapes", SAE paper 980036, 1998.
18. George, P. L., Hecht, F. & Saltel, E., "Constraint of the Boundary and Automatic Mesh Generation", 2nd Int. Numerical Grid Conf., Miami, 1988.
19. Ghia, Ghia, and Shin, "Flow Within a Lid Driven Cavity", Journal of Computational Physics, Vol. 48, pp. 387-411, 1982
20. Gibson, M.M. and Launder, B.E., "Ground Effects on Pressure Fluctuations in the Atmospheric Boundary Layer", J. Fluid Mech., 86, p491, 1978.
21. Gillieron, P., Samuel, S. and Chometon, F., "Potential of CFD in Analysis of Under-Bonnet Airflow Phenomena", SAE paper 1999-01-0802, 1999.
22. Graysmith, J., Baxendale, A.J. & Haynes, T., "Validating Two Codes for External Flow", I. Mech. E. seminar "The Validation of Computational Techniques in Vehicle Design, Stage One: CFD", April 1994.

23. Green, P. J. & Sibson, R., "Computing Dirichlet Tessellations in the Plane", *The Computer Journal*, Vol. 21, No. 2, pp168-173, 1977.
24. Grun, N., "Simulating External Vehicle Aerodynamics with Carflow", SAE 960679, 1996.
25. Gu, C. Y., Jones, I. P., Simcox, S., Ramnefors, M. & Svantesson, J., "Vehicle Aerodynamics Using CFDS-FLOW3D", Royal Aeronautical Society Conference on Vehicle Aerodynamics, Loughborough, July 1994.
26. Hajiloo, A., Williams, J., Hacket, J. E., and Thompson, S. A., "Limited Mesh Refinement Study of the Aerodynamic Flow Field Around a Car-Like Experimental Fluid Dynamics", SAE 960677, 1996.
27. Han, T., "Computational Analysis of Three Dimensional Turbulent Flow Around a Bluff Body in Ground Proximity", *AIAA Jnl*, Vol 27, No. 9, pp1213-1219, 1989.
28. Han, T., Sumantran, V., Harris, C., Kuzmanov, T., Huebler, M. and Zak, T., "Flow-Field Simulations of Three Simplified Vehicle Shapes and Comparisons with Experimental Measurements", SAE 960678. 1996.
29. Harinouchi, N., Yoshihiro, K. and Tagayashi, Y., "Numerical Investigation of Vehicle Aerodynamics with Overlaid Grid System", SAE 950628, 1995.
30. Hashiguchi, M., Kawaguchi, K., Yamasaki, R. & Kuwahara, K., "Computational Study of the Wake Structure of a Simplified Ground-Vehicle Shape with Base Slant", SAE technical paper 890597, International Congress and Exposition, Detroit, 1989.
31. Hashiguchi, M., Ohta, T. & Kuwahara, K., "Computational Study of Aerodynamic Behaviour of a Car Configuration", AIAA paper, 871386, 1987.
32. Hawkins, I.R., Simcox, S. & Shaw, C.T., "Predicting the Flow Characteristics and Aerodynamic Forces of Road Vehicles Using Computational Fluid Dynamics", AEA Technology Internal Paper.
33. Heckbert, P. S. & Bossen, F. J., "A Pliant Method for Anisotropic Mesh Generation", 5th International Meshing Round Table, Pittsburgh, October 1996.

34. Hucho, W, et al., "Aerodynamics of Road Vehicles", ISBN 0-408-01422-9, Butterworths, 1987.
35. Jones, W.P. & Launder, B.E., "Prediction of Low Reynolds Number Phenomena with a Two Equation Model of Turbulence", Int. J. Heat and Mass Transfer, 16, p1189, 1973.
36. Kallinderis, Y., Khawaja, A. & McNorris, H., "Hybrid Prismatic Grid Generation for Complex Geometries", NASA. Lewis Research Center Report, "Surface Modeling, Grid Generation, and Related Issues in Computational Fluid Dynamic (CFD) Solutions". pp 311-332, Mar. 1995.
37. Kawguchi, K., Hashiguchi, M., Yamasaki, R. & Kuwahara, K., "Computational Study of the Aerodynamic Behaviour of a Three Dimensional Car Configuration", SAE Technical Paper 890598, International Congress and Exposition, Detroit, 1989.
38. Kataoka, T., China, H., Nakagawa, K., Yanagimoto, K. & Yoshida, M., "Numerical Simulation of Road Vehicle Aerodynamics and Effect of Aerodynamic Devices", SAE Paper 910597, Trans., Vol.100, Sect. 6, 1991.
39. Khan, M.A., "Numerical Prediction of Buoyant and Non-Buoyant Turbulent Impinging Flows", Ph.D. thesis, Univ. of London, 1993.
40. Kim, J., Kline, S.J. & Johnstone, J.P. "Investigation of a reattaching turbulent shearing layer : flow over a backward facing step". J. Fluid Eng., ASME Trans., 102, 302-308, 1980.
41. Kitoh, K. & Kobayashi, T., "A Review of CFD Methods and Their Application to Automobile Aerodynamics", SAE paper 920338, Trans., vol. 101, sect. 6, 1992
42. Kuriyama, T., "Numerical Simulation on Three Dimensional Aerodynamics using SCRYU", Proceedings of the 2nd International Conference on Super Computing in the Automotive Industry, 1988.
43. Larsson, L., Bromberg, L. & Janson, C., "A Zonal Method for Predicting External Automobile Aerodynamics", SAE Paper 910595, 1991.

44. Launder B. E. & Spalding D. B., " The Numerical Computation of Turbulent Flows", Computer Methods in Applied Mechanics and Engineering, 3:269--289, 1974.
45. Leonard, B.P., "A Stable and Accurate Convective Modelling Procedure Based on Quadratic Upstream Interpolation", Comp. Method. Appl. Mech. Eng., 19, pp59-98, 1979.
46. Little, A.R. & Manners, A.P., "Predictions of the Pressure Losses in 2D and 3D Model Dump Diffusers", ASME Paper 1993-GT-184, International Gas Turbine and Aeroengine Congress and Exposition, Cincinnati, Ohio, 24-27 May, 1993.
47. Lohner, R. & Parikh, P., "Generation of Three Dimensional Unstructured Grids by the Advancing-Front Method", Int. J. Num. Meth. Fluids 1988, Vol. 8, pp1135-1149.
48. Lohner, R., "Some Useful Data Structures for the Generation of Unstructured Grids", Communications in Applied Num. Meths., Vol. 4, pp123-135, 1988.
49. Manners, A.P., "The Calculation of the Flows in Gas Turbine Combustion Systems", Ph.D. thesis, Univ. of London, 1988.
50. Manners, A.P. & King, R.A., "Grid Generation for Complex Gas Turbine Combustion Systems", New Techniques in Mathematics and Computational Modelling of Turbulent Diffusion and Mixing Industrial and Environmental Problems, Loughborough, 26-28 March, 1991.
51. Mavriplis, D. J., "An Advancing-Front Delaunay Triangulation Algorithm Designed for Robustness", ICASE Report No. 92-49, 1992.
52. Mavriplis, D. J., "Unstructured Mesh Generation and Adaptivity", ICASE Report No. 95-26, 1995.
53. Morel, T., "The Effects of Base Slant on the Flow Pattern and Drag of Three Dimensional Bodies With Blunt Ends", Proceedings of Symposium on Aerodynamic Drag Mechanisms of Bluff Bodies and Road Vehicles, (Editors G. Sovran et al.), Plenum Press, New York, pp191-226, 1978.

54. Muller, J-D., "The Advancing-Front Method and The Delaunay Triangulation, A Review with a look at Data Structures, Vertex Generation and Grid Quality", VKI lecture series on Grid Generation 1994.
55. Ono, K., Himeno, R., Fujitani, K. & Uematsu, Y., "Simultaneous Computation of the External Flow around a Car Body and the Internal Flow Through its Engine Compartment", SAE Trans. vol 101 section 6, 920342, 1992.
56. Okumura, K. and Kuriyama, T., "Practical Aerodynamic Simulations (C_D , C_L and C_{ym}) Using a Turbulence Model and 3rd-Order Upwind Scheme", SAE 950629, 1995.
57. Papadimitriou, C., "The Prediction of Turbulent Stable-Stratified Buoyant Flows", Ph.D. thesis, Univ of London, 1985.
58. Parthasarathy, V. N, Graichen, C. M. & Hathaway, A. F., "A Comparison of Tetrahedron Quality Measures", Finite Elements in Analysis and Design 15, pp255-261, 1993.
59. Passmore, M. A. & Le Good, G. M. , "A Detailed Drag Study Using The Coast-Down Method", SAE paper 940420, 1994.
60. Patankar, S.V. & Spalding D.B., "A Calculation Procedure for Heat, Mass and Momentum Transfer in Three-Dimensional Parabolic Flows", Int. J. Heat and Mass Transfer, 15, p1787, 1972.
61. Pearson, W. E., Manners, A. P. and Passmore, M. A., "Prediction of the Flow Around a Bluff Body in Close Proximity to the Ground", Royal Aeronautical Society Conference on Vehicle Aerodynamics, Loughborough, July 1994
62. Perzon, S. and Janson, J., "On Comparisons Between CFD Methods and Wind Tunnel Tests on a Bluff Body", SAE 1999-01-0805, 1999.
63. Pien, W., Hutchings, B. J., "Computation of Three Dimensional Vehicle Aerodynamics Using FLUENT/BFC", Proceedings of the 2nd International Conference on Super Computing in the Automotive Industry, 1988.
64. Pirzadeh, S., "Structured Background Grids for Generation of Unstructured grids by Advancing Front Method", AIAA Journal, Vol 31, No. 2, pp257-265, 1993.

65. Pirzadeh, S., "Unstructured Viscous Grid Generation by the Advancing Layers Method", AIAA Journal, Vol 32, No. 8, pp1735-1737, 1994.
66. Preparata, F. P., & Shamos, M. I., "Computational Geometry, an Introduction.", Texts and Monographs in Computer Science. Springer- Verlag, 1985.
67. Przekwas A. J., Jiang Y. & Tan Z., "Unstructured adaptive grid solution methodology for Automotive Aerodynamics", SAE Paper 970142 (SP-1232), 1997.
68. Raghu, S., Heil, F. and Santamarina, A., "Windshield Spray Performance at High Vehicle Speeds", SAE paper 1999-01-0803, 1999.
69. Ramnefors, M., Perzon, S. & Davidsson, L., "Accuracy in Drag Predictions on Automobiles", Royal Aeronautical Society Conference on Vehicle Aerodynamics, Loughborough, July 1994
70. Ramnefors, M., Bensryd, R., Holmberg, E. and Perzon, S., "Accuracy of Drag Predictions on Cars Using CFD - Effect of Grid Refinement and Turbulence Models", 960681, 1996.
71. Rawnsley, S. M. & Tatchell, D. G., "Application of the PHOENICS Code to the Computation of the Flow Around Automobiles", SAE paper 868217, International Congress and Exposition, Detroit, Feb 1986.
72. Rhee C.M. & Chow W.L., "A Numerical Study of the Turbulent Flow Past an Isolated Airfoil", AIAA-82-0998, AIAA Jnl., 21, No. 11, pp1525-1532, 1983.
73. Richter, R., "Discontinuity Capturing Using Auto-Adaptive Finite Elements", 5th International Meshing Round Table, Pittsburgh, October 1996.
74. Shaw C.T. & Simcox S., "The Numerical Prediction of the Flow Around a Simplified Vehicle Geometry", Proceedings of the 2nd International Conference on Super Computing in the Automotive Industry, 1988.
75. Shaw C.T., "Predicting Vehicle Aerodynamics Using Computational Fluid Dynamics - A Users Perspective", SAE Paper 880455, 1988.
76. Shir C.C., "A Preliminary Numerical Study of Atmospheric Turbulent Flows in the Idealised Planetary Boundary Layer", J. Atmos. Sci., 30, p1327, 1973.

87. Yamada A. & Ito S., "Computational Analysis of Flow Around a Simplified Vehicle-Like Body", SAE Paper 930293, International Congress and Exposition, Detroit, March 1-5, 1993.
88. Yanagimoto K., Nakagawa K. China H., Kimura T., Yamamoto M. & Sumi T., "The Aerodynamic Development of a Small Speciality Car", SAE Paper 940325, 1994.

